VOLUME 77 AUGUST 2, 1973 / NUMBER 16

JPCHAx

THE JOURNAL OF PHYSICAL CHEMISTRY

PUBLISHED BIWEEKLY BY THE AMERICAN CHEMICAL SOCIETY

THE JOURNAL OF

PHYSICAL CHEMISTRY

AMERICAN CHEMICAL SOCIETY, *1155 Sixteenth St., N.W., Washington, D.C. 20036*

Books and Journals Division

JOHN K CRUM *Director*
RUTH REYNARD *Assistant to the Director*

CHARLES R. BERTSCH *Head, Editorial Processing Department*
D. H. MICHAEL BOWEN *Head, Journals Department*
BACIL GUILEY *Head, Graphics and Production Department*
SELDON W. TERRANT *Head, Research and Development Department*

 Published biweekly by the American Chemical Society at 20th and Northampton Sts., Easton, Pa. 18042. Second-class postage paid at Washington, D. C., and at additional mailing offices.

All manuscripts should be sent to *The Journal of Physical Chemistry*, Department of Chemistry, University of Minnesota, Minneapolis, Minn. 55455.

Additions and Corrections are published once yearly in the final issue. See Volume 76, Number 26 for the proper form.

Extensive or unusual alterations in an article after it has been set in type are made at the author's expense, and it is understood that by requesting such alterations the author agrees to defray the cost thereof.

The American Chemical Society and the Editor of *The Journal of Physical Chemistry* assume no responsibility for the statements and opinions advanced by contributors.

Correspondence regarding accepted copy, proofs, and reprints should be directed to Editorial Processing Department, American Chemical Society, 20th and Northampton Sts., Easton, Pa. 18042. Head: CHARLES R. BERTSCH. Assistant Editor: EDWARD A. BORGER. Editorial Assistant: JOSEPH E. YURVATI.

Advertising Office: Centcom, Ltd., 142 East Avenue, Norwalk, Conn. 06851.

Business and Subscription Information

Send all new and renewal subscriptions *with payment* to: Office of the Controller, 1155 16th Street, N.W., Washington, D. C. 20036. Subscriptions should be renewed promptly to avoid a break in your series. All correspondence and telephone calls regarding changes of address, claims for missing issues, subscription service, the status of records, and accounts should be directed to Manager, Membership and Subscription Services, American Chemical Society, P.O. Box 3337, Columbus, Ohio 43210. Telephone (614) 421-7230.

On changes of address, include both old and new addresses with ZIP code numbers, accompanied by mailing label from a recent issue. Allow four weeks for change to become effective.

Claims for missing numbers will not be allowed (1) if loss was due to failure of notice of change in address to be received before the date specified, (2) if received more than sixty days from date of issue plus time normally required for postal delivery of journal and claim, or (3) if the reason for the claim is "issue missing from files."

Subscription rates (1973): members of the American Chemical Society, $20.00 for 1 year; to nonmembers, $60.00 for 1 year. Those interested in becoming members should write to the Admissions Department, American Chemical Society, 1155 Sixteenth St., N.W., Washington, D. C. 20036. Postage to Canada and countries in the Pan-American Union, $5.00; all other countries, $6.00. Single copies for current year: $3.00. Rates for back issues from Volume 56 to date are available from the Special Issues Sales Department, 1155 Sixteenth St., N.W., Washington, D. C. 20036.

Subscriptions to this and the other ACS periodical publications are available on microfilm. Supplementary material not printed in this journal is now available in microfiche form on a current subscription basis. For information on microfilm or microfiche subscriptions, write Special Issues Sales Department at the address above.

Notice to Authors last printed in the issue of June 21, 1973

THE JOURNAL OF

PHYSICAL CHEMISTRY

Volume 77, Number 16 August 2, 1973

JPCHAx 77(16) 1929–2020 (1973)
ISSN 0022-3654

COMMUNICATIONS TO THE EDITOR

■ Supplementary material for this paper is available separately, in photocopy or microfiche form. Ordering information is given in the paper.

*In papers with more than one author, the asterisk indicates the name of the author to whom inquiries about the paper should be addressed.

AUTHOR INDEX

ANNOUNCEMENT

On the last two pages of this issue you will find reproduced the table of contents of the July 1973 issue of the Journal of Chemical and Engineering Data.

THE JOURNAL OF
PHYSICAL CHEMISTRY

VOLUME 77, NUMBER 16 AUGUST 2, 1973

Reaction of Dinitrogen Pentoxide with Water

E. D. Morris, Jr.,* and H. Niki

Scientific Research Staff, Ford Motor Company, Dearborn, Michigan 48121 *(Received March 16, 1973)*
Publication costs assisted by the Ford Motor Company

Dinitrogen pentoxide is formed in the atmosphere by the reaction of O_3 and NO_2. One possible fate of N_2O_5 is the reaction $N_2O_5 + H_2O \rightarrow 2HNO_3$; however, a reliable rate constant for this reaction has not been available. In this report the reaction has been shown to proceed both *via* heterogenous and gas-phase mechanisms. An upper limit has been determined for the rate constant of 1.3×10^{-20} cm^3 molecule^{-1} sec^{-1} at 25°.

The reaction of NO_2 and O_3 in photochemical smog produces N_2O_5 *via* the mechanism

$$O_3 + NO_2 \longrightarrow O_2 + NO_3 \quad (1)$$

$$NO_3 + NO_2 \rightleftharpoons N_2O_5 \quad (2)$$

The subsequent fate of N_2O_5 affects the rate of NO_2 decay and the ultimate O_3 level. When N_2O_5 is placed in a glass vessel that has been rigorously baked under high vacuum to remove water and then conditioned to N_2O_5, the reaction

$$NO_3 + NO_2 \longrightarrow NO_2 + NO + O_2 \quad (3)$$

competes with reaction 2 to destroy N_2O_5. Under these conditions the half-life is known to be about 6 hr.[1-4]

In the study of the photolysis of NO_2 in the presence of HNO_3, Jaffe and Ford[5] state that a rate constant on the order of magnitude of 10^{-18} cm^3 molecule^{-1} sec^{-1} for the reaction

$$N_2O_5 + H_2O \longrightarrow 2HNO_3 \quad (4)$$

is necessary to explain their experimental data. This value has been frequently quoted in the literature as a gas-phase rate constant. In the same study these authors derive a rate constant of the order of magnitude 10^{-11} cm^3 molecule^{-1} sec^{-1} for the reaction

$$O + HNO_3 \longrightarrow OH + NO_3 \quad (5)$$

However, a more recent study[6] has shown $k_5 < 2 \times 10^{-14}$ cm^3 molecule^{-1} sec^{-1}. Thus the mechanism assumed by Jaffe and Ford appears to be erroneous. Another estimate of the rate constant for reaction 4 has been made in this laboratory[7] from data[8] on the photochemical oxidation of propylene in the presence of oxides of nitrogen at 50% relative humidity. To explain the observed NO_2 and O_3 profiles, a value of k_4 was needed that is several orders of magnitude smaller than that suggested by Jaffe and Ford. If $k_4 = 10^{-18}$ was used in the kinetic analysis, the predicted removal rate of NO_2 was much faster than the experimental results and the predicted O_3 level too low. Thus a more reliable study of the kinetics and mechanism of reaction 4 is required for the assessment of the role of N_2O_5 in smog formation. In the present paper, we have investigated the kinetic behavior of N_2O_5 in the presence of H_2O using long-path infrared spectroscopy.

Experimental Section

The reaction vessel was a Pyrex cylinder 12-in. i.d. and 36 in. in length. Water and N_2O_5 were measured *in situ* with a Perkin-Elmer 421 infrared spectrometer equipped with a 40-m path length cell. The optical system consisting of mirrors, mirror mountings, and optical bench was placed inside the Pyrex reactor. All metal parts except the mirror surfaces were coated with Teflon. Plexiglas flanges were used to couple the Pyrex cylinder to the infrared instrument. This apparatus was originally designed to minimize the wall decomposition of ozone. The lifetime of ozone at the 1 ppm level was typically 10 hr. Between experiments the reactor was evacuated to below 0.1 Torr with a mechanical pump. The leak rate under vacuum

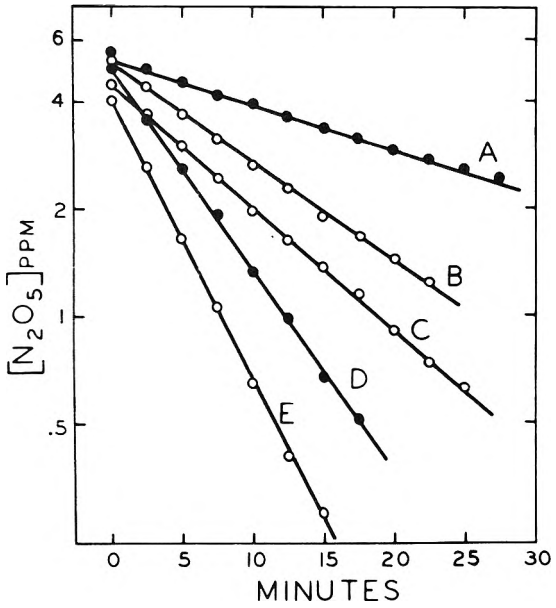

Figure 1. Exponential decay of N_2O_5 at various water concentrations: curve A, "dry;" curve B, 3.2×10^{16}; curve C, 6.1×10^{16}; curve D, 12.4×10^{16}; curve E, 17.5×10^{16} molecules/cm^3.

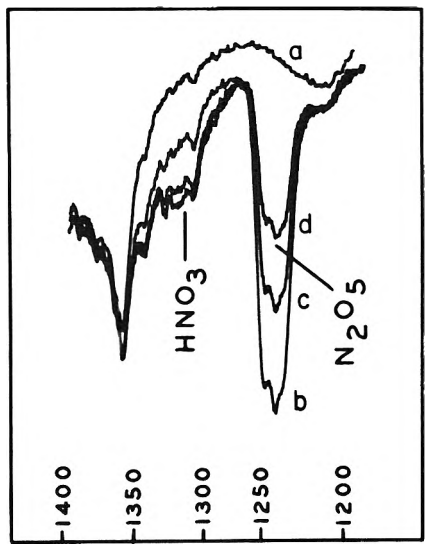

Figure 2. Increase in HNO_3 as N_2O_5 decays in the dry system: (a) background, (b) initial scan, (c) after 10 min, (d) after 20 min.

was 10 Torr in 24 hr. After the cell was allowed to stand idle overnight, the next experiment consistently gave a faster decay of N_2O_5 than subsequent runs. Therefore, the standard procedure was adopted of treating the cell with 6 ppm of N_2O_5 prior to experiments to recondition the walls to a reproducible state.

N_2O_5 was generated either directly in the reaction cell, or by an independent preparation, stored in a cold trap. To generate N_2O_5 in the cell, 12 ppm of NO_2 was added to the cell containing 25 ppm of O_3 from ozonized oxygen. This produced a mixture of 6 ppm of N_2O_5 and residual O_3. At this initial concentration of O_3, NO_2 has a half-life of 10 sec and is virtually all converted to N_2O_5 within 1–2 min. Pure N_2O_5 was prepared according to the method of Schott and Davidson.[9] In this method NO_2 is added to a stream of dried oxygen which has been passed through a silent discharge ozonizer. The flow of NO_2 is reduced until the brown color is no longer visible downstream of the mixing point. When the proper flows are established, N_2O_5 can be collected in a trap at Dry Ice temperature. The N_2O_5 was introduced by flowing helium as a carrier gas through the trap and into the reaction chamber. This flow was continued until ir absorption indicated approximately 6 ppm of N_2O_5. This initial concentration was required to monitor the decay over an order of magnitude with adequate detection sensitivity. Thus this initial concentration was used in most experiments.

The concentration of N_2O_5 was measured by following the infrared absorption at 1245 cm^{-1}. At the end of each experiment, excess NO was added to convert any remaining N_2O_5 to NO_2. This method was used to determine the baseline accurately. Several water peaks in the region 1560–1500 cm^{-1} were calibrated both by filling the cell with room air of known humidity and also by adding measured amounts of water-saturated air to the cell. In actual experiments, once calibrations were made, water was introduced by flowing compressed air through a bubbler into the cell. The ir absorption at several wavelengths was then used to determine the water concentration. As measured by this method, the "dry" system contained less than 0.5×10^{16} molecules/cm^3 of water. Experiments were preformed at a total pressure of 650 Torr with argon as a diluent. Independent experiments have shown that even at this pressure there is constant mixing within the cell. Gas introduced at one end of the reactor reached the opposite end in 1–2 min.

Results

When 6 ppm of N_2O_5 in dry argon was placed in the Pyrex reaction cell, it decayed with a half-life of 20–30 min. From the reported unimolecular dissociation rate, a half-life on the order of 6 hr was expected. A plot of ln $[N_2O_5]$ *vs.* time appears nearly linear (curve A, Figure 1). However, closer examination of several such plots reveals a consistent deviation from linearity. If a straight line is drawn through the data, a first-order decay constant between 0.035 and 0.050 min^{-1} is obtained with either pure N_2O_5 or excess O_3 plus NO_2. The decay rate of N_2O_5 with an initial concentration of 6 ppm reproducibly fell between these limits for all experiments without added water. During the decay of N_2O_5, the infrared absorption due to HNO_3 was observed to increase.[10] Figure 2 shows the growth of the HNO_3 peak as N_2O_5 decreases. This nitric acid will disappear from the gas phase if allowed to stand in the reactor overnight. To determine whether concentration affected the rate of decay, 50 ppm of N_2O_5 was added to the cell. Since this amount of N_2O_5 reduces the infrared intensity to nearly zero, decay measurements had to be delayed until N_2O_5 was reduced to about 10 ppm. Under these conditions, a decay rate of 0.013 min^{-1} was observed.

The effect of added water on the N_2O_5 decay was determined for concentrations up to 18×10^{16} molecules/cm^3 (20% relative humidity). Higher concentrations of water would give decay rates too rapid to measure accurately. In the first set of experiments, 25 ppm of O_3 (ozonized oxygen), the desired amount of water, and diluent argon were added to the cell to a total pressure of 200 Torr. The water concentration was then measured by ir absorption

at the calibrated wavelengths. The spectrometer was set at 1245 cm^{-1} to monitor N_2O_5 and 12 ppm of NO_2 plus argon was added to a pressure of 650 Torr. N_2O_5 rapidly reached a maximum, and after 1–2 min began to decay exponentially. The plots of ln $[N_2O_5]$ against reaction time exhibited good linear behavior over a decade (Figure 1). The plot of d ln $[N_2O_5]/dt$ against $[H_2O]$ (Figure 3, curve A) gives a straight line with an intercept corresponding to the rate measured in the dry system. If the rate of the "background" decay is assumed to remain constant when water is added, the slope of this line then corresponds to a second-order rate constant of 1.3×10^{-20} cm^3 $molecule^{-1}$ sec^{-1}.

The effect of water was also studied with pure N_2O_5 which had been previously prepared and stored in a cold trap. Water was added and measured by the procedure mentioned above. N_2O_5 was introduced in a helium carrier to give 6–8 ppm. Argon was used to bring the total pressure to 650 Torr. The decay of N_2O_5 was again found to be exponential. The plot of d ln $[N_2O_5]/dt$ *vs.* $[H_2O]$ (Figure 3, curve B) gives a second-order rate constant of 1.3×10^{-20} cm^3 $molecule^{-1}$ sec^{-1} identical with that measured with excess O_3 present. In addition, experiments were performed at a total pressure of 200 Torr. The results were indistinguisable from those at 650 Torr.

To determine whether the walls had an effect on the N_2O_5 decay, the Pyrex cylinder was lined with a sleeve of 1/16-in. aluminum. This sleeve represents about 50% of the cell surface area. The remainder consists of the Plexiglas end flanges, gold-plated mirrors, and the Teflon-coated optical bench. The aluminum was conditioned by exposing it to ozone a number of times. Ozone then showed good stability in the aluminum-lined cell. When 6 ppm of N_2O_5 was first introduced, its decay was much faster than in the Pyrex system. Higher concentrations of N_2O_5 were added to treat the surfaces. Returning to the standard condition of 6 ppm of N_2O_5 in dry argon, the decay was much slower and in succeeding experiments the lifetime of N_2O_5 continued to increase. When the decay rate settled down between 0.060 and 0.070 min^{-1}, a water dependence experiment was carried out with pure N_2O_5. A plot of d ln $[N_2O_5]/dt$ *vs.* $[H_2O]$ gives a rate constant of approximately 2×10^{-20} cm^3 $molecule^{-1}$ sec^{-1}. In another set of experiments, a Teflon (TFE) sheet was used to cover the Pyrex surface. The decay of N_2O_5 in dry argon was then the same as in the Pyrex system. Adding water gave a rate constant of $1.5–2.0 \times 10^{-20}$ cm^3 $molecule^{-1}$ sec^{-1}. The data obtained using aluminum or Teflon sleeves show much more scatter than in the glass system, most likely because of the brief conditioning periods used. Thus an extensive effort was not expended to try to obtain a precise rate constant with these wall materials. The data are good enough to show there is not a major change when aluminum or Teflon are used.

Discussion

The observed decay of N_2O_5 in a dry system is much faster than expected solely from the unimolecular decay mechanism. Since the formation of HNO_3 was observed, reaction of N_2O_5 must be occurring with water adsorbed on the walls of the reactor. The heterogenous nature of this reaction is consistent with the fact that (1) the decay rate depends on the initial N_2O_5 concentration, (2) curvature is observed in the ln $[N_2O_5]$ *vs.* time plots, and (3) the rate is sensitive to the wall conditioning. From previous investigations of N_2O_5 decay, it appears that a thorough procedure of baking and high vacuum is required to minimize wall effects. Since the reactor used here was not subjected to such treatment, the observed short lifetime is understandable. The purpose of the present study is to investigate the effect of gas-phase water on N_2O_5; thus the walls of the reactor are going to contain adsorbed water. The exact numerical rate obtained for this wall effect is probably unique to the specific geometry and surface to volume ratio used here. However, a similar effect can be expected in most photochemical smog reactors.

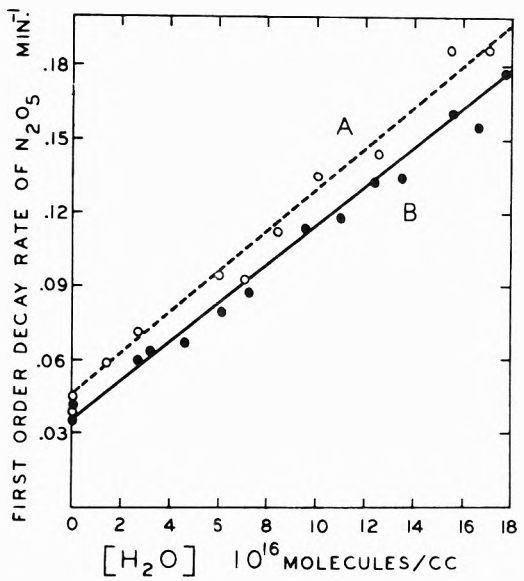

Figure 3. Rate of N_2O_5 decay as a function of H_2O: curve A, NO_2 + excess O_3; curve B, pure N_2O_5.

A number of experimental observations suggest that the increased decay with added water is due to a gas-phase reaction. The decay of N_2O_5 is exponential and shows first-order dependence on gas-phase water concentration. If the reaction is heterogenous, the amount of adsorbed water must be directly proportional to the gas-phase water concentration. Experiments with either pure N_2O_5 or NO_2 in excess O_3 give an apparent bimolecular rate constant of 1.3×10^{-20} cm^3 $molecule^{-1}$ sec^{-1}. The change in wall materials from Pyrex to aluminum to Teflon had only a small effect on this rate constant. It is very unlikely that the relationship between adsorbed and gas-phase water would be the same for the three different wall materials. Changing the total pressure from 650 to 200 Torr had no effect. It would be difficult to explain these observations in terms of a heterogenous reaction, although the possibility cannot be ruled out entirely. In any case, the present results clearly show the rate constant for the gas-phase reaction $N_2O_5 + H_2O$ to be equal to or less than 1.3×10^{-20} cm^3 $molecule^{-1}$ sec^{-1} at 25°. This value is two orders of magnitude smaller than the estimate of Jaffe and Ford. Thus Niki, Daby, and Weinstock[7] were justified in using a smaller rate for k_4 in their smog mechanism. A number of other atmospheric models[11] have also incorporated the reaction of N_2O_5 with water. Some of these authors used Jaffe and Ford's estimate of k_4 while others used a value to suit their data. All these models should be reevaluated in light of the present work. It has been shown that the reaction of N_2O_5 with water most likely occurs by both heterogenous and gas-phase mecha-

nisms. In the atmosphere, the reaction of N_2O_5 to form HNO_3 would be expected to be affected both by humidity and by reaction on particulate matter.

References and Notes

(1) Review by F. Daniels and R. A. Alberty, "Physical Chemistry," Wiley, New York, N. Y., 1955, p 342.
(2) Review by H. S. Johnston, "Gas Phase Reaction Rate Theory," Ronald Press, New York, N. Y., 1966, p 14.
(3) F. Daniels and E. H. Johnston, *J. Amer. Chem. Soc.*, **43**, 53 (1921).
(4) R. A. Ogg, Jr., *J. Chem. Phys.*, **15**, 377 (1947); **15**, 613 (1947).
(5) S. Jaffe and H. W. Ford, *J. Phys. Chem.*, **71**, 1832 (1967).
(6) E. D. Morris, Jr., and H. Niki, *J. Phys. Chem.*, **75**, 3193 (1971).
(7) H. Niki, E. E. Daby, and B. Weinstock, "Mechanism of Smog Reactions," *Advan. Chem. Ser.*, **No. 113** (1972).
(8) A. P. Altshuller, S. L. Kopczynski, W. A. Lonneman, T. L. Becker, and R. Slater, *Environ. Sci. Technol.*, **1**, 899 (1967); and also private communication.
(9) G. Schott and N. Davidson, *J. Amer. Chem. Soc.*, **80**, 1841 (1958).
(10) R. E. Nightingale, A. R. Downie, D. L. Rotenberg, B. Crawford, Jr., and R. A. Ogg, Jr., *J. Phys. Chem.*, **58**, 1047 (1954).
(11) For example, H. S. Johnston, *Science*, **173**, 517 (1971); T. A. Hecht and J. H. Seinfeld, *Environ. Sci. Technol.*, **6**, 47 (1972); H. Levy, II, *Planet. Space Sci.*, **20**, 919 (1972); P. J. Crutzen, *J. Geophys. Res.*, **76**, 7311 (1971).

Reaction of HO_2 with O_3

R. Simonaitis and Julian Heicklen*

Department of Chemistry and Ionosphere Research Laboratory, Pennsylvania State University, University Park, Pennsylvania 16802

(Received April 2, 1973)

Publication costs assisted by the National Science Foundation

Ozone was photolyzed with 2537-Å radiation in the presence of excess O_2 and H_2 at 225, 250, and 298°K. The quantum yield of O_3 disappearance, $-\Phi\{O_3\}$, was measured. The $O(^1D)$ atom produced in the photolysis reacted with H_2 to initiate the chain decomposition of O_3 by HO_2 radicals: $HO_2 + O_3 \rightarrow HO + 2O_2$ (2). The chains were terminated by the reaction $2HO_2 \rightarrow H_2O_2 + O_2$ (18). The detailed reaction mechanism is given and leads to the simple rate law $-\Phi\{O_3\} - 1 = k_2[O_3]/(k_{18}I_a)^{1/2}$, where I_a is the absorbed intensity. From plots of $-\Phi\{O_3\} - 1$ *vs.* $[O_3]/I_a^{1/2}$, $k_2/k_{18}^{1/2}$ was found to be $1.9 \times 10^{-8} \exp(-2000/RT)$ $cm^{3/2}/sec^{1/2}$. If k_{18} is taken to be 3.0×10^{-12} cm^3/sec, independent of temperature, then $k_2 = 3.3 \times 10^{-14} \exp(-2000/RT)$ cm^3/sec, where $R = 1.987$ cal/mol °K.

Introduction

For a long time it has been known[1,2] that the photodecomposition of O_3 with radiation between 2100 and 2800 Å in the presence of H_2O leads to a long chain decomposition of O_3. Norrish and his coworkers[3-5] suggested that the chain decomposition could proceed *via* the reactions

$$HO + O_3 \longrightarrow HO_2 + O_2 \quad (1)$$

$$HO_2 + O_3 \longrightarrow HO + 2O_2 \quad (2)$$

For a time it was believed that this sequence was an important mechanism for O_3 destruction in the stratosphere.

De More[6] raised objections to reactions 1 and 2, based on a comparison with Kaufman's results.[7] De More proposed that the chain steps were

$$HO^* + O_3 \longrightarrow H + 2O_2 \quad (3)$$

$$H + O_3 \longrightarrow HO^* + O_2 \quad (4)$$

where HO^* is vibrationally excited HO. Support for this hypothesis was obtained from the liquid-phase photolysis of O_3 at −186°. In that system, the addition of O_2 suppressed the chain indicating that O_2 scavenged the H atoms and that HO_2 did not react with O_3, at least at low temperatures in the liquid phase. The failure of the Norrish mechanism appeared confirmed with the flash-photolysis results of Langley and McGrath[8] who reported that low-lying levels of HO ($v = 0,1$) did not react with O_3, *i.e.*, $k_1 < 10^{-16}$ cm^3/sec. Furthermore, Potter, *et al.*,[9] found that HO^* ($v = 9$) reacted readily with O_3, thus substantiating reaction 3. The reaction scheme of De More was adopted by Lissi and Heicklen[10] in their studies of the photolysis of wet ozone, even though this scheme required that H_2O be extremely inefficient in quenching HO^*. Also the Norrish mechanism has been discarded in recent aeronomical models of the stratosphere.[11]

Recently, however, evidence has appeared which indicates that reaction 1 may be important. Coltharp, *et al.*,[12] have now measured the reactivity of HO^* with O_3 for each vibrational level between 2 and 9, and find rate coefficients varying from 2×10^{-12} cm^3/sec for $v = 2$ to 8×10^{-12} cm^3/sec for $v = 9$. Extrapolation of their data suggests that for $v = 0$, the rate coefficient will be orders of magnitude greater than 10^{-16} cm^3/sec. Also, Kaufman and Anderson[13] have preliminary results indicating that $k_1 \sim 6 \times 10^{-14}$ cm^3/sec.

It appears that the report of Langley and McGrath[8] may be incorrect. If so, the conclusion of De More[6] may also be in error, and the Norrish mechanism may be operative. The only measurement for k_2 was done at −186° in the liquid phase.[6] Perhaps at higher temperatures in the

gas phase reaction 2 can be important. In view of the importance of reaction 2 in regard to the possible destruction of O_3 in the stratosphere by H_2O emitted from the supersonic transport, we have measured the rate coefficient for reaction 2 at stratospheric temperatures, and those results are reported here.

After our work was completed, a new report by De More[14] came to our attention (not published at the time of this writing). He has measured k_1 at 300°K and obtains a value of 8×10^{-14} cm³/sec in reasonable agreement with the values suggested by the other recent work.[12,13] He also obtained an approximate value of $\sim 3 \times 10^{-15}$ cm³/sec for k_2 at 300°K.

In our work HO_2 radicals were produced from the photolysis of O_3 at 2537 Å in the presence of excess H_2 and O_2. The $O(^1D)$ atoms produced from the photolysis of O_3 react with H_2 to produce HO radicals and H atoms. The HO radicals react with H_2 to give H_2O and more H atoms. All the H atoms then add to O_2 to produce HO_2 radicals. The quantum yield of O_3 removal, $-\Phi\{O_3\}$, is measured; from this measurement, the importance of reaction 2 is determined.

Experimental Section

The experiments were performed in a conventional Hg-free high-vacuum glass line equipped with Teflon stopcocks with Viton O rings. The cylindrical quartz reaction cell was 10 cm long and 5 cm in diameter. The cell was enclosed in an insulated box through which cold N_2 could be circulated for low-temperature measurements.

The radiation was from a Phillips 93109E low-pressure Hg resonance lamp. Before entering the reaction cell, the radiation was passed through a cell with chlorine vapor to remove radiation above 3000 Å and a Corning CS 9-54 filter to remove radiation below 2200 Å. Thus, the effective radiation entering the reaction cell was at 2537 Å.

Ozone pressures were measured spectrophotometrically, and could be monitored continuously. It was established that Beer's law was obeyed at all temperatures. The absorption cross sections measured were 1.04×10^{-17} and 0.98×10^{-17} cm² respectively at 298 and 225°K in good agreement with the accepted value[15] of 1.12×10^{-17} cm² at 298°K. Quantum yields of O_3 decay were obtained from the initial rate of O_3 removal. The actinometry employed was from the low-pressure photolysis of O_3, for which $-\Phi\{O_3\} = 5.0$.[10]

The O_3 was prepared from a tesla coil discharge of O_2. It was distilled at −186° before use. Prepurified Grade H_2 and Extra Dry Grade O_2 from the Matheson Co. were used after passage through a trap at −196°.

Results

The results of the photolysis of O_3 in the presence of H_2 and O_2 at 225, 250, and 298°K are shown in Table I. Most of the experiments were performed at H_2 pressures of 614 Torr and O_2 pressures of 86 Torr. The O_3 pressure was varied from 48 to 266 mTorr, almost a factor of 6. The absorbed intensity, I_a, was varied from 0.065 to 54 mTorr/min, a factor of 830. The quantum yield of O_3 disappearance, $-\Phi\{O_3\}$, rises from a lower limiting value of one as the O_3 pressure is raised or I_a is reduced. In fact, the table indicates that $-\Phi\{O_3\}$ can be correlated with the parameter $[O_3]/I_a^{1/2}$.

In one series of runs at 298°K, the O_2 pressure was varied from 5.8 to 86 Torr, a factor of 15. Except for the experiment at 5.8 Torr of O_2, there is no effect of O_2 pressure on $-\Phi\{O_3\}$. Even with 5.8 Torr, $-\Phi\{O_3\}$ has only risen from 4.2 to 6.4. If the O_2 is omitted altogether, the O_3 consumption is almost instantaneous at first, but slows down as the O_2 produced in the reaction accumulates in the system.

In another series of runs at 298°K, the H_2 pressure was reduced. A reduction from 614 to 314 Torr did not change

TABLE I: Photolysis of O_3 at 2537 Å in the Presence of Excess H_2 and O_2[a]

$[O_3]/I_a^{1/2}$ (mTorr min)$^{1/2}$	$[O_3]$, mTorr	I_a, mTorr/min	$-\Phi\{O_3\}$
	$T = 225$°K		
130	66	0.26	2.7
189	134	0.50	3.6
540	145	0.070	6.8
600	150	0.065	6.0
600	150	0.065	7.0
	$T = 250$°K		
93	86	0.87	2.9
150	94	0.39	3.9
159	120	0.57	3.7
166	133	0.64	3.3
194	137	0.50	4.0
204	140	0.48	5.3
470	165	0.120	8.7
540	200	0.135	9.3
600	208	0.120	10.5
	$T = 298$°K		
14	57	16.0	1.2
20	100	25.7	1.8
31	254	54.0	2.2
52	48	0.83	2.7
53	63	1.39	2.7
54	63	1.39	2.6
68	70	1.04	2.2
73	100	1.88	3.2
73	100	1.88	3.3
76	123	2.60	3.2
99	115	1.38	6.4[b]
99	115	1.38	4.4[c]
99	115	1.38	4.2[d]
99	115	1.38	4.2
108	115	1.13	4.4[e]
108	115	1.13	5.7[f]
120	205	2.90	6.4
148	109	0.55	6.5
158	209	1.76	6.4
188	266	1.99	7.0
345	97	0.079	8.5
358	107	0.090	10.6
359	95	0.070	10.0
530	210	0.156	16.0
615	246	0.160	16.0
700	254	0.130	20.0

[a] Except where indicated $[H_2] = 614$ Torr, $[O_2] = 86$ Torr. [b] $[H_2] = 694$ Torr, $[O_2] = 5.8$ Torr. [c] $[H_2] = 680$ Torr, $[O_2] = 19$ Torr. [d] $[H_2] = 661$ Torr, $[O_2] = 39$ Torr. [e] $[H_2] = 314$ Torr, $[O_2] = 86$ Torr. [f] $[H_2] = 125$ Torr, $[O_2] = 85$ Torr.

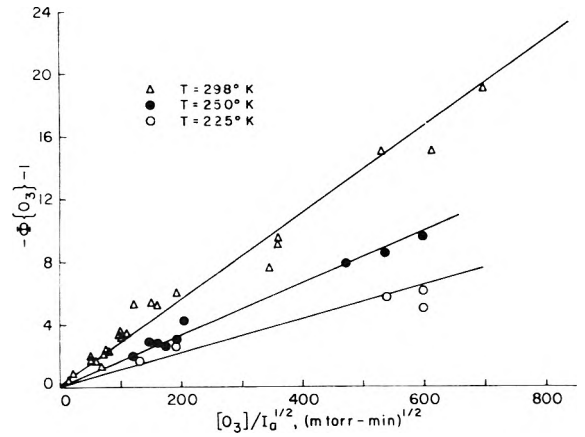

Figure 1. Plots of $-\Phi\{O_3\} - 1$ *vs.* $[O_3]/I_a^{1/2}$ in the photolysis of O_3 at 2537 Å in the presence of excess H_2 and O_2 at various temperatures.

$-\Phi\{O_3\}$, but when the H_2 pressure was reduced to 125 Torr, $-\Phi\{O_3\}$ rose from 4.2 to 5.7.

Discussion

The results can be understood in terms of a chain mechanism initiated by the photolysis of O_3. The photolysis of O_3 at 2537 Å is known to give $O_2(^1\Delta)$ and $O(^1D)$ all the time[10]

$$O_3 + h\nu \longrightarrow O_2(^1\Delta) + O(^1D) \quad (5)$$

The $O_2(^1\Delta)$ fragment might react, in principle, with any of the gases

$$O_2(^1\Delta) + O_3 \longrightarrow 2O_2 + O(^3P) \quad (6)$$

$$O_2(^1\Delta) + O_2 \longrightarrow 2O_2 \quad (7)$$

$$O_2(^1\Delta) + H_2 \longrightarrow \text{products} \quad (8)$$

The rate constant for reaction 6 is[16,17] 5×10^{-11} exp$(-5650/RT)$ cm^3/sec. For reaction 7, $k_7 = 2 \times 10^{-18}$ cm^3/sec at room temperature,[18,19] and can be no faster at lower temperatures. Apparently reaction 8 is so slow that its rate coefficient has never been measured. Thus reaction 8 can be ignored, but both reactions 6 and 7 can play a role in our system.

The $O(^3P)$ atom produced in reaction 6 might also react with any of the gases

$$O(^3P) + O_3 \longrightarrow 2O_2 \quad (9)$$

$$O(^3P) + O_2 + M \longrightarrow O_3 + M \quad (10)$$

$$O(^3P) + H_2 \longrightarrow HO + H \quad (11)$$

For the above reactions $k_9 = 1.3 \times 10^{-11}$ exp$(-4400/RT)$ cm^3/sec,[20,21] $k_{10} = 6.6 \times 10^{-35}$ exp$(1014/RT)$ cm^3/sec[22] for Ar as a chaperone, and $k_{11} = 2.9 \times 10^{-11}$ exp$(-9450/RT)$ cm^3/sec.[23] Consequently for all of our experiments, reactions 9 and 11 are unimportant.

The $O(^1D)$ atom produced in the primary photolytic act could also react with all the gases

$$O(^1D) + O_3 \longrightarrow 2O_2 \quad (12)$$

$$O(^1D) + O_2 \longrightarrow O(^3P) + O_2 \quad (13)$$

$$O(^1D) + H_2 \longrightarrow HO + H \quad (14)$$

TABLE II: Values of $k_2/k_{18}^{1/2}$ as a Function of Temperature

T, °K	$k_2/k_{18}^{1/2}$, (mTorr min)$^{-1/2}$	$10^{10}k_2/k_{18}^{1/2}$, cm$^{3/2}$/sec$^{1/2}$ [a]
298	0.0277	6.4
250	0.0164	3.4
225	0.0108	2.1

[a] $k_2/k_{18}^{1/2} = 1.9 \times 10^{-8}$ exp$(-2000/RT)$ cm$^{3/2}$/sec$^{1/2}$, with R = 1.987 cal/mol °K.

For these reactions, the relative reactivities are[10,24-26] $k_{12}/k_{13}/k_{14} = 10/1/10$. Thus in all of our experiments, reactions 12 and 13 can be neglected.

The HO radical produced in reaction 14 might react with either O_3 or H_2

$$HO + O_3 \longrightarrow HO_2 + O_2 \quad (1)$$

$$HO + H_2 \longrightarrow H_2O + H \quad (15)$$

The rate coefficients for the reactions are $k_1 \sim 10^{-13}$ cm^3/sec at 298°K,[12-14] and $k_{15} = 3.7 \times 10^{-11}$ exp$(-5150/RT)$ cm^3/sec.[23] Thus, for all of our experiments, with the possible exception of that with 125 Torr of H_2, reaction 1 is unimportant. Of course, the HO radicals produced in reaction 14 could be excited to the fourth vibrational level, in which case k_1 could be as large as 2.8×10^{-12} cm^3/sec.[12] However, it would be expected that k_{15} would be enhanced even more than k_1 by vibrational excitation of HO, so that reaction 1 would still be of no consequence.

It is of interest to note that even if the rate coefficients were in error and that reaction 1 dominated reaction 15, rather than *vice versa*, the results would not be much affected. If HO radicals produced in reaction 14 reacted by reaction 1 rather than reaction 15, $-\Phi\{O_3\}$ would only be greater by one. For HO radicals produced in the chain steps, *i.e.*, reactions 2 and 4, $-\Phi\{O_3\}$ would only double if reaction 1 dominated over reaction 15.

The H atoms produced in reactions 14 and 15 might react with either O_3 or O_2

$$H + O_3 \longrightarrow HO^* + O_2 \quad (4)$$

$$H + O_2 + M \longrightarrow HO_2 + M \quad (16)$$

The rate coefficients at 298°K are $k_4 = 2.6 \times 10^{-11}$ cm^3/sec,[27] and $k_{16} = 1.6 \times 10^{-12}$ cm^6/sec for Ar as a chaperone.[28] Thus, reaction 16 is completely dominant over reaction 4 for all the experiments except the one with only 5.8 Torr of O_2. For this experiment, reaction 4 plays a measurable role, and $-\Phi\{O_3\}$ is enhanced. At temperatures below 298°K, k_4 can only be smaller and k_{16} larger; reaction 4 can be ignored.

The HO_2 radical produced in reaction 16 might react with either O_3 or H_2

$$HO_2 + O_3 \longrightarrow HO + 2O_2 \quad (2)$$

$$HO_2 + H_2 \longrightarrow H_2O_2 + H \quad (17)$$

and both of these reactions must be considered.

The hydrogen-bearing radicals, H, HO, and HO_2, are regenerated in chain steps from each other and lead to the chain decomposition of O_3. In order to terminate the chain, one or more of these radicals must be destroyed in radical-radical reactions. Experimentally it is easy to decide which radicals are involved, because the chain-carrying step is with a different reactant gas for each radical.

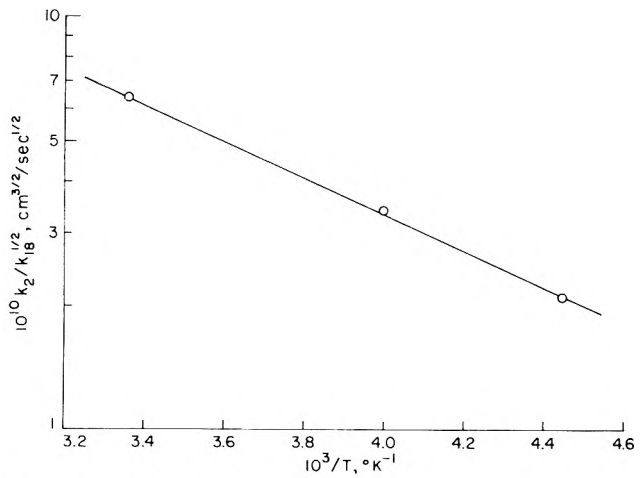

Figure 2. Arrhenius plot for $k_2/k_{18}^{1/2}$.

Thus, the chain-propagating step for H is reaction with O_2; for HO, reaction with H_2; and for HO_2, reaction with O_3 (reaction of HO_2 with H_2 does not lead to O_3 destruction). Consequently, the fact that increasing the O_2 or H_2 pressures does not increase $-\Phi\{O_3\}$ means that neither H nor HO can be involved in chain-terminating reactions. The only chain-terminating step is

$$2HO_2 \longrightarrow H_2O_2 + O_2 \qquad (18)$$

The complete reaction scheme needed to explain the results consists of reactions 2, 5–7, 10, and 14–18. This mechanism leads to the very simple rate law

$$-\Phi\{O_3\} - 1 = k_2[O_3]/(k_{18}I_a)^{1/2}$$

Plots of $-\Phi\{O_3\} - 1$ *vs.* $[O_3]/I_a^{1/2}$ are shown at each temperature in Figure 1. The plots are linear and pass through the origin. The fact that the plots pass through the origin is experimental verification that the HO radicals produced in reaction 14 do not react with O_3 to any appreciable extent, for if they did, the intercept would be positive.

The slopes of the plots in Figure 1 give $k_2/k_{18}^{1/2}$ and they are listed in Table II. The value at 298°K of 6.4×10^{-10} $cm^{3/2}/sec^{1/2}$ agrees well with the approximate value of 9×10^{-10} $cm^{3/2}/sec^{1/2}$ found by De More.[14] The Arrhenius plot for $k_2/k_{18}^{1/2}$ is shown in Figure 2. The plot is linear and yields an Arrhenius expression $k_2/k_{18}^{1/2} = 1.9 \times 10^{-8} \exp(-2000/RT)$ $cm^{3/2}/sec^{1/2}$. We estimate the uncertainty in this expression to be about 25% in the preexponential factor and 10% in the activation energy.

The rate coefficient for reaction 18 has been measured at 298°K to be 3.0×10^{-12}, 3.6×10^{-12}, and 1.0×10^{-11} cm^3/sec respectively by Foner and Hudson,[29] Paukert and Johnston,[30] and Hochanadel, *et al.*[31] If we accept the value of 3.0×10^{-12} cm^3/sec, then k_2 becomes 1.1×10^{-15} cm^3/sec at 298°K. Since reaction 18 is a radical–radical reaction, it must have little or no activation energy. If k_{18} is 3.0×10^{-12} cm^3/sec, independent of temperature, then $k_2 = 3.3 \times 10^{-14} \exp(-2000/RT)$ cm^3/sec, with $R = 1.987$ cal/mol °K. This low preexponential factor is expected since two bonds are broken simultaneously in reaction 2.

Acknowledgment. We wish to thank Professor Marcel Nicolet for useful discussions and encouragement. This work was supported by the Atmospheric Sciences Section of the National Science Foundation through Grant No. GA-12385 and the National Aeronautics and Space Administration through Grant No. NGL-009-003 for which we are grateful.

References and Notes

(1) E. Warburg, *Sitzungsber. Kgl. Preuss. Akad. Wiss.*, 644 (1913).
(2) G. S. Forbes and L. J. Heidt, *J. Amer. Chem. Soc.*, **56**, 1671 (1934).
(3) W. D. McGrath and R. G. W. Norrish, *Nature (London)*, **182**, 235 (1958).
(4) W. D. McGrath and R. G. W. Norrish, *Proc. Roy. Soc., Sec. A*, **254**, 317 (1960).
(5) R. G. W. Norrish and R. P. Wayne, *Proc. Roy. Soc., Sec. A*, **288**, 361 (1965).
(6) W. B. De More, *J. Chem. Phys.*, **46**, 813 (1967).
(7) F. Kaufman, *Ann. Geophys.*, **20**, 106 (1964).
(8) K. F. Langley and W. D. McGrath, *Planet. Space Sci.*, **19**, 413 (1971).
(9) A. G. Potter, Jr., R. N. Coltharp, and S. D. Worley, *J. Chem. Phys.*, **54**, 992 (1971).
(10) E. Lissi and J. Heicklen, *J. Photochem.*, **1**, 39 (1972).
(11) Climatic Impact Assessment Program Conference, Cambridge, Mass., Feb 1972.
(12) R. N. Coltharp, S. D. Worley, and A. E. Potter, Jr., *Appl. Opt.*, **10**, 1786 (1971).
(13) F. Kaufman and J. G. Anderson, Climatic Impact Assessment Program Conference, Cambridge, Mass., Nov 1972.
(14) W. B. De More, *Science*, **180**, 735 (1973).
(15) M. Ackerman, "Mesopheric Models and Related Experiments," Reidel Publishing Co., Dordrecht, 1971, p 149.
(16) F. D. Findlay and D. R. Snelling, *J. Chem. Phys.*, **54**, 2750 (1971).
(17) K. H. Becker, W. Groth and U. Schurath, *Chem. Phys. Lett.*, **14**, 489 (1972).
(18) I. D. Clark and R. P. Wayne, *Proc. Roy. Soc., Sec. A*, **314**, 111 (1969).
(19) R. P. Steer, R. A. Ackerman, and J. N. Pitts, Jr., *J. Chem. Phys.*, **51**, 843 (1969).
(20) D. C. Krezenski, R. Simonaitis, and J. Heicklen, *Int. J. Chem. Kinet.*, **3**, 467 (1971).
(21) J. L. McCrumb and F. Kaufman, *J. Chem. Phys.*, **57**, 1270 (1972).
(22) R. E. Huie, J. T. Herron, and D. D. Davis, *J. Phys. Chem.*, **76**, 2653 (1972).
(23) D. L. Baulch, D. D. Drysdale, and A. C. Lloyd, "High Temperature Reaction Rate Data," Department of Physical Chemistry, Leeds University, No. 2 (1968).
(24) R. A. Young, G. Black, and T. G. Slanger, *J. Chem. Phys.*, **49**, 4758 (1968).
(25) G. Paraskevopoulos and R. J. Cvetanović, *J. Amer. Chem. Soc.*, **91**, 7572 (1969).
(26) P. M. Scott and R. J. Cvetanović, *J. Chem. Phys.*, **54**, 1440 (1971).
(27) L. F. Phillips and H. I. Schiff, *J. Chem. Phys.*, **37**, 1233 (1962).
(28) T. Hikida, J. A. Eyre, and L. M. Dorfman, *J. Chem. Phys.*, **54**, 3422 (1971).
(29) S. N. Foner and R. L. Hudson, *Advan. Chem. Ser.*, **No. 36**, 42 (1962).
(30) T. T. Paukert and H. S. Johnston, *J. Chem. Phys.*, **56**, 2824 (1972).
(31) C. J. Hochanadel, J. A. Ghormley, and P. J. Ogren, *J. Chem. Phys.*, **56**, 4426 (1972).

Photochemistry of Cyclohexanone. II. Second and Third Singlet Excited States[1]

Robert G. Shortridge, Jr.,[2] and Edward K. C. Lee*

Department of Chemistry, University of California, Irvine, California 92664 *(Received January 15, 1972)*

The results of the vacuum ultraviolet photolyses (174.5 and 193.1 nm) of cyclohexanone involving the $^1(\sigma_{CC}^* \leftarrow n)$ and $^1(\sigma_{CO}^* \leftarrow n)$ transitions are reported. Substantial product yields of C_2H_4, C_3H_6, and c-C_3H_6 produced at low pressures are indicative of new photodecomposition channels which become available at high energies, because these C_2 and C_3 products had not been observed previously (or in insignificant amounts if observed) in photolyses at $\lambda_{ex} \geq 253.7$ nm where the $^1(\pi^* \leftarrow n)$ transition is involved. For the mixture of 1.0 Torr of cyclohexanone and 1.8 Torr of O_2, the observed C_2, C_3, and C_5 hydrocarbon product ratios are 1.0:0.3:1.0 at λ_{ex} 174.5 nm whereas they are 0.4:0.1:1.0 at λ_{ex} 193.1 nm. A mechanism involving trimethylene and acyltrimethylene biradicals as well as acylpentamethylene biradicals (*via* α-cleavage) is invoked in order to explain the observed product distribution from the short wavelength photodecomposition. Furthermore, in the photolysis of cyclohexanone-*2-t* an excessive amount of C_2H_4 is produced indicating possible importance of the β-cleavage process by which the tritium-labeled biradical $\dot{C}H_2CH_2$-C(=O)-$\dot{C}$HT or $\dot{C}H_2$-CHT-C(=O)-$\dot{C}H_2$ (presumably "singlet" species) competes for ring closure and pressure stabilization *vs.* its unimolecular decomposition. The primary dissociating precursors are postulated to be the vibrationally hot S_0^* and S_1^* states produced *via* rapid internal conversion of the S_3 and S_2 states.

Introduction

The gas-phase photochemistry of cyclohexanone excited in its $\pi^* \leftarrow n$ absorption region has been studied by numerous research groups in the past 40 years,[3-8] and it has been reviewed *extensively*.[9] Two main photoproducts formed in the ($n\pi^*$) state photochemistry of cyclohexanone are (1) decarbonylation to give 1-pentene or cyclopentane plus CO and (2) photoisomerization to 5-hexenal involving an intramolecular H atom migration

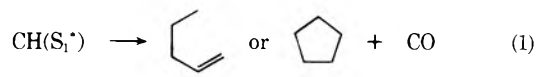

(1)

$$CH(S_1^*) \rightarrow \rightarrow \text{5-hexenal} \qquad (2)$$

For cyclohexanone, three other high-energy absorption bands corresponding to the $\sigma_{CO}^* \leftarrow n$, $\sigma_{CC}^* \leftarrow n$, and $\pi^* \leftarrow \pi$ electronic transitions are known.[10] A study of photolysis in its fourth excited singlet state ($\pi^* \leftarrow \pi$), involving short vacuum uv excitation $\lambda_{ex} \leq 147.0$ nm, has been reported recently.[11] While the above study was in progress, we initiated a study of the photochemical kinetics of cyclohexanone excited to its second and third excited states, $\sigma_{CO}^* \leftarrow n$ at λ_{ex} 195 nm and $\sigma_{CC}^* \leftarrow n$ at λ_{ex} 175 nm. The present paper deals with this long vacuum uv photolysis of cyclohexanone in the gas phase, with the hope of determining the primary photoproduct distributions and the changes in the primary physical processes effected by the high photoexcitation energy. In analogy with the long vacuum uv photolysis studies[12,13] of cyclobutanone, we expected to observe higher decomposition/stabilization (D/S) ratios and to observe new photodecomposition channels.

Experimental Section

Chemicals. Cyclohexanone (Baker and Adamson) was used after drying with Drierite ($CaSO_4$) under vacuum, and gas chromatographic analysis showed no detectable impurity. Approximately 1 ml of this cyclohexanone was tritium labeled at the α position, as described elsewhere.[14] The specific activity of this sample was determined to be ~2 Ci/mol. The propylene and one of the samples of propane used in this study were of Phillips Petroleum's Research Grade. The second sample of propane was of Instrumental Grade from Matheson (99% + purity). Dry oxygen of 99.5% purity (USP Grade) from the National Compressed Gas Co. and Air Products was used. Dry, oil-free helium, Hi-Pure nitrogen (99.96% + by volume) from Liquid Carbonic, and ultrahigh (99.97%) purity methane (Matheson) were also used in this study.

Vacuum and Photochemical Apparatus. Most of the samples were handled on the grease-free and mercury-free combination glass and metal vacuum line which was described previously.[15] Additionally, a new vacuum line was used to fill samples requiring very low pressures of ketone and radical scavengers. It employed 4-mm in-line glass Teflon valves (Fisher and Porter) in order to minimize the absorption of the ketones. Pressures could be accurately measured using a capacitance manometer (MKS Baratron Type 77 electronic pressure meter with 77H-30 pressure head). A 82.9-ml cell with two Supracil quartz windows (2 in. o.d.) and a Teflon needle valve (4 mm, Fischer and Porter), and a 479-ml cell with two Suprasil windows and a Teflon valve were used.

The absorption spectra of the $^1(\sigma_{CO}^* \leftarrow n)$ and $^1(\sigma_{CC}^* \leftarrow n)$ electronic transitions of cyclohexanone, which were obtained by Udvarhazi and El-Sayed,[10a] indicate that the carbon resonance line (193.1 nm) should efficiently cause excitation to the $^1(\sigma_{CO}^* \leftarrow n)$ state, while the nitrogen resonance lines (174.5 and 174.3 nm) should effect excitation to the $^1(\sigma_{CC}^* \leftarrow n)$ state. Accordingly carbon and nitrogen resonance flow lamps were constructed similar to those described by Davis and Braun.[16] The desired radiation was produced by allowing the mixtures of either 1% CH_4 or 1% N_2 in helium to flow continuously through a lamp that was positioned in the waveguide of a Raytheon microwave power generator (Model PGM-10, 85 W of con-

tinuous wave power output at 2450 MHz with a UG 435A/U waveguide flange accessory).

A 0.3-m McPherson vacuum ultraviolet monochromator was used to check the spectral purity of the carbon and nitrogen atom resonance lamps at the 200-nm region. The spectral purity of the longer wavelength region was also checked, and revealed some impurity radiation in the 220–300-nm region with both lamps.

The intensities of both lamps are rated in the 10^{15} photon/sec region.[16] In the operation of the carbon resonance lamp, the photolysis cell was typically placed about 7 cm from the Suprasil window of the lamp with a convex silica lens of 100-mm focal length placed in the light path immediately in front of the cell window. This arrangement effectively filtered out the 165.7-nm resonance line and passed only the 193.1-nm line. However, no such spacing was maintained during the operation of the nitrogen resonance lamp, inasmuch as the 174.5-nm resonance line is the only radiation produced between the Suprasil cutoff (~165 nm) and the λ <200-nm region, and the oxygen in the atmosphere absorbs quite strongly in the 175-nm region. Therefore, the photolysis cell was always placed flush against the window of the nitrogen resonance lamp. All photolysis runs were made at 23°.

A carbonaceous deposit was found to build up on the window of the carbon resonance lamp during operation. This progressively reduced the transmitted intensity of the resonance radiation and imposed the requirement that the lamp be cleaned after each run, or after each 20 to 30 min of operation during a prolonged irradiation. The removal of the carbonaceous deposit was accomplished by flowing oxygen through the lamp while subjecting it to a microwave discharge. No such deposits were encountered in the operation of the nitrogen resonance lamp.

Product Analysis. The majority of the analyses of the volatile hydrocarbon products were made with a conventional radio gas chromatographic setup.[17] The radiochemical yields were monitored by an internal β proportional counting apparatus, coupled to a Dyna-Print (EFCO Systems, Inc.). Macroscopic product yields were monitored by a thermistor detector (Microdetector Systems, Model 1000, Carle Instruments) connected to a 1-mV Honeywell potentiometer recorder, equipped with a disk chart integrator.

In order to greatly increase the sensitivity and accuracy of the macroscopic product yield data as well as the specific activity data, a hydrogen flame ionization detector (Perkin-Elmer Model F-11) was employed at times. The actual product separations were accomplished by either of two dimethylsulfolane columns described previously.[8] In addition, a 15-ft Silica Gel column was used to analyze for HT in a few runs.

Samples were handled in a manner similar to that described elsewhere[18] for product analysis.

Quantum Yield. It was not possible to measure the product quantum yields under the present experimental circumstances. But we believe that the sum of the quantum yields of primary processes (or parent disappearance) could easily be unity at low pressures employed here, since the product quantum yield of cyclohexanone-2-*t* at low pressures and 253.7 nm, which is at the lower energy than 193.1 or 174 nm, was found to be unity.

Results

In the present study, cyclohexanone was irradiated at both 193.1 and 174.5 nm in the presence of O_2 as the long-lived free-radical scavenger. It was also irradiated in the presence of propylene as the radical scavenger at 193.1 nm.

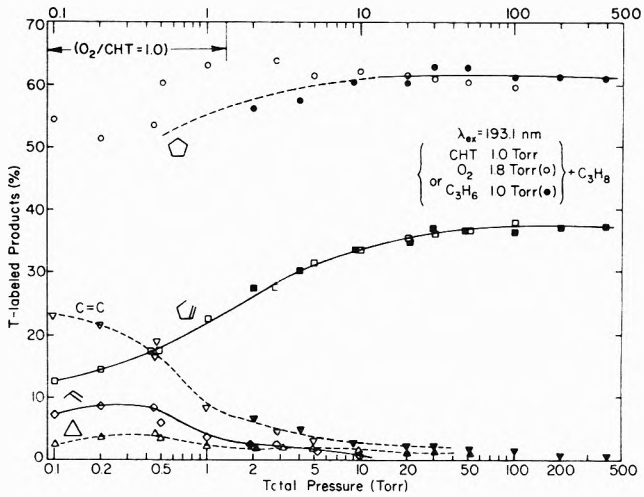

Figure 1. Tritium-labeled product distribution from the 193.1-nm photolysis of cyclohexanone-2-*t* vs. total pressure.

TABLE I: Ratio of Tritium-Labeled Products in the Propylene-Scavenged Photolysis of CHT at 193.1 nm[a]

Run no.	C_3H_6, Torr	Total activity,[b] 10^3 dpm	C_2^*/C_5^*	C_3^*/C_5^*	C_2^*/C_3^*	CP*/PE*
531	0	185	0.081	0.043	1.90	2.04
537	2	141	0.056	0.031	1.78	1.91
532	7	81	0.028	0.022	1.27	1.79
533	18	99	0.024	0.017	1.44	1.73
534	28	117	0.021	0.014	1.50	1.69
535	48	129	0.018	0.012	1.49	1.71
536	98	132	0.012	0.009	1.34	1.68
579	198	126	0.008	0.007	1.19	1.65
578	398	102	0.007	0.008	0.91	1.64

[a] All runs contained 1.0 Torr of CHT and 1.0 Torr of C_3H_6 in a 82.9-ml photolysis cell. They were irradiated for 5.0 min, and the distance between the lamp and the cell windows was 3.0 cm. [b] Observed hydrocarbon products up to C_5.

The use of the high specific activity cyclohexanone-2-*t* (CHT) led to a complication in product analysis. During storage, β-radiation from the tritium decay (E_{max} = 18.6 keV) of this sample caused sufficient self-radiation damage to result in the formation of products found similarly in the photolysis. Subjecting the labeled samples to several freeze–pump–thaw cycles at Dry Ice or warmer temperatures removed the majority of the radiation damaged products prior to photolysis, thus preventing them from interfering in the analysis of the photoproducts. This purification procedure was repeated every few days during a series of runs.

Propylene- and O_2-Scavenged Photolysis of CHT at 193.1 nm. The results of the pressure variation series in which each sample contained 1.0 Torr of cyclohexanone-2-*t* (CHT) and 1.0 Torr of propyelene and varying pressures of propane pressurizing gas (up to 398 Torr) are shown in Figure 1. Similarly, the results of the O_2-scav-

TABLE II: Ratio of Tritium Labeled Products in the O_2-Scavenged Photolysis of CHT at 193.1 nm[a]

Run	C_3H_6, Torr	CHT, Torr	O_2, Torr	Total activity,[b] 10^3 dpm	C_2^*/C_5^*	C_3^*/C_5^*	C_2^*/C_3^*	CP^*/PE^*
605	0	0.05	0.05	9	0.34	0.15	2.3	4.36
604	0	0.10	0.10	14	0.33	0.19	1.7	3.55
606	0	0.25	0.25	42	0.24	0.18	1.4	3.11
593	0	0.25	0.25	17	0.16	0.12	1.4	3.22
592	0	0.50	0.50	34	0.09	0.07	1.3	2.78
584	0	1.0	1.8	64	0.05	0.04	1.1	2.30
588	2.2	1.0	1.8	67	0.03	0.03	1.1	2.00
585	7.2	1.0	1.8	77	0.02	0.02	1.0	1.83
586	17.2	1.0	1.8	71	0.02	0.02	1.2	1.73
587	27.2	1.0	1.8	67	0.02	0.02	0.9	1.69
590	47.2	1.0	1.8	62	0.01	0.01	0.9	1.65
591	97.2	1.0	1.8	90	0.01	0.01	1.1	1.57

[a] All runs but no. 605, 604, and 606 (in 479-ml cell) were made with a 82.9-ml cell. All runs were irradiated for 5 min, and the distance between the lamp and cell windows was 7.0 cm. A 10-cm focal length silica lens was used for collimation. [b] Observed hydrocarbon products up to C_5.

TABLE III: Molar Product Yields (Units of 10^{-9} mol)[a] in the Photolysis of Cyclohexanone at 193.1 and 174.5 nm

Run no.	662L[b]	664[b]	660[b]	663[b]	661[b]	665[c]
P_{CH}, Torr	0.1	0.25	1.0	1.0	1.0	1.0
P_{O_2}, Torr	0.1	0.25	1.8	14	160	1.8
C_2H_4	3.4_7	2.2_7	3.2_6	1.9_0	0.58	13.8_7
C_3H_6	0.46	0.30	0.41	0.21	0.06_5	1.6_9
$c\text{-}C_3H_6$	0.26	0.20	0.45	0.35	0.26	2.0_6
$1\text{-}C_5H_{10}$	0.46	0.42	2.2_3	2.9_4	2.9_6	3.1_5
$c\text{-}C_5H_{10}$	1.5_4	1.4_0	5.4_3	5.7_1	6.5_6	10.0_8
(C_2/C_5)	1.73	1.24	0.42	0.22	0.06	1.05
(C_3/C_5)	0.36	0.28	0.11	0.06	0.03	0.28
$(c\text{-}C_5H_{10}/1\text{-}C_5H_{10})$	3.33	3.36	2.4_3	1.95	2.22	3.20
(C_2/C_3)	4.84	4.49	3.80	3.40	1.81	3.70

[a] Accuracy was probably in the $\pm 10^{-11}$ mol region. [b] Photolysis (5 min) at 193.1 nm in the 82.9-ml cell, ~7-cm spacing including a quartz 10-cm focal length silica lens between the lamp and photolysis cell. Run 662L was made with a 479-ml cell. [c] Photolysis (2 min) at 174.5-nm in the 82.9-ml cell, photolysis cell placed flush against lamp window.

enged photolysis series containing 1.0 Torr of CHT, 1.8 Torr of O_2, and varying pressures of propane, as high as 98 Torr, are shown in Figure 1. It is obvious here that labeled ethylene, propylene, and cyclopropane, which were produced only in trace amounts in the ($\pi^* \leftarrow$ n) region,[8] account for a significant fraction of the observed hydrocarbon products. However, increasing pressure quenches the majority of the C_2 and C_3 product yields.

Inasmuch as small amounts of the tritium-labeled 1-butene, isopentane, *n*-pentane, and 1,4-pentadiene, amounting to less than a total of ~6%, were produced only in the propylene-scavenged series, and not in the corresponding O_2-scavenged series, it was concluded that they arise from free-radical recombination reactions at low pressures. Consequently, labeled cyclopentane, 1-pentene, cyclopropane, propylene, and ethylene were identified as primary photochemical products.

The total labeled product yields observed up to C_5 hydrocarbons are tabulated in Tables I and II, together with the labeled product ratios $C_2H_3T/\Sigma C_5H_9T$ (C_2^*/C_5^*), $\Sigma C_3H_5T/\Sigma C_5H_9T$ (C_3^*/C_5^*), $C_2H_3T/\Sigma C_3H_5T$ (C_2^*/C_3^*), and $c\text{-}C_5H_9T/1\text{-}C_5H_9T$ (CP^*/PE^*). Because of the carbonaceous deposits on the window of the photolysis cell during irradiation, it is difficult to accurately assess the relative quantum yields of the total labeled products, but they are nearly independent of C_3H_6 pressure (up to ~400 Torr) as shown in Table I and in the lower half of the runs listed in Table II. The attenuation of 193.1-nm radiation due to the absorption by CHT is nearly proportional to the pressure of CHT as indicated by the total labeled product yield shown in a set of run no. 605, 604, and 606 (or 593, 592, and 583) in Table II. The C_2 and C_3 product yields as well as cyclopentane/1-pentene ratio are decreasing with the increasing pressure as expected, because C_2, C_3, and CP are produced from the vibrationally hot precursors which can be collisionally quenched or deactivated at high pressures.

Photolysis of Unlabeled Cyclohexanone at 193.1 nm. The flame ionization detector was used to analyze the products of a parallel O_2-scavenged series in which unlabeled cyclohexanone (CH) was photolyzed. In this series O_2 rather than propane was used as the pressurizing gas, inasmuch as the propane mass peaks would have interferred with the analysis of the mass peaks of the C_2 and C_3 photolytic products.[19] The results are shown in Table III in the form of molar product yields, together with the corresponding product ratios which appeared in Tables I and II. In Table IV the normalized specific activities of the five primary products are tabulated. Duplicate runs were necessary to generate this data, one in which CHT was photolyzed and subsequently analyzed by radio gas chromatography, and the other in which unlabeled CH was photolyzed and then analyzed with the flame ionization detector. It should be noted that the macroscopic ethylene yield is much larger than expected on the basis of a conventional α-cleavage mechanism. This interesting result will be considered at length in the Discussion section.

O_2-Scavenged Photolysis of Cyclohexanone-2-t at 174.5 nm. The nitrogen resonance lamp was utilized to determine the effect on the product distribution of pumping an additional ~20 kcal/mol of photoexcitation energy into the CHT and CH. As expected, somewhat higher yields of C_2 and C_3 products were observed at 174.5 nm than at 193.1 nm at each corresponding total pressure. The tritium-labeled product yields and the decomposition to stabilization ratios for the labeled products are of interest.

TABLE IV: Specific Activities[a] of the Photoproducts from Cyclohexanone-2-*t* (Units of 10^{11} dpm mol)

Run no. (R)[b]	604	593	584	585	591	606
(M)[c]	662	664	660	663	661	665
λ_{ex}, nm	193.1	193.1	193.1	193.1	193.1	174.5
P_{CH}, Torr	0.1	0.25	1.0	1.0	1.0	1.0
P_{O_2}, Torr[d]	0.1	0.25	1.8	14	~160	1.8
$P_{C_3H_8}$, Torr[d]				7	~97	
Ethylene	7.8 ± 0.3	5.4 ± 0.2	4.9 ± 0.3	4.8 ± 0.3	9.7 ± 0.6	6.9 ± 0.4
Propylene	24.2 ± 1.2	19.2 ± 0.9	18.0 ± 0.9	11.3 ± 0.9	9.0 ± 3.2	18.7 ± 0.7
Cyclopropane	18.8 ± 1.8	15.2 ± 1.3	16.1 ± 0.6	16.0 ± 0.9	16.9 ± 1.2	15.1 ± 0.2
1-Pentene	39.2 ± 1.8	43.6 ± 2.3	44.2 ± 0.7	44.6 ± 0.4	44.6 ± 1.0	42.5 ± 0.8
Cyclopentane[a]	(41.9 ± 1.8)	(41.9 ± 0.8)	(41.9 ± 0.6)	(41.9 ± 0.4)	(41.9 ± 0.5)	(41.9 ± 0.4)

[a] The variation in light intensity between the duplicate runs had to be accounted for. The value of the specific activity of cyclopentane was chosen to be 419 × 10^{10} dpm mol which is approximately the value obtained in a single radio gas chromatographic analysis in which the macroscopic data (thermistor detector) and radiochemical data were simultaneously obtained. [b] Radiochemical data from the photolysis of CHT. [c] FID data from the photolysis of CH. [d] Higher pressures of oxygen were required to achieve an approximately equivalent amount of pressure quenching, due to the greater collision efficiency of C_3H_8 (see ref 15).

TABLE V: Tritium-Labeled Product Yields (Units of 10^2 dpm) in the O_2-Scavenged Photolysis of Cyclohexanone-2-*t* at 174.5 nm[a]

Run no.	611	608	609	610
P_{CHT}, Torr	0.25	1.0	1.0	1.0
P_{O_2}, Torr	0.25	1.8	1.8	1.8
$P_{C_3H_8}$, Torr	0	0	7.2	97.2
C_2H_3T	112.8	174.7	99.1	62.9
C_3H_5T	38.4	57.5	28.9	4.4
c-C_3H_5T	28.9	56.4	42.5	26.4
1-C_5H_9T(PE*)	49.7	243.1	428.3	515.6
c-C_5H_9T(CP*)	192.1	767.5	1072.5	998.3
Total activity	422	1300	1671	1607
(C_2*/C_5*)	0.46_7	0.17_3	0.06_6	0.04_2
(C_3*/C_5*)	0.27_8	0.11_3	0.04_8	0.02_0
(C_2*/C_3*)	1.68	1.53	1.39	2.04
(CP*/PE*)	3.87	3.16	2.50	1.94

[a] All samples were photolyzed for 2 min in a 82.9-ml photolysis cell, flush against lamp window.

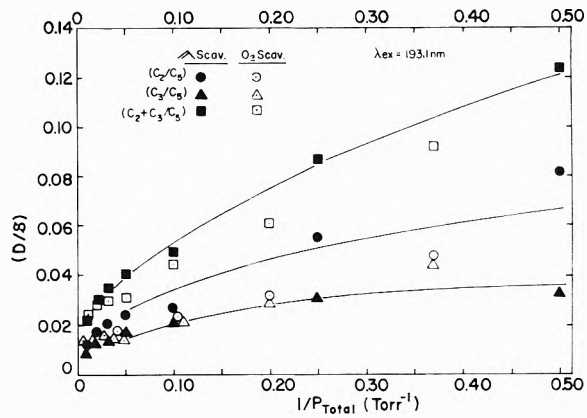

Figure 2. Stern–Volmer plot for the 193.1-nm photolysis of cyclohexanone-2-*t*. (D/S) ratios, *vs.* reciprocal pressure.

They are shown in Table V. It should also be noted that the last pair of parallel runs in Table IV were also photolyzed at 174.5 nm.

The secondary photolysis of the olefinic primary products at 174.5 nm was undoubtedly occurring in these samples. A small yield of HT was observed when a Silica Gel column was employed for the analysis of one of the 174.5-nm runs, and was presumably a secondary photolysis product. Accordingly, the percentage conversion was kept as low as possible to minimize this complication, and it was kept typically much less than a few per cent. No HT was found in 193.1-nm photolysis.

Discussion

Pressure Effect and Energy Photopartitioning. The observed increasing importance of the C_2 and C_3 decomposition product formation at the higher photoexcitation energy (150 kcal/mol) corresponding to the $\sigma_{CO}^* \leftarrow$ n electronic transition is well illustrated in Figure 2, which consists of a Stern–Volmer type plot of two (D/S) ratios obtained in both the propylene- and O_2-scavenged photolysis of CHT at 193.1 nm. Specifically, the labeled product yield ratios, (C_2*/C_5*) and (C_3*/C_5*), plotted against the inverse total pressure, definitely exhibit curvature. Campbell and Schlag[12] have attributed such curvature to energy photopartitioning phenomena, in which the available photoexcitation energy is partitioned between the two fragments of a primary photolytic reaction, with each fragment receiving a rather wide internal energy distribution. Accordingly, the observed curvature suggests the probable involvement of a vibrationally hot C_5H_9T* intermediate species (formed along with CO in a primary photochemical process) which is capable of either decomposition to the C_2 and C_3 products or stabilization to yield the C_5 products. The curvature could be suggestive of a direct pathway for the production of the C_2 and C_3 products from ring-opened CHT diradical intermediates, in addition to their production from the unimolecular decomposition of the C_5H_9T species.

Figure 3 shows the corresponding Stern–Volmer type plot of the results of the 174.5-nm O_2-scavenged photolysis of CHT. As expected, the (D/S) ratios at the same total pressures are higher at 174.5 nm than at 193.1 nm by a factor of 2–3.

Similarly, the macroscopic data obtained from the photolysis of unlabeled cyclohexanone (CH) was employed to construct the Stern–Volmer plot which appears in Figure 4. The most striking feature of this plot is the extremely large value of the (C_2/C_5) ratio, particularly in the low-pressure region. This anomalously high macroscopic ethylene yield suggests that there exists a photodecomposition pathway by which ethylene is produced without the concomitant production of propylene or cyclopropane.

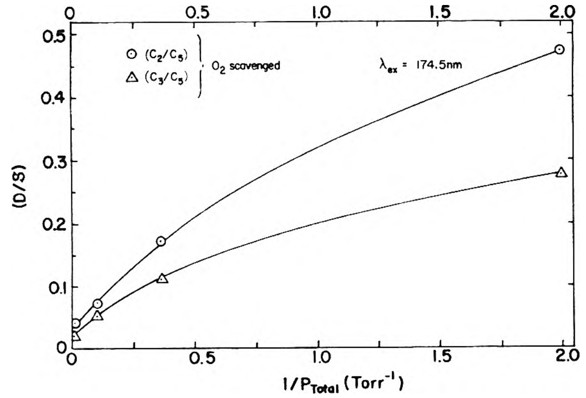

Figure 3. Stern–Volmer plot for the 174.5-nm photolysis of cyclohexanone-2-*t*, (D/S) ratios, *vs.* reciprocal pressure.

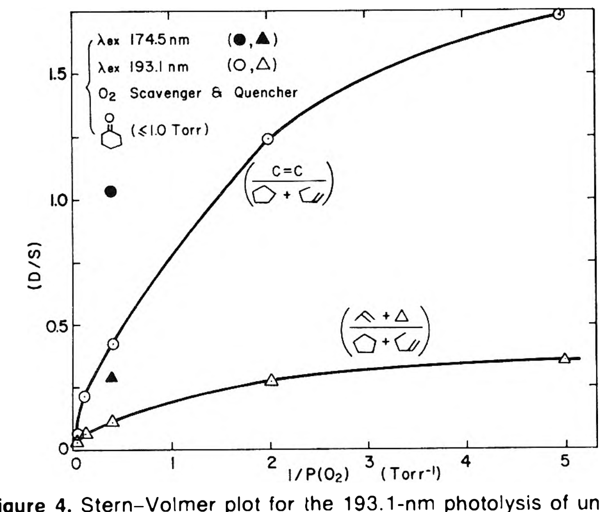

Figure 4. Stern–Volmer plot for the 193.1-nm photolysis of unlabeled cyclohexanone, (D/S) ratios, *vs.* reciprocal pressure.

The cyclopentane to 1-pentene (CP/PE) ratio increases from 1.5 to 4, with decreasing pressure as well as with increasing photoexcitation energy. Similar trends were also observed in the $^1(\pi^* \leftarrow n)$ region, where the ratio itself ranged from 0.3 to 0.8[8] Assuming that both of these C_5 products arise from the proposed pentamethylene biradical intermediate, this behavior may be rationalized at least qualitatively on the basis of the activation energies for the product-forming reactions.

Benson[20] has estimated the activation energy for the ring-closure reaction of the C_5 biradical to be ~8.3 kcal/mol from the observed overall activation energy of the reaction

and further justified this value by estimating that 4–5 kcal/mol were required to overcome the potential barrier for the free rotation of ethyl groups in linear alkanes, plus an additional ~3.5 kcal/mol required to overcome the steric strain imposed by the cis–cis conformation of the biradical required for the cyclization process.[21] Similar reasoning may be employed to estimate the activation energy for the 1,4 hydrogen migration necessary for 1-pentene formation. In this case, the same potential barrier to rotation must be overcome. However, consideration of the five-membered transition state presumably involved in the 1-pentene formation indicates that the biradical will have a less strained cis–gauche conformation. Hence, the activation energy should be correspondingly lower, ~7 kcal/mol.

Specific Activity Distribution of the Products of λ_{ex} *193.1-nm Photolysis.* Inasmuch as the conventional α-cleavage mechanism cannot account for the excessive production of the unlabeled C_2H_4, the uncommon β-cleavage process could possibly explain the observed specific activity distribution shown in Table IV. Scheme I illustrates

Scheme I

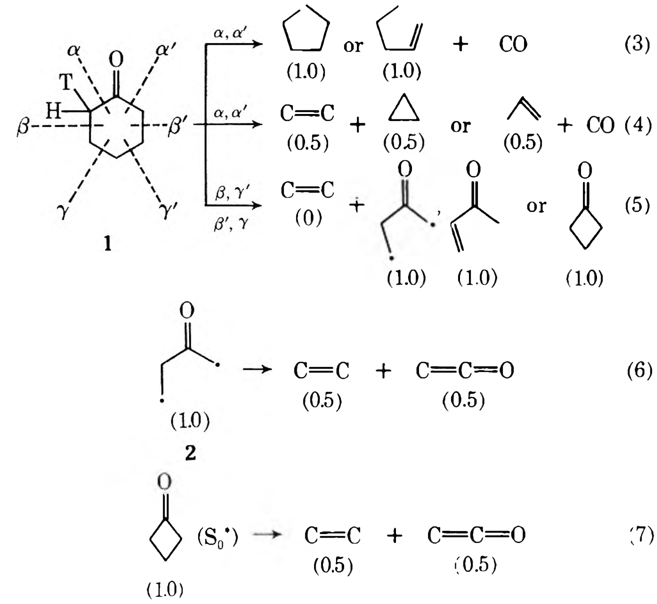

the relative specific activity distribution of the tritium-labeled products (shown in parentheses) expected of α-(or α'-) and β-(or β'-) cleavage processes, if the secondary kinetic isotope effect of tritium labeling is assumed to be of negligible importance. Decomposition mode 3 is important in the $^1(\pi^* \leftarrow n)$ photochemistry of cyclohexanone,[3-11] and decomposition mode 7 is well known from the thermal unimolecular decomposition study[22] and the photoactivation study.[23] The other decomposition modes are less conventional and require further proof. The most significant feature of this mechanistic scheme is that the ethylene initially produced by the $\beta\gamma'$- (or $\beta'\gamma$-) cleavage *via* decomposition process 5 is expected to be *unlabeled.* Only through the secondary decomposition of the labeled biradical $\cdot CH_2\text{-}C(=O)\text{-}CHT\text{-}CH_2\cdot$ could ethylene be produced with a relative specific activity value of 0.5 as shown in decomposition process 6. Of course, a "concerted" mechanism rather than the biradical mechanism could explain satisfactorily the experimental results.

It is obvious that a mechanism involving the combination of the α- and β-cleavage processes is consistent with the observed "low" specific activity of ethylene compared to the average specific activity of the two isomeric C_5 products. The relative specific activity of ethylene has a minimum value of 0.11 at a total pressure of 22 Torr (run no. 585 and 661) in Table IV, where presumably β-cleavage process 5 is most significant. At the lower pressures, the secondary decomposition process 6, involving the vibrationally hot C_4 biradical 2, which counteracts the trend of decreasing specific activity set by β-cleavage pro-

cess 5, becomes important, and at the higher pressures β-cleavage process 5 seems to be quenched more effectively than α-cleavage process 4. Therefore, the α-cleavage precursor appears to be shorter lived than the β-cleavage precursor. It is also possible that the vibrationally hot pentamethylene intermediate 3 directly produced from α-

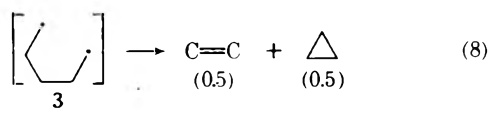

3 (8)

cleavage of an excited cyclohexanone (S_1*)[8] may give rise to ethylene and cyclopropane as shown in decomposition process 8. This process could, if not quenched effectively at low pressure, then also account for the increasing specific activity of ethylene at low pressure.

α-Cleavage Vs. β-Cleavage Mechanisms. Assuming decomposition processes 4 and possibly 3 involves the intermediacy of pentamethylene 3 as in reaction 8, we can determine what fraction of the photoexcited cyclohexanone molecules decompose *via* β-cleavage relative to that fraction undergoing α-cleavage, β/α. This is shown in Figure 5 plotted from the data given in Table III. The ratio of the quantity (C_2 − C_3), representing the "extra" ethylene arising from β-cleavage, to the quantity (C_3 + C_5), representing the total α-cleavage yield, is plotted *vs.* the total pressure. The ratio is approximately 1.0 in the low-pressure region, but is rather efficiently pressure quenched. This value of unity does not agree very favorably with a value of ~4 which was estimated for the β/α cleavage ratio obtained by de Mayo and Verdun in a recent pyrolysis study of cyclohexanone and two of its deuterated isomers, 2,2,6,6-cyclohexanone-d_4 and 4-cyclohexanone-d_1.[24] Hence, there is no compelling reason to postulate that the vibrationally hot ground state of cyclohexanone (S_0*) is an important precursor in the short-wavelength photolysis system. However, it is probably the precursor of a minor fraction of the observed products, particularly at low pressure, since the primary process leading to the β-cleavage process is equally probable at λ_{ex} 193.1 nm at low pressure as the α-cleavage process. At a total pressure of 1 Torr, nearly 50% of the β-cleavage product is quenched, indicating that the precursor lifetime of (S_0*) is ~0.1 μsec. The preferred β-cleavage of the highly vibrationally excited S_0* species raises an intriguing structure/reactivity question.

A much more likely precursor of the ring opened C_6 biradicals formed by the α-cleavage is the vibrationally hot (S_1*) state, consistent with the $^1(\pi^* \leftarrow n)$ photochemistry.[8] It is probable that the β-cleavage process may be due to the rapid internal conversion of $S_2 \rightsquigarrow S_0$; the "local" symmetry of the $^1(\sigma_{CO}^* \leftarrow n)$ state[10] is B_1 in the C_{2v} group[25] whereas A_1 is the ground state of cyclohexanone in the "local" C_{2v} group, hence the radiationless transition of $S_2 \rightsquigarrow S_0$ is not strictly allowed on electronic symmetry grounds alone, but may take place due to vibrationally induced or promoted radiationless transitions.

The γ-cleavage process, if it occurs, may also account for a minor fraction of the C_2 and C_3 products

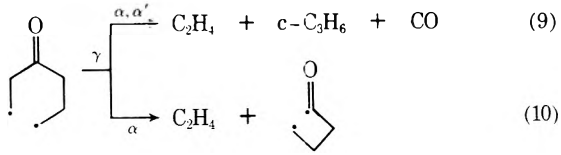

$\xrightarrow{\alpha,\alpha'}$ C_2H_4 + c-C_3H_6 + CO (9)

$\xrightarrow{\alpha}$ C_2H_4 + (10)

Inasmuch as the products of process 9 are identical with those of α-cleavage reaction 4, and process 10 produces the same final product as β-cleavage reaction 5 Scheme I, the evidence for or the necessity to postulate the γ-cleavage process is lacking at this moment.

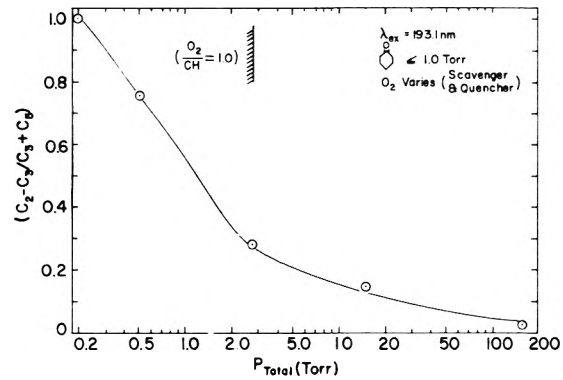

Figure 5. Ratio of β-cleavage products to α-cleavage products, (C_2 − C_3/C_3 + C_5), *vs.* total pressure.

α-Cleavage Process. A mechanism involving the intermediacy of the (S_1*) species (excess vibrational energy of over 60 kcal/mol) with a unimolecular decomposition rate constant $k_E \geq 10^{10}$ sec^{-1} at 193.1 nm is consistent with previous investigations of cyclic ketones in the $^1(\pi^* \leftarrow n)$ region;[8] the fluorescence lifetime of the S_1 state is expected to decrease with increasing photoexcitation energy,[26] and the actual decarbonylation step may take place directly from the S_1* manifold.

The results of Hoffmann's recent study of extended Hückel theory calculations[27] predict that the concerted cycloaddition-cycloreversion reaction 11 will be allowed in

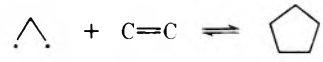

(11)

the ground state. This was explained by the fact that at the equilibrium CCC bond angle of 125° for the trimethylene species, the more stable of the two molecular orbitals responsible for the 1,3 interaction in the trimethylene, is the one derived from the *antisymmetric* combination of the terminal $2p_z$ orbitals, rather than the symmetric one.[27] From the appropriate correlation diagram, it was found that this antisymmetric trimethylene molecular orbital correlates with a low-lying filled antisymmetric molecular orbital of cyclopentane. Therefore, it is possible that a fraction of the observed C_2 and C_3 products, which appeared to arise from the decomposition of a C_5 precursor, were produced *via* the concerted cycloreversion of cyclopentane.[27-29]

1-Pentene Yield. The increase in the relative yield of the C_2 and C_3 products is observed in Tables I and II to be accompanied by a much larger decrease in the relative yield of 1-pentene-*t* than in the relative yield of cyclopentane-*t*. However, this should not necessarily be construed as evidence against the occurrence of the concerted decomposition of cyclopentane, inasmuch as the further complication of the decomposition of vibrationally hot 1-pentene-*t* to yield labeled *ethyl* plus *allyl* radicals appears to have occurred in the low-pressure runs, based on the results of the propylene- as well as the O_2-scavenged series. These radicals were scavenged in the presence of oxygen, but reacted further to produce labeled C_5, C_6, and more complex products *via* radical-radical recombination reactions in the propylene scavenged runs. This behavior is reminiscent of the low-pressure decomposition of vibra-

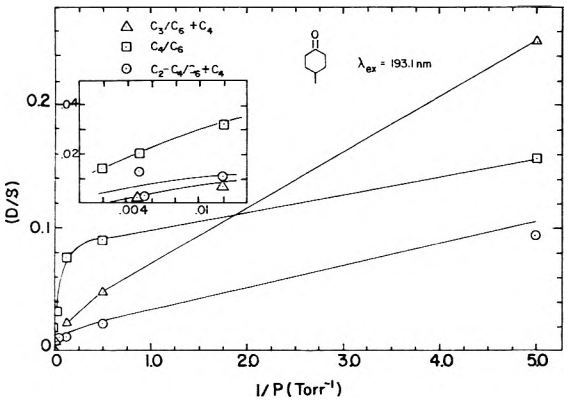

Figure 6. Stern–Volmer plot for the 193.1-nm photolysis of 4-methylcyclohexanone, (D/S) ratios, *vs.* reciprocal pressure.

tionally hot propylene-*t* in the short wavelength photolysis of cyclobutanone-2-*t*.[13] Furthermore, readers should be reminded that 1-pentene is 13.5 kcal/mol less stable than cyclopentane on the basis of the known thermochemistry and of the pressure dependence kinetic data.[8]

If the vibrationally hot S_1* species "predissociates" on the S_1 manifold to a singlet biradical, the role of a triplet intermediate in the decomposition mechanism at 193.1 nm must be negligible.

β-Cleavage Process. The β-cleavage process in $^1(\sigma_{CO}^* \leftarrow n)$ photolysis of CHT is important, particularly at low pressures, although it is considered unimportant in the $^1(\pi^* \leftarrow \pi)$ photolysis of cyclohexanone at λ_{ex} 147.0 nm.[11] It is puzzling that the specific activity of ethylene is uniformly lower throughout the pressure ranges studied than that expected for the β/α cleavage ratio of 1.0 (see Table IV). This may mean that the β/α cleavage ratio is greater than 1.0 or that the secondary tritium isotope effect is such that α'-cleavage is much more favored than α-cleavage (see Scheme I) or that the production rate of C_2H_3T *via* C_5H_9T decomposition is slower than that of C_2H_4 *via* C_5H_{10} decomposition. β/α cleavage ratio is certainly very low in high-pressure runs, above total pressure of 20 torr as shown in Figure 1, much more lower than the ratio found in Figure 5. It would be desirable to obtain the yields of methyl vinyl ketone and cyclobutanone in the future. Further detailed work would be necessary to find the reason for this apparent self-inconsistency. However, the preliminary photolysis work of 4-methylcyclohexanone at 193.1 nm shows the importance of the β-cleavage mechanism.[30] A Stern–Volmer plot for the product distribution (D/S) is shown in Figure 6, indicating that at low pressure the β/α cleavage ratio, $C_3/(C_4 + C_6)$, is over 0.2 where C_3 is C_3H_6, and C_4 is the sum of methylcyclopentane and 3-methyl-1-pentene.

Energetics and Rate Parameters. The endothermicities of the overall decarbonylation reactions which produce cyclopentane, 1-pentene, and ethylene plus propylene from cyclohexanone (S_0) have previously been calculated from standard enthalpies of formation at 298°K as 8.2, 21.7, and 44.1 kcal/mol, respectively.[8] Similarly using the principles of group additivity,[31] it was estimated that the α-cleavage step required an activation energy of 75 kcal/mol.[8]

In a similar manner, it may be calculated that β-cleavage of cyclohexanone requires the expenditure of ~78 kcal/mol, practically identical with that required for α-cleavage, and that the endothermicities of the following two overall reactions which proceed *via* an initial β-cleavage step are

$$CH \longrightarrow C_2H_4 + CH_3COCHCH_2 \qquad \Delta H = 36 \text{ kcal/mol}$$

$$CH \longrightarrow 2C_2H_4 + CH_2CO \qquad \Delta H = 65 \text{ kcal/mol}$$

As mentioned earlier, the observed lack of significant pressure quenching of the total C_5 product yield at pressures as high as 400 Torr of C_3H_6 indicates that the rate of α-ring cleavage of cyclohexanone in its (S_1*) state must be appreciably higher than the collision frequency at that pressure ($10^{9.8}$ sec^{-1}). Hence, the fairly efficient observed pressure quenching of the C_2 and C_3 products (see Figure 1) indicates that an additional precursor of the C_2 and C_3 products whose lifetime is in the range of 10^{-7} sec must exist.

In Table VI, the pertinent rate parameters have been calculated for the various unimolecular decomposition reactions of the cyclohexanone system at a photoexcitation energy corresponding to 193.1-nm photolysis. Included in this table are the entropy and the enthalpy of activation (ΔS^* and E_a) required for the formation of each transition state from the appropriate ring-opened cyclohexanone species, and the corresponding logarithm of the preexponential factor (log A) of each reaction which is related to the entropy of activation by the following formula of the transition state theory

$$A = (ekT/h)\exp(\Delta S^*)/R \text{ sec}^{-1}$$

TABLE VI: Calculated Rate Parameters for Some of the Unimolecular Decomposition Reactions of the Cyclohexanone Systems[a]

Reaction	E_z, kcal/mol	E_a,[c] kcal/mol	E,[b] kcal/mol	Log k_E, sec^{-1}
a	94	9	76	10.42
b	94	22.5	76	8.75
c	94	23	73	8.56
d	94	24.5	73	8.49

[a] For all reactions $\Delta S^* = -8$ G/mol and $A = 10^{11.48}$ sec^{-1}. [b] E is excess vibrational energy possessed by the species about to undergo unimolecular decomposition. $E = E_{h\nu} + \langle E_{th}\rangle - E_{rx}$, where $E_{h\nu}$ is the photoexcitation energy, $\langle E_{th}\rangle$ is the average thermal energy at 298°K, and E_{rx} is the endothermicity of the primary reaction which produces the intermediate which would undergo the specified unimolecular decomposition. [c] Calculated by Benson's method.

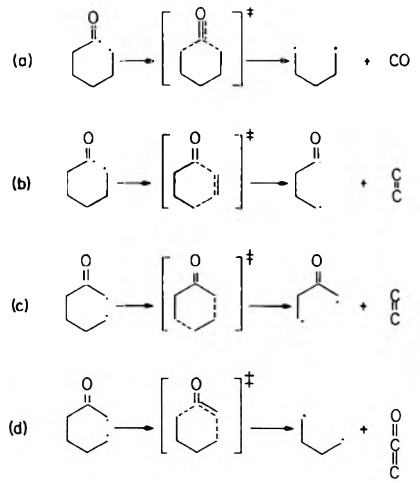

The specific rate constant is

$$k_E = A[(E - E_a + E_z)/(E + E_z)]^{s-1}$$

where E_z is the zero-point vibrational energy, s is the number of oscillators ($s = 46$), E is the excess internal energy possessed by the species about to undergo each unimolecular decomposition reaction, and k_E is the energy dependent unimolecular rate constant for each reaction as calculated by the approximate formulation of the RRKM theory due to Rabinovitch, *et al.*[32]

As expected, the specific rate constant for the formation of the C_5 products is much greater than the typical collision frequency, owing to its low activation energy of 9 kcal/mol. Hence it is not surprising that this reaction is unquenchable in the pressure range investigated. On the other hand, the specific rate constant for the formation of the (C_2 + C_3) products *via* α-cleavage as well as those for both β-cleavage reactions are estimated to be in the $\leq 10^9$ sec^{-1} ranges owing to activation energies ranging from 22–25 kcal/mol and are in fact quenched by a few torr of pressure.

Wavelength Effect. Scala and Ballan[11] excited cyclohexanone to the fourth or higher excited singlet state. In view of the different excited states involved and the difference in the amount of excited energy pumped into the molecule, as compared to our study, It should not be too surprising if the reactive precursors and the decomposition mechanism operative in the fourth excited singlet state are much different from those involved in the lower excited states. At the present time, a thorough comparison of them would be premature, though desirable, in the absence of more spectroscopic information and more detailed kinetic information.

Conclusion

It was found in the present study that new decomposition channels become accessible to cyclohexanone as the photoexcitation energy is increased to the point at which the second and third excited singlet states are populated. Ethylene and cyclopropane are produced *via* this new decomposition channel.

The one significant finding of this short wavelength investigation, however, was the apparent involvement of a β-cleavage process to produce unlabeled ethylene plus a C_4 biradical species, $\cdot CH_2CH_2COCH_2\cdot$, which decomposes to ethylene and ketene unless it is collisionally stabilized. Its occurrence was diagnosed from the product specific activity data obtained from the photolysis of cyclohexanone-2-*t*, *i.e.*, from the very low specific activity of ethylene compared with that of the C_5 products. However, the specific activity data cannot be explained satisfactorily in quantitative terms, and the exact evaluation of the β-cleavage yield requires further studies.

Inasmuch as the low pressure limiting value of the (C_2 − C_3/C_3 + C_5) ratio, which measures the ratio of β/α cleavage, is close to unity, which is much lower than the ratio of ~4/1 observed in the pyrolysis study,[24] it is proposed that the (S_0*) state is the likely principal precursor of the β-cleavage products, whereas the (S_1*) state is the precursor of the α-cleavage products.

A higher activation energy required for the formation of the β-cleavage products from their diradical precursor than that required for the C_5 products produced *via* α-cleavage is apparently responsible for the observed preferential pressure quenching of the β-cleavage products.

References and Notes

(1) This research has been supported by the National Science Foundation Grant No. GP 28010X. A part of this work was presented at the 161st National Meeting of the American Chemical Society, Los Angeles, Calif., March 28–April 2, 1971, and this paper was abstracted from the Ph.D. Thesis of R. G. Shortridge, Jr., University of California, Irvine, 1971.
(2) NDEA Predoctoral fellow 1967–1970.
(3) (a) O. D. Saltmarsh and R. G. W. Norrish, *J. Chem. Soc.*, 455 (1935); (b) C. H. Bamford and R. G. W. Norrish, *ibid.*, 1521 (1938).
(4) S. W. Benson and G. B. Kistiakowsky, *J. Amer. Chem. Soc.*, **64**, 80 (1942).
(5) J. R. Dunn and K. O. Kutschke, *Can. J. Chem.*, **32**, 724 (1954).
(6) F. E. Blacet and A. Miller, *J. Amer. Chem. Soc.*, **79**, 4327 (1957).
(7) R. Srinivasan, *J. Amer. Chem. Soc.*, **81**, 2601 (1959).
(8) R. G. Shortridge, Jr., and E. K. C. Lee, *J. Amer. Chem. Soc.*, **92**, 2228 (1970).
(9) (a) R. Srinivasan, *Advan. Photochem.*, **1**, 84 (1963); (b) J. G. Calvert and J. N. Pitts, Jr., "Photochemistry," Wiley, New York, N. Y., 1966, p 389; (c) R. B. Cundall and A. S. Davies, *Progr. React. Kinet.*, **3**, 147 (1967); (d) P. J. Wagner and G. S. Hammond, *Advan. Photochem.*, **5**, 21 (1968).
(10) (a) A. Udvarhazi and M. A. El-Sayed, *J. Chem. Phys.*, **42**, 3335 (1965); (b) W. C. Johnson, Jr., and W. T. Simpson, *ibid.*, **48**, 2168 (1968).
(11) A. A. Scala and D. G. Ballan, *J. Phys. Chem.*, **76**, 615 (1972).
(12) (a) R. J. Campbell, Ph.D. Thesis, Northwestern University, 1967; (b) R. J. Campbell and E. W. Schlag, *J. Amer. Chem. Soc.*, **89**, 5103 (1967).
(13) R. G. Shortridge, Jr., W. Yang, and E. K. C. Lee, *Mol. Photochem.*, **1**, 325 (1969).
(14) H. O. Denschlag and E. K. C. Lee, *J. Amer. Chem. Soc.*, **90**, 3628 (1968).
(15) N. E. Lee and E. K. C. Lee, *J. Chem. Phys.*, **50**, 2094 (1969).
(16) D. Davis and W. Braun, *Appl. Opt.*, **7**, 2071 (1968).
(17) J. K. Lee, E. K. C. Lee, B. Musgrave, Y.-N. Tang, J. W. Root, and F. S. Rowland, *Anal. Chem.*, **34**, 741 (1962).
(18) E. K. C. Lee, *J. Phys. Chem.*, **71**, 2804 (1967).
(19) Use was made of an earlier estimate[15] of 1.7 as the relative collisional efficience of C_3H_8 with respect to that of O_2, in order to determine what pressure of O_2 was necessary to be as effective as a given pressure of propane.
(20) H. E. O'Neal and S. W. Benson, *J. Phys. Chem.*, **72**, 1866 (1968).
(21) H. M. Frey and R. J. Ellis, *J. Chem. Soc.*, 4470 (1965).
(22) M. N. Das, F. Kern, T. D. Coyle, and W. D. Walters, *J. Amer. Chem. Soc.*, **76**, 6271 (1954).
(23) N. E. Lee and E. K. C. Lee, *J. Chem. Phys.*, **50**, 2094 (1969).
(24) P. de Mayo and D. L. Verdun, *J. Amer. Chem. Soc.*, **92**, 6079 (1970).
(25) W. D. Chander and L. Goodman, *J. Mol Spectrosc.*, **35**, 232 (1970).
(26) (a) G. M. Breuer and E. K. C. Lee, *J. Phys. Chem.*, **75**, 989 (1971); (b) R. G. Shortridge, Jr., C. F. Rusbult, and E. K. C. Lee, *J. Amer. Chem. Soc.*, **93**, 1863 (1971).
(27) R. Hoffmann, *J. Amer. Chem. Soc.*, **90**, 1475 (1968).
(28) See, for example, more recent articles on the trimethylene *ab initio* calculation and its reactions: (a) P. J. Hay, W. J. Hunt, and W. A. Goddard, III, *J. Amer. Chem. Soc.*, **94**, 638 (1972); (b) W. A. Goddard, III, *ibid.*, **94**, 793 (1972).
(29) It should be noted that the ethylene-*t* produced from such a cyclopentane-*t* precursor would have only 40% as much activity as the C_5 precursor, with the remaining 60% of the activity incorporated into the C_3H_5T products.
(30) Unpublished work of R. G. Shortridge, Jr., Ph.D. Thesis, University of California, Irvine, 1971.
(31) S. W. Benson, F. R. Cruickshank, D. M. Golden, G. R. Haugen, H. E. O'Neal, A. S. Rogers, R. Shaw, and R. Walsh, *Chem. Rev.*, **69**, 279 (1969).
(32) (a) B. S. Rabinovitch and R. W. Diesen, *J. Chem. Phys.*, **30**, 735 (1959); (b) D. W. Setser and B. S. Rabinovitch, *Can. J. Chem.*, **40**, 1425 (1962).

An Electron Spin Resonance Study of Metal Ion Photoinduced Reactions of Glycine and Alanine Peptides

I. Rosenthal,* R. Poupko, and D. Elad

Department of Organic Chemistry and Isotope Department, The Weizmann Institute of Science, Rehovot, Israel *(Received February 8, 1973)*

Publication costs assisted by The Weizmann Institute of Science

An esr study of the free radicals produced in glycine- and alanine-containing peptides by ultraviolet irradiation in the presence of transition metal ions has been carried out at low temperature. Two processes are distinguished: (a) the cleavage of the carbon–carbon bond at the carboxyl end of the peptide with the subsequent generation of the appropriate peptide free-radical entity, and (b) the abstraction of an "activated" hydrogen atom from the peptide molecule. In the latter reaction a preference for the glycine residues is observed. The predominance of either process depends on the nature of the "sensitizing" salt, the pH of the solution, and the carboxyl and protecting group.

Introduction

It has been previously reported that aliphatic α-amino acids undergo facile decarboxylation upon irradiation in the presence of transition metal salts to give free radicals which could be detected at room and low temperatures.[1] The loss of carbon dioxide in the photosensitized irradiation of the monocarboxylic acids led to the formation of free radicals of the type $^{+}NH_3\dot{C}R_1R_2$ according to the following reaction

$$\overset{+}{N}H_3CR_1R_2COO^- + M^{n+} \xrightarrow{h\nu} \overset{+}{N}H_3\dot{C}R_1R_2 + CO_2 + M^{(n-1)+}$$

When the amino acid contained two carboxylic groups, *e.g.*, aspartic acid, decarboxylation took place at the position further removed from the amino group.

The present study aims at the investigation of new photosensitized reactions of peptides for synthetic purposes as well as the identification of the reactive species concerned, in view of the possible subsequent reactions of such transients with other cellular components, *e.g.*, nucleic acids. We have, therefore, extended our previous studies on the photochemical reactions of amino acids in the presence of metal ions to peptides. In this work an esr study of the light-induced reaction of a number of glycine and alanine peptides with transition metal salts has been performed to further elucidate the possible reactive sites generated in these systems. In the course of this investigation it was found that several types of reactions occurred in the peptide through the electronic excitation of the salt, and the free-radical intermediates in these reactions could be characterized by esr.

Experimental Section

The protected amino acids and peptides used in this work were prepared by standard procedures, and were chromatographically pure. The electron spin resonance spectra were recorded with a Varian E12 esr spectrometer. The temperature dependence was studied using a Varian E257 variable temperature unit. The temperature was monitored by placing a thermocouple in the vicinity of the sample during measurements. The ultraviolet irradiations were accomplished with an Osram 200-W high-pressure mercury lamp housed in a Wild reflector. A cut-off Corning filter 7380 (2 mm) placed in front of the lamp efficiently removed any light of wavelength shorter than 350 nm. The experimental procedure consisted of the ultraviolet irradiation of an aqueous solution of the amino acid (*ca.* 0.1 *M*) and the inorganic salt (0.01 *M*) contained in a 3-mm diameter quartz tube at −180° in the cavity of the spectrometer.

$K_3Fe(CN)_6$ and $Ce(ClO_4)_4$ were used as "sensitizers." $K_3Fe(CN)_6$ was of analytical grade. $Ce(ClO_4)_4$, 0.5 *M*, was prepared from analytical $Ce(SO_4)_2$ and $Ba(ClO_4)_2$ as a solution in $HClO_4$.

Although obtained in amorphous frozen lattice, the esr spectra were symmetrical and the hyperfine coupling constants could be measured to an accuracy of ±1 G. For certain radicals, computer-simulated spectra were plotted on the assumption that they were composed of broad Lorentzian lines.

Results and Discussion

The photosensitized cleavage of amino acid derivatives by transition metal salts was investigated to extend the scope of the similar reactions with isolated amino acids to models more closely related to biopolymers. Glycine and alanine derivatives of the form R′NH-CH(R)-COOR″ and synthetic peptides of these two aliphatic amino acids were principally investigated in this study. The different side chain groups of the amino acids facilitate the identification of the resulting paramagnetic species. The results of the reactions studied are summarized in Table I.

At −180°, the reaction of amino acids studied with photoexcited $K_3Fe(CN)_6$ follows two main reaction pathways: (1) loss of the carboxyl group and (2) hydrogen atom abstraction. In the neutral or slightly acid media (pH ≥3), the esr spectra obtained are associated with the radical produced in the reaction

$$R'NH-\underset{\displaystyle R}{\underset{|}{CH}}-COOR'' \longrightarrow R'NH-\underset{\displaystyle R}{\underset{|}{CH}}\cdot$$

TABLE I

Peptide	Radical generated	pH[c]	Photosensitizer: $K_3Fe(CN)_6$ No. of hyperfine components	$K_3Fe(CN)_6$ hfs, G	Photosensitizer: $Ce(ClO_4)_4$ No. of hyperfine components	$Ce(ClO_4)_4$ hfs, G
Acetylglycine	$CH_3CONH\dot{C}H_2$	Neutral	Triplet	19	Triplet[a]	19
	$CH_3CONH\dot{C}HCOOH$	Acid	Doublet	18		
Glycylglycine	$^+NH_3CH_2CONH\dot{C}H_2$	Neutral	Triplet	19	Triplet	19
	$^+NH_3CH_2CONH\dot{C}HCOOH$	Acid	Doublet	18		
Alanylglycine	$^+NH_3\dot{C}HCONHCH_2$ $\quad CH_3$	Neutral	Triplet	19	Triplet	19
	$^+NH_3\dot{C}HCONH\dot{C}HCOOH$ $\quad CH_3$	Acid	Doublet	18		
Acetylalanine	$CH_3CONH\dot{C}HCH_3$	Neutral	Quintet	22	Quintet[a]	22
	$CH_3CONH\dot{C}COOH$ $\quad CH_3$	Acid	Quartet	20		
Glycylalanine	$^+NH_3CH_2CONH\dot{C}HCH_3$	Neutral	Quintet	22	Quintet	22
	$^+NH_3CH_2CONH\dot{C}COOH$ $\quad CH_3$	Acid	Quartet	20		
Alanylalanine	$^+NH_3\dot{C}HCONH\dot{C}HCH_3$ $\quad CH_3$	Neutral	Quintet	22	Quintet	22
	$^+NH_3\dot{C}HCONH\dot{C}COOH$ $\quad CH_3 \quad CH_3$	Acid	Quartet	20		
AcGlyOEt	$CH_3CONH\dot{C}H_2$	Neutral	Triplet[a]		Triplet	18
	$CH_3CONH\dot{C}HCOOC_2H_5$	Acid	Doublet	17		
AcGlyGlyOMe	$CH_3CONHCH_2CONH\dot{C}H_2$	Neutral	Triplet	18	Triplet	18
	$-NH\dot{C}HCO-$	Acid	Doublet	18		
AcGlyGlyNH$_2$	$-NH\dot{C}HCO-$	Neutral or acid	Doublet	18	Doublet	18
AcAlaOMe	$CH_3CONH\dot{C}HCH_3$	Neutral	Quintet	22		
		Acid	Unresolved spectrum			
AcGlyAlaOMe	$CH_3CONHCH_2CONH\dot{C}HCH_3$	Neutral	Quintet	22		
	$CH_3CONH\dot{C}HCONHCHCOOCH_3$ $\quad CH_3$ $\quad CH_3$	Acid	Doublet[b]	19		
AcAlaGlyOMe	$CH_3CONH\dot{C}HCONHCH_2$	Neutral	Triplet	19		
	$CH_3CONH\dot{C}HCONHCHCOOCH_3$ $\quad CH_3$	Acid	Doublet	17		
AcGlyAlaNH$_2$	$CH_3CONH\dot{C}HCONHCHCONH_2$ $\quad CH_3$	Neutral or acid	Doublet[b]	19	Doublet	19
AcGlyAlaAlaOMe	$CH_3CONH\dot{C}HCO(NH\dot{C}HCOO)_2OCH_3$ $\quad CH_3$	Neutral	Doublet + quartet	20	Doublet	20
	$^+-NH\dot{C}CO-$ $\quad CH_3$					
		Acid	Unresolved spectrum			
(Ala)$_3$	$-NH-\dot{C}H-CH_3$	Neutral	Quintet	22		
	$-NH-\dot{C}-CO-$ $\quad CH_3$	Acid	Quartet	20		
(Ala)$_4$	$-NH-CH-CH_3$	Neutral	Quintet	22		
		Acid	Unresolved spectrum			
Polyglycine	$-NH-\dot{C}H-CO-$	Neutral or acid	Doublet	18		
Polyalanine	$-NH-\dot{C}-CO-$ $\quad CH_3$	Neutral	Quartet	20		

[a] Contains a minor additional structure due to an unidentified radical. [b] Traces of a quartet due to the radical generated by hydrogen atom abstraction from alanine could be distinguished. [c] The pH values are related only to $K_3Fe(CN)_6$ induced reactions. Those induced by $Ce(ClO_4)_4$ were carried out exclusively in acid media.

Irradiation of $CH_3CONHCH_2COOH$ under these conditions gave a triplet which indicates the localization of the paramagnetic center at a $-CH_2-$ group. Three possible radicals derived from acetylglycine may exhibit such a hyperfine splitting; two of these result from carbon-nitrogen and carbon-carbon bond cleavage, $\dot{C}H_2$-COOH and $CH_3CONH\dot{C}H_2$, respectively. The third possible intermediate might be generated by abstraction of a hydrogen atom, $CH_2CONHCH_2COOH$. The cleavage of the carbon-nitrogen bond or abstraction of a hydrogen from the ter-

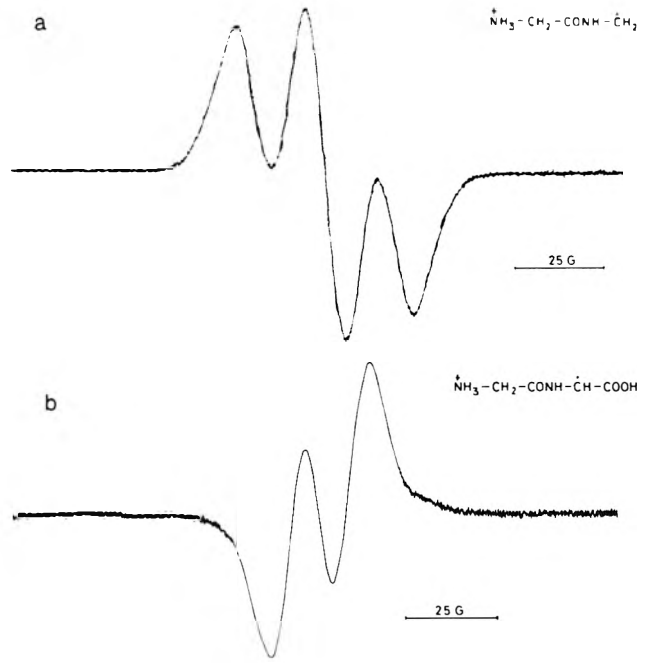

Figure 1. Esr spectra of paramagnetic species produced by reaction of glycylglycine with photoexcited $K_3Fe(CN)_6$ (a) in neutral medium and (b) in acid medium.

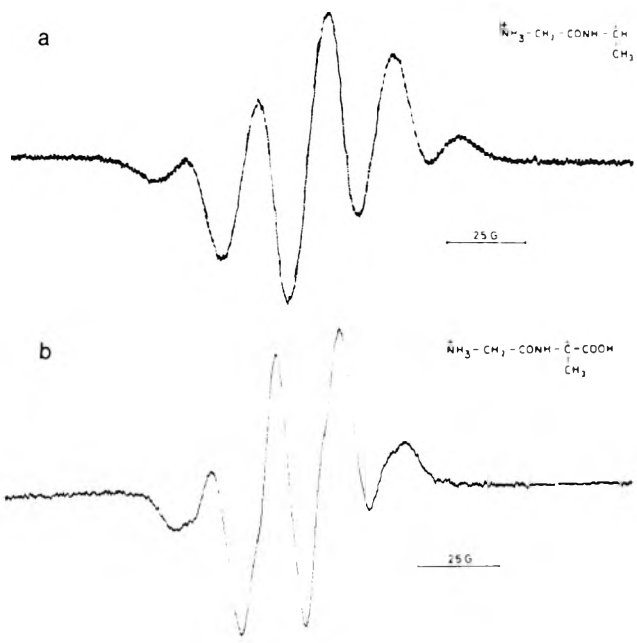

Figure 2. Esr spectra of paramagnetic species produced by reaction of alanylalanine with photoexcitec $K_3Fe(CN)_6$ (a) in neutral medium and (b) in acid medium.

minal methyl group, however, would produce a spectrum inconsistent with the data found in this work. Thus, for the radical $\dot{C}H_2$–COOH generated in solution by hydrogen atom abstraction from acetic acid by hydroxyl radical, Dixon, *et al.*,[2] reported a hyperfine splitting constant of 21.8 G. Similarly, the coupling constant of the radical $\dot{C}H_2CONH_2$ which has a similar environment to the hypothetical $\dot{C}H_2CONHCH_2COOH$ was found to be 21.3 G.[3,4] Since the value measured in this work is only 19 G, both structures can be excluded. Furthermore, in view of the previous study with isolated amino acids,[1] as well as from the five-line spectrum of acetylalanine, it seems reasonable that the radical was formed as a result of decarboxylation, *i.e.*, $CH_3CONH\dot{C}H_2$. The same radical, obtained from *N*-methylacetamide by ultraviolet irradiation in the presence of H_2O_2[4] or by irradiation with high-energy electrons[5] in fluid solutions, exhibited the following coupling constants: $a^H(CH_2)$ = 18.89–19.0 G, a^N = 2.07–2.20 G, $a^H(CH_3)$ = 3.85–4.07 G. No splitting corresponding to $a^H(NH)$ was observed in either case.

The decarboxylation reaction occurs even when the carboxyl end is protected by a methyl ester group. However, it is completely suppressed when the protective group is an amide. Figures 1a and 2a exemplify the radicals generated by this kind of cleavage from glycylglycine and glycylalanine, respectively. Thus, photolysis of glycylglycine in the presence of $K_3Fe(CN)_6$ in neutral media yielded a three-line spectrum with a mean splitting of 19 G attributed to the radical $^+NH_3CH_2CONH\dot{C}H_2$. Under similar conditions, a five-line spectrum with an almost binominal distribution of the intensities of the components (1:4:6:4:1) was recorded for glycylalanine. This hyperfine structure clearly emerges from an unpaired electron localized at the methine group at the alanine moiety ($a^H(CH) \cong a^H(CH_3) \cong 22$ G).

In acid media, pH 1, the free peptides as well as those protected by ester group yield a different type of paramagnetic species whose esr spectra could consistently be interpreted in terms of abstraction of an "activated" hydrogen atom according to the reaction

$$R'NH-\underset{\displaystyle R}{\underset{|}{CH}}-COOR'' \longrightarrow R'NH-\underset{\displaystyle R}{\underset{|}{\dot{C}}}-COOR''$$

Thus, for example, photolysis at −180° of glycylglycine in an aqueous solution of $K_3Fe(CN)_6$ acidified with $HClO_4$ gave a two-line spectrum (Figure 1b), evidently due to the presence of one vicinal proton. Consequently the structure of this radical is assumed to be $^+NH_3CH_2CONH\dot{C}HCOOH$. Under the same irradiation conditions, glycylalanine displayed a four-line spectrum attributed to $^+NH_3CH_2CO-NH\dot{C}(CH_3)COOH$ (Figure 2b).

The amide protected peptides yield only the radical generated by hydrogen atom abstraction regardless of the pH, *i.e.*, in neutral or acid media.

When hydrogen atom abstraction occurs from "homogenous" (*i.e.*, glycylglycine and alanylalanine) unprotected dipeptides, the radical is localized at the C terminal acid. This is shown by the absence of additional splitting from terminal amino protons. The hyperfine splitting constants measured in this work for these types of radicals compare very well with those reported in literature. Thus α-acetylglycine radical, $CH_3CONH\dot{C}HCOOH$, generated in solution at room temperature or in single crystal, exhibited hyperfine coupling constants a^H = 17.33 G[5,6] and 18 G,[7] respectively; α-glycylglycine radical $^+NH_3CH_2CONHCH-COOH$, $a^H(CH)$ = 16.2[8] and 18.3 G;[7] α-acetylalanine radical $CH_3CONHC(CH_3)COOH$ in single crystal $a^H(CH_3)$ = 19 G.[7] Nevertheless, when a hydrogen atom is abstracted from an alanine residue, the present data cannot distinguish between isomeric radicals $-NH-\dot{C}(CH_3)-CO-$ and $-NH-CH(\cdot CH_2)-CO-$, yet the increased stability of the tertiary radical as compared to the primary one strongly favors its generation. The structural assignment for the rest of radicals studied has been made according to similar considerations. When polyglycine and polyalanine served as

the substrate, the hydrogen atom abstraction process was found to occur predominantly even in a neutral medium; this could be due to statistical reasons rather than electronic or conformational ones.

It is noteworthy that the generation of the radical by hydrogen atom abstraction is slower than the decarboxylation process. This was shown by comparison of the relative spin concentration of the two types of radicals derived from the same peptide in two parallel experiments under identical conditions of concentrations and ultraviolet-light flux. At intermediate pH, *i.e.*, 2–3, both types of radicals were generated concomitantly. Thus, when glycylglycine was irradiated at pH 5.8–7 in the presence of $K_3Fe(CN)_6$ only a triplet signal was recorded. At pH values 2–3 a doublet overlapping the triplet could be discerned whereby at lower pH the doublet signal was predominant. Finally, at pH ≤ 1 the only detectable signal was a doublet. On warming the mixture of the two radicals to $-90°$, the one generated by the loss of the carboxyl group disappeared, affording facile identification of the second radical produced by hydrogen atom abstraction. The higher stability of the latter radical could be expected due to the degree of substitution at the carbon atom where the odd electron is localized (secondary *vs.* primary), as well as due to the extra stabilization induced by the presence of the vicinal carboxyl group. However, the possibility that the radicals are selectively quenched by reaction with $Fe(CN)_6^{2-}$ or $Fe(CN)_6^{3-}$ cannot be excluded. The assumption that $R\dot{C}HCOOH$ radical is generated by an $R\dot{C}H_2$ type radical through hydrogen atom abstraction according to the equation

$$R\dot{C}H_2 + RCH_2COOH \longrightarrow RCH_3 + R\dot{C}HCOOH$$

can be eliminated since, when $R\dot{C}H_2$ radical disappears, the intensity of the $R\dot{C}HCOOH$ signal does not increase. Furthermore, at pH 7 when only $R\text{-}\dot{C}H_2$ type radical is generated, on warming, the signal disappears without generation of any secondary radical.

The present metal ion initiated photochemical reaction of amino acids involves the absorption of light by $K_3Fe(CN)_6$, mainly due to the absorption band at 405 nm. Checks were made with solution of peptides in the absence of $K_3Fe(CN)_6$ to ensure that direct photolysis of the substrate was insignificant. The intense absorption of $Fe(CN)_6^{3-}$ at 405 nm has been assigned as ligand to metal charge transfer transition (CTTM).[9] Charge transfer excited states of this type tend to give redox decomposition in which the metal is reduced and a neighboring species is oxidized. Consequently, a possible mechanism for the decarboxylation reactions of the unprotected acids in neutral media involves as a primary process an intermediate step in which electron transfer from the dissociated carboxyl group of the amino acid to excited $Fe(CN)_6^{3-}$ ion occurs with the subsequent loss of carbon dioxide.

$$Fe(CN)_6^{3-} + RCOO^- \xrightarrow{h\nu}$$
$$Fe(CN)_6^{2-} + RCOO^{\cdot} \longrightarrow Fe(CN)_6^{2-} + \dot{R} + CO_2$$

Alternatively, this reaction can occur during, or immediately after, the transition of $Fe(CN)_6^{3-}$ ion back to the ground state. The nascent ground-state molecule will be highly vibrationally excited and may thus in some degree resemble the transition state of a thermal reaction path. The fact that carboxylic acids undergo a thermally induced facile oxidative decarboxylation in the presence of inorganic ions as Pb^{IV} [10] or Ce^{IV} [11] supports such an assumption. In a strongly acidic media the ionization of the carboxyl group is repressed, and the solvent may replace the amino acid as the oxidized counterpart in the photochemical redox decomposition of $Fe(CN)_6^{3+}$. This reaction may take place inside the aquated ion $Fe(CN)_5(H_2O)^{2-}$,[9] generated photochemically as a primary product from photoexcited $Fe(CN)_6^{3-}$. In such a case, a hydroxyl radical $\dot{O}H$ can be formed by electron transfer from the water ligand to excited Fe^{3+} ion.[12] Abstraction of a hydrogen atom by the hydroxyl radical thus formed can explain the formation of radicals observed at low pH values.

$$\dot{O}H + R\text{-}CH_2COOH \longrightarrow H_2O + R\dot{C}HCOOH$$

However, esters also behave differently in neutral or acid solution and obviously the decarboxylation of esters is inexplicable by an electron transfer mechanism as suggested for free acids. Consequently, it is tempting to speculate that a common mechanism for all compounds studied involves an intermolecular energy transfer step, which is pH dependent, from the excited $Fe(CN)_6^{3-}$ to the peptide. A similar photochemical decarboxylation of aliphatic acids free or protected, competitive to a hydrogen atom abstraction process in the presence of UO_2^{2+}, was recently reported.[13]

A final comment concerns the selectivity of the process of hydrogen atom abstraction to glycine residues. While in unprotected mixed dipeptides, alanylglycine and glycylalanine, the hydrogen atom abstraction occurs from the C terminal amino acid, in protected mixed dipeptides, the abstraction of hydrogen occurs predominantly from glycine independent of its position. The preferential reactivity of glycine toward hydrogen atom abstraction is contrary to the expectation that tertiary free radicals would be formed in preference to secondary ones, *i.e.*, that alanine free-radical centers would be preferred to those of glycine. Although no explanation for this effect can be presented, it is interesting to note that a similar observation has been made in acetone-photoinitiated generation of amino acid free radicals.[14]

Several compounds were also photolyzed in the presence of $Ce(ClO_4)_4$ instead of $K_3Fe(CN)_6$ as sensitizer. With $Ce(ClO_4)_4$, in spite of the strong acidic medium, the major process is loss of carboxyl group; however, hydrogen atom abstraction occurred when the carboxyl group was protected as an amide. Such a difference in behavior between transition metal salts as sensitizers in photochemical processes has also been observed by Greatorex, *et al.*, for U(VI) and Ce(IV).[13]

This work provides further indication that $K_3Fe(CN)_6$-photoinduced reactions lead to the formation of free radicals in amino acids and peptides, although the reaction may take a different pathway when applied to peptides as compared to isolated amino acids. It is noteworthy that the hydrogen atom abstraction process predominates in the reactions of peptides, thus making them of potential use for synthetic purposes; also, it seems plausible that this process will be the predominant one in metal ion photoinduced reactions of proteins and enzymes, when the metal is specifically bound to the protein.

References and Notes

(1) R. Poupko, I. Rosenthal, and D. Elad, *Photochem. Photobiol.*, 17, 395 (1973).

(2) W. T. Dixon, R. O. C. Norman, and A. L. Buley, *J. Chem. Soc.*, 3625 (1964).
(3) P. Smith and P. B. Wood, *Can. J. Chem.*, **44**, 3085 (1966).
(4) R. Livingston and H. Zeldes, *J. Chem. Phys.*, **47**, 4173 (1967).
(5) P. Neta and R. W. Fessenden, *J. Phys. Chem.*, **75**, 738 (1971).
(6) H. Paul and H. Fisher, *Ber. Bunsenges. Phys. Chem.*, **73**, 972 (1969).
(7) A. Fisher in "Landolt-Bornstein," New Series, Vol. 1, K. H. Hellwege and A. M. Hellwege, Ed., Springer Verlag, Berlin, 1965.
(8) H. Tahigushi, H. Hatano, H. Hasegawa, and T. Maruyama, *J. Phys. Chem.*, **74**, 3063 (1970).
(9) L. Moggi, F. Bolletta, V. Bazani, and F. Scandola, *J. Inorg. Nucl. Chem.*, **28**, 2589 (1966).
(10) J. K. Kochi, R. A. Sheldon, and S. S. Lande, *Tetrahedron*, **25**, 1197 (1969).
(11) R. A. Sheldon and J. K. Kochi, *J. Amer. Chem. Soc.*, **90**, 6688 (1968).
(12) J. H. Baxendale and J. Magee, *Trans. Faraday Soc.*, **51**, 205 (1955).
(13) D. Greatorex, R. J. Hill, T. J. Kemp, and T. J. Stone, *J. Chem. Soc., Faraday Trans. 1*, **68**, 2059 (1972).
(14) J. Sperling and D. Elad, *J. Amer. Chem. Soc.*, **93**, 967 (1971).

Reactions of Hydroxyl Radicals with Some Hydrogen Halides

G. A. Takacs and G. P. Glass*

Department of Chemistry, Rice University, Houston, Texas 77001 *(Received March 14, 1973)*

Publication costs assisted by the Petroleum Research Fund

The reactions of OH with HCl and HI have been studied in a fast flow system. Hydroxyl radicals were generated by NO_2 titration of atomic hydrogen, and concentrations of OH, Cl, and I were determined at various reaction times from their epr spectra. At 295 K, rate constants obtained for reactions 1 and 2 were $(6.4 \pm 1.5) \times 10^{-13}$ and $(1.3 \pm 0.5) \times 10^{-11}$ cm^3 molecule^{-1} sec^{-1}, respectively: OH + HCl → H_2O + Cl (1); and OH + HI → H_2O + I (2). Using these values, and others obtained from the literature, a comparison was made of the rate constants and activation energies of the reactions of OH with HCl, HBr and HI.

Introduction

Hydrogen halides are known to inhibit hydrogen[1] and hydrocarbon combustion.[2] The efficiency of these compounds in preventing flame propagation decreases in the order HI > HBr > HCl.[1] The inhibitor acts primarily by reacting with atomic hydrogen, and thus it prevents the chain branching reaction, H + O_2 → HO + O, from generating radicals. However, reaction also occurs between OH and the hydrogen halide, and this leads to a reduction in inhibitor concentration. Rates for these reactions of OH have not been well established.

Only one previous measurement of the rate of reaction 1 has been made. Wilson, *et al.*,[2] report a rate constant of 1.28×10^{-11} cm^3 molecule^{-1} sec^{-1} at 1920–1940 K from a study of the structure of CH_4-O_2 flames inhibited with HCl. However, this value may be low because no account was taken of HCl formed in the reaction of Cl with CH_4. No measurement of reaction 2 has been reported.

$$OH + HCl \longrightarrow H_2O + Cl \quad (1)$$

$$OH + HI \longrightarrow H_2O + I \quad (2)$$

In this study we have measured the rates of reactions 1 and 2 directly in a fast discharge flow apparatus. The rate of removal of OH and the rate of formation of halogen atoms have been followed using epr.

Experimental Section

The discharge flow system and the epr spectrometer have been described in detail previously.[3,4] The 20-mm i.d. flow tube was operated at pressures of 0.5 to 1.5 Torr, and linear flow speeds were maintained in the range 1300–1900 cm/sec.

Atomic hydrogen was produced by microwave discharge of a dilute mixture of H_2 in Ar, and OH was generated from it by reaction with NO_2.[3] A moveable inlet system consisting of two concentric tubes, with the inner tube of 3 mm o.d. extending 2.25 cm beyond the end of the 6-mm o.d. outer tube, allowed the halide to be added 2.25 cm downstream from the point of production of OH.

Flow rates of HI and HCl were determined from the rate of pressure drop from bulbs of known volumes. HCl (Matheson 99.0%) was used directly from the lecture bottle. HI (Matheson 98%) was stored at Dry Ice temperature and was outgassed at liquid nitrogen temperature prior to each experiment. A small amount of Dow Corning oil (Type 704) was placed above the mercury in the manometer in order to protect it from the reaction with HI.

The reactions were followed by monitoring the epr spectra of OH, Cl($^2P_{3/2}$) and I($^2P_{3/2}$). Absolute concentrations of these radicals were measured by double integration of their spectra.[3] Epr transition probabilities for all of these species have been reported by Westenberg.[5]

Results

Preliminary experiments showed that the fluorinated halocarbon wall coating[4,6] used in this study prevented measurable wall recombination of I and Cl. I($^2P_{3/2}$) was generated by titrating atomic hydrogen with excess HI. No measurable decrease in its concentration was observed out to a reaction time of 15 msec, and the ratio of I($^2P_{3/2}$) formed to H($^2S_{3/2}$) removed was measured as 0.97 ± 07. Atomic chlorine was produced by titrating H with excess Cl_2, and no measurable wall reaction was observed at reaction times shorter than 15 msec.

TABLE I: Experimental Conditions and Results for the Reaction of OH with HCl

(Ar), 10^{14} molecules cm^{-3}	$(H)_0$, 10^{14} molecules cm^{-3}	$(NO_2)_0$, 10^{14} molecules cm^{-3}	$(HCl)_0$,[a] 10^{14} molecules cm^{-3}	$(Cl)_i$,[b] 10^{14} molecules cm^{-3}	$(OH)_i$,[b] 10^{14} molecules cm^{-3}	$(HCl)_i$,[b] 10^{14} molecules cm^{-3}	k_1, 10^{-13} cm^3 molecule^{-1} sec^{-1}	
							From Figure 1	From computation
240	10.1	9.22	9.28	0.78	0.21	8.50	6.4	6.6
244	6.79	7.90	6.56	0.71	0.34	5.85	7.4	5.5
250	5.35	4.96	4.70	0.55	0.24	4.15	8.4	6.4
236	5.98	6.52	7.13	0.79	0.17	6.34	7.9	7.6
241	3.92	3.62	9.52	0.65	0.09	8.87	6.2	6.7
217	4.89	5.13	8.35	0.71	0.20	7.64	6.9	6.5
230	3.21	3.74	8.17	0.60	0.17	7.57	6.2	5.6

Av value of $k_1 = 6.4 \pm 0.7 \times 10^{-13}$ cm^3 molecule^{-1} sec^{-1}

[a] HCl added 2.25 cm downstream from NO_2 inlet. [b] At initial OH measuring point (approximately 3 cm downstream of HCl inlet).

The reaction of OH with hydrogen halide was studied by adding sufficient excess halide to the flow tube to ensure that the major portion of OH was removed by reaction with the halide, and less than 10% removed by reactions 3–5.

$$OH + OH \longrightarrow H_2O + O \quad (3)$$

$$OH + O \longrightarrow H + O_2 \quad (4)$$

$$OH \longrightarrow wall \quad (5)$$

An initial approximate estimate of k_1 (or k_2) was obtained from the experimental data by ignoring the OH removed in reactions 3–5. The concentration of halide was assumed to be constant throughout the measured reaction zone, and the rate constant was estimated from the first-order integrated rate expression

$$2.3 \log (OH)_0/(OH) = k(HX)t$$

where $(OH)_0$ is the OH concentration measured at some arbitrary point chosen to represent $t = 0$.

This rate constant was used as an initial trial value in a computer program that takes account of the entire reaction sequence 1 through 5. The program, which has been described in detail previously,[7] compared the concentration of OH measured at various reaction times with that estimated by integrating the rate equation pertaining to reactions 1–5. Values of k_1 (or k_2) that gave the best fit between the measured and calculated OH concentrations were computed. In this analysis, k_3 and k_5 were taken as 1.60×10^{-12} cm^3 molecule^{-1} sec^{-1} and 60 sec^{-1}, respectively.[4]

The rate constant, k_1, for the reaction of OH with HCl was estimated as $(6.4 \pm 0.7) \times 10^{-13}$ cm^3 molecule^{-1} sec^{-1}. Individual values of k_1 determined from computer analysis of each experiment are listed in Table I. This table also identifies the initial reactant concentrations used in each experiment, values of (OH), (HCl), and (Cl) determined at the initial measuring position (3.3 cm downstream of the HCl inlet), and values of k_1 obtained from plots of log (OH) against reaction time. All measurements were made using mixtures containing a large excess of HCl. The concentration of OH was generally monitored over a reaction time of 13 msec, and during this time, it decreased to $1/14$–$1/65$ of its original value. A typical experimental OH decay curve is shown in Figure 1.

The reaction of OH with HI was studied only with some difficulty. Initial experiments showed the reaction to be very fast. Therefore, in order to obtain adequate spacial resolution along the flow tube, the reaction rate was reduced by lowering reactant concentrations. Unfortunately, this resulted in epr signals having a smaller S/N ratio, and thus a compromise had to be reached between adequate spacial resolution and measurable epr spectra.

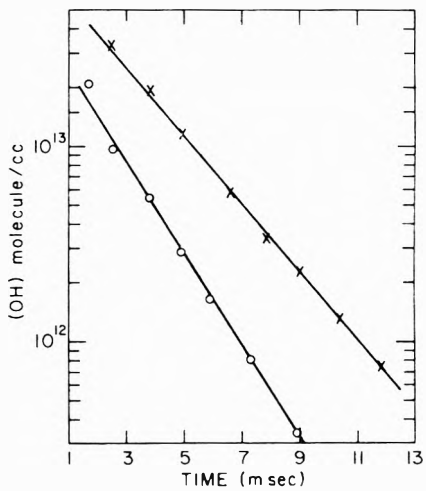

Figure 1. Plot of log (OH) *vs.* time for reaction of OH with HCl: O, (HCl) = 8.50×10^{14} molecule/cm^3 in reaction zone; X, (HCl) = 5.85×10^{14} molecule/cm^3 in reaction zone; flow speed = 1340 cm/sec; total pressure = 0.81 Torr.

The reactant concentrations finally chosen are shown in Table II. Using these, the reaction could be studied over a reaction time of ~4 msec, and during this time the OH concentration decreased by an order of magnitude to a final measurable concentration of $2\text{–}5 \times 10^{11}$ molecules/cm^3. Sample plots of (OH) *vs.* reaction time are shown in Figure 2. The rate constant k_2 was estimated by computer analysis of the OH decay as $(1.3 \pm 0.5) \times 10^{-11}$ cm^3 molecule^{-1} sec^{-1}.

Several measurements were made of the ratio of atomic halogen formed to OH removed, in order to check for competing or side reactions of OH that could complicate the interpretation of the kinetic data. The stoichiometry of the reaction of OH with HCl was studied by comparing it with that of the reaction, $H + HCl \rightarrow H_2 + Cl$, which could be followed by turning off the NO_2 flow. The ratio of $Cl(^2P_{3/2})$ formed from OH to that formed by an equal amount of atomic hydrogen was measured as 1.1 ± 0.1.

TABLE II: Experimental Conditions and Results for the Reaction of OH with HI

(Ar), 10^{14} molecules cm^{-3}	$(H)_0$, 10^{14} molecules cm^{-3}	$(NO_2)_0$, 10^{14} molecules cm^{-3}	$(HI)_0$,[a] 10^{14} molecules cm^{-3}	$(I)_i$,[b] 10^{14} molecules cm^{-3}	$(OH)_i$,[b] 10^{14} molecules cm^{-3}	$(HI)_i$,[b] 10^{14} molecules cm^{-3}	k_2, 10^{-11} cm^3 molecule^{-1} sec^{-1}	
							From Figure 2	From computation
212	4.39	4.73	1.73	1.02	0.054	0.71	1.6	1.3
233	4.70	4.05	2.32	1.30	0.032	1.02	1.3	1.3
232	4.70	4.06	1.77	1.29	0.039	0.48	2.5	2.4
226	2.70	3.26	2.13	0.95	0.022	1.18	1.2	1.1
226	2.70	3.28	1.70	0.97	0.035	0.73	1.2	1.2
284	3.14	5.05	2.98	0.93	0.039	2.05	0.7	0.5

Av value of $k_2 = 1.3 \pm 0.5 \times 10^{-11}$ cm^3 molecule^{-1} sec^{-1}

[a] HI added 2.25 cm downstream from NO_2 inlet. [b] At initial OH measuring position (~3 cm downstream from HI inlet).

The reaction with HI was studied as follows. Excess HI was added to atomic hydrogen, and the resulting iodine atom concentration was measured 7.5 cm (5 msec) downstream of the HI inlet. Then, NO_2 was admitted to the flow stream through a separate probe located at the HI inlet, and [I] was remeasured. Results for several experiments are shown in Table III. Two conclusions are immediately apparent: (i) both NO and NO_2 react rapidly with atomic iodine; (ii) when account is taken of the amount of atomic iodine removed in the well known reaction[8]

$$I + I + NO \longrightarrow I_2 + NO$$

it is seen that the amount of iodine formed by reaction 2 is identical with that formed by the reaction, $H + HI \rightarrow H_2 + I$.

All of the kinetic measurements reported in this paper were performed at 295 K in the presence of a small excess of atomic hydrogen. Unfortunately, this prevented us from estimating the rate constants for reactions 1 and 2 from halogen atom growth measurements, because both HCl and HI react with atomic hydrogen to yield additional halogen atoms. However, the alternative procedure, namely, over-titrating H with NO_2, was avoided because it is known that NO_2 reacts with OH,[9] and because the results in Table III show that it also reacts quite rapidly with atomic iodine.

Discussion

The rate constants computed for reactions 1 and 2 are approximately 10% lower than those that were obtained from Figures 1 and 2 by ignoring the effects of reactions 3-5. Thus the values obtained are not significantly affected by the factor of 3 uncertainty in our present knowledge of k_3.[3,10,11] This fact can be confirmed using data shown in Tables I and II. In the presence of HCl, wall recombination of OH (with $k_5 = 60$ sec^{-1}) occurs at a rate that is, on the average, 12% of that of reaction 1. Reaction 3 is much less important. In fact, even at the initial measuring point, where [OH] is highest and the contribution from reaction 3 greatest, the rate of reaction 3 is only 3-14% of that of reaction 1, and during the course of the reaction this contribution decreases by over an order of magnitude. In the presence of HI, wall recombination accounts for only 4% of the OH decay, and the rate of reaction 3 is never more than 1.5% of that of reaction 2.

The rate constant for the reaction of OH with HCl was measured as 6.4×10^{-13} cm^3 molecule^{-1} sec^{-1}, with a

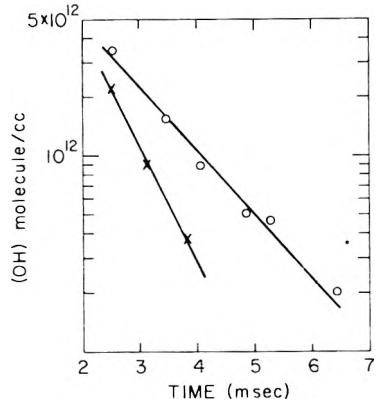

Figure 2. Plot of log (OH) vs. time for reaction of OH with HI: X, (HI) = 1.18×10^{14} molecule/cm^3 in reaction zone; O, (HI) = 0.73×10^{14} molecule/cm^3 in reaction zone; flow speed = 1365 cm/sec.

standard deviation of ±11%. However, the probable error is likely to be greater than this because of uncertainties in our knowledge of k_5, and because of the oversimplified treatment of the gas flow pattern.[12] For the reaction of OH with HI, the rate constant was measured as $1.3 \pm 0.5 \times 10^{-11}$ cm^3 molecule^{-1} sec^{-1}. The larger standard deviation in this value is mainly the result of the uncertainty introduced by our measurement of the HI concentration in the reaction zone. This uncertainty arises because a considerable fraction of the initial HI was removed in the mixing zone prior to the first measuring point, by rapid reaction with OH and untitrated atomic hydrogen. The amount remaining was estimated as $(HI)_0 - (I)$, and the absolute value of the atomic iodine concentration could be measured only to ±10% using epr.

The rate of reaction 1 has been measured previously at 1920-1940 K by Wilson, *et al.*[2] Combining that value with ours, k_1 can be expressed in Arrhenius form as $2.1 \times 10^{-11} \exp(-2060/RT)$ cm^3 molecule^{-1} sec^{-1}. Unfortunately, the high-temperature value, which was estimated from the growth of HCl, may be somewhat low due to the neglect of the reaction, $Cl + CH_4 \rightarrow HCl + CH_3$. If this is so, then the activation energy estimated above is also low. It is difficult to estimate the error in the high-temperature rate constant, but doubling it increases the activation energy to 2.6 kcal/mol.

Reactions of OH with several hydrogen halides are compared in Table IV. As can be seen, the preexponential fac-

TABLE III: Stoichiometry of Reaction 2[a]

$[H]_0$	$[HI]_0$	$[NO_2]_0$	(I) with NO_2/ (I) withcut NO_2	Fraction of H[b] reacting with NO_2	[NO] formed from NO_2	Fraction I removed by NO[c]
7.0×10^{14}	11.1×10^{14}	2.3×10^{14}	0.97	0.15	1.05×10^{14}	0.03
7.0×10^{14}	10.0×10^{14}	3.3×10^{14}	0.96	0.22	1.54×10^{14}	0.05
7.0×10^{14}	13.8×10^{14}	7.0×10^{14}	0.92	0.44	3.08×10^{14}	0.10
7.0×10^{14}	12.5×10^{14}	33.5×10^{14}	0.40	0.82	5.74×10^{14}	0.18

[a] All concentrations in molecule cm^{-3}. [b] Est mated using data from L. F. Phillips and H. I. Schiff, *J. Chem. Phys.*, **37**, 1233 (1962), for the rate of reaction $H + NO_2 \rightarrow OH + NO$, and a rate constant of 2.1×10^{-11} cm^3 molecule^{-1} sec^{-1} for the reaction $H + HI \rightarrow H_2 + I$. The latter value was measured in this laboratory. [c] Calculated using the rate constant for, $I + I + NO \rightarrow I_2 + NO$, from ref 8, assuming all the NO to be formed within 1 msec.

TABLE IV: Rates of Reaction of OH with HCl, HBr and HI[a]

Halogen	k(295 K)	Measured activation energy, kcal/mol	Potential energies of activation from BEBO method, kcal/mol	Preexponential factor	Collision no.[c]	Heat of reaction,[d] kcal/mol
Cl	6.4×10^{-13}	2.06	0.3	2.2×10^{-11}	2.75×10^{-10}	−16.1
Br	5.1×10^{-12} [b]	1.15[b]	0.4	3.7×10^{-11} [b]	2.79×10^{-10}	−31.7
I	1.3×10^{-11}	<1.9[e]	0.7	$>1.3 \times 10^{-11}$	3.08×10^{-10}	−47.9

[a] All rate constants measured in units of cm^3 molecule^{-1} sec^{-1}. [b] Measured in ref 4. [c] Calculated from transport properties. [d] For reaction $OH + HX \rightarrow H_2O + X(^2P_{3/2})$. [e] Calculated assuming unit steric factor.

tors for the reaction with HCl and with HBr are similar. If this pattern holds, the activation energy for the reaction with HI can be calculated as 0.6 kcal/mol. It is interesting to note that the activation energies appear to decrease in a systematic manner and, to a first approximation, to be inversely proportional to the heats of reaction. However, care should be taken in drawing such conclusions, since recent work[13] has shown that curved Arrhenius plots may be encountered when studying reactions over a wide temperature range.

Table IV includes the results of several BEBO calculations reported by Johnston.[14] The activation energies estimated using the BEBO method are much lower than the values measured, and the variation from halide to halide is different from that observed. This discrepancy between BEBO prediction and experiment is similar to that previously found[15,16] for the series $Cl + HX \rightarrow HCl + X$ and $O + HX \rightarrow OH + X$ (X = Cl, Br, and I).

In both of these series, the triplet repulsion between the incoming and outgoing group is quite small, and this results in: (i) predicted transition states that lie very early in the entrance valleys of the potential energy surfaces and (ii) low activation energies. Our calculations suggest that the series $OH + HX \rightarrow H_2O + X$ fits this pattern very well. Here again, the triplet repulsion is small, the transition states are located in the entrance valleys of the potential energy surfaces with values of bond order n_1 greater than 0.94, and the predicted activation energies are very low.

In these experiments, no determination was made of the initial yield of $(^2P_{1/2})$ halogen atoms although reactions 1 and 2 are exothermic enough to produce $Cl(^2P_{1/2})$ and $I(^2P_{1/2})$, respectively. Unfortunately, $Cl(^2P_{1/2})$ is quenched on every collision with atomic hydrogen,[17] and $I(^2P_{1/2})$ is efficiently quenched at the walls.[18] Thus, in our apparatus, any electronically excited atoms would be quenched prior to detection. An unsuccessful search for the epr spectra of $Cl(^2P_{1/2})$, which has been observed previously by Carrington, *et al.*,[19] following microwave discharge of CF_3Cl, tends to support this conclusion.

Acknowledgments. Acknowledgment is made to the donors of the Petroleum Research Fund, administered by the American Chemical Society, for the support of this research. The authors wish to thank the Robert A. Welch Foundation of Houston, Texas, for the use of the epr spectrometer.

References and Notes

(1) R. N. Butlin and R. F. Simmons, *Combust. Flame*, **12**, 447 (1968).
(2) W. E. Wilson, Jr., J. T. O'Donovan, and R. M. Fristrom, *Symp. Combust. 12th*, 929 (1969).
(3) J. E. Breen and G. P. Glass, *J. Chem. Phys.*, **52**, 1082 (1970).
(4) G. A. Takacs and G. P. Glass, *J. Phys. Chem.*, **77**, 1060 (1973).
(5) A. A. Westenberg, *J. Chem. Phys.*, **43**, 1544 (1965).
(6) Flowtube coated by MarChem Inc., P.O. Box 6914, Houston, Tex. 77005.
(7) J. E. Breen and G. P. Glass, *Int. J. Chem. Kinet.*, **3**, 145 (1970).
(8) G. Porter, Z. G. Szabo, and M. G. Townsend, *Proc. Roy. Soc. Ser. A*, **270**, 493 (1962).
(9) A. A. Westenberg and N. deHaas, *J. Chem. Phys.*, **57**, 5375 (1972).
(10) F. Kaufman, *Ann. Geophys.*, **20**, 106 (1964).
(11) G. Dixon-Lewis, W. E. Wilson, and A. A. Westenberg, *J. Chem. Phys.*, **44**, 2877 (1966).
(12) F. Kaufman, *Can. J. Chem.*, **47**, 1917 (1969), discusses this source of error.
(13) F. Dryer, N. Naegeli, and I. Glassman, *Combust. Flame*, **17**, 270 (1971).
(14) H. S. Johnston, "Gas Phase Reaction Rate Theory," Ronald Press, New York, N. Y., 1966, p 212.
(15) G. A. Takacs and G. P. Glass, *J. Phys. Chem.*, **77**, 1182 (1973).
(16) M. H. Mok and J. C. Polanyi, *J. Chem. Phys.*, **51**, 1451 (1969).
(17) R. J. Donovan and D. Husain, *Chem. Rev.*, **70**, 509 (1970).
(18) D. Husain and J. R. Wiensenfeld, *Trans. Faraday Soc.*, **63**, 1349 (1967).
(19) A. Carrington, D. H. Levy, and T. A. Miller, *J. Chem. Phys.*, **45**, 4093 (1966).

Isocyanate Intermediates in the Reaction NO + CO over a Pt/Al_2O_3 Catalyst

Mark L. Unland

Corporate Research Department, Monsanto Company, St. Louis, Missouri 63166 *(Received March 23, 1973)*

Publication costs assisted by Monsanto Company

Infrared spectroscopy has been used to observe intermediates formed in the interaction of NO and CO on the surface of a Pt/Al_2O_3 catalyst. The general procedure was to dose a clean surface at elevated temperature with the desired gas or gas mixture, cool to room temperature, and observe the infrared spectrum of the adsorbed species in the 4000-1200-cm^{-1} region. When mixtures of CO and NO containing excess or stoichiometric amounts of CO were used, the infrared spectrum contained strong bands at 2267 and 2148 cm^{-1} which were not observed when the sample was treated similarly with known reactants or products or when treated with the reactant mixture below 200°. Labeling experiments and consideration of other factors lead to the assignment of the 2267-cm^{-1} band to a Pt-NCO species and the 2148-cm^{-1} band to an $(NCO)^-$ anion. The discovery of these intermediates provides a new mechanistic pathway and possible alternative to previous explanations of NH_3 formation in the catalytic treatment of automobile exhaust.

Introduction

Control of automobile exhaust pollution is proving to be a technical as well as a political challenge. The technical problem can be separated into two categories: the oxidative removal of carbon monoxide and hydrocarbons and the reductive removal of nitrogen oxides (NO + NO_2). The motivation for the present study comes from a desire to better understand the mechanisms and problems involved in catalytic removal of nitrogen oxides. It has long been recognized[1] that reduction of NO_x with the CO also present in auto exhaust could provide an efficient means of removal providing the proper catalyst could be found. The catalyst requirements are stringent since it must operate satisfactorily under a large variety of conditions in actual use where extremes of temperature and exhaust composition are commonplace. In addition to removing the undesired components, the catalyst must not produce any undesirable side products such as HCN or NH_3. For example, it is known that automobiles equipped with catalytic converters operating under the fuel-rich conditions necessary for NO_x removal often produce easily detectable amounts of ammonia.[2-4] This ammonia is generally considered to be the result of a reaction between NO and hydrogen which is either already present or has been generated *in situ* by a water-gas shift mechanism[5] or from cracking of hydrocarbons. Shelef and Gandhi[6] have concluded that hydrogen generated from the water-gas shift is much more effective in the reduction of NO than molecular hydrogen already present or derived from hydrocarbons in the exhaust. The findings to be presented here offer yet another possibility.

Thus, the present study is an attempt to further understand the mechanism of the reaction NO + CO over a typical auto exhaust catalyst, Pt/Al_2O_3, by use of infrared spectroscopy where one has the possibility of studying the adsorption[7,8] (physical and chemical) of the reactants, products, and intermediates on the catalyst surface.

Experimental Section

A quartz cell similar to that described by Peri[9] was constructed and used in conjunction with a conventional vacuum and gas handling system capable of evacuation to 10^{-6} Torr. The samples were deposited on a 25 × 4-mm CaF_2 disk which could be moved from a heated section into the infrared beam at will without opening the cell. Baymal[10] (E. I. du Pont de Nemours & Co., Inc.), an alumina powder consisting of boehmite fibrils which swell in water to form a colloidal solution, was used for these studies to form the completely inorganic, clear-to-translucent films on a smooth surface by casting from an aqueous dispersion. Minimal flaking and crazing of the film occurred when air dried and calcined under vacuum to the 350–600° necessary to dehydrate the boehmite fibrils to high surface area γ-alumina. The small size of the fibrils (≤50 Å in diameter) minimizes ir scattering losses which are often a problem when working with solid samples.

The sample was prepared by using 13 ml of solution containing 0.0105 g of platinum from $H_2PtCl_6 \cdot 2H_2O$ to disperse 0.30 g of Baymal powder (calculated to give ~0.21 g of γ-Al_2O_3 after calcination). Five drops of the dispersion was spread on a 25 × 4-mm CaF_2 disk and air dried to a coherent film. Another film was cast on the other side and the whole process repeated so that a total of 20 drops (containing 10–15 mg of solid) were used in preparing the sample. The sample was then placed in the cell and heated under vacuum to 400° for 4–5 hr to convert the Baymal to γ-Al_2O_3. The sample, at 400°, was treated with 100 Torr of O_2 for 1.5 hr, evacuated for 15–20 min, treated with 100 Torr of H_2 for 1 hr, and cooled under vacuum. The resulting sample showed 67% transmission at 2500 cm^{-1} and contained ~5% Pt/Al_2O_3.

In order to provide a reproducible starting point for each of the experiments, the practice of "cleaning" the surface immediately before each experiment was adopted. The following procedure was used: (a) evacuate while sample is heated to 400°; (b) treat with 100 Torr of oxygen for 30 min at 400°; (c) evacuate at 400° for 15 min; (d) treat with 100 Torr of hydrogen for 30 min at 400°; and (e) evacuate for 15 min at 400°. With the temperature adjusted to the desired value, the sample cell was filled to 100 Torr with the gas or gas mixture. All gases were of lecture bottle quality (except for the use of prepurified N_2), from

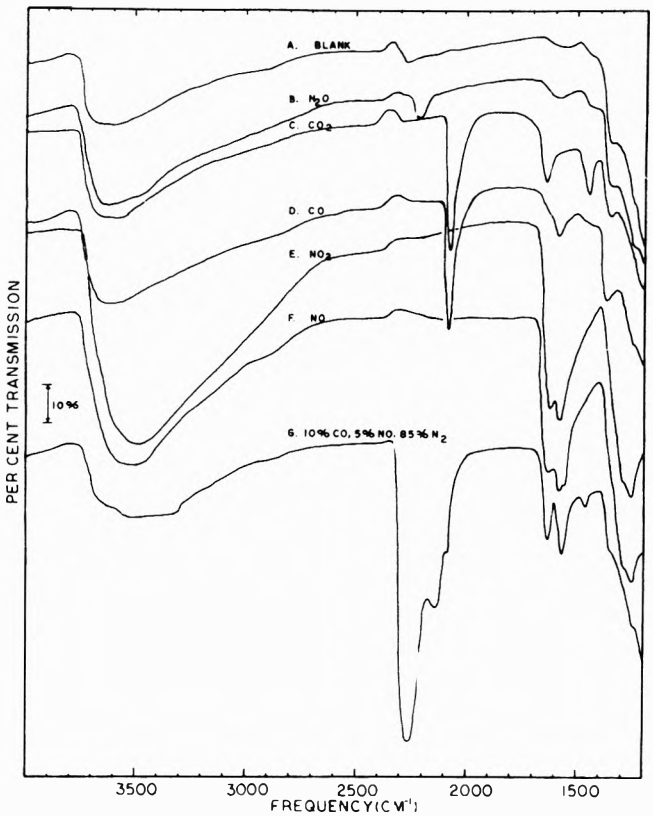

Figure 1. 5% Pt/Al_2O_3 dosed at 400° with 100 Torr of the reactants and possible products involved in the NO + CO reaction. Also shown is the spectrum observed after dosing the sample with a 10% CO, 5% NO, and 85% N_2 blend under the same conditions. The sample was cleaned at 400° before each run.

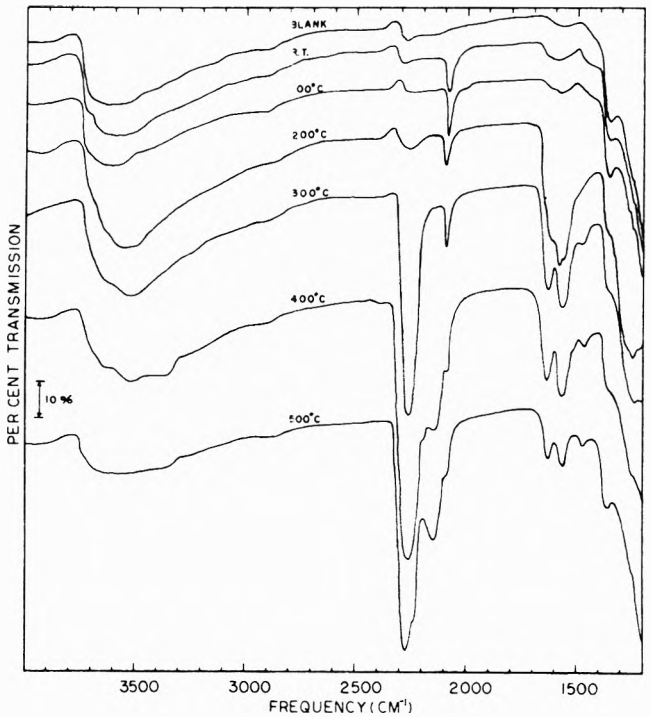

Figure 2. Spectra observed at room temperature and 1 Torr pressure after dosing the 5% Pt/Al_2O_3 sample with 100 Torr of a 10% CO, 5% NO, and 85% N_2 blend at various temperatures. The sample was cleaned at 400° before each run.

Matheson Co., and were used without further purification.

The infrared spectra were recorded on a Perkin-Elmer Model 337 infrared spectrophotometer equipped with ordinate scale expansion and a Perkin-Elmer Model 165 recorder. The instrument was calibrated against a 0.05-mm polystyrene film or a mixture of NO and CO gas using the normal slit program which was used for all runs discussed in this paper. On very sharp peaks the accuracy is judged better than ±2 cm^{-1} but on the very broad and sometimes weak peaks observed with the Pt/Al_2O_3 sample the accuracy is estimated as ±5 cm^{-1}.

In order to establish reference points for this particular sample, the individual spectra of the reactants and probable products of the NO + CO reaction were obtained. In each case the sample was cleaned as described earlier, dosed with 100 Torr of the gas or gas mixture at 400° for 30 min, and cooled to ≤50° under 100 Torr pressure. After cooling, the gas pressure was reduced to ~1 Torr to eliminate gas-phase contribution to the spectrum.

Results

The spectra for the cleaned sample and adsorbed N_2O, CO_2, NO_2, or NO are shown in Figure 1 along with the spectrum obtained when the sample was treated with a gas mixture of 10% CO, 5% NO, and 85% N_2 under the same conditions. Because the adsorbed species of interest in this work show strong ir absorptions in the region between 2100 and 2300 cm^{-1}, it is worth emphasizing that neither CO_2 nor N_2O which have strong gas phase adsorptions in this region (2349.3 and 2223.5 cm^{-1}, respectively[11]) show a strong band when adsorbed onto the Pt surface under the conditions of these experiments. The fact that none of the reference spectra gives a clue to the identity of the strong bands observed at 2267 and 2148 cm^{-1} when the reaction mixture is adsorbed onto the hot Pt surface is an indication that we may be observing reaction intermediates.

Even with the aid of the reference spectra the assignment of only one of the bands observed in Figure 1G is clear. The shoulder at 2088 cm^{-1} is due to a linearly adsorbed CO species. This band is observed to move to lower frequency and finally disappear as the sample is evacuated, in agreement with earlier observations by Eischens, Francis, and Pliskin.[12] The cause of this effect has been attributed to either interaction effects between adsorbed molecules[12] or adsorption on distinct surface sites of different coordination thereby causing changes in the strength of the carbon–platinum bond which in turn changes the C–O stretching frequency.[13] Other experiments on a well calcined Al_2O_3 sample using the reaction mixture and conditions of Figure 1G produced only very weak bands similar to the spectrum labeled "blank" in Figure 1. This indicates that the important chemisorption and reaction sites were on the Pt and not the Al_2O_3 surface.

Temperature Experiments. To gain more information about the nature of the bands observed in Figure 1G, a series of temperature experiments were carried out on Pt/Al_2O_3 using a 10% CO, 5% NO, 85% N_2 gas blend. After cleaning the sample at 400° as described earlier, the temperature was adjusted to various values between room temperature and 500° before dosing, cooling, and recording the spectra in the manner used previously. The recorded spectra are displayed in Figure 2.

The more intense bands do not appear until the sample temperature is in the vicinity of 200° at which point a broad band system in the vicinity of 1580 cm^{-1} is ob-

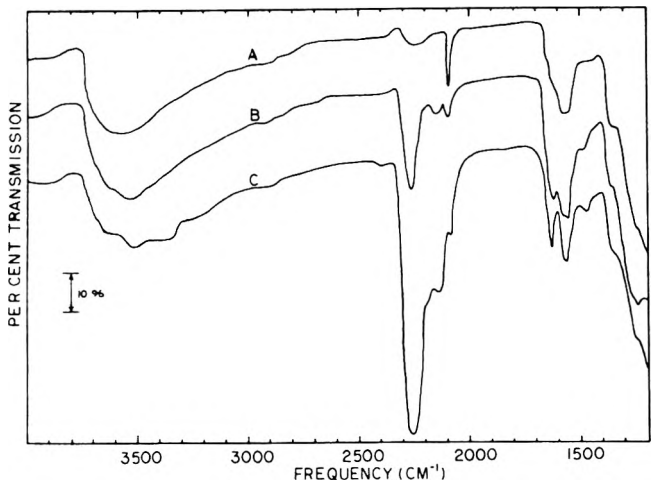

Figure 3. Spectra observed at room temperature and 1 Torr pressure after dosing the 5% Pt/Al_2O_3 sample at 400° with 100 Torr of (A) 10% CO, 15% NO, and 75% N_2; (B) 10% CO, 10% NO, and 80% N_2; and (C) 10% CO, 5% NO, and 85% N_2 gas blends. The sample was cleaned at 400° immediately before each run.

served. This band is quite similar to that observed in Figure 1F, the reference spectra for NO adsorbed on this sample.

The strong band at 2267 cm^{-1} and the features at 1634 and 1469 cm^{-1} do not appear until the sample temperature is raised to 300°. The fact that the 2148-cm^{-1} band mentioned earlier does not appear at the same temperature as the strong band at 2267 cm^{-1} is an indication that these bands arise from either entirely different species or, possibly, from similar species adsorbed on quite different surface sites.

At 400° the medium intensity band at ~2148 cm^{-1} first appears. There is also evidence of a weak unresolved band at ~2197 cm^{-1} which was not apparent in earlier spectra at 400° (see Figure 1G). It is possible that these higher temperature bands are due to reaction of some of the other surface species. For example, there appears to be a significant decrease in the intensity of the 1634-, 1580-, and 1469-cm^{-1} bands in the 500° spectrum as opposed to 400° and lower scans.

In summary, the temperature experiments on the Pt/Al_2O_3 sample show that the bands in Figure 1G at 2267 and 2148 cm^{-1} are not due to the same adsorbed species and that there is a third unresolved band intermediate between them which is quite dependent on temperature. From the temperature at which these bands appear and since they are probably not due to adsorbed reactants or products, it appears possible that they arise from intermediates in the reduction of NO with CO over the Pt/Al_2O_3 catalyst.

Reaction Mixture Variations. Blends were prepared with 10% CO and 15%, 10%, and 5% NO in nitrogen and these were dosed onto the clean Pt/Al_2O_3 sample at 400° in the usual manner. The results are shown in Figure 3. Examination of spectrum A in Figure 3 shows that when NO is in excess over the CO the prominent bands at 2267, 2148, 1633, and 1469 cm^{-1} do not appear. When stoichiometric amounts of NO and CO are used in the reaction mixture, bands appear at 2267 and 2141 cm^{-1}, although they are much weaker than when CO is in excess. Bands at 1620 cm^{-1} and 1482 cm^{-1} are also now in evidence. From Figure 3B, the band shape of the unresolved doublet

TABLE I: Isotope Shift Studies[a] for Pt/Al_2O_3 Sample

10% CO, 5% NO, cm^{-1}	10% ^{13}CO, 5% NO, cm^{-1}	$^{13}C-^{12}C$, cm^{-1}	10% CO, 5% ^{15}NO, cm^{-1}	$^{15}N-^{14}N$, cm^{-1}	Comments
2261	2199	−62	2249	−12	-NCO
2130	2074	−56	2112	−18	$[NCO]^-$ or -CN ?
2083	2034	−49	2084	+1	CO
1633	1621	−12	1622	−11	>C=N— ?
1564	1522	−42	1588	−6	$CO_3^{2-} + NO_3^-$?
1472	1474	+2	1472	0	? CO_3^{2-} (very weak)

[a] Clean sample dosed at 400° with 100 Torr of mixture, cooled to ≤50° and evacuated to 1 Torr. From an estimate of the experimental reproducibility on measuring broad bands, a shift of 5–6 cm^{-1} is on the borderline of being significant.

at 1568 cm^{-1} is quite similar to that observed in the NO reference spectra of Figure 1F.

The main conclusion from this set of experiments is that the species giving rise to the bands at 2267 and 2148 cm^{-1} require excess CO before they are formed. If NO is in excess it will either react with these species or otherwise prevent their formation in appreciable concentrations.

^{13}C and ^{15}N Labeling. For these experiments a fresh catalyst sample was prepared as described earlier. Also, the instrument was calibrated with gaseous CO and NO since the producibility was found to be much improved over using polystyrene film with its much broader bands. The calibration of the instrument was checked daily during the labeling experiments to detect any instrument changes. Probably as a result of using a different sample, the observed frequencies reported in Table I do not agree exactly with those discussed above, but the qualitative appearance of the spectra from the present sample is nearly identical to spectrum G in Figure 1.

The gas mixture compositions were all 10% CO, 5% NO, and 85% N_2 as before. The unsubstituted mixture was run twice, once before and once after the labeling experiments, to make sure that the sample had not changed and to check reproducibility. The frequencies of the bands in the before and after runs agreed to within 2 cm^{-1}. No analysis of the gas composition in the cell was made except for the qualitative observation of NO, CO, CO_2, and N_2O after reaction. The large volume of gas, the small amount of catalyst, and the limited reaction time combined to prevent complete conversion of the NO and CO

From Table I it is evident that the species giving rise to the intense bands at 2261 and 2130 cm^{-1} contain both carbon and nitrogen atoms. The species absorbing at 2083, 1564, and 1472 cm^{-1} appear to contain only carbon atoms and are assigned to CO and two different CO_3^{2-} species, respectively. It is interesting that the CO_3^{2-} band at 1564 cm^{-1} did not appear in either the CO or CO_2 reference spectra of Figure 1. The 60-cm^{-1} shift on ^{15}N substitution and the appearance of some of the spectra such as the 200° run in Figure 2 and run B in Figure 3 lead to the belief that the band at 1564 cm^{-1} is not due purely to CO_3^{2-} but also contains contributions from nitrogen containing species possibly nitrate ions. Since the band at 1633 cm^{-1} is reasonably sharp, it is probable that it is due to a single species which, the labeling experiments show, must contain both carbon and nitrogen. The most probable assignment of the 1633 cm^{-1} band is to a species such as an imine or substituted imine which contains a carbon-

nitrogen double bond. Such structures are known[14] to absorb in the 1633-1640-cm^{-1} region.

In line with consideration of reactions 6-9 (to be discussed later) an experiment was conducted in which the 2261- and 2130-cm^{-1} bands were formed on the Pt/Al_2O_3 sample as usual. Then, at room temperature, 5 Torr of H_2O vapor was admitted to the sample cell, allowed to stand for 30 min, evacuated to ≤ 0.01 Torr, and a spectrum was obtained. It was found that the 2130-cm^{-1} band had been completely removed and the 2261-cm^{-1} band was sharply decreased in intensity whereas prolonged pumping without H_2O treatment produced no intensity changes. To determine the sensitivity of the 2261- and 2130-cm^{-1} bands to molecular H_2, a series of experiments was conducted in which H_2 was contacted at various temperatures with the sample which had previously been treated to produce these bands. The sample was dosed with 100 Torr of H_2, heated to the desired temperature, cooled back to $\leq 50°$, and the spectrum was recorded. The sample spectrum was also observed after heating to 400° under vacuum and cooling to $\leq 50°$. The intensity of the 2261-cm^{-1} band remained unchanged at 150° but decreased on treatment at 265 and 350°; evacuation at 400° caused still more loss of intensity.

Discussion

With regard to the reference spectra of Figure 1, it is interesting to note the similarity of the CO_2 and CO spectra after adsorption onto the Pt/Al_2O_3 surface at 400°. Both show a strong peak at about 2075 cm^{-1} which is due to a linear chemisorbed CO species.[12,15] In the case of CO_2, the CO species must come from the dissociation of CO_2 to CO and a CO_3^{2-} species. The latter probably gives rise to one or both of the bands observed at 1638 and 1449 cm^{-1} in Figure 1C.

The main question to be resolved is the identity of the species giving rise to the very intense band at 2261-2267 cm^{-1} and its medium intensity partner at 2130-2148 cm^{-1}. Because of the prominence of these bands and their temperature dependence, it was felt that a correct assignment would lead to mechanistic insights into the CO + NO reaction over a Pt/Al_2O_3 catalyst.

Disregarding for the moment the important point that the species contains both carbon and nitrogen, there are several possibilities for species absorbing in this region. For example, Millen and Watson[16] report a frequency of 2238 cm^{-1} for the nitrosonium ion in $NO^+AlCl_4^-$. However, it would be difficult to reconcile the dependence of the observed bands at 2261 and 2130 cm^{-1} upon having excess CO in the reaction mixture with their assignment to an NO^+ species. Further, the NO and NO_2 reference spectra in Figure 1 gave no hint of bands above 1700 cm^{-1}.

One might consider the possibility that the bands are due to adsorbed CO, but this is quite unlikely as 2261 cm^{-1} is higher than known carbonyl absorptions and the appearance of a carbonyl only at high temperatures in the presence of NO would be difficult to rationalize. The 2130-cm^{-1} band is certainly in the carbonyl region since the band for gaseous CO is centered at 2143 cm^{-1} but again the dependence of the species on the presence of NO would be hard to understand.

In general, 2200-2500 cm^{-1} is sparsely populated in terms of the number of groups absorbing infrared radiation in this region. A brief check of standard structure correlation tables shows that alkynes, nitriles, isocyanides, and isocyanates generally have infrared absorptions in this frequency range. Taking into account the labeling experiments which show that the species contains both carbon and nitrogen atoms, we believe the most plausible of these possibilities is the -NCO or isocyanate structure. The infrared spectrum and structure of the HNCO molecule is known[17] and the strongest band is assigned to the asymmetric stretch at 2274 cm^{-1} for the vapor phase and 2246 cm^{-1} in the solid. Davison[18] has measured this band in eight organic isocyanates and found that all give an extremely intense characteristic absorption at 2269 ± 6 cm^{-1}. Also, Beck and Smedal[19] find that $\nu a(NCO)$ = 2236 cm^{-1} in the infrared spectrum of the anion $[W(CO)_5NCO]^-$ in acetone and Beck and Fehlhammer[20] report $\nu a(NCO)$ = 2234 cm^{-1} in $[(C_6H_5)_3P]_2PT(NCO)_2$. From the above, a frequency of 2261 cm^{-1} is reasonable for an isocyanate species attached to the surface of a Pt/Al_2O_3 catalyst.

The other possibility, nitriles, are known to have C≡N stretching frequencies which would coincide more closely with the medium intensity band at 2130 cm^{-1}. For example, HCN, ClCN, BrCN, and ICN have C≡N stretching frequencies of 2089, 2201, 2187, and 2158 cm^{-1}, respectively.[21] The assignment of the 2130-cm^{-1} band to a nitrile would be compatible with a mechanism whereby a CO molecule might attack a surface M-NCO group to give CO_2 and an isonitrile intermediate which would rearrange to an M-CN species or, more probably, to the surface combination of carbon and nitrogen atoms. However, the isotope shift data shown in Table I argues against the M-CN species since $KAu(CN)_2$[22] and $Hg(CN)_2$[23] both show ^{15}N shifts of 31 cm^{-1} in the ν_3 absorption whereas Maki and Desius[24] report an ^{15}N shift of 17 cm^{-1} for the ν_3 absorption of a cyanate ion in a KI host lattice. However, in $KAu(CN)_2$ a ^{13}C shift of 47 cm^{-1} is observed.[22] In view of the above, the band at 2261 cm^{-1} is assigned to a covalently bonded isocyanate group and the 2130-cm^{-1} band is assigned to a cyanate ion although a —C≡N species cannot be completely ruled out for the latter.

The assignment of the 2261-cm^{-1} band to an isocyanate reaction intermediate has interesting mechanistic implications for the reaction of NO and CO over Pt on Al_2O_3 at elevated temperatures. For example, one might speculate on the following possible reaction pathway.

$$NO \xrightarrow[T \geq 300°]{Pt/Al_2O_3} N_{ads} + O_{ads} \quad (1)$$

$$N_{ads} + CO \longrightarrow -NCO_{ads}(2261\ cm^{-1}) \quad (2)$$

$$O_{ads} + CO \longrightarrow CO_2 \quad (3)$$

$$-NCO_{ads} + NO \longrightarrow N_2 + CO_2 \quad (4)$$

$$2NO + 2CO \longrightarrow N_2 + 2CO_2 \quad (5)$$

In addition to the above reactions, the following would also seem possible.

$$-NCO_{ads} + H_2O \longrightarrow -OH_{ads} + HNCO \quad (6)$$

$$HNCO + H_2O \longrightarrow \underset{\text{(carbamic acid)}}{H_2NCOOH} \longrightarrow NH_3 + CO_2 \quad (7)$$

Or, as surface reactions

$$-NCO_{ads} + H_2O \longrightarrow -NH_{2ads} + CO_2 \quad (8)$$

$$-NH_{2ads} + H_2O \longrightarrow -OH_{ads} + NH_3 \quad (9)$$

The net result of reactions 6–9 would be to provide a pathway to NH_3 in a NO–CO–H_2O-containing mixture which would not go through the water–gas shift reaction usually proposed[5] for copper-containing catalyst systems. Weaver, *et al.*,[25] have shown that precious metal catalysts will also promote the water–gas shift reaction in auto exhaust gases; however, in experiments conducted in our laboratory, conditions of catalyst composition, feed composition, and temperature have been noted in which appreciable NH_3 formation occurs with reaction mixtures containing NO, CO, and H_2O, but little or no reaction of the carbon monoxide was observed with NO absent under otherwise identical conditions. Thus, there is no indication of water–gas shift reaction occurring at those conditions. Previously, our rationalization of this observation had been that the NO was somehow catalyzing the water–gas shift reaction to produce hydrogen molecules or atoms which reacted with the NO to form NH_3. It would now seem that reactions 6–9 offer a possible pathway to NH_3 which does not require intermediate formation of hydrogen.

Because the intensity of the –NCO band is decreased drastically by H_2O at room temperature whereas elevated temperatures are required with molecular H_2, one may conclude that the rate of reaction of surface isocyanate with H_2O is much faster than the reaction with H_2. Of course, in the NO + CO + H_2 system, once CO_2 is formed the water–gas shift reaction can produce H_2O over a good shift catalyst such as Ru/Al_2O_3. Thus, the observation that –NCO is relatively inactive toward H_2 does not rule out the possibility that –NCO may play a role in the NO + CO + H_2 system discussed by Shelef.[6]

Summary

A variety of experiments dealing with the infrared spectra of species adsorbed on a Pt/Al_2O_3 surface during the reduction of NO with CO at elevated temperatures have led to the assignment of the most intense band as an isocyanate species. The possible importance of such a surface species should not be overlooked since it could be involved in the formation of NH_3 in automotive catalytic converters containing noble metals. At this point, the importance of an isocyanate intermediate route to NH_3 cannot be assessed since the experimental conditions used in the present study are far removed from the real world of auto exhaust.

Acknowledgment. The author wishes to thank Drs. D. Forster, J. W. Gambell, and J. F. Roth for suggestions, discussion, and encouragement regarding this work.

References and Notes

(1) J. F. Roth and R. C. Doerr, *Ind. Eng. Chem.*, **53**, 293 (1961).
(2) L. S. Bernstein, K. K. Kearby, A. K. S. Romar, J. Vardi, and E. E. Wigg, "Application of Catalysts to Automotive NO_x Control," SAE Paper No. 710014, 1971.
(3) J. E. Hunter, Jr., "Effect of Catalytic Converters on Automotive Ammonia Emissions," presented to Central States Section of the Combustion Institute, Ann Arbor, Mich., Mar 1971.
(4) G. H. Meguerian and C. R. Lang, "NO_x Reduction Catalysts for Vehicle Emission Control," SAE Paper No. 710291 1971.
(5) R. L. Klimisch and G. J. Barns, "The Chemistry of Catalytic Nitrogen Oxide Reduction in Automotive Exhaust Gas," presented at the Spring Symposium of the Catalysis Clubs of Philadelphia and New York, Princeton, N. J., May 1971.
(6) M. Shelef and H. S. Gandhi, "Ammonia Formation in the Catalytic Reduction of Nitric Oxide. III. The Role of Water-Gas Shift, Reduction by Hydrocarbons, and Steam Reforming," presented at the 39th American Chemical Society Chemical Engineering Symposium in Chicago, Jan 18–19, 1973.
(7) M. L. Hair, "Infrared Spectroscopy in Surface Chemistry," Marcel Dekker, Inc., New York, N. Y., 1967.
(8) L. H. Litle, "Infrared Spectra of Adsorbed Species," Academic Press, New York, N. Y., 1966.
(9) J. B. Peri and R. B. Hannan, *J. Phys. Chem.*, **64**, 1526 (1960).
(10) J. Bugosh, R. L. Brown, J. R. McWhorter, G. W. Sears, and R. J. Sippel, *Ind. Eng. Chem., Prod. Res. Develop.*, **1**, 157 (1962).
(11) G. Hertzberg, "Molecular Spectra and Molecular Structure. II. Infrared and Raman Spectra of Polyatomic Molecules," Van Nostrand-Reinhold Co., New York, N. Y., 1945, pp 274, 278.
(12) R. P. Eischens, S. A. Francis, and W. A. Pliskin, *J. Phys. Chem.*, **60**, 194 (1956).
(13) G. Blyholder, *J. Phys. Chem.*, **68**, 2272 (1964).
(14) P. L. Prichard and G. W. Polly, *J. Amer. Chem. Soc.*, **76**, 5169 (1954).
(15) R. P. Eischens, W. A. Pliskin, and S. A. Francis, *J. Chem. Phys.*, **22**, 1786 (1954).
(16) D. J. Millen and D. Wattson, *J. Chem. Soc.*, 1369 (1957).
(17) G. Hertzberg and C. Reid, *Discuss. Faraday Soc.*, **9**, 92 (1950).
(18) W. H. T. Davison, *J. Chem. Soc.*, 3712 (1953).
(19) W. Beck and H. S. Smedal, *Angew. Chem. Int. Ed. Engl.*, **5**, 253 (1966).
(20) W. Beck and W. P. Fehlhammer, *Angew. Chem.*, **79**, 146 (1967).
(21) W. G. Penney and G. B. B. M. Sutherland, *Proc. Roy. Soc., Ser. A*, **156**, 654 (1936).
(22) L. H. Jones, *J. Chem. Phys.*, **27**, 468 (1957).
(23) L. H. Jones, *J. Chem. Phys.*, **27**, 665 (1957).
(24) A. Maki and J. C. Desius, *J. Chem. Phys.*, **31**, 772 (1959).
(25) J. H. Jones, E. E. Weaver, J. T. Kummer, K. Otto, and M. Shelef, "Selective Catalytic Reactions of Hydrogen with Nitric Oxide in the Presence of Oxygen," presented at the joint metting of AIChE and Instituto Mexicano de Inegenierson, Denver, Colo., Aug 30–Sept 2, 1970.

Butene Isomerization over Zinc Oxide and Chromia

C. C. Chang, W. C. Conner, and R. J. Kokes*

Department of Chemistry, The John Hopkins University, Baltimore, Maryland 21218 *(Received March 30, 1973)*

Publication costs assisted by the Petroleum Research Fund and the National Science Foundation

Rate studies of butene isomerization over zinc oxide indicate that self-poisoning occurs during the course of the reaction but that initial rates on freshly activated catalysts yield reproducible data. The initial rate of 1-butene isomerization is zero order and the initial cis/trans selectivity is 13, whereas the equilibrium ratio is 0.26. High (relative to equilibrium) selectivity is also observed for *cis*-butene as the reactant but not for *trans*-butene. Over chromia, the kinetic cis/trans selectivity (2–3) shows only a relatively small deviation from the equilibrium ratio when degassed at 450°, but severe (750°) degassing increases the ratio to values as high as 50. Attempts to connect the selectivity change with dehydroxylation of active sites and increased stability for adsorbed π-allyls were unsuccessful. Ir studies on zinc oxide show that the surface reaction is rate controlling and probably occurs *via* adsorbed π-allyls. Unexpected stability patterns were found with the adsorbed precursors of *cis*-butene as the most stable species. Interpretation of these effects suggests that the π-complexes resemble those of d^{10} metals such as silver, whereas π-allyls resemble allyl anions in solution more than ligands of transition metals. A mechanism is proposed which involves *syn* and *anti* π-allyls as intermediates and their interconversion *via* a dynamic σ–π equilibrium. The mechanism, coupled with kinetic and ir data, yields a rather detailed, if speculative, picture of the free energy surface that defines the course of the reaction.

Introduction

Double-bond isomerization of olefins (at or below room temperature) over metals[1] and metal complexes[2] probably occurs *via* the formation of an alkyl by addition of a hydrogen atom followed by alkyl reversal with removal of a different hydrogen atom to yield isomerized olefin. Over metal oxide hydrogenation catalysts,[3-5] however, this alkyl reversal does not occur readily; hence, an alternative mechanism must be operative. Burwell and coworkers[3] have suggested that the isomerization over chromia may occur *via* removal of a hydrogen atom from the olefin to form an allylic species followed by readdition of the hydrogen atom to a different carbon atom to form isomerized olefin. For some time, the evidence for adsorbed allylic species was entirely mechanistic. Recent infrared studies with zinc oxide, however, suggest allylic species form readily. Studies with propylene,[6] the simplest olefin that can form an adsorbed allyl, reveal two kinds of adsorbed species, one weakly bound and one strongly bound. The weakly bound species results from nondissociative adsorption to form a surface π complex; this species is the reactive species in hydrogenation[7] and is characterized (in part) by a double-bond stretching frequency shifted down by about 30 cm^{-1}. A similar species has been observed for ethylene.[8] The strongly bound species results from dissociative adsorption to form a hydrogen bound to an oxide ion and an allylic species bound to a zinc ion, similar to the π-allyl ligand in transition metal complexes;[6] this allyl species is the intermediate in "isomerization" of labeled propylenes and is characterized (in part) by a double-bond frequency shifted down by about 100 cm^{-1}. Thus, for propylene, at least, the evidence is clear cut that a π-allyl is the intermediate in isomerization.

Results for butene isomerization would be expected to be more complex. Propylene forms only two surface species, the π complex and the π-allyl. Butenes would be expected to form *five* surface species: π-complexes of 1-butene, *cis*-butene and *trans*-butene, and *syn* and *anti* π-allyls. The π-allyls would have the following structures

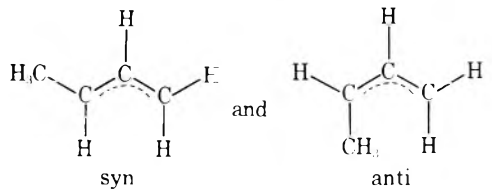

syn anti

wherein the carbon skeleton and the nonmethyl hydrogens are in the same plane. *trans*-Butene can form only the syn isomer; *cis*-butene can form only the anti isomer; but 1-butene could form either isomer. A brief study of butene isomerization over zinc oxide[9] provided some evidence for these species, but characterization of the species and the surface sequences was incomplete. It is the purpose of this paper to supply a more detailed picture of these surface sequences by a combination of ir and kinetic studies on zinc oxide. We also include, for comparison, a few observations on butene isomerization over chromia catalysts.

Experimental Section

Zinc oxide used in these studies was Kadox-25 supplied by the New Jersey Zinc Co. Chromia was prepared following the procedure of Burwell, *et al.*,[10] *i.e.*, urea–chromic nitrate precipitation followed by activation in flowing nitrogen at 450°. Tank hydrogen and deuterium were purified by passage through degassed charcoal, and the butenes (CP) were purified by chromatography prior to use.

Kinetic butene isomerization runs were made in a 228-cm^3 circulating system at room temperature. Samples were withdrawn periodically for chromatographic analysis over a 12-ft dimethylsulfolane column immersed in an ice bath. For the kinetic runs the zinc oxide (0.5 g) was activated by the following sequence: evacuation while heating to 480°, 1-hr treatment in circulating hydrogen, 1-hr evac-

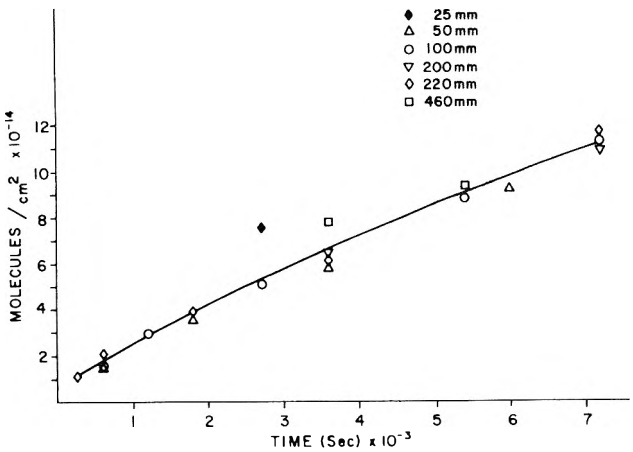

Figure 1. Conversion *vs.* time for butene-1 at various pressures.

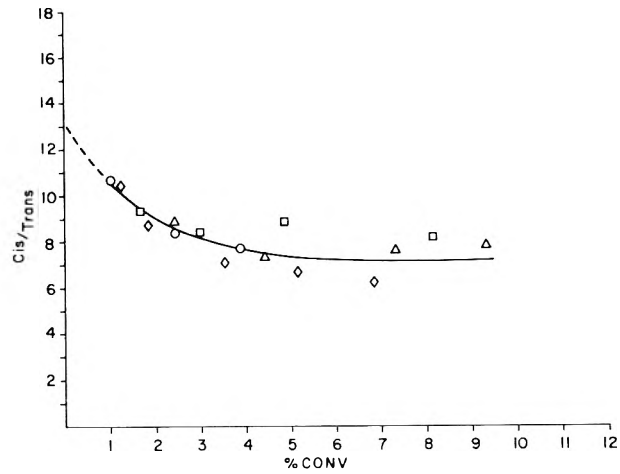

Figure 2. Selectivity *vs.* conversion for butene-1. Different symbols are for check runs.

uation, and 1-hr treatment in circulating oxygen. Circulating hydrogen and oxygen were continuously dried by a liquid nitrogen trap in the circulation loop. Following this, the catalyst was cooled to room temperature in circulating oxygen and briefly evacuated. Between runs the catalyst was degassed at 480° for 6 hr. This yielded a catalyst with an area of 8.3 m^2/g. Details of sample preparation and infrared observations (all at room temperature) are given elsewhere.[6] After activation of the chromia in nitrogen, the catalyst was evacuated and used for several isomerization runs. For runs over microcrystalline α-chromia, the catalyst was heated under vacuum for 2 hr at 750°.[11] The surface area decreased from 137 to 22 m^2/g as a result of the high-temperature treatment. Between runs the catalyst was degassed for 4 hr at 400°.

Results

Conversion of Butenes on Zinc Oxide. In their studies of butene isomerization, Hightower and Hall[12] found that the conversion could be represented by plots first order in the distance from equilibrium for reactants. The equation, although approximate, held up to relatively high conversions and served as a useful synopsis for examination of poisoning and related effects. In our studies with zinc oxide we found that this equation did not fit the data over a wide range. Furthermore, in runs where the reaction was carried to equilibrium, the rate became exceedingly slow. These and other features of the conversion *vs.* time strongly suggested that poisoning occurred as exposure time to reactants increased. Purification of reactants by chromatographic fractionation and variations in pretreatment did not eliminate this poisoning; hence, it was concluded that the poisoning stemmed from the reactants themselves. Because of this self-poisoning (which we found to be unavoidable) we limited our study to initial reaction rates on freshly activated samples.

Figure 1 shows a plot of the initial conversion of 1-butene (in molecules/cm^2) *vs.* time for initial pressures ranging from 25 to 460 mm. The data are best represented by a single line slightly curved with an initial slope corresponding to 2×10^{11} molecules/cm^2 sec. Since this rate is independent of pressure, the reaction is zero order in the initial stages. Fragmentary results for isomerization rates of *cis* and *trans*-butenes suggest that the rates are zero order for these isomers, too.

Figure 2 shows the cis/trans ratio as a function of the per cent conversion of 1-butene at a pressure of 100 mm for several runs. The initial extrapolated ratio is about 13. Since at 25° the cis/trans ratio at equilibrium is 0.26,[13] the high initial ratio must be determined by kinetic factors. The initial selectivity, like the initial rates, was independent of pressure.

TABLE I: Selectivity for Butene Isomerization

Reactant	Selectivity	Experimental	Equilibrium	Prejudice[a]
1-Butene	*cis*/*trans*-butene	10.5	0.26	40.5
cis-Butene	1-Butene/trans	0.95	0.04	23.7
trans-Butene	1-Butene/cis	0.10	0.15	0.7

[a] Prejudice is the ratio of the experimental selectivity to that for the equilibrium mixture.[13]

As the catalyst aged with successive activations, there were gradual, progressive changes in both selectivity and activity. Table I lists the initial selectivities for an aged catalyst in a series in which the reactant was cycled among the three *n*-butenes several times. These initial selectivities were determined by extrapolations similar to that indicated in Figure 2 and are reproducible to about 10%. The selectivity for butene-1 conversion for the aged catalyst was slightly lower than that from Figure 1 for the fresh catalyst, whereas the selectivity values for *cis*-butene isomerization are in good agreement with those reported earlier.[8] In Table I we have also listed the equilibrium ratios of the isomers that define the various selectivities together with a defined term, *prejudice*, which provides a measure of the deviation of the kinetic selectivities from the equilibrium values. It is noteworthy that the prejudice is quite large for both *cis*- and 1-butene as reactants but rather small for *trans*-butene as the reactant. Rate data for isomers other than butene-1 were not determined with any great precision, but they did indicate that these rates, while slower, were within a factor of 2 of those for 1-butene.[14] Given the equilibrium ratios (1-butene 3%, *cis*-butene 20%, and *trans*-butene 77%) and the measured selectivities, it is clear that we cannot combine such forward and reverse rates to yield the equilibrium constant. This does not mean the kinetic data are invalid. These data apply to *initial* rates for which the kinetics are *zero* order; under these conditions, as we shall see in the discussion section, the relative initial rates give no information on equilibrium constants.

TABLE II: Double-Bond Stretching Frequencies for Butenes

Molecule	Gas phase, cm^{-1} Assigned[a]	π-complex cm^{-1} Predicted[b]	π-complex cm^{-1} Found	π-allyl cm^{-1} Predicted[b]	π-allyl cm^{-1} Found
trans-Butene	1676[a] (o)	1641 (w)	1640 (m)	1584[c] (w)	1582[c] (m)
cis-Butene	1660 (m)	1625 (m)	1625 (s)	1568[d] (m)	1572[d] (m)
1-Butene	1645 (s)	1610 (s)	1610 (s)	1584[c] (w) 1568[d] (m)	1572 (m)

[a] Raman active only. [b] See text. [c] *syn*. [d] *anti*

Earlier studies on zinc oxide suggested that the active sites consisted of a limited number of zinc–oxygen pair sites on the surface capable of heterolytic cleavage of sufficiently acidic carbon–hydrogen bonds.[4,15] In this picture the allylic species, which is bound to the zinc half of the active site, should have considerable carbanionic character. Thus, isomerization of butenes over zinc oxide would be expected to resemble base-catalyzed reactions (allyl carbanion mechanism) more than acid-catalyzed reactions (carbonium ion mechanism) or the metal catalyzed reactions (alkyl reversal mechanism). The cis/trans ratio from 1-butene provides a clue to polar character of the intermediate. For base-catalyzed reactions[16,17] the cis/trans ratio is usually 10 or greater; for acid-[12] or metal-catalyzed reactions[18] the ratio is usually of the order of unity. Thus, the high cis/trans ratio[10-13] over zinc oxide supports the view that active sites consist of zinc–oxide pair sites that behave as an acid–base pair.

In the acid–base picture of the active sites on zinc oxide[6,15] water adsorption (a poison for hydrogenation reactions) is pictured as

$$\mathrm{Zn{-}O + H_2O \longrightarrow \overset{OH}{\underset{|}{Zn}}\overset{H}{\underset{|}{-O}}}$$

Such a process could generate Brønsted acidity and, in this case, a different mechanism for 1-butene isomerization might prevail that would lead to lower cis/trans ratios. Accordingly, we made a cursory study of the effect of adsorbed water on butene isomerization. Water is a deadly poison at room temperature; in its presence, no isomerization of butene is observed. As water is removed by degassing at successively higher temperatures, the activity is completely restored but, even for the partially reactivated catalyst, the cis/trans ratio is much greater than unity; hence, our efforts to change the catalysis of isomerization from a basic to a (less efficient) acidic mechanism by adsorption of water on the active sites was unsuccessful.

Kinetic Studies on Chromia. It has been noted that zinc oxide and other metal oxide hydrogenation catalysts have many features in common.[4] There is, however, one rather striking difference. Over zinc oxide addition of deuterium to ethylene leads to 98–100% dideuterio addition, but addition of deuterium to propylene leads to only 55% dideuterio addition.[6] The difference in the behavior of the two olefins was ascribed to formation of a stable π-allyl by propylene followed by exchange of the dissociated species. Over chromia, with the usual activation (450°), however, both ethylene *and* propylene add deuterium to with 98–100% dideuterio addition.[3] Recent studies by Cross and Leach[11] reveal that chromia activated at 450° gave rather low initial cis/trans ratios (about 2) in 1-butene isomerization. Accordingly, it would appear that if the π-allyl formed on chromia, it had rather different reactivity characteristics.

In our studies we also found cis/trans ratios of 2 for 1-butene isomerization over chromia activated at 450°. In further agreement with Cross and Leach[11] the higher temperature (750°) activation led to a substantial increase in rate and cis/trans selectivity. In a sequence of runs over a chromia sample activated at the higher temperature, we found the initial cis/trans ratio progressively changed with aging from 8 to values of the order of 50. On the basis of the criteria described earlier, this suggests a change in mechanism to one dominated by an allylic species with considerable carbanion character. Accordingly, we supposed that addition of deuterium to propylene over the high-temperature form of chromia would lead to more extensive scrambling in the product propanes as we found for zinc oxide. Experiments designed to test this conjecture were carried out, but scrambling in the propane product was no more evident in the chromia showing high cis/trans selectivity than in chromia showing low cis/trans selectivity. Thus, although the high-temperature chromia is more similar to zinc oxide than the low-temperature form, qualitative (as well as quantitative) differences in these catalysts are still evident.

Infrared Studies of Butenes on Zinc Oxide. The most characteristic region of the ir for the predicted π and π-allyl species (five for butenes) is the double-bond region. Earlier ir studies with ethylene and propylene[4] plus the known fundamental frequencies for gaseous butenes[19] permit us to make reasonable predictions on the location of these bands for adsorbed butenes. In π-bonded species the double-bond frequency is shifted down from that for the gaseous species by an amount related to the heat of binding.[4] Thus, we find a smaller shift (23 cm^{-1}) for the less strongly adsorbed, π-bonded ethylene than that (30 cm^{-1}) for the more strongly adsorbed, π-bonded propylenes. For butenes, π-bonded species are even more tightly held; hence, we assume the shift in double-bond frequency will be about 35 cm^{-1}. Table II lists the assigned positions for gaseous double-bond frequencies and the predicted frequencies for the corresponding adsorbed π-complexes. Alongside each frequency in parentheses, we list relative intensities. Intensity predictions for adsorbed species are based on the assumption (roughly true for ethylene and propylene) that the relative intensities for π complexes parallel those for gaseous species. If the π-allyls have carbanion character, one would expect the stability of that formed from propylene, with the negative charge on the two primary carbon atoms, to be more strongly held than those from butenes, with the negative charge on primary and secondary carbons. Experimental observations support this view: strongly held butenes are slightly more readily removed by evacuation than propylenes. If we assume that the double bond shift is related to the heat of binding, the shift for π-allyls of propylene (107 cm^{-1}) should be greater than that for π-allyls of butene. For the

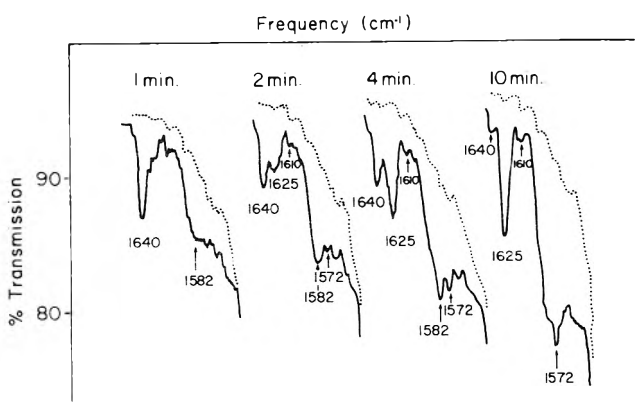

Figure 3. Spectrum of zinc oxide after admission of a dose of *trans*-butene.

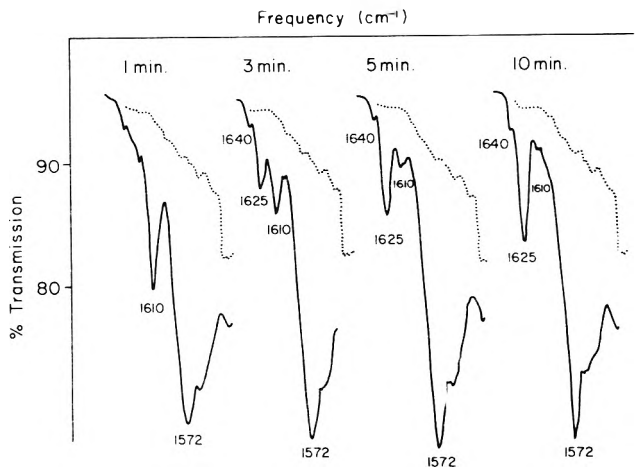

Figure 4. Spectrum of zinc oxide after admission of a dose of butene-1.

sake of specificity we shall assume that this shift for butenes is 92 cm^{-1}, *i.e.*, about 15% less than that for propylene. These predicted values are also listed in Table II. The "predicted" relative intensities for these π-allyls are, once again, based on the relative gas-phase intensities for the butenes most closely related to these allyls, *i.e.*, *cis* for *anti* and *trans* for *syn*. Such intensity "predictions" for π-allyls are clearly less believable than for the π complexes since π-allyl formation involves dissociation. The predicted positions of these five frequencies are sufficiently different so that they should be readily distinguishable; hence, if the picture is correct, we can expect to see bands for all five adsorbed species from these butenes.

Repeated sequential scans were made of the 1550–1700-cm^{-1} region of the spectrum following admission of a dose (0.25 cm^3) of *cis*-butene to a zinc oxide sample. Under these conditions all of the butene is adsorbed; the π-allyl sites should be saturated and the remaining butene should be in π-complex form. The observed spectrum then contains no contributions from gaseous butenes. Immediately after *cis*-butene is admitted to the zinc oxide, a band appears in the OH region; in the double-bond region, a sharp band is seen at 1625 cm^{-1} and this is accompanied by a broad band centered at 1572 cm^{-1}. The band at 1625 cm^{-1} decays slightly with time and weak bands appear at 1610 and 1640 cm^{-1}. The three bands at 1640, 1625, and 1610 cm^{-1} correspond to the π-bonded *trans*-, *cis*-, and 1-butene, and the sequence of change corresponds to isomerization of the π complexes. The equilibrium concentrations of butenes in the gas phase are in the order: *trans*-butene (77%), *cis*-butene (20%), and 1-butene (3%). The relative intensities of the surface bands after no further change occurs is 1625 $\gg$ 1640 $\approx$ 1610 cm^{-1}. Thus, the equilibrium intensities do not follow the sequence for gas-phase equilibrium, and we must conclude that the extinction coefficients differ as suggested in Table II and/or the surface complex equilibrium is drastically different from that for the gas phase. The band that appears initially at 1572 cm^{-1} is assigned to the *anti*-π-allyl, which is the only π-allyl that can be formed from *cis*-butene. The position agrees well with the "predicted" value (1568 cm^{-1}). As equilibrium is approached, one might expect a band corresponding to the *syn* π-allyl at about 1584 cm^{-1} to form and increase in intensity and this increase should be accompanied by a decrease in intensity of the *anti* π-allyl band. In our observations, however, we see *no* decrease in the 1572-cm^{-1} band intensity and *no* band formation assignable to a *syn* π-allyl.

Figure 3 shows repeated scans when *trans*-butene (0.25 cm^3) is admitted to zinc oxide. In the first scan a sharp band at 1640 cm^{-1}, corresponding to π-bonded *trans*-butene, is evident and a broad band at about 1570 to 1580 cm^{-1} has started to form. In the second scan the sharp band at 1640 cm^{-1} has decreased and a band is evident at 1625 cm^{-1} (corresponding to formation of π-bonded *cis*-butene) along with a weak band at 1610 cm^{-1} (corresponding to π-bonded 1-butene); hence, isomerization of the surface complex is evident. Once again, as equilibrium is approached, the intensities of the π-bonded species are 1625 $\gg$ 1640 $\approx$ 1610 cm^{-1} as found with *cis*-butene. By the time the second scan is made, the broad band shows a definite peak at 1582 cm^{-1}. This band is assigned to the *syn* π-allyl which is the only π-allyl that can be formed directly from *trans*-butene. As equilibrium is approached, this peak decreases and a new peak develops at 1572 cm^{-1}, the *anti* π-allyl band. Finally, at equilibrium we see no evidence for the *syn* π-allyl band; only the *anti* π-allyl band is evident.

Figure 4 shows repeated scans when a dose of 1-butene is admitted. The sequence for π-complexed butenes agrees with expectations, but the π-allyl region reveals some unexpected features. Initially, 1-butene would be expected to form both *syn* and *anti* π-allyls; furthermore, there is no obvious kinetic or steric reason why one of these π-allyls should be formed preferentially. Nevertheless, the spectrum clearly shows that, whereas a strong band assignable to the *anti* π-allyl (1572 cm^{-1}) is evident throughout, there is no evidence of a band assignable to the *syn* π-allyl. Accordingly, given the relative intensity of the π-allyl bands suggested by the *trans*-butene data, we are forced to the conclusion that 1-butene exhibits a strong preference for the formation of the *anti* π-allyl rather than the *syn* π-allyl.

Figure 5 shows the results of a detailed observation of the band intensities in the deformation region when 0.25 cm^3 of 1-butene is added to zinc oxide. Clearly, we are following the *surface* isomerization rate. We cannot equate relative intensities for different species to relative amounts because the extinction coefficients differ, but for any one species, intensities are proportional to amounts. It is particularly noteworthy that, throughout the course of the surface reaction, the π-allyl intensity remains essentially constant, whereas the intensity of the π complexes change dramatically. We can obtain an estimate of

the rate of the surface isomerization process from these intensities.[20] It is clear that the dose of 0.25 cm^3 of 1-butene would be completely converted in about 400 sec if the initial rate persisted. From the amount of catalyst and its area, we can compute the rate per unit area. Thus, the ir data suggest that the *surface* process, which appears to be zero order in π-complex, proceeds with a rate of 2×10^{11} (molecules/cm^2)/sec. The *catalytic* rate and order quoted earlier was the same within experimental error.

If doses of butene are added at low enough temperatures, only the spectrum of the π complex is observed. When the sample is allowed to warm up, an OH band appears along with the appropriate π-allyl band at 1572 or 1582 cm^{-1}. *Isomerization occurs only after the π-allyl band forms;* this, together with the kinetic data in Figure 5, suggests the π-allyl is an intermediate in the surface isomerization sequence.

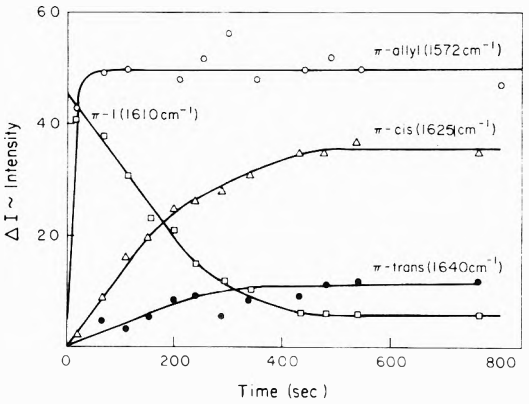

Figure 5. Intensities of surface species formed from butene-1 *vs.* time.

Discussion

Before we attempt to formulate a detailed kinetic scheme for butene isomerization, it is useful to itemize those more primitive conclusions that are independent of the analysis.

(1) Adsorption-Desorption Is Fast Compared to the Surface Reactions, Which Are Rate Controlling. The simplest sequence that describes isomerization involves adsorption of reactants, surface reaction, and desorption of products, *viz.*

$$A + * \rightleftarrows A \cdot * \rightleftarrows B \cdot * \rightleftarrows B + *$$

where A and B are gaseous reactants and products and * represents the site. If adsorption or desorption were the rate-determining step, we would expect the rate of the surface process ($A\cdot * \rightleftarrows B\cdot *$) to be faster than the catalytic process. Actually, the rate of the surface process (as gauged by the ir data in Figure 5) is the same as that of the overall, zero-order, catalytic process; hence, the surface process is rate controlling and adsorption-desorption is a relatively fast step.

(2) The Surface π-Allyl Behaves as an Intermediate. In the surface process for 1-butene isomerization (Figure 5) the π-allyl is formed immediately and remains constant during the course of the reaction. This, plus the low-temperature data, suggests that the active sites are saturated with π-allyls and these are intermediates. The observed zero-order kinetics for the overall catalysis and the surface reaction would be expected for such a picture. Observations for *cis* and *trans*-butene isomerization at and below room temperature also support this view.

(3) The Relative Stability of π-Complexed Butenes at Equilibrium Is Different from That for the Gaseous Species. When a small dose of one of the *n*-butenes is admitted to zinc oxide, the initial scan shows predominantly the band characteristic of that π-complexed butene. The size of the dose and this initial band intensity provide a rough measurement of the extinction coefficient for each π-complexed species.[21] From these extinction coefficients and the band intensities, we can estimate the relative amounts of π-complexed butenes at any time.[20] When surface equilibrium is achieved, the relative amounts are trans:cis:1-butene = 30:100:10. This is different from the gas phase equilibrium, trans:cis:1-butene = 100:26:4.

(4) The anti π-allyl Is More Stable Thermodynamically Than the syn π-Allyl. The *anti* and the *syn* π-allyl form first from *cis*-butene and *trans*-butene, respectively. Since the initial intensity of the *syn* π-allyl band from a dose of *trans*-butene is not much different from the initial intensity of the *anti* π-allyl band from a dose of *cis*-butene, the extinction coefficients must be comparable; hence, uncorrected band intensities provide a rough gauge of the relative amounts of these two complexes. As surface equilibrium is approached starting with any of the *n*-butenes, the *anti* π-allyl band becomes or remains strong, whereas the *syn* π-allyl band becomes or remains undetectable; hence, we conclude that the *anti* π-allyl is much more stable thermodynamically than the *syn* π-allyl. Estimates suggest the anti form is favored by a factor of *at least* 5; in later analysis we shall assume (for specificity) that the factor *is* 5.

(5) Butene-1 Forms the anti π-Allyl Preferentially. Abstraction of an allylic hydrogen from 1-butene can lead to either the *syn* or *anti* π-allyl, and there is no obvious reason why one of these should be favored. Nevertheless, only the *anti* π-allyl band is observed when a dose of 1-butene is added to the catalyst; hence, the ir data reveal that 1-butene forms primarily (the more stable) *anti* π-allyl.

(6) Direct Interconversion of syn and anti π-Allyls Occurs. Given the fast adsorption-desorption step, the reaction sequence is determined by the surface processes. If only π complexes and π-allyls were involved, the surface sequence for cis–trans isomerization would be

$$\pi\text{-}cis \rightleftarrows anti \rightleftarrows \pi\text{-butene-1} \rightleftarrows syn \rightleftarrows \pi\text{-}trans$$

Thus, butene-1 would be the sole initial product in the isomerization of *cis*- (or *trans*-) butene. It is found, however, that *cis*-butene forms *both* 1-butene and *trans*-butene initially and *trans*-butene forms *both* 1-butene and *cis*-butene initially; hence, the above sequence is, at best, incomplete. We can, however, retain the attractive features of this sequence if we postulate that there is an additional step, not yet specified, for direct anti–syn interconversion, *viz.*

$$\begin{array}{ccccccc} & & & & \pi\text{-butene-1} & & \\ & & & & \swarrow\!\!\uparrow \quad \downarrow\!\!\searrow & & \\ \pi\text{-}cis & \rightleftarrows & anti & \rightleftarrows & syn & \rightleftarrows & \pi\text{-}trans \end{array}$$

Then butene-1 need not be the initial product in cis–trans isomerization even when adsorption-desorption of π complexes is the fast step.

(7) Interconversion of syn and anti π-Allyls Is a Relatively Slow Process. The data in Figure 3 show that *trans*-butene forms initially the *syn* π-allyl and that, in the

course of the isomerization, syn to anti conversion takes place slowly. Since *cis*-butene is quite evident before the *anti* π-allyl band is developed, it seems clear that the rate constant for interconversion is small relative to that for conversion of *anti* π-allyl to the *cis* π-complex. Similarly, since *trans*-butene is formed from *cis*-butene under conditions such that the *syn* π-allyl is not observed, the rate constant for anti to syn conversion must be small relative to that for conversion of the *syn* π-allyl to the *trans* π-complex. Since the syn to anti conversion, which is actually shown to be slow, is in the direction favored by stability, the reverse process, anti to syn, will be even slower.

The principal features of butene isomerization can be accommodated by the following kinetic sequence.

$$\pi\text{-}cis\ C_4H_8 + * \rightleftarrows X_1(anti\ \pi\text{-allyl}) \quad (1)$$

$$\pi\text{-}trans\ C_4H_8 + * \rightleftarrows X_2(syn\ \pi\text{-allyl}) \quad (2)$$

$$\pi\text{-}C_4H_8\text{-}1 + * \rightleftarrows X_1 \quad (3)$$

$$\pi\text{-}C_4H_8\text{-}1 + * \rightleftarrows X_2 \quad (4)$$

$$X_1 \rightleftarrows X_2 \quad (5)$$

This scheme is an oversimplification insofar as X_1 and X_2 represent the π-allyl *and* the detached hydrogen and step 5, the interconversion, may involve a multistep process. Despite these oversimplifications, we shall use these equations as the basis for our analysis simply because they are tractable and do represent the principal features of the supposed mechanism. There are ten rate constants associated with the above system of equations: k_1 and k_{-1} for the first forward and reverse step, etc. Not all of these are independent. For example, application of the principle of microscopic reversibility results in the relationship

$$k_3k_5k_{-4} = k_{-3}k_{-5}k_4 \quad (6)$$

Other such restrictions which relate equilibrium concentrations of π complexes or π-allyls can also be derived. The overall catalysis includes steps for the adsorption and desorption of π complexes. If these steps are sufficiently fast, however, the initial formation of gaseous products is equal to the rate of formation of π complex. Since this is the case for 1-butene isomerization and greatly simplifies the analysis, we shall assume that it holds true for all initial rates.

Application of the steady-state approximation to X_1 and X_2 results in relatively complex equations, but, if we restrict ourselves to initial rates, some simplification occurs. For example, the initial rate of formation of *cis*- and *trans*-butene from butene-1 is given by $k_{-1}X_1$ and $k_{-2}X_2$ where X_1 and X_2 are the steady state concentrations in the limit where the concentrations of *cis*- and *trans*-butene are both zero. The forms of these steady-state concentrations are

$$X_1 = \frac{A(b)}{C + (A + B)(b)}, \quad X_2 = \frac{B(b)}{C + (A + B)(b)} \quad (7)$$

where A, B, and C are combinations of rate constants and (b) is the concentration of π-complexed 1-butene. Equations of parallel form are derivable for the initial stages when *cis* or *trans*-butene are reactants; of course, different combinations of rate constants are used and the concentration of the *cis* or *trans*-butene π-complexes, respectively, replaces that for 1-butene. With such equations there are two limiting forms for the rate expression: zero order or first order in reactant. As might be expected, when it is zero order the surface coverage with X_1 plus X_2 adds up to 1 and the sites are saturated. If one equates the rate expressions for 1-butene to *cis*-butene and vice versa *at equilibrium*, one, of course, defines the equilibrium concentrations of *cis*- and 1-butene. If one equates the *initial* rate of conversion of 1-butene to *cis*-butene and vice versa, one defines the equilibrium concentrations *if and only if the reaction is in the first order limit*.[22] Thus, the fact that our relative initial rate data for the various isomers bear little relation to their thermodynamic equilibrium is expected for the observed zero-order role dependence.

Equations for the initial selectivity are

$$\frac{\text{cis}}{\text{trans}} = \frac{k_{-1}}{k_{-2}}\left[\frac{k_3(k_{-2} + k_{-4}) + k_{-5}(k_3 + k_4)}{k_4(k_{-1} + k_{-3}) + k_5(k_3 + k_4)}\right] \quad (8)$$

$$\frac{\text{trans}}{\text{1-butene}} = \frac{k_{-2}k_5}{k_{-3}(k_{-2} + k_{-4}) + k_{-3}k_{-5} + k_{-4}k_5} \quad (9)$$

$$\frac{\text{1-butene}}{\text{cis-butene}} = \frac{k_{-4}(k_{-1} + k_{-3}) + k_5k_{-4} + k_{-5}k_{-3}}{k_{-1}k_{-5}} \quad (10)$$

These equations hold regardless of the overall order of the reaction; hence, we expect the initial selectivity to be independent of the initial pressure, as found. The product of these three ratios with rearrangements becomes

$$\frac{k_5k_3k_{-4}}{k_{-5}k_4k_{-3}} \times \frac{\left\{k_{-2} + k_{-4} + k_{-5} + \frac{k_4k_{-5}}{k_3}\right\}\left\{k_{-1} + k_{-3} + k_5 + \frac{k_{-5}k_{-3}}{k_{-4}}\right\}}{\left\{k_{-1} + k_{-3} + k_5 + \frac{k_5k_3}{k_4}\right\}\left\{k_{-2} + k_{-4} + k_{-5} + \frac{k_{-4}k_5}{k_{-3}}\right\}} \quad (11)$$

If we use the interrelationship specified by eq 6, we find this product reduces to

$$\left\{\frac{\text{cis}}{\text{trans}}\right\}\left\{\frac{\text{trans}}{\text{1-butene}}\right\}\left\{\frac{\text{1-butene}}{\text{cis}}\right\} = 1 \quad (12)$$

It should be emphasized that this relation is independent of the order of the initial rate; since it holds even under conditions when the initial rates do not define the equilibrium (*e.g.*, in the zero-order limit), this product rule is a quite general relation.[23] When we construct this product from the data in Table I, we obtain 1.1; hence, the relation applies to our data within the assumed experimental error.

Further analysis requires that we make some estimates of the relative values of the rate constants. The ir data suggests the following are appropriate: (a) the rate constants k_4 and k_{-4}, which provide for the interconversion of 1-butene and the *syn* π-allyl are negligible compared with all other rate constants; (b) the rate constant k_{-5}, which determines the rate of direct conversion of *syn* to *anti* π-allyl, is small compared to k_{-2}, which determines the rate of conversion from *syn* π-allyl to the *trans* π complex. Application of these approximations (sequentially) to eq 8-10 yields

$$\frac{\text{cis}}{\text{trans}} \approx \frac{k_{-1}}{k_{-2}}\frac{k_3(k_{-2} + k_{-5})}{k_5k_3} \approx \frac{k_{-1}}{k_5} \quad (13)$$

$$\frac{\text{trans}}{\text{1-butene}} \approx \frac{k_{-2}k_5}{k_{-5}(k_{-2} + k_{-5})} \approx \frac{k_5}{k_{-5}} \quad (14)$$

$$\frac{\text{1-butene}}{\text{cis-butene}} \approx \frac{k_{-5}k_{-3}}{k_{-1}k_{-5}} = \frac{k_{-3}}{k_{-1}} \quad (15)$$

The relative values of the rate constants that are defined by selectivities determine the relative free energies of the corresponding transition states, and the relative equilibrium concentrations estimated by ir determine the relative free energies for surface species. Such levels for surface, gas-phase, and transition states are indicated in Figure 6 and the positions of these levels would be the same for any consistent standard states for gaseous and adsorbed states, respectively. Dotted lines between gaseous and adsorbed species represent large unspecified shifts in origin; for traditional, ideal standard states the shift for adsorbed species would be negative by about 10 kcal. Relative levels for π and π-allyl species were not established quantitatively by our data; accordingly, a break in the solid lines is used to denote quantitative uncertainty, but the relative magnitudes are believed to be qualitatively correct. Numbers above maxima indicate the relevant kinetic steps.

The free energy diagram provides a concise summary of the isomerization process. For 1-butene isomerization the *anti* π-allyl is formed rapidly and preferentially *via* the lower free energy barrier 3 until the sites for π-allyls are saturated. The *anti* π-allyl forms *cis*-butene *via* 1 much more readily than it can convert directly to the relatively unstable *syn* π-allyl (*via* 5) and further react (*via* 2) to form *trans*-butene; hence, the high prejudice for cis relative to trans (41) stems from the difficulty of direct anti to syn conversion. In the conversion of *trans*-butene to its isomers, syn formation is relatively rapid and conversion to the anti form is the hard step. Once the anti is formed, it readily forms cis (*via* 1); formation of 1-butene (*via* 3) is more difficult. It is interesting to note, however, that the partitioning of anti into cis and 1-butene occurs with little prejudice (0.7), which suggests the transition states (1 and 3) reflect the relative stabilities of the product isomers. Finally, in isomerization of *cis*-butene we again rapidly cover the surface sites with the *anti* π-allyl. Conversion to 1-butene (*via* 3) is straightforward, but conversion to *trans*-butene requires (*via* 5) the difficult, direct π-allyl conversion; hence, once again, the prejudice is high (24) because the direct interconversion step does not reflect the relative stability of the product isomer.

The evidence is strong that direct syn–anti conversion occurs, but neither experiments nor analysis indicates the mechanism by which this is achieved. The behavior of π-allyl ligands in complexes, which we believe bear some similarities to the surface complex, does suggest a mechanism by which such interconversion can be achieved. It is often found[24] that these π-allyl complexes are dynamic; that is, the allyl ligand undergoes syn–anti interconversion without detachment of the ligand from the metal. The most reasonable pathway for interconversion involves formation of a σ-allyl from the π-allyl.[4] Usually (but not always[25]) the concentration of σ-allyl is so small that ir measurements do not reveal its presence, and its existence is deduced from the details of the averaged nmr spectrum. If the same character holds for the adsorbed π-allyls, a suitable pathway for the required syn–anti interconversion is provided, but the σ-allyl on the surface would be at

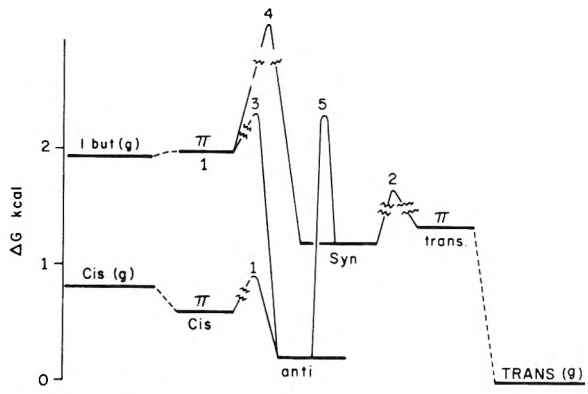

Figure 6. Free energy profile (see text).

such a low concentration that it would be difficult to observe by ir studies.

The reversal of the stability for the π complexes of *cis* and *trans*-butene compared to that of the gaseous isomers is, at first glance, surprising. Nevertheless, this is the behavior one finds for π complexes of d^{10} metals, such as silver. Quinn and Glew[26] have determined the thermodynamic functions for the formation of a variety of olefin (ol) complexes of the type $AgBF_4(ol)_2$. The equilibrium constant for the formation of the *cis*-butene complex is about 25 times that for the formation of the *trans*-butene complex. Infrared studies show that the shift in double-bond frequency relative to that for the gaseous isomers is comparable for the two complexes (just as we find for adsorbed butenes). Since the correlation of ΔH to $\Delta\nu$ continues to hold, the ΔH values are also comparable; hence, the stability difference stems mainly from differences in entropies of complex formation. The dominant role of the entropy suggests that the stability difference stems from configurational factors. Hartley[27] has also invoked steric factors to explain the relative stability of similar complexes of transition metals. He takes the view that, in *cis*-olefin complexes, the plane of the double bond may tilt slightly to reduce steric interference between the bulky groups of the olefin and the other ligands attached to the metal. Such a tilt for *trans*-olefin complexes relieves no strain, and the resulting constraint can lead to a lesser stability for the complex of the *trans*-olefin. We believe such steric factors are likely to play a major role in adsorbed species, and they lead naturally to the enhanced relative stability of the adsorbed *cis* π-complex.

The stability pattern for π-allyls on zinc oxide is *not* similar to that usually found for ligands of metal complexes; in fact, for cobalt complexes[28] the reverse stability order, syn greater than anti, prevails. Thus, the bonding of the surface complex may be significantly different from that in complexes. We have already noted that the adsorbed species appear to have a large amount of anionic character; hence, in the limit, we might expect these π-allyls to approach the behavior of allylic anions in solution, which probably exist as ion pairs. In solution, the *cis* anion is known to be much more stable than the *trans* anion. Thus, the greater stability of the adsorbed *anti* π-allyl supports the view that it resembles a surface-stabilized *cis* anion. Explanations for the relative stability of the anions have been suggested,[29] but we feel these explanations are *ad hoc* and may not prevail. Accordingly, the main point we wish to make is that the stability pattern for adsorbed π-allyls resembles that of the allyl anions in

solution; regardless of the reason for the stability pattern,[30] this similarity suggests adsorbed π-allyls have considerably more carbanion character than one usually finds for ligands attached to transition metals.

Finally, we should note that our simple attempts to elucidate the effect of degassing on the nature of the sites of oxides failed completely. These experiments were carried out with the prejudice that dehydroxylation of the active sites (water removal) stabilized the π-allyl on chromia and zinc oxide. (A similar interpretation could be applied to the effect of degassing on aluminas.[31]) Concomitant studies of butene isomerization and deuteration of propylene on chromia as a function of severity of degassing failed to support this view. Furthermore, poisoning of zinc oxide sites by water failed to reduce the high cis/trans ratio. Thus, the high cis/trans ratio does not stem simply from complete dehydroxylation of active sites nor does it appear to stem from stabilization of π-allyls by some unspecified mechanism. In short, there was no good explanation for these effects and our studies did not improve the situation.

Acknowledgment. Acknowledgment is made to donors of the Petroleum Research Fund, administered by the American Chemical Society, for partial support of this research. This research was also aided by funds from the National Science Foundation under Grant 34034X.

References and Notes

(1) G. C. Bond, "Catalysis by Metals," Academic Press, New York, N. Y., 1962.
(2) R. Cramer, *Accounts Chem. Res.*, **1**, 186 (1968).
(3) R. L. Burwell, Jr., A. B. Littlewood, M. Cardew, G. Pass and C. T. H. Stoddart, *J. Amer. Chem. Soc.*, **82**, 6272 (1960); for a recent extensive review, see R. L. Burwell, Jr., G. L. Haller, K. C. Taylor and J. F. Read, *Advan. Catal.*, **20**, 1 (1969).
(4) R. J. Kokes and A. L. Dent, *Advan. Catal.*, **22**, 1 (1972).
(5) K. Tanaka, H. Nihira, and A. Ozaki, *J. Phys. Chem.*, **74**, 4510 (1970).
(6) A. L. Dent and R. J. Kokes, *J. Amer. Chem. Soc.*, **92**, 1092, 6709, 6718 (1970).
(7) S. Naito, T. Kondo, M. Ichikawa, and K. Tamaru, *J. Phys. Chem.*, **76**, 2184 (1972).
(8) A. L. Dent and R. J. Kokes, *J. Phys. Chem.*, **74**, 3653 (1970).
(9) A. L. Dent and R. J. Kokes, *J. Phys. Chem.*, **75**, 487 (1971).
(10) R. L. Burwell, Jr., and H. S. Taylor, *J. Amer. Chem. Soc.*, **58**, 697 (1936).
(11) N. E. Cross and H. F. Leach, *J. Catal.*, **21**, 239 (1971).
(12) J. W. Hightower and W. K. Hall, *Chem. Eng. Progr.*, **73**, 122 (1967).
(13) D. M. Golden, K. W. Eggers, and S. W. Benson, *J. Amer. Chem. Soc.*, **86**, 5416 (1964).
(14) The rate of *cis*-butene isomerization in this study was greater by a factor of 2 or 3 than that (4×10^{10} (mol/sec)/cm^2) reported in earlier studies.[9] Larger samples (10 g *vs.* 0.5 g) were used in this earlier study and conversions were higher; hence, we can ascribe the rate differences to more effective activation or more accurate initial rates in the present study. In truth, however, we have no evidence that explains this discrepancy.
(15) R. J. Kokes, *Intra-Sci. Chem. Rep.*, **6**, 77 (1972).
(16) W. O. Haag and H. Pines, *J. Amer. Chem. Soc.*, **82**, 387 (1960).
(17) S. Bank, A. Schriescheim, and C. A. Rowe, Jr., *J. Amer. Chem. Soc.*, **87**, 3224 (1965).
(18) G. C. Bond and P. B. Wells, *Advan. Catal.*, **15**, 91 (1964).
(19) N. Sheppard and D. M. Simpson, *Quart. Rev. Chem. Soc.*, **6**, 1 (1952).
(20) It is evident from the typical expanded-scale spectrum in Figure 4 that the base line for band intensity measurements is uncertain: the true base line could be that for the degassed sample (dotted line) or it could be shifted by perturbation of the background band (at 1525 cm^{-1}) by the adsorbed species. Furthermore, for weak bands appearing as shoulders, correction for band overlap can be quite large. These factors mean that the intensities for *weak* bands are subject to large errors. Since our procedures for measuring intensities gave effectively upper limits, we would estimate that, *at equilibrium*, the relative intensities for the weak bands for π-bonded *trans* and 1-butene could be too high by as much as a factor of 2. By way of contrast, intensity measurements for strong bands are subject to smaller percentage errors and these errors are likely to cancel when we deal with changes in these intensities; hence, the rate estimates, which are based on intensity *changes* for strong bands, are probably reliable to 10 to 20%.
(21) This is most reliable when the dose is admitted at low enough temperatures (*e.g.*, $-80°$) so that no π-allyls are formed.
(22) This conclusion is not a peculiarity of this particular sequence of reactions but appears to be quite general.
(23) Hightower and Hall[12] have utilized this product in the analysis of their data. For their data, however, the rates were first order and defined the equilibrium.
(24) See P. W. N. M. van Leeuwen and A. P. Praat, *Chem. Comm.*, 365 (1970), and references therein.
(25) F. A. Cotton, J. W. Faller, and A. Mosco, *Inorg. Chem.*, **6**, 179 (1967).
(26) H. W. Quinn and D. N. Glew, *Can. J. Chem.*, **40**, 1103 (1962).
(27) F. R. Hartley, *Chem. Rev.*, **69**, 809 (1969).
(28) D. W. Moore, H. B. Jonassen, and T. B. Joyner, *Chem. Ind. (London)*, 1304 (1960).
(29) S. Bank, *J. Amer. Chem. Soc.*, **87**, 3245 (1965).
(30) Infrared data clearly suggest that the relative stability of adsorbed π and π-allyl complexes favors the precursors of *cis*-butene. Support for this conclusion is offered by flash desorption experiments,[9] which indicate that the flash-desorbed gas is richer in *cis*-butene than the gas phase previously in contact with the adsorbed phase.
(31) J. Hightower and W. K. Hall, *J. Phys. Chem.*, **71**, 1014 (1967).

Reactivity of Boria–Silica Surface Hydroxyl Groups

M. L. Hair and W. Hertl*

Research and Development Laboratories, Corning Glass Works, Corning, New York 14830 *(Received February 26, 1973)*

Publication costs assisted by Corning Glass Works

The kinetics of the reactions of several coupling agents with a SiOH–BOH surface have been compared with the reactions on a pure silica surface. The following was noted. (1) The presence of the boron on the surface enhances the reactivity of the surface silanol groups. (2) The B–OH group is more reactive than the Si–OH group. (3) For the coupling agents studied the surface bond formed is fairly stable to 400° *in vacuo*. (4) The surface bonds formed with the silanol groups are partially hydrolyzable with water vapor at 400°, and the bonds formed with the B–OH groups are completely hydrolyzable. (5) The B–OH groups on the surface are present in both single and geminal configurations. (6) The presence of the boron on the boria–silica surface causes a larger decrease in the extinction of the silanol band with increasing temperature than occurs on silica. The extinctions of the various hydroxyls show different temperature effects although the changes in integrated intensity are similar.

Introduction

As a result of adsorption, infrared, and kinetic studies of the bonding reactions of various reagents with the surface of silica, the surface chemical properties of high surface area silica are now fairly well understood and reactivity can mainly be attributed to surface silanol groups. Of more immediate practical interest to the catalytic chemist and materials scientist, however, are the surface chemical properties of aluminosilicates and borosilicates and the effect of small quantities of impurities on the reactivity. In order to generate some understanding of the borosilicates in particular, well-defined silica surfaces have been treated with boron halides and water so that they contain boranol as well as silanol groups. An infrared spectroscopic–kinetic study was then undertaken of the reactions of a variety of surface bonding agents and the kinetic data compared and contrasted to data obtained previously for the same reactions on a pure silica surface.[1-3]

Since the chemical properties will be compared to those of a pure silica surface, the important chemical properties of silica surfaces will be summarized here. These are the following.

(1) The chemical bonding sites on the silica surface are principally the freely vibrating hydroxyl groups (identified by a sharp ir absorption at 3747 cm^{-1}). With the silica used here about 40% of these groups have been identified as being in a single configuration and 60% in a geminal configuration[2] (*i.e.*, 60% of the OH groups are sufficiently close together to concurrently react bifunctionally with $SiCl_4$).

(2) The freely vibrating hydroxyl groups are monoenergetic, *i.e.*, the reactivity of all the OH groups is the same. No particular preference is shown in the reactivity of the single or geminal groups, the presence of these groups being defined by the stoichiometry of the reactions rather than by any difference in reactivity.

(3) Since these free OH groups are monoenergetic, physical adsorption results in the same fraction of OH groups being covered, for a given temperature and pressure, whether there are many or few OH groups on the surface.

Because of the above properties, a straightforward integrated rate equation can be applied to the reaction curve obtained from any of the reactions of the bonding reagents with the hydroxyl groups, and a linear plot obtained. In the case of the monofunctional bonding agents a first-order rate equation is used; with di-, tri-, and tetrafunctional bonding agents a 1.6-order rate equation is used. (As discussed previously, this 1.6-order comes about because 60% of the OH groups are in a geminal configuration.)[2]

This report, therefore, describes and discusses the reactions of a number of bonding agents on a surface containing silanol and boranol groups and compares the properties of this surface with that of pure silica.

Experimental Section

The apparatus and experimental procedures used were as previously described.[3]

To prepare the boron-containing surface, a pressed silica disk was heated to 800° in order to obtain a surface containing only "free" hydroxyl groups (evidenced by the band at 3747 cm^{-1}). The silica disk was then mounted in the reaction cell and treated with BCl_3 until the silanol groups had all reacted (1 or 2 min at room temperature). After pumping, the sample was then treated with water vapor in order to hydrolyze the B–Cl present on the surface. This reaction is well documented in the literature.[4,5] Upon hydrolysis, a small band due to the B–OH group appears (3703 cm^{-1}) and the silanol band reappears in part. This procedure was repeated several times until the intensities of the silanol and boranol bands were about equal. The sample was then heated to 400° and ready for use. Spectra taken at various stages of this procedure are shown in Figure 1. It should be pointed out that, on occasion, boric acid condensed out on the cell windows after this procedure.

After preparing the sample, the surface was treated with monochlorotrimethylsilane, trimethylmethoxysilane, dimethyldichlorosilane, or hexamethyldisilazane. The surface reaction was carried out by admitting the reagent gas to the furnace containing the sample and allowing it to

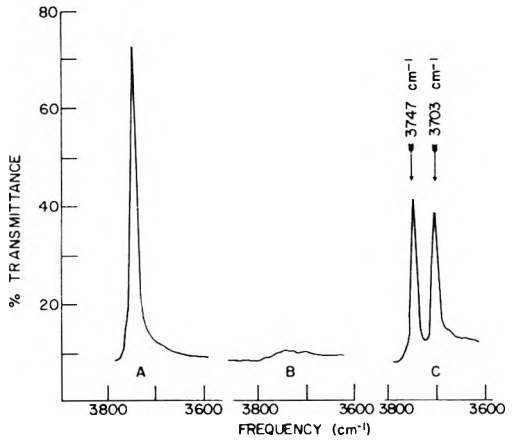

Figure 1. Spectra of (A) Si–OH band prior to reaction; (B) after reaction with BCl_3; (C) after heating to 400° following three BCl_3/hydrolysis treatments.

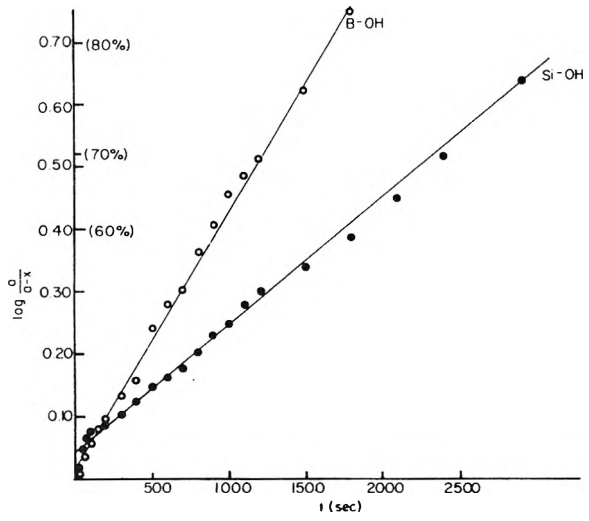

Figure 2. First-order kinetic plots for the reaction of 150 Torr of monochlorotrimethylsilane at 100° with the B–OH (O) and Si–OH (●) groups on the boria–silica surface.

react for a short period of time. After evacuation, a spectrum was taken and the procedure repeated. The intensities of the silanol and boranol bands were measured during the course of the reaction and the data subjected to kinetic analysis.

In reactions with chlorosilanes, HCl is one of the reaction products. Thus, it is important to know if HCl reacts with the surface. Hydrogen chloride was added to the SiOH–BOH sample at several temperatures. In no case was any change observed in the intensities of the Si–OH or B–OH bands and it is concluded that no detectable amount of reaction takes place between HCl and the OH groups on the surface under these reaction conditions.

For measuring the extinction values and integrated areas of the hydroxyl bands up to 400°, the sample was first heated to 400° *in vacuo* and then returned to room temperature. Spectra were recorded at 30, 150, 200, 300, 400, 350, 250, 100, and 30°. No significant differences were observed between the first and last spectra recorded at 30°. Narrow slits, very slow scan speeds, and 10× abscissa expansion were used when recording these spectra.

Results and Discussion

Reaction curves were obtained for the various coupling agents studied. From these reaction curves various order-

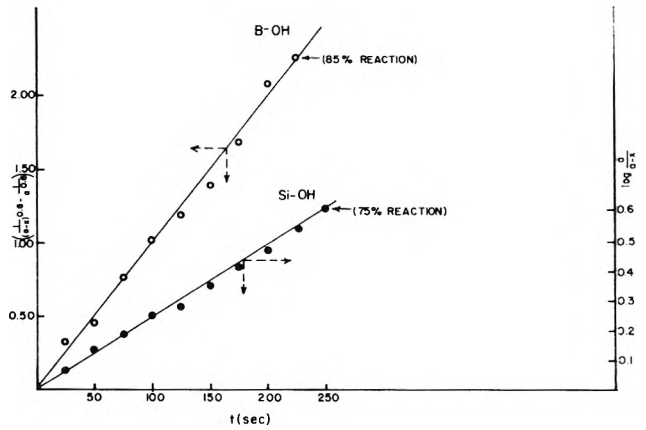

Figure 3. Kinetic plots for the reaction of 10 Torr of trimethylmethoxysilane at 80° with the B–OH and Si–OH groups on the boria–silica surface. The left-hand ordinate, for B–OH groups (O), is a 1.6-order rate expression; the right-hand ordinate, for Si–OH groups (●), is a first-order rate expression.

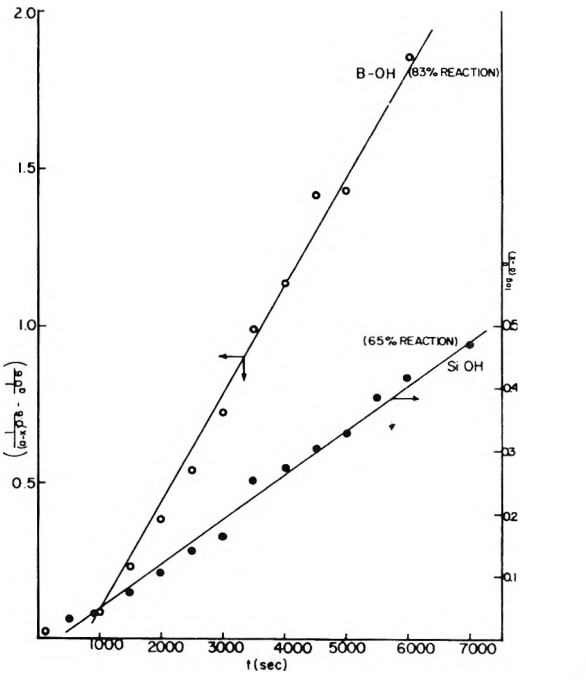

Figure 4. Kinetic plots for the reaction of 90 Torr of dimethyldichlorosilane at 100° with the B–OH and Si–OH groups on the boria–silica surface. The left-hand ordinate, for B–OH groups (O), is a 1.6-order rate expression; the right-hand ordinate, for Si–OH groups (●), is a first-order rate expression.

integrated rate equations were used until a linear plot was obtained. These calculations have been described previously.[1-3] As before, the order of the reaction is interpreted as the number of hydroxyl groups removed on average from the system when one adsorbed molecule reacts.

Table I gives the data for the orders of reaction observed when each of the four coupling agents was allowed to react with the Si–OH and the B–OH groups on the boria–silica surface. For comparison the reaction orders observed on a pure silica surface are also given, as well as the temperatures or pressures of reagent required to obtain approximately the same reaction rate. Some representative kinetic plots are given in Figures 2–5.

The first-order plots obtained when monochlorotrimethylsilane reacts with the silanol and boranol groups are linear to greater than 75% reaction (Figure 1). This is impor-

TABLE I

Coupling agent	Silica surface: Temp or pressure for convenient reaction rate of SiOH on SiO_2	Silica surface: Reaction order for Si-OH	Boria-silica surface: Temp or pressure for equivalent reaction rate of SiOH on boria-silica	Boria-silica surface: Reaction order for Si-OH	Boria-silica surface: Reaction order for B-OH
Trimethylchlorosilane (Figure 2)	300°	1.0	100°	1.0	1.0
Trimethylmethoxysilane (Figure 3)	150	1.6	80	1.0	1.6
Dimethyldichlorosilane (Figure 4)	350	~1.6	100–150	1.0	1.6
Hexamethyldisilazane (Figure 5)	10 Torr at 31°	2.0	0.2 Torr at 31°	1.0	1.0

tant as it implies that the silanol groups on the surface are still monoenergetic and that the boranol groups are also monoenergetic.

Three other facts are also immediately apparent from the plots and the data in Table I: (1) the boranol groups are considerably more reactive than the silanol groups; (2) the silanol groups on the boria-silica surface are much more reactive than on a pure silica surface; and (3) the reaction order of the silanol groups on the boria-silica surface is lower than on a silica surface, for the polyfunctional coupling agents.

In all the experiments carried out with dimethyldichlorosilane the initial part (first 10%) of the B-OH reaction was very slow, but the reason for this is not clear. When this reaction was carried out at 400°, the Si-OH group reacted slightly faster than the B-OH group. This effect would be expected if the activation energy for the reaction with the Si-OH group were higher than that for the B-OH group.

On a pure silica surface hexamethyldisilazane (HMDS) follows a second-order kinetic law. As discussed previously,[2] this is probably due to the formation of a reactive product, all of which reacts rapidly with the surface, so that when one HMDS molecule reacts with the surface, two OH groups are removed.

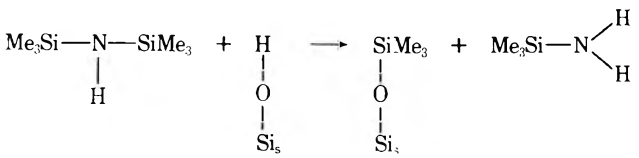

followed by

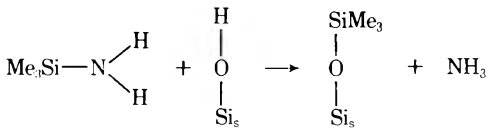

With the silanol-boranol surface, however, both the silanol and the boranol groups follow a first-order rate law. This immediately suggests that under these conditions the product of the first reaction leaves the system and does not react further with the surface.

Two important chemical properties for surface bonding reagents are thermal stability and stability against hydrolysis. To determine these properties, each treated sample was heated to 400° *in vacuo* and a spectrum taken at room temperature. The sample was then heated to 400° and water vapor was added to the system. After evacuation and cooling to room temperature another spectrum

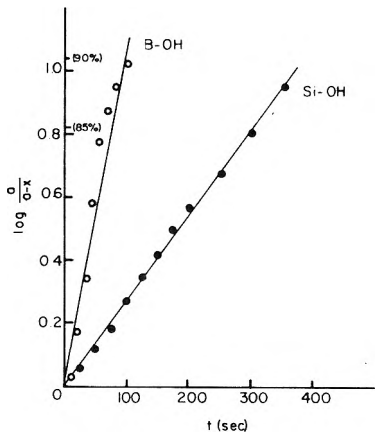

Figure 5. First-order kinetic plots for the reaction of 0.2 Torr of hexamethyldisilazane at 31° with the B-OH (O) and Si-OH (●) groups on the boria-silica surface.

was taken. (The spectra were all taken at the same temperature, since there is a large temperature coefficient for the band extinction values. This will be discussed below.) The bonded methoxy- and chlorosilane products showed some decrease in the intensity of the C-H stretching bands after the thermal treatment, showing that these do decompose slightly. The HMDS product was completely stable to the thermal treatment. In no case did any hydroxyl groups reappear. All the reagents, however, are reactive to water vapor at high temperature. The spectra taken after the hydrolysis showed that the C-H stretching band intensities were greatly reduced, part of the silanol bands reappeared, and virtually all the B-OH reappeared. Boric acid was found deposited on the cell windows after the high-temperature hydrolysis, indicating that this is one of the reaction products from the hydrolysis. Since the B-OH intensity was about the same as initially, this boron was probably present on the surface in addition to the boron which gives rise to the B-OH groups.

Spectral Features of SiOH-BOH Surfaces. Figure 6 shows plots of the extinction values and of the integrated areas under the Si-OH and B-OH bands at various temperatures up to 400°. Also given are the extinctions and integrated areas of the Si-OH band on pure silica, silica with a small amount of B-OH, and porous glass. It is seen that the integrated areas decrease about 15–20% over the range 30–400°. This 15–20% decrease over this temperature range has been reported in the literature for other types of surfaces containing OH groups.[6-8] The interesting point, however, is the wide variation in extinctions over this temperature range for the different surfaces. The sila-

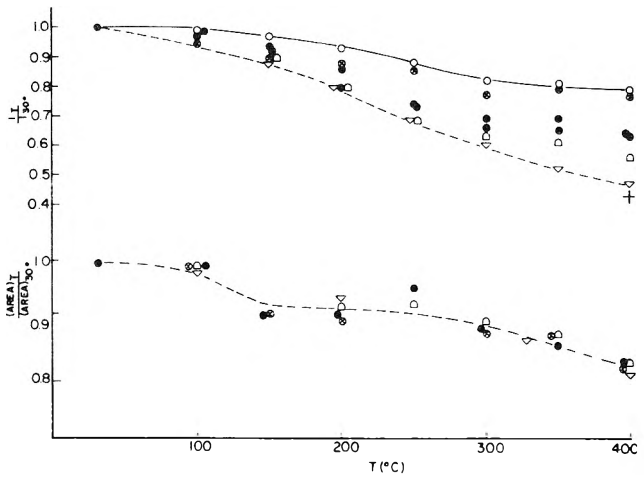

Figure 6. (Top) Variation of the OH band extinction at various temperatures (I_T) with respect to the band extinction at 30° ($I_{30°}$). (Bottom) Variation of the integrated area of the OH band at various temperatures ($area_T$) with respect to the integrated area at 30° ($area_{30°}$): ●, SiOH on Silica; ○, SiOH on silica with small amount BOH; ⊗, SiOH on porous glass; △, SiOH on silica–boria surface; ▽, BOH on silica–boria surface; +, SiOH on Aerocat Triple A silica–alumina catalyst.

nol bands on the porous glass and the silica containing a trace of BOH decreased only about 22%, whereas on pure silica the silanol band decreased about 35%. On the SiOH–BOH surface the silanol band decreased 45% and the BOH band decreased 53%.

The question of changes in intensity of the fundamental OH vibration bands has been addressed by Fripiat and coworkers[6] who postulate that the increased band widths and decreased extinctions can be attributed to a proton delocalization process. Cant and Hall[7] extended this data to surface hydroxyl groups of biotite, muscovite, silica gel, alumina, silica–alumina gel, and decationated Y zeolite. They also noted changes in extinction as a function of hydroxyl type though they were more concerned with the observation that the bands all behave similarly as far as changes in integrated intensity were concerned.

The absorbance of a fundamental band is a function of the Einstein coefficient of absorption (proportional to the square of the transition moment) and the fraction of the OH oscillators in the initial and final levels. For any two freely vibrating hydroxyl groups it is not unreasonable to expect that the *change* of integrated intensity with temperature will be very similar. The extinction at any wavelength, however, will be strongly dependent on the electron distribution in the band. Thus, more acidic OH groups will show a greater lowering in intensity with temperature (*i.e.*, a broadening of the band) than will more basic groups. This is borne out by the present experiments. Kinetically it was observed that large amounts of boron enhanced the reactivity of the silanol groups, and the chemical activities of the B–OH, Si–OH on boria–silica, and SiOH groups follow the changes in extinction.

Why trace amounts of boron should cause a lesser decrease in the extinction of the band with increasing temperature is not clear. It is of interest to note, however, the correspondence between the sample with only a small amount of boron on the surface and the porous glass which is known to contain only about 3% B_2O_3 as total impurity. Low and Ramasubramanian[9] have suggested that in porous glass the boron oxide is present in "islands" on the surface, and presumably this does not affect the "silica" too much. Perhaps in our high-boron samples the boron is in close proximity to the silanol groups in a manner similar to that suggested for silica–alumina cracking catalysts.[10,11] If this speculation is correct, it is of interest to examine the change in extinction of the terminal hydroxyl groups (Si–OH) on such catalysts. The data obtained at 30 and 400° on a commercial silica–alumina cracking catalyst (Aerocat Triple A) is shown in Figure 6. At 400° the extinction of the OH group has decreased by about 57%. This is presumably the most active hydroxyl group and gives the largest change in extinction of the samples measured.

The kinetic and spectroscopic data presented in this paper demonstrate the large effect that relatively small quantities of impurity can have on the surface properties of silica. It is well established in the literature[9,12,13] that boron impurities introduced into silica create additional surface sites of the "Lewis acid type" which are capable of chemisorbing ammonia and other electron-donating molecules. The present work shows that such impurities also change the kinetic order and chemical reactivity of the silanol groups on the surface. These groups are unchanged in frequency and have usually been assumed to be the same as those occurring on a pure silica surface. In the reaction of silane coupling agents with silica surfaces (for chromatography, enzyme coupling, dyeing, etc.) the change in kinetic order caused by such impurities could cause complications in the end use of the final product. For instance, when using a bifunctional silane, a change in reaction order from, say, 1.6 to 1.0 would leave a surface containing many more unreacted functional groups, which could then take part in further adsorption processes.

Note

A reviewer has commented that "in spite of previous publications, I am still waiting for an unambiguous proof that there is really an OH group bound to boron." He points out that a group such as

would give the SiOH group a high activity, a high mobility, and therefore a high temperature coefficient. It is difficult to provide unambiguous proof that the band at 3703 cm^{-1} is indeed a BOH group rather than an SiOH group of lower frequency. However, the following arguments may be applied.

(1) The infrared method used in this paper clearly shows that there is a group at 3747 cm^{-1} which changes in reactivity and reaction order when boron is added to the surface. It shows no change in frequency from the pure silica surface and, therefore, it must be concluded that the effect of boron near to a silanol group is to change the reactivity of that group *without* changing its frequency. (*N.B.* The intensity may change). There is no evidence that suggests that the boron should *also* interact in such a way as to cause a unique 40-cm^{-1} frequency shift. Thus it seems reasonable (although not proven) to assign the 3703-cm^{-1} band to a BOH group, the shift to lower frequency being reasonable in view of the lower electronegativity of the boron atom, and in agreement with previous workers.

(2) In the analagous silica–alumina systems, where the gross change in catalytic properties associated with the introduction of alumina into the silica network is well known and a similar positioning of trivalent ions around the SiOH group has been postulated, only one OH group is in general observed, and that appears at essentially the same frequency as it does in the original silica surface.[14]

References and Notes

(1) M. L. Hair and W. Hertl, *J. Phys. Chem.*, **73**, 2372 (1969).
(2) W. Hertl and M. L. Hair, *J. Phys. Chem.*, **75**, 2133 (1971), and references therein.
(3) W. Hertl, *J. Phys. Chem.*, **72**, 1248 (1968).
(4) H. P. Boehm, M. Scheider, and F. Arendt, *Z. Anorg. Allg. Chem.*, **320**, 43 (1963).
(5) F. H. Hambleton and J. A. Hockey, *J. Catal.*, **13**, 35 (1969).
(6) J. J. Fripiat, H. Bosmans, and P. G. Rouxhet, *J. Phys. Chem.*, **71**, 1097 (1967).
(7) N. W. Cant and W. K. Hall, *Trans. Faraday Soc.*, **64**, 1093 (1968).
(8) J. W. Ward, *J. Catal.*, **9**, 396 (1967).
(9) M. J. D. Low and N. Ramasubramanian, *J. Phys. Chem.*, **71**, 3077 (1967).
(10) H. A. Benesi, *J. Phys. Chem.*, **61**, 970 (1957).
(11) J. B. Uytterhoeven, L. G. Christner, and W. K. Hall, *J. Phys. Chem.*, **69**, 2117 (1965).
(12) M. L. Hair, "Infrared Spectroscopy in Surface Chemistry," Marcel Dekker, New York, N. Y., 1967.
(13) N. W. Cant and L. H. Little, *Can. J. Chem.*, **43**, 1252 (1965).
(14) M. R. Basila, *J. Phys. Chem.*, **66**, 2223 (1962).

Interaction Energy between a Gas Molecule and a Gold Film

D. Lando, J. F. Bohland,*[1]

Engineering Research Center, Western Electric Company, Incorporated, Princeton, New Jersey 08540

and W. C. Hahn

Department of Metallurgy and Materials Science, Lehigh University, Bethlehem, Pennsylvania 18015

(Received March 5, 1973)

Publication costs assisted by Bell Telephone Laboratories, Whippany, New Jersey

The experimental techniques developed by Lando and Slutsky are used to obtain high coverage adsorption isotherms (5 to 31 molecular layers) for benzene, carbon tetrachloride, cyclohexane, and octane physically adsorbed on a flat gold surface. The potential energy of interaction of the molecule and a gold surface is calculated using the Frenkel–Halsey–Hill equation. In all cases the interaction energy is found to vary with the inverse square of the molecule to metal distance.

Introduction

There has been considerable interest for many years in the nature of gas–metal interactions.[2-7] Experimental support for the proposed theories, however, has been limited by experimental difficulties. Recently, Lando and Slutsky[8,9] utilized new experimental techniques to measure the high coverage portion of several physical adsorption isotherms. They studied the interaction between a gold surface and several different nonpolar, organic molecules and found the potential energy of interaction to be a function of the inverse square of the molecule to metal distance. Those results did not agree with any of the previously proposed theories. The work presented here is an independent confirmation of the inverse square relationship. In addition, interaction constants for substances not studied by Lando and Slutsky are presented.

Physical adsorption isotherms were gravimetrically determined for the adsorption of benzene, carbon tetrachloride, cyclohexane, and octane on gold. The vapor pressure of an adsorbed film is related to the molecular interaction energy through the Frenkel[10]–Halsey[11]–Hill[12-14] equation

$$\frac{U(Z) - U'(Z)}{kT} = \ln \frac{P}{P_0} \qquad (1)$$

where $U(Z)$ is the potential energy of interaction of an adsorbate molecule at distance Z from the adsorbent surface, $U'(Z)$ is the interaction energy of an adsorbate molecule at distance Z from its bulk liquid, k is Boltzmann's constant, T is the absolute temperature, P is the vapor pressure of the adsorbed film, and P_0 is the vapor pressure of the bulk liquid. In the development of eq 1 it is necessary to assume that the entropy of an adsorbed molecule is equal to the entropy of a molecule in the bulk liquid. This is a valid assumption at very high coverages where the properties of the adsorbed film approach those of the bulk liquid.

Experimental Section

The gold electrodes on a resonating quartz crystal serve as the adsorbent surfaces. Sauerbrey[15] showed that for a crystal resonating in the thickness-shear mode the frequency change due to mass added to the antinodal surfaces is given by

$$-\Delta f / f = \Delta m / m \qquad (2)$$

where Δf is the change in frequency, f is the initial frequency, Δm is the mass added to the surface of the crystal, and m is the mass of the crystal. In order for this equation to be valid, the added mass must be uniformly distributed on the crystal surface.

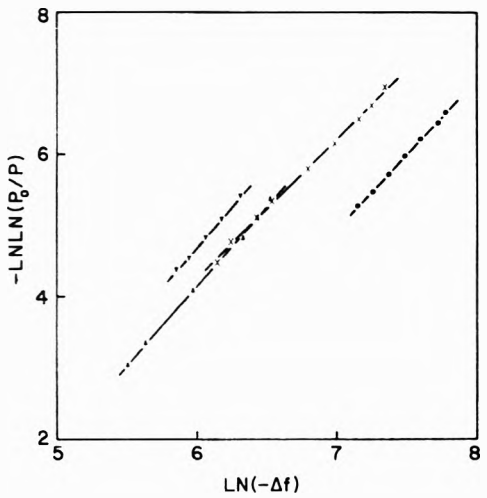

Figure 1. $-\ln \ln (P_0/P)$ *vs.* $\ln (-\Delta f)$ for benzene (▼), carbon tetrachloride (●), cyclohexane (×), and octane (▲)

The quartz crystal microbalance consists of a crystal mounted in an adsorption cell, an oscillator to drive the crystal, a frequency counter, a digital to analog converter, and a strip chart recorder.

The AT-cut crystals used in this work are cut to resonate at 5 MHz in the fundamental thickness-shear mode. The precise angle of cut within the AT-cut range is chosen to give a zero temperature coefficient of frequency at 25°. The crystals are in the form of circular plates 1.498 cm in diameter and 0.0334 cm thick. The major surfaces of the crystals are polished to within a half wavelength of sodium light. The gold electrodes on the crystal, which serve as the adsorbent surfaces, were vacuum deposited to a thickness of about 3000 Å.

The adsorption and reference cells are formed by connecting a glass-windowed viewing port to an electrical feedthrough. The quartz crystal is mounted in the adsorption cell on a pair of the feedthrough conductors. When in operation, a copper block is mounted over the cells in order to minimize thermal gradients between the cells.

A differential capacitance manometer is used to measure the adsorbate pressure in the adsorption cell relative to its saturation vapor pressure in the reference cell. Pressure differences can be measured from 0.0001 to 100 mm. For all but the lowest pressure measurements, three significant figures can be read.

The adsorption cell is pumped at high temperature to a pressure of less than 10^{-8} mm in order to thoroughly remove sorbed material from the gold surfaces. In order to avoid contamination from backstreaming pump oil, the vacuum system employs sorption pumps for roughing and an ion pump for high vacuum pumping.

During the adsorption run the adsorption and reference cells are immersed in a water bath where the temperature is controlled to within ±0.002°.

Results and Discussion

At high coverages where the thickness of the adsorbed film is proportional to the number of molecular layers, the Halsey[11] isotherm may be written as

$$\ln (P/P_0) = C/Z^n \qquad (3)$$

where C and n are constants. The thickness of the sorbed layer Z can then be related to the measured frequency changes through eq 2.

TABLE I: Interaction Constants

Substance	Coverage, Å	n	$kTC \times 10^{28}$, erg cm²	$B \times 10^4$, erg/cm
Benzene[a]	35.3–55.8	2.26	0.695	0.0673
Carbon tetrachloride[b]	71.6–133.0	2.12	1.11	0.106
Cyclohexane[a]	51.5–176.2	1.94	1.25	0.112
Octane[a]	31.0–86.2	2.22	1.93	0.123

[a] At 25.0°. [b] At 21.8°.

$$-\frac{\Delta f}{f} = \frac{\Delta m}{m} = \frac{\rho_a^2 A_a Z}{\rho_q A_q t_q} = \frac{2\rho_a k Z}{\rho_q t_q} \qquad (4)$$

where ρ_a is the density of the adsorbate, A_a is the area available for adsorption on one of the gold electrodes, $\rho_q = 2.65$ g/cm³ is the density of quartz, A_q is the geometric area of the gold electrode, $t_q = 0.0334$ cm is the thickness of the quartz crystal, and $k = A_a/A_q$ is the roughness factor of the gold film. Substitution of eq 4 into eq 3 gives

$$\ln (P/P_0) = C'C/(-\Delta f)^n \qquad (5)$$

where $C' = (2\rho_a k f/\rho_q t_q)^n$ = constant. Taking the logarithm of both sides of eq 5 gives

$$\ln \ln (P_0/P) = \ln (-C'C) - n \ln (-\Delta f) \qquad (6)$$

A plot of $-\ln \ln (P_0/P)$ *vs.* $\ln (-\Delta f)$ is shown in Figure 1. Straight lines are fitted to the data points by the method of least squares, and the slopes of these lines which according to eq 6 correspond to the power n are listed in Table I.

When the values of n in Table I are compared with their corresponding ranges of coverage, it is apparent that the two materials for which the widest ranges of coverage are given yield values of n closest to 2. It is also seen that the data obtained for these materials are at higher coverages than the other data. It is felt, therefore, that $n = 2$ accurately describes long-range interactions with metals.

The deviations from $n = 2$ can be explained by the degree of cleanliness of the gold surface. Some measurements were made in which the crystal was not sufficiently baked, and n was found to range between 1.36 and 2.86. The ranges of n shown in Table I are obtained with a more thorough baking procedure. The deviations from $n = 2$ are therefore attributed to interactions with at least a partial layer of foreign material adsorbed on the gold surface.

With $n = 2$ eq 5 becomes

$$\ln (P/P_0) = C'C/(-\Delta f)^2$$

with $C' = (2\rho_a k f/\rho_q t_q)^2$. The value of $C'C$ can be calculated from the slope of a plot of $1/(\Delta f)^2$ *vs.* $\ln P/P_0$. In Figure 2 these plots are presented for the substances studied. Straight lines are fitted to the data by the least-squares method.

The constant C' can be calculated if the roughness factor k is known. Lando and Slutsky[8] experimentally found the roughness factor of an evaporated gold electrode to be equal to 1 within experimental error. The value of k for these calculations is assumed to be 1.

The values of C are calculated by dividing $C'C$ by C'. These constants used with eq 3 and 1 give the potential energy difference between an adsorbed molecule and a

molecule in the bulk liquid

$$U(Z) - U'(Z) = kTC/Z^2 \quad (7)$$

Wade and Slutsky[16] used a similar approach to determine the interaction energy between heptane and quartz. They obtained an inverse cube relationship with distance; this is expected for a nonmetallic adsorbent. Comparing the results for metallic and nonmetallic adsorbents leads to the conclusion that the interaction with the bulk liquid U' is an inverse cube function and that at high coverages it is small compared with the inverse square interaction with the metal. Therefore, at high coverages eq 7 becomes

$$U(Z) = kTC/Z^2 \quad (8)$$

The values of kTC for the substances studied are listed in Table I. In order to obtain a general interaction equation, the polarizabilities of the molecules are considered. Since the interaction energy is expected to vary directly with the molecular polarizability,[4,6] eq 8 may be written as

$$U(Z) = B\alpha/Z^2$$

where $B = kTC/\alpha$ and α is the molecular polarizability the gas molecule. The values obtained for B are listed in Table I.

Using the average value of B from Table I, the general interaction equation is

$$U(Z) = 0.102 \times 10^{-4}\alpha/Z^2 \text{ erg/cm}$$

This compares favorably with the results of Lando and Slutsky[8] who obtained a constant of 0.174×10^{-4} erg/cm.

It is concluded that the long-range potential energy of interaction between nonpolar molecules and a metal surface is a function of the inverse square of the molecule to metal distance. This relationship which was first observed by Lando and Slutsky[8,9] has now been independently confirmed. These results do not agree with the various theories which have been proposed to describe molecule–metal interactions. The proposed theories predict an inverse cube relationship.

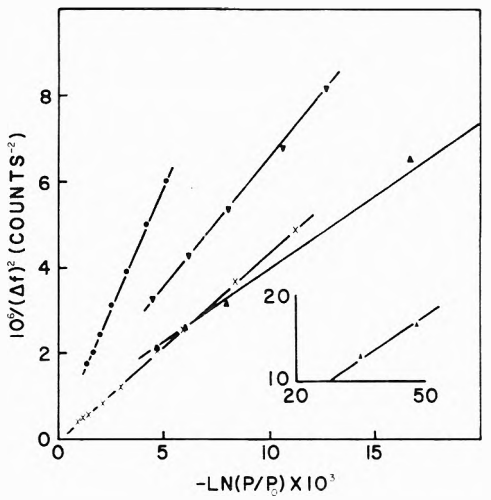

Figure 2. $1/(\Delta f)^2$ *vs.* $-\ln(P/P_0)$ for benzene (▼), carbon tetrachloride (●), cyclohexane (×), and octane (▼).

References and Notes

(1) Present address, Bell Telephone Laboratories, North Andover, Mass. 01845.
(2) (a) J. E. Lennard-Jones, *Trans. Faraday Soc.*, **28**, 333 (1932). (b) J. Bardeen, *Phys. Rev.*, **58**, 727 (1940).
(3) H. Margenau and W. G. Pollard, *Phys. Rev.*, **60**, 128 (1941).
(4) E. S. R. Prosen and R. G. Sachs, *Phys. Rev.*, **61**, 65 (1942).
(5) H. G. B. Casimir and D. Polder, *Phys. Rev.*, **73**, 360 (1948).
(6) I. Ye Dzyaloshinskii, I. M. Lifshitz, and L. P. Pitaevskii, *Advan. Phys.*, **10**, 165 (1961).
(7) C. Mavroyannis, *Mol. Phys.*, **7**, 593 (1963).
(8) D. Lando and L. J. Slutsky, *Phys. Rev. B*, **2**, 2863 (1970).
(9) D. Lando and L. J. Slutsky, *J. Chem. Phys.*, **52**, 1510 (1970).
(10) J. Frenkel, "Kinetic Theory of Liquids," Clarendon Press, Oxford, 1946.
(11) G. D. Halsey, *J. Chem. Phys.*, **16**, 931 (1948).
(12) T. L. Hill, *J. Chem. Phys.*, **17**, 590 (1949).
(13) T. L. Hill, *J. Chem. Phys.*, **17**, 668 (1949).
(14) T. L. Hill, *J. Phys. Chem.*, **54**, 1186 (1950).
(15) G. Sauerbrey, *Z. Phys.*, **155**, 206 (1959).
(16) W. H. Wade and L. J. Slutsky, *J. Chem. Phys.*, **40**, 3994 (1964).

Spectra and Structure of Phosphorus–Boron Compounds. III.[1a] Vibrational Studies of Trimethylphosphine–Borane and Trimethylphosphine–Borane-d_3

J. D. Odom, B. A. Hudgens,[1b] and J. R. Durig*

Department of Chemistry, University of South Carolina, Columbia, South Carolina 29208 *(Received November 20, 1972)*

Publication costs assisted by the National Science Foundation

The infrared (33–4000 cm^{-1}) and Raman (0–3000 cm^{-1}) spectra of $(CH_3)_3PBH_3$ and $(CH_3)_3PBD_3$ have been recorded for the solid state at low temperatures. The spectra have been interpreted in detail on the basis of C_{3v} molecular symmetry and $P4/nmm$ space group symmetry. The valence force field model has been utilized in calculating the frequencies and potential energy distribution. The calculated potential constants for the adduct are compared to those previously reported for the Lewis base moiety and the differences are shown to be consistent with the structural changes found upon adduct formation. The P–B stretch was found to be extensively mixed with the P–C stretch. The P–B force constant was found to have a value of 2.37 mdyn/Å which seems consistent with the adduct stability.

Introduction

Trimethylphosphine–borane is an addition compound which was first prepared by Burg and Wagner[2a] by mixing diborane(6) and trimethylphosphine at low temperatures. The adduct is a crystalline solid which melts at 103° and is stable toward dissociation. There is no evidence for dissociation at room temperature and the adduct can be heated to 200° before appreciable decomposition occurs. Bryan and Kuczkowski[2b] recently published the microwave spectrum and determined the P–B bond distance for this adduct to be 1.901 ± 0.007 Å. This distance is considerably longer than the corresponding one (r_{P-B} = 1.836 ± 0.012 Å) obtained[3] for F_3PBH_3, yet the latter molecule is extensively dissociated at 0°. Recently Durig, *et al.*,[4] measured the microwave spectrum and determined the P–B bond distance in H_3PBH_3, which is completely dissociated at 0°, to be 1.937 ± 0.005 Å. These facts, along with earlier studies,[2b] indicate that the usual correlations between bond strength and bond length are not applicable for these compounds.

Little vibrational data are available for boron–phosphorus adducts. The present investigation was undertaken to determine if there is a correlation between the P–B bond length and the frequency of the P–B stretch, along with the corresponding force constant. The complete normal coordinates were calculated to gain additional information about the properties of the P–B bond and the extent of the mixing of the fundamental modes.

Experimental Section

All preparative work was carried out in a conventional high-vacuum system employing greaseless stopcocks.[5] Trimethylphosphine was obtained from Strem Chemicals, Inc., and was purified on a variable-temperature vacuum fractionation column[6] (vapor pressure 158 mm at 0°; lit. 158).[5] Isotopically normal diborane(6) was prepared by the addition of KBH_4 to hot polyphosphoric acid and deuteriodiborane(6) was prepared in a similar reaction using $NaBD_4$. Both diborane(6) species were purified by passage through a −160° bath (*i*-C_5H_{12} slush) into a trap held at −196° (liquid nitrogen). Purity was checked by vapor pressure measurement,[5] infrared,[7] and mass spectra.[8] The trimethylphosphine–borane and –borane-d_3 were prepared by the reaction of $(CH_3)_3P$ and the appropriate diborane(6) species.[2a] The $(CH_3)_3PBH_3$ and $(CH_3)_3PBD_3$ were purified by vacuum fractionation using a −45° bath (chlorobenzene slush) and a −196° bath. The trimethylphosphine–borane species were retained in the −45° bath and any unreacted trimethylphosphine and diborane(6) were retained in the −196° trap.

The far-infrared spectra of $(CH_3)_3PBH_3$ and $(CH_3)_3PBD_3$ were recorded between 33 and 350 cm^{-1} with a Beckman IR-11 double-beam grating spectrophotometer which was purged with dry nitrogen. The instrument was calibrated with water vapor frequencies.[9] The low-temperature cell used has been described elsewhere.[10] The sample was allowed to sublime slowly onto a silicon substrate which was in thermal contact with a brass heat sink cooled by a Dry Ice–2-propanol slush.

The mid-infrared spectra were recorded from 4000 to 250 cm^{-1} with a Perkin-Elmer 621 grating spectrophotometer which was purged with dry nitrogen gas and calibrated in the usual manner.[9,11] The spectra were recorded with the sample held at −78° in a cell with CsI windows.

A Cary Model 82 Raman spectrophotometer equipped with a Coherent Radiation Model 52-A argon ion laser was used to record the Raman spectra from 0 to 4000 cm^{-1}. The compounds were condensed in glass capillaries and sealed with a torch. The capillaries and a thermocouple were placed in a cold cell similar to the one described by Miller and Harney[12] which was cooled by a stream of nitrogen gas. Spectra were also recorded at room temperature but no differences were observed between these data and those obtained at *ca.* −140°.

Results and Discussion

The infrared and Raman spectra of $(CH_3)_3PBH_3$ and $(CH_3)_3PBD_3$ are shown in Figures 1-3. A molecular symmetry of C_{3v}, with the C_3 axis coincident with the P–B bond, and "local" C_3 symmetry for the methyl tops was assumed for trimethylphosphine–borane. From group theory, one predicts the molecule to have $10A_1$, $5A_2$, and

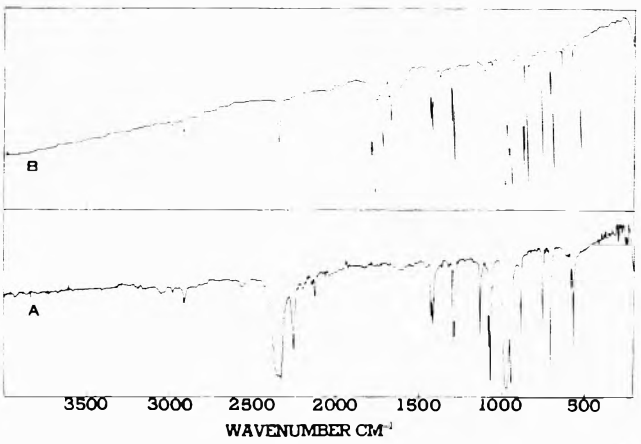

Figure 1. Raman spectra of $(CH_3)_3PBH_3$ (A) and $(CH_3)_3PBD_3$ (B) recorded with a sample temperature of −140°.

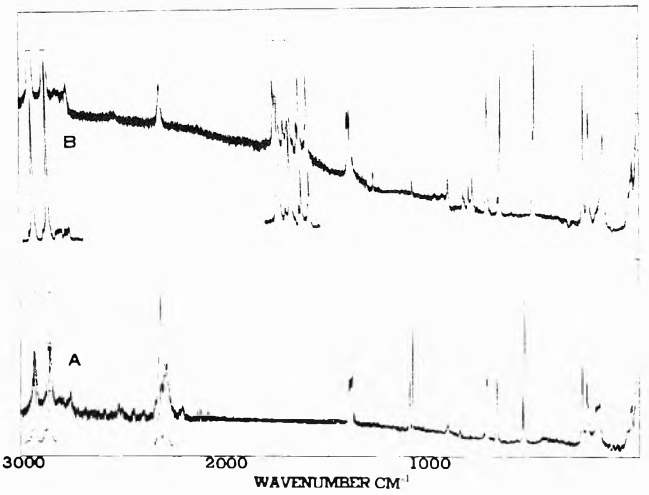

Figure 2. Mid-infrared spectra of $(CH_3)_3PBH_3$ (A) and $(CH_3)_3PBD_3$ (B) (solid phase) recorded at −78°.

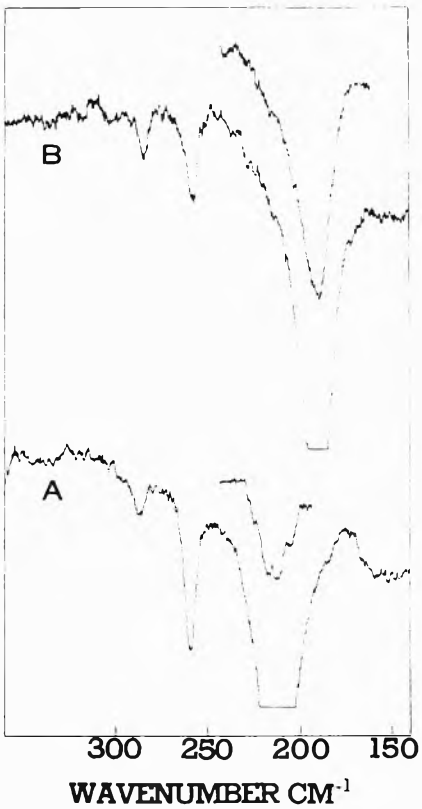

Figure 3. Far-infrared spectra of $(CH_3)_3PBH_3$ (A) and $(CH_3)_3PBD_3$ (B) (solid phase) recorded at −78°.

15E modes. The five "silent" A_2 vibrations were not observed even in the solid state.

The crystal structure at room temperature has been reported[13] to be $P4/nmm \equiv D_{4h}^7$ with two molecules per primitive cell, which means it is disordered. This cell has sites of D_{2d} or C_{4v} for the accommodation of two molecules but neither symmetry is a subgroup of the C_{3v} molecular symmetry. Therefore, no effects due to the site symmetry are expected and the splitting due to the factor group should be quite small. Thus, the intramolecular vibrations can be interpreted on the basis of the molecular symmetry.

CH_3 Modes. The two antisymmetric CH_3 stretching modes observed in trimethylphosphine collapsed into a single, intense, sharp, Raman band at 2982 cm^{-1} for the adduct (Figure 1). The corresponding infrared band is very weak which is in marked contrast to the strong infrared absorption observed in trimethylphosphine[14] for the corresponding fundamental. As with the antisymmetric CH_3 stretches, the symmetric CH_3 stretches, ν_2 and ν_{18}, are accidentally degenerate at 2918 cm^{-1} and are totally insensitive to deuteration of the BH_3 group.

As was observed in trimethylphosphine by Park and Hendra,[14] the three methyl antisymmetric deformations are not degenerate; however, the separation between the bands is less in the adduct than for those in the parent Lewis base. A decrease in the separation of ν_{22} (E) and ν_5 (A_1) in the adduct is also observed for the symmetric methyl deformations. The intensities of the antisymmetric and the symmetric deformations in the infrared spectrum are observed to be reversed with the symmetric deformations becoming more intense in the adduct.

The methyl rocks are the only methyl modes to show any sensitivity to deuteration of the borane group. In the "light" compound, the ν_7 (A_1) and ν_{24} (E) modes form a broad, strong band centered at 980 cm^{-1}. Upon deuteration of the borane group, the frequency of the A_1 mode increases to 989 cm^{-1} and the frequency of the E decreases to 960 cm^{-1}. The second E mode, ν_{25}, at 946 cm^{-1} is unaffected by the deuteration.

C-P Skeletal Modes. The symmetric C-P stretch (A_1) is strongly mixed with the P-B stretch. This stretch, which is observed at 708 (^{11}B) and 713 cm^{-1} (^{10}B) in the "light" compound, shifts to 692 cm^{-1} upon deuteration of the BH_3. The symmetric C-P stretch in trimethylphosphine was found at 653 cm^{-1}. The antisymmetric stretch, which, of course, does not couple with the P-B stretch, is observed at 756 cm^{-1} in both isotopic species. The frequencies of both the symmetric and antisymmetric C-P stretches are found to be 50 cm^{-1} higher in the adduct than in the parent Lewis base.

In trimethylphosphine, the C-P bond is formed using a sp^3 orbital of the carbon with orbitals of the phosphorus which are presumably intermediate in hybridization between sp^3 and p^3. When the adduct is formed, the phosphorus undergoes a rehybridization to a value closer to sp^3. The C-P bond length decreases from 1.841 ± 0.003 Å[15a] in the parent Lewis base to 1.819 ± 0.010 Å[2b] in the adduct. The C-P-C angle opens from 99.1 ± 0.2°[15a] in trimethylphosphine to 105.0 ± 0.4° in $(CH_3)_3PBH_3$. The increase in the two C-P stretching frequencies is attributed

TABLE I: Observed and Calculated Vibrational Frequencies for $(CH_3)_3PBH_3$[a]

$(CH_3)_3PBH_3$		$(CH_3)_3P$[b]		$(CH_3)_3PBH_3$	
Infrared ν, cm^{-1}	Raman $\Delta\nu$, cm^{-1}	Infrared ν, cm^{-1}	Raman $\Delta\nu$, cm^{-1}	calcd, cm^{-1}	Assignment and approximate description
				2983	
2983 vw	2986 vw	2978	2969	2982	ν_1 (A_1), ν_{16} (E), ν_{17} (E) CH_3 antisymmetric stretch (100%)
			2954	2983	
2913 w	2916 vs	2900	2894	2913	ν_2 (A_1), ν_{18} (E) CH_3 symmetric stretch (100%)
				2913	
2362 s	2367 s			2355	ν_{19} (E) BH_3 antisymmetric stretch (100%)
2335 s	2335 vs			2332	ν_3 (A_1) BH_3 symmetric stretch (100%)
2266 wm					
2254	2254 w				
1429 wm	1432 m	1441		1420	ν_{20} (E)
1421 wm	1426 m	1430	1421	1419	ν_{21} (E) CH_3 antisymmetric deformations (100%)
1412 w	1418 m	1416		1420	ν_4 (A_1)
1304 wm	1314 w			1306	ν_{22} (E) CH_3 symmetric deformations (100%)
1293 m		1283	1293	1294	ν_5 (A_1)
1133 m	1137 m			1136	ν_{23} (E) BH_3 antisymmetric deformation (100%)
	1122 s				
1081 m				1087	ν_6 (A_1) $^{10}BH_3$ symmetric deformation (95%)
				1078	ν_6 (A_1) $^{11}BH_3$ symmetric deformation (82%)
1069 s	1069 w				
			973	985	ν_7 (A_1) CH_3 rock (100%)
980 vs				972	ν_{24} (E) CH_3 rock (82%)
946 s	946 w	940	948	944	ν_{25} (E) CH_3 rock (95%)
888 m	889 w			887	ν_{28} (E) BH_3 rock (90%)
756 m	758 ms	709	708	756	ν_{27} (E) C_3P antisymmetric stretch (100%)
	713 m			715	ν_8 (A_1) C_3P symmetric stretch (70%) and P–^{10}B stretch (30%)
708 s	708 vs		653	712	ν_8 (A_1) C_3P symmetric stretch (75%) and P–^{11}B stretch (25%)
583 w	583 m			579	ν_9 (A_1) P–^{10}B stretch (60%) and P–C (40%)
571 m	571 s			564	ν_9 (A_1) P–^{11}B stretch (65%) and P–C (35%)
286 w	288 ms	298	305	285	ν_{10} (A_1) C_3P symmetric deformation (90%)
258 m	262 m	255	263	257	ν_{28} (E) C_3P antisymmetric deformation (100%)
211 s	211 m			209	ν_{30} (E) BPC_3 bend (95%)
95 w					lattice mode (libration, E_u?)
	43 w				lattice mode (translation?)

[a] Abbreviations used: m, medium; s, strong; w, weak; v, very. [b] Data taken from ref 15b and 18. Infrared data are for the vapor and the Raman frequencies are for the liquid state.

to the decrease in the P–C bond length. Since the methyl groups are farther apart in the adduct than in the free base, the CH_3 stretching modes do not couple among the methyl tops and, similarly, the coupling of the other methyl modes is smaller. Durig, *et al.*,[15b] assigned the bands at 298 and 255 cm^{-1} to the symmetric, A_1, and antisymmetric, E, C_3–P deformations of $(CH_3)_3P$, respectively. In the adduct, these modes are observed at 286, ν_{10} (A_1), and 258, ν_{28} (E), respectively. Even though the frequency of the symmetric mode decreases the CPC force constant is found to increase.

BH_3 Modes. In the "light" compound the symmetric, ν_3, and the antisymmetric, ν_{19}, BH_3 stretching modes form a broad strong band with two distinct maxima. On deuteration, the antisymmetric mode shifts from 2362 to 1772 cm^{-1}. The symmetric stretch, which is observed at 2335 cm^{-1} in the "light" compound and at 1668 cm^{-1} in the deuterated molecule, shows a larger isotopic shift. Bands in the "light" compound at 1133 and 1069 cm^{-1} are observed to shift to 831 and 849 cm^{-1}, respectively, on deuteration. The bands at 1133 and 831 cm^{-1} are assigned to the antisymmetric BH_3 and BD_3 deformation, respectively, and the bands at 1069 and 849 cm^{-1} are assigned to the corresponding symmetric motion. The BH_3 rocking mode is observed to shift from 888 to 692 cm^{-1} with deuteration. The isotopic shift factors for these three bending modes are 1.37, 1.26, and 1.28 for the antisymmetric and symmetric BH_3 deformations and the BH_3 rock, respectively.

P–B Stretch and CPB Bend. The P–B stretch is observed as a doublet. One band is centered at 571 cm^{-1} and shifts to 526 cm^{-1} on deuteration and a second one, one-fourth as intense as the first, is centered at 583 cm^{-1} and shifts to 533 cm^{-1} upon deuteration. The measured isotopic shifts are less than theoretical as would be expected, since the P–B stretch is strongly mixed with the C–P symmetric stretching motion. The CPB bending mode observed at 211 cm^{-1} in the light compound shifts to 190 cm^{-1} with deuteration.

The methyl torsion of E symmetry and none of the five vibrations with A_2 symmetry were observed. For the Lewis base the two methyl torsions were observed at 268 (E) and 223 cm^{-1} (A_2) in the Raman spectrum of the solid. The degenerate methyl torsion could easily be obscured by the degenerate skeletal deformation in the adduct, whereas both the A_2 methyl and borane torsional modes could lie under the strong CPB bending motion at 211 and 190 cm^{-1} in the "light" and "heavy" molecules, respectively. The band is skewed to the high-frequency side, but it was not possible to resolve a shoulder.

The BH_3 torsion was found to have a frequency of 197 ± 5 cm^{-1} in the F_3PBH_3 molecule from which a barrier of

TABLE II: Observed and Calculated Vibrational Frequencies for $(CH_3)_3PBD_3$[a]

$(CH_3)_3PBD_3$		$(CH_3)_3P$[b]		$(CH_3)_3PBD_3$	
Infrared ν, cm^{-1}	Raman ν, cm^{-1}	Infrared ν, cm^{-1}	Raman ν, cm^{-1}	calcd, cm^{-1}	Assignment and approximate description
		2988		2983	
2982 vw	2982 vs	2978	2969	2982	ν_1 (A_1), ν_{16} (E), ν_{17} (E) CH_3 antisymmetric stretch (100%)
		2968		2983	
		2915			
2913 w	2912 vs	2900	2894	2913	ν_2 (A_1), ν_{12} (E) CH_3 symmetric stretch (100%)
		2890		2913	
1789 s	1793 m			1792	ν_{19} (E) $^{10}BD_3$ antisymmetric stretch (100%)
1772 vs	1777 s			1771	ν_{19} (E) $^{11}BD_3$ antisymmetric stretch (100%)
1717 s	1721 s				
1677 w	1681 w				
1665 m	1668 m			1669	ν_3 (A_1) BD_3 symmetric stretch (100%)
	1629 m				
1428 m		1441		1420	ν_{20} (E)
1419 s		1430	1421	1419	ν_{21} (E) CH_3 antisymmetric deformations (100%)
1412 m		1416		1420	ν_4 (A_1)
1301 m	1312 w	1312	1312	1306	
		1297			ν_{22} (E) CH_3 symmetric deformations (100%)
					ν_5 (A_1)
		1283	1293	1294	
989 vs			973	988	ν_7 (A_1) CH_3 rock (95%)
960 m	952 w	953		969	ν_{24} (E) CH_3 rock (95%)
944 vs		940		941	ν_{25} (E) CH_3 rock (100%)
		935			
872 vs					
865 s				869	ν_6 (A_1) $^{10}BD_3$ symmetric deformation (80%) and P–B stretch (20%)
849 vs	845 w			850	ν_6 (A_1) ^{11}BD symmetric deformation (80%) and P–B stretch (20%)
	831 w			821	ν_{23} (E) BD_3 antisymmetric deformation (100%)
		716			
756 s	759 s	709	708	760	ν_{27} (E) C_3P antisymmetric stretch (92%)
		706			
692 s	693 s		653	689	ν_8 (A_1) C_3P symmetric stretch (90%)
				678	ν_{26} (E) BD_3 rock (90%) and C_3P antisymmetric stretch (10%)
	632 w				?
533 m	533 m			540	ν_9 (A_1) P–^{10}B stretch (70%) and C_3P symmetric stretch (30%)
526 vs	526 vs			530	ν_9 (A_1) P–^{11}B stretch (70%) and C_3P stretch (30%)
283 w	286 s	305*		283	ν_{10} (A_1) C_3P symmetric deformation (90%)
256 m	261 s	287*		257	ν_{28} (E) C_3P antisymmetric deformation (100%)
190 vs	188 ms			192	ν_{30} (E) BPC_3 bend (95%)
95 w					lattice mode
	43 m				lattice mode

[a,b] See corresponding footnotes to Table I.

3.24 ± 0.15 kcal/mol was calculated.[3] In a recent investigation of H_3PBH_3 the barrier to internal torsion was found to be 2.47 ± 0.05 kcal/mol with a corresponding frequency of 225 cm^{-1}. We had hoped to compare the barrier to internal rotation of the BH_3 group for the $(CH_3)_3PBH_3$ molecule to those previously reported by observing the BD_3 torsion, but the site symmetry in the crystal apparently was not sufficient to activate this A_2 mode. Product rule calculations were used to test the assignments of both the A_1 and E symmetry species.

Normal Coordinate Calculations

The calculation of the normal coordinates was undertaken as an aid in describing the fundamental vibrations. The analysis was made using the Wilson *GF*-matrix method[16] and programs written by Schachtschneider.[17] The *G* matrix was calculated using structural parameters determined by Bryan and Kuczkowski.[2b] The frequencies were weighted by $(1/\lambda)$ in the least-squares routine. Initial force constants for the CPC angle and C–P stretch were taken from the published values of Rosenbaum, *et al.*[18] The initial force constants for the P–B stretch and BH_3 motions were taken from the work of Berschied and Purcell.[19] Typical values for the methyl group force constants were selected from the work of Duncan.[20] An initial force field of 24 force constants was employed to fit 54 frequencies. Since the $J'WJ$ matrix is important to the calculation of least-squares fit, the determinant of the matrix was tested for singularity after each iteration and the magnitude compared to the trace of the matrix as described by Schachtschneider.[17] The calculated frequencies for $(CH_3)_3PBH_3$ and $(CH_3)_3PBD_3$ are listed in Tables I and II with average errors of 0.3 and 0.4%, respectively. In the calculation of the final force field, only the 22 force constants (Table III) with magnitudes greater than 0.02 mdyn/Å were used. The following interaction force constants were included in some of the initial calculations, but were found not to appreciably improve the fit: F_Q, F_β, F_δ,

TABLE III: Internal Force Constants for $(CH_3)_3PBH_3$ and $(CH_3)_3PBD_3$

Force constant	Group	mdyn/Å²
K_R	P–B stretch	2.37 ± 0.02
K_Q	P–C stretch	3.65 ± 0.02
K_r	B–H stretch	2.986 ± 0.006
K_q	C–H stretch	4.782 ± 0.004
H_α	<CPC bend	0.92 ± 0.01
H_β	<CPB bend	0.55 ± 0.01
H_γ	<HBH bend	0.375 ± 0.002
H_δ	<PBH bend	0.622 ± 0.003
H_σ	<HCH bend	0.499 ± 0.002
H_ρ	<PCH bend	0.595 ± 0.002
F_q	C–H stretch/C–H stretch	0.054 ± 0.002
F_r	B–H stretch/B–H stretch	0.088 ± 0.003
F_{RQ}	P–B stretch/P–C stretch	0.04 ± 0.01
$F_{R\beta}$	P–B stretch/<CPB bend	0.33 ± 0.04
$F_{R\delta}$	P–B stretch/<PBH bend	0.244 ± 0.06
$F_{Q\rho}$	P–C stretch/<PCH bend	0.608 ± 0.005
F_α	<CPC bend/<CPC bend	0.085 ± 0.09
$F_{Q\alpha}$	P–C stretch/CPC bend	−0.28 ± 0.02
$F_{Q\beta}$	P–C stretch/CPB bend	−0.05 ± 0.03
$F_{Q\delta}$	P–C stretch/HBP bend	0.16 ± 0.02
$F_{\beta\delta}$	CPB bend/HBP bend	0.15 ± 0.02
$F_{\beta\rho}$	CPB bend/HCP bend	0.07 ± 0.01

F_ϕ, $F_{\alpha\phi}$, $F_{\gamma\delta}$, and $F_{\alpha\beta}$. The ten principle force constants during the latter stages of refinement were invariant to changes in the interaction force constants.

The methyl force constants associated with the CH_3 stretch and <HCH are comparable to those calculated for the hydrocarbons. The increase in the C–P stretching force constant from 2.78[18] to 3.65 mdyn/Å in the adduct is partially attributed to the decrease in the P–C bond length associated with the opening of the CPC angle. The P–B force constant of 2.37 mdyn/Å is significantly larger than the 2.04 mdyn/Å reported[19] for this constant in the H_3PBH_3 molecule. In our calculation we used both the ^{10}B and ^{11}B data, whereas the calculation on the H_3PBH_3 molecule was done without isotopic data and a HOVFF was used. The P–B force constant (valence force field) in F_3PBH_3 was found[21] to be 2.46 mdyn/Å. It is unfortunate that the P–B force constant for the H_3PBH_3 molecule has not been calculated from the same force field as the other two molecules, but if it is assumed that it would not be significantly different for a simple valence force field one can compare the force constants and bond lengths for these molecules. The P–B bond length[4] of 1.937 Å in H_3PBH_3 is the longest of the three compounds and the force constant is the smallest. Phosphine–borane is completely dissociated at ambient temperature and it is considerably less stable than trimethylphosphine–borane[2b] which has a P–B bond distance of 1.90 Å. Thus, the P–B force constants for these two molecules reflect both the bond lengths and adduct stabilities. However, when one compares the P–B force constant of 2.46 mdyn/Å for F_3PBH_3 with the extremely short P–B bond length[3] of 1.836 Å the value seems quite low. This bond length is similar to P–C bond lengths and one would expect comparable force constant values. Since trifluorophosphine–borane is extensively dissociated at 0°, this low force constant value may reflect the stability of this adduct. Thus, with this limited amount of data, it appears that there may be a correlation of the P–B force constant with the adduct stabilities.

The PED indicated that the only significant vibrational coupling was between the P–C and P–B stretching modes for the "light" molecule. However, for the $(CH_3)_3PBD_3$ molecule, there was some coupling among the BD_3 bending modes with the CH_3 rock and the P–B stretch.

Discussion

It appears that the fundamental vibrations for these adducts can be reasonably well predicted from the normal vibrations of the individual Lewis base along with the "group frequencies" of the BH_3 moiety. The major change resulted from the shortening of the P–C bond with coordination which was also accompanied by an opening of the CPC angle.

On the basis of the $P4/nmm \equiv D_{4h}^7$ crystal symmetry with the two molecules occupying D_{2d} sites, the optical and acoustical translations span the $B_{1g} + E_g$ = OT and $E_u + A_{2u}$ = AT, respectively. Thus, only one translational lattice mode should be observed in either spectrum and it is the E_g mode which should be Raman active. A weak, relatively sharp Raman line was observed at 43 cm^{-1} which is tentatively assigned to this translational mode. The six librations have $A_{2g} + B_{1u} + E_g + E_u$ symmetry with the E_u and E_g being active in the infrared and Raman spectra, respectively. The infrared band at 95 cm^{-1} is tentatively assigned to the E_u librational mode which is consistent with the general observation that the librational modes are at a higher frequency than the translational modes.

Thomas[13] reported a phase change at −22° but no evidence could be found for a spectral change in either the Raman intermolecular or intramolecular modes. The explanation for the failure to observe any spectral changes with phase transition is not readily apparent.

Trimethylphosphine–borane satisfies Timmermans' criteria[22] of globular structure which frequently leads to the formation of a plastic crystal. It is quite possible that the high-temperature disorder phase is plastic in nature. Further physical studies on this crystal would be interesting.

Acknowledgment. The authors gratefully acknowledge the financial support of this work by the National Science Foundation by Grant No. GP-33780.

References and Notes

(1) (a) For part II, see J. D. Odom, S. Riethmiller, J. D. Witt, and J. R. Durig, *Inorg. Chem.*, **12**, 1123 (1973). (b) Taken in part from the thesis of B. A. Hudgens to be submitted to the Department of Chemistry in partial fulfillment of the Ph.D. degree.
(2) (a) A. B. Burg and R. I. Wagner, *J. Amer. Chem. Soc.*, **75**, 3872 (1953); (b) P. S. Bryan and R. L. Kuczkowski, *Inorg. Chem.*, **11**, 553 (1972).
(3) R. L. Kuczkowski and D. R. Lide, Jr., *J. Chem. Phys.*, **46**, 357 (1967).
(4) J. R. Durig, Y. S. Li, L. A. Carreira, and J. D. Odom, *J. Amer. Chem. Soc.*, **95**, 2491 (1973).
(5) D. F. Shriver, "The Manipulation of Air-Sensitive Compounds," McGraw-Hill, New York, N. Y., 1969.
(6) J. Dobson and R. Schaeffer, *Inorg. Chem.*, **9**, 2183 (1970).
(7) W. J. Lehman, C. O. Wilson, J. F. Ditter, and I. Shapiro, *Advan. Chem. Ser.*, **No. 32**, 139 (1961).
(8) I. Shapiro, C. O. Wilson, J. F. Ditter, and W. J. Lehman, *Advan. Chem. Ser.*, **No. 32**, 127 (1961).
(9) R. T. Hall and J. M. Dowling, *J. Chem. Phys.*, **47**, 2454 (1967); **52**, 1161 (1970).
(10) F. G. Baglin, S. F. Bush, and J. R. Durig, *J. Chem. Phys.*, **47**, 2104 (1967).
(11) IUPAC, "Tables of Wavenumbers for the Calibration of Infrared Spectrometers," Butterworths, Washington, D. C., 1961.
(12) F. A. Miller and B. M. Harney, *Appl. Spectrosc.*, **24**, 291 (1970).
(13) R. Thomas, *Diss. Abstr.*, **26**, 3069 (1965).
(14) P. J. D. Park and P. J. Hendra, *Spectrochim. Acta, Part A*, **24**, 2081 (1968).

(15) (a) D. R. Lide and D. E. Mann, *J. Chem. Phys.*, **29**, 914 (1958); (b) J. R. Durig, S. M. Craven, and J. Bragin, *J. Chem. Phys.*, **53**, 38 (1970).
(16) E. B. Wilson, J. C. Decius, and C. Cross, "Molecular Vibrations, The Theory of Infrared and Raman Vibrational Spectra," McGraw-Hill, New York, N. Y., 1955.
(17) J. H. Schachtschneider, Technical Report No. 231-64 and 57-65, Shell Development Company.
(18) E. J. Rosenbaum, D. J. Rosenbaum, D. J. Rubin, and C. R. Sandberg, *J. Chem. Phys.*, **8**, 366 (1940).
(19) J. R. Berschied, Jr., and K. F. Purcell, *Inorg. Chem.*, **11**, 930 (1972).
(20) J. L. Duncan, *Spectrochim. Acta*, **20**, 1197 (1964).
(21) S. J. Meischen, Ph.D. Thesis, University of South Carolina, 1972.
(22) J. Timmermans, *J. Phys. Chem. Solids*, **18**, 1 (1961).

Far-Infrared Spectra and Barrier to Internal Rotation of Ethanethiol

A. S. Manocha,[1]

Mellon Institute of Science, Carnegie-Mellon University, Pittsburgh, Pennsylvania 15213

W. G. Fateley,*

Department of Chemistry, Kansas State University, Manhattan, Kansas 66506

and T. Shimanouchi

Department of Chemistry, Faculty of Science, The University of Tokyo, Bunkyo-ku, Tokyo, Japan *(Received March 26, 1973)*

Publication costs assisted by Kansas State University

Far-infrared spectra of CH_3CH_2SH and CH_3CH_2SD have been examined in the vapor phase. SH torsional frequencies corresponding to different rotamers are observed. Doublets are observed for the torsional fundamental vibrations of the light and for the hot bands (*i.e.*, $1 \rightarrow 2$ transition) of the heavy molecule in the gauche conformation. The barrier to internal rotation has been calculated using one-dimensional theory and a potential expanded in a Fourier cosine series. Good agreement between the calculated and observed frequencies is obtained with a potential of the form $V(\alpha) = -[43\ (+22)/2](1 - \cos\alpha) - [137\ (\pm7)/2](1 - \cos 2\alpha) + [474\ (\pm2)/2](1 - \cos 3\alpha) - [13\ (\pm1)/2](1 - \cos 6\alpha)$. Methyl torsional frequencies are observed at 247.5, 233.5, and 220.5 cm^{-1} in the light molecule. The barrier to internal rotation around the C–C bond is calculated to be 1359 ($\pm$16) cm^{-1}.

Introduction

In recent years, internal rotation around single bonds has attracted a great deal of attention and research efforts because of its importance in elucidating the nature of nonbonded forces. Such studies should lead to a better understanding of chemical reactivity and conformations found in macromolecules. However, most of the work till now has been on molecules with symmetric rotors, mainly, CH_3, CX_3 (X = F, Cl). The real challenge remains in understanding internal rotation and potential energy shapes in molecules containing asymmetric rotors. Recently a number of microwave studies have reported some results on molecules with asymmetric rotors. A complete compilation of these studies can be found in a recent review article by Wilson.[2] However, it is apparent that the potential function has been fully characterized in only a limited number of cases. Frequently, these measurements are accompanied by large uncertainties in the calculated barrier parameters. The large errors arise because the microwave measurements rely heavily on calculations of torsional levels from intensities of rotational lines, whereas vibrational transitions observed in the infrared and Raman spectra provide a direct and more accurate measure of these energy levels.

To better characterize the shape of the potential function for asymmetric top molecules, the observation of hot bands is required. These hot bands allow the precise description of the energy levels approaching very closely to the maximum in the barrier thereby allowing a very accurate characterization of the torsional potential. Such has been the case for ethyl chloride and a limited number of other molecules. For this reason, ethanethiol serves as an excellent choice for the barrier description about the C–S bond since its rich far-infrared spectrum provides sufficient data to allow the accurate determination of the potential hindering internal rotation. Furthermore, the observation of methyl torsional frequencies provides an accurate value of the barrier to internal rotation around the C–C bond in ethanethiol.

Method of Calculation

The torsional vibrational mode can be simply separated from the other intramolecular modes where intramolecular mixing is not present. (In the case of ethanethiol, Shi-

manouchi and workers have shown that the -SH and -SD torsional frequency is virtually uncoupled from any other intramolecular mode.[3] Note this may not be true for the CH_3 torsion which is discussed later in this paper.) A one-dimensional approximation of the torsional Hamiltonian can be written as

$$H = p_\alpha F(\alpha) p_\alpha + V(\alpha) \quad (1)$$

where α = torsional angle, p_α = momentum conjugate to α and is equal to $-i\hbar(\mathrm{d}/\mathrm{d}\alpha)$, and $F(\alpha)$ = one-half the effective inverse moment of inertia.

For the special case of a molecule possessing a plane of symmetry at $\alpha = 0$, we can expand $F(\alpha)$ and $V(\alpha)$ in the following cosine series

$$F(\alpha) = F_0 + F_1 \cos\alpha + F_2 \cos 2\alpha + F_3 \cos 3\alpha + \cdots \quad (2)$$

$$V(\alpha) = \frac{V_1}{2}(1 - \cos\alpha) + \frac{V_2}{2}(1 - \cos 2\alpha) + \frac{V_3}{2}(1 - \cos 3\alpha) + \cdots \quad (3)$$

V_i represent the Fourier coefficients of the series and describe the shape of the barrier to internal rotation. Most potential functions are adequately described by the first three terms, *i.e.*, V_1, V_2, and V_3 of eq 3 and an additional higher order term may be evaluated when the spectrum is rich in hot bands. However, in cases where there is a symmetric CX_3 rotor, and V_1, V_2, V_4, V_5 are zero, one often needs only V_3 and possibly the next symmetry-allowed V_6 term.[4]

$F(\alpha)$ is determined from the geometry of the molecule. Only in special cases of the symmetric top where the center of gravity of the top is found on the rotor axis will $F(\alpha)$ be independent of the angle α. Such is the case for rotation around C-C bond.

The quantum mechanical form for the first term, $p_\alpha F(\alpha) p_\alpha$, in eq 1 is

$$\frac{1}{2}[p_\alpha^2 F(\alpha) + F(\alpha) p_\alpha^2] + f(\alpha)$$

Here $f(\alpha)$ represents the pseudo potential which is indistinguishable from the actual potential $V(\alpha)$. The magnitude of $f(\alpha)$ is very small compared to the other terms in eq 1 and, therefore, is neglected in the torsional equation.

The potential parameters, V_i, are determined by solving the torsional equation numerically using free rotor basis. These basis functions can be further reduced to sine and cosine terms. To expediate the solution it is desirable to choose the initial set of parameter values close to the real solution. These parameters, chosen *a priori*, are then iterated to fit the observed frequencies. Convergence of calculated *vs.* the observed torsional frequencies is achieved very rapidly from this program.

Experimental Section

Ethanethiol was obtained from the Aldrich Chemical Co. The compound was dried by passing through Linde 3-Å molecular sieves in a vacuum line. CH_3CH_2SD was prepared from CH_3CH_2SH by the procedure described in ref 5. The deuterated compound was finally dried by letting it stand over preheated molecular sieves overnight.

The far-infrared spectra of CH_3CH_2SH and CH_3CH_2SD were recorded on a Digilab FTS-14 Fourier transform spectrometer operating in the double beam mode. A 6-μ Mylar beam splitter was used to cover the range 300–100 cm^{-1}. A piece of black polyethylene was used to filter out the unwanted higher frequency output of the mercury lamp. A 10-cm gas cell equipped with polyethylene windows was used for the vapor studies. The resolution of the instrument was better than 0.5 cm^{-1} throughout the region and the frequencies are accurate to ±0.2 cm^{-1}. A triangular apodization function was used in transforming the interferograms.

Figure 1. Far-infrared spectrum of CH_3CH_2SH (pressure, 180 Torr; path length, 10 cm).

The far-infrared spectrum of CH_3CH_2SH is shown in Figure 1. The band at 192 cm^{-1} of the light molecule shows rotational fine structure. Further, the Q branch of this band was found to be split by 1.2 cm^{-1}. Another distinct band appears at 158 cm^{-1}. The bands on the higher frequency side are in the expected region for methyl torsion but could not be confirmed in the spectrum of the deuterated compound. This appears to be a common feature in other compounds such as ethylamine, isopropylamine, *tert*-butylamine, and 2-propanethiol which have also been investigated in this laboratory and will be reported in another publication. Three sharp bands were observed in the -SD torsional region of the heavy molecule and the band at 134 cm^{-1} was also found to be split by 1.1 cm^{-1} as shown in Figure 2.

Interpretation

Internal Rotation around C-S Bond. Ethanethiol may be expected to appear in three stable conformations, a trans and two equivalent gauche forms as shown

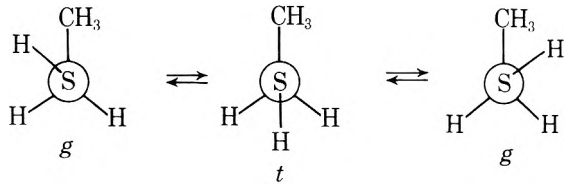

Smith, Devlin, and Scott[6] recorded the mid-infrared spectrum of the compound in the gas phase and noted that it was remarkably similar to that of CH_3CH_2Cl with the exception of those bands involving the -SH group. They examined the spectra in glass, liquid, and crystalline states in search of evidence indicating the presence of a second rotamer. The spectrum of the crystalline form differed slightly from those of the glass and liquid by only one weak band at 783 cm^{-1}. This band appeared in the glass and liquid spectra but disappeared on crystallization; hence it was concluded by these investigators that it could not be due to a combination band as it appeared in

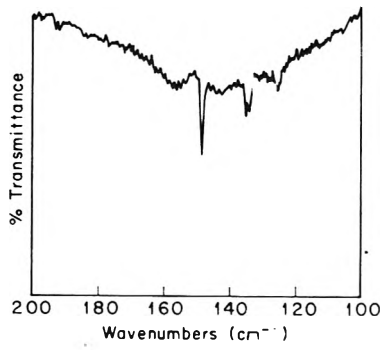

Figure 2. Far-infrared spectrum of CH_3CH_2SD (pressure, 180 Torr; path length, 10 cm).

glass even at liquid nitrogen temperatures. Smith, *et al.*,[6] chose to assign the absorption at 783 cm^{-1} to the $-CH_2$ rocking mode of the less stable form while the same vibrational mode for the more stable isomer was assigned to a lower frequency at 737 cm^{-1}. They attributed the lower frequency of the latter to interaction with the C–S–H bending mode and used arguments regarding the mixing of modes to distinguish the more stable form of C_1 symmetry (gauche) from the less stable form with C_s symmetry (trans). The energy difference between the two forms by heat capacity measurements was estimated to be 100 cm^{-1}.

In addition, Scott and Crowder[7] recorded the far-infrared spectrum and observed only one band at 191 cm^{-1} belonging to –SH torsion. From the calculated band envelopes and calorimetric data of Smith, *et al.*,[6] Shimanouchi and coworkers[3] assigned the bands at 190 and 158 cm^{-1} as due to the gauche and trans forms, respectively. Our observation at higher resolution capability which found the splitting of the 192-cm^{-1} band due to tunnelling between the two equivalent gauche conformations, confirms their assignment for this band. The 158-cm^{-1} band, which is too high in frequency to be a hot band of the gauche form but demonstrates shift upon deuteration, is assigned to the fundamental of the trans rotamer. The maximum of the P branch of the gauche fundamental in the heavy molecule appears at 142.5 cm^{-1} (see Figure 2). The sharp band at 134 cm^{-1}, which is also found to be split, is assigned to the hot bands of the gauche form. The magnitude of the splitting of this band agrees with that predicted by Shimanouchi and coworkers.[3] We note that this cannot be the R branch envelope of the hot band, 1 → 2, representing the gauche rotamer, for by comparison the P–R structure of the gauche fundamental, we can expect these shoulders to be weak.

Using the same value of $F(\alpha)$ as reported by Shimanouchi and coworkers[3] and the procedure previously discussed, a potential function was determined to fit the experimentally observed frequencies of the *heavy molecule*. A small V_6 term was necessary to explain the anharmonicity of the gauche well. The iteration was achieved in three cycles starting from initial guestimates of V_1 = 10.0, V_2 = 10.0, and V_3 = 500.0 cm^{-1}. The final set of iterated values for the potential terms are $V_1 = -43$ (±22), $V_2 = -137$ (±7), $V_3 = 474$ (±2), and $V_6 = -13$ (±1) cm^{-1}. To check these potential terms, the same potential function was then used to calculate the torsional frequencies for the light molecule. The observed and calculated values agree very well and are given in Table I along with their assignments. The gauche frequencies are reproduced very

TABLE I: Torsional Frequencies (in cm^{-1}) of Ethanethiols. Observed *vs.* Calculated and Assignments

	Transition	Obsd	Calcd
	CH_3CH_2SH		
g	$0_+ \rightarrow 1_-$	193.0	193.0
g	$0_- \rightarrow 1_+$	191.8	191.8
t	$0 \rightarrow 1$	158.0	160.5
	CH_3CH_2SD		
g	$0_\pm \rightarrow 1_\pm$	148.5	148.5
g	$1_+ \rightarrow 2_-$	135.1	135.1
g	$1_- \rightarrow 2_+$	134.0	134.0
t	$0 \rightarrow 1$	125.0	125.0

well and the discrepancy of 2.5 cm^{-1} in the trans fundamental of the light molecule can be attributed mainly to the approximate structure used in the calculation of *F*.

The appearance of the methyl torsion in only the light molecules suggests a coupling of this vibration with another intramolecular mode. The fact that the methyl torsion does not appear in the CH_3CH_2SD, where the –SD torsion moves to a lower frequency and farther away from the $-CH_3$ torsional frequency, indicates that the thiol torsion is the source of this intensity enhancement for the methyl torsion. In the normal coordinate analysis by Shimanouchi, *et al.*,[3] such a coupling could not be ruled out from consideration. However, the excellent fit between the observed –SH torsional frequencies and those calculated utilizing the potential constants determined from the –SD torsional frequencies (Table I) strongly suggest that these cross terms between the –SH and the $-CH_3$ torsion are small and unimportant. (Preliminary investigation by Tsuboi (University of Tokyo) and in our laboratories suggest that cross terms will be very important in interpretating the torsional frequencies in $CH_3CH_2NH_2$ and deuterated derivatives.) Thus, the problem of internal rotation can be treated adequately as two separate one-dimensional torsions. It should be noted that the potential terms evaluated by this treatment may have small effective contributions resulting from neglecting these cross terms. It is hoped in future investigation, *e.g.*, $CH_3CH_2NH_2$ and the deuterated derivative, that there will be adequate data to describe the coupling in rotors. Unfortunately, the limited data found here do not allow such an evaluation of cross terms.

The calculated potential energy curves and the torsional energy levels are shown in Figure 3. From the potential curve the energy difference between the gauche and trans forms is found to be 123.0 cm^{-1} and the gauch form has a dihedral angle of 117°.

Internal Rotation around C–C Bond. Three weak absorption bands appear at 247.5, 233.5, and 220.5 cm^{-1} in the light molecule. The absorption maximum at 247.5 cm^{-1} is assigned to the methyl torsional fundamental. This series of torsional frequencies are very similar to the torsional frequency observed for ethyl chloride[4] at 250.5, 237, and 215 cm^{-1}. The spacings between the observed transitions suggest that 233.5- and 220.5-cm^{-1} bands belong to the upper-stage transitions, *i.e.*, hot bands, of the fundamental frequency at 247.5 cm^{-1}. The observation of only one series of torsional frequencies may be due to (i) an overlap of the methyl torsional frequencies of the two rotamers or (ii) that the methyl torsion is just not observed for the second rotamer. Previous studies on *n*-pro-

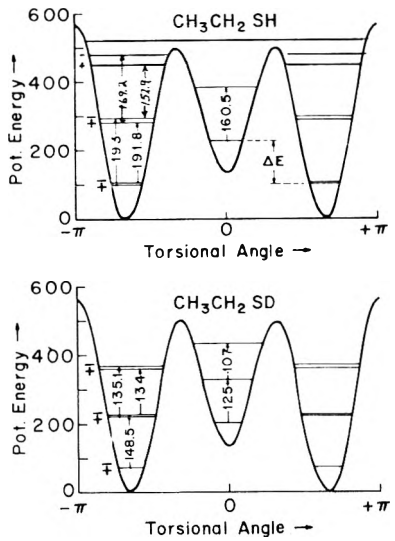

Figure 3. Calculated potential energy function and torsional energy levels of CH_3CH_2SH and CH_3CH_2SD.

TABLE II: Methyl Torsional Frequencies (in cm^{-1}) of Ethanethiol. Observed *vs.* Calculated and Assignments[a]

Transition	ν_{obsd}	ν_{calcd}
0 → 1	247.5	247.0
1 → 2	233.5	234.5
2 → 3	220.5	220.0

[a] F = 5.8579 cm^{-1}; V_3 = 1359 (±16) cm^{-1}; V_6 = −24 (±8) cm^{-1}.

pyl halides[8,9] indicate that the methyl torsional barriers for the two rotamers are very similar. Therefore the orientation of the $-CH_2X$ group demonstrates little effect on the barriers and this is observed in our studies on ethanethiol. Also F shows very little dependence on the rotamer form as shown by the following values: F_{gauche} = 5.8579; F_{trans} = 5.9233 cm^{-1}. A potential with V_3 and V_6 terms was determined to fit the observed frequencies (see Table II).

A few model calculations were carried out to study the effect of variation of F on the potential terms. The calculations were made by varying the value of F in steps of 0.2 cm^{-1} and then iterating V_3 and V_6 to obtain the best fit with the experimental frequencies. The results are shown in Table III. The calculations clearly demonstrate that the potential terms are heavily dependent upon the value of F used in the calculations and one should be quite cautious in interpreting the potential terms obtained from poorly determined molecular structure. Fortunately, the value of F is insensitive to minor uncertainties in the structural parameters of the framework for a methyl top and the previously determined value of V_3 is relatively unchanged by further refinements in the geometrical parameters of the framework.

Higher Order Terms. In the case of rotors with threefold symmetry, only the V_3 term of the potential function can be evaluated when we are limited to observing the fundamental torsional frequency. However, in cases where a spectrum rich in hot bands is observed, one sometimes finds different values of V_3 calculated from these different transitions.[4] Of course, there must be only one value of V_3. These differences in the values of V_3 cannot be accounted for by changes in the geometry, *i.e.*, adjustments

TABLE III: Potential Terms for Different Assumed Values of F (cm^{-1})

F	V_3	V_6	Δ^a
6.2	1315.6	−31.2	1.8
6.0	1340.8	−26.9	1.6
5.8579[b]	1359.1	−23.5	1.5
5.8	1366.8	−22.1	1.4
5.6	1393.7	−16.8	1.2
5.4	1421.4	−10.8	1.1

[a] $\Delta = \Sigma_i(\nu_i^{calcd} - \nu_i^{obsd})^2$. [b] Calculated from structure in the gauche form.

of F alone. Inclusion of the higher order term, V_6, is found to be very effective in bringing the values of V_3 in closer agreement. Small values of V_6, which represent a distortion of the potential well from parabolic shape have been reported in the literature.[10] The exact physical significance of these reported values is not clear because many factors can give a V_6 term, such as: (1) inaccuracy in the value of F used, resulting from a poorly determined molecular geometry which could be more serious in asymmetric rotors as discussed above; (2) variation of F for the different torsional levels, which actually has been found to be quite small in a few cases studied extensively; (3) nonrigid effects, *e.g.*, an opening of the HCH angle in the CH_3 group;[11] (4) inaccuracies in the exact location of the Q branch centers; the potential parameters are found to be very sensitive to the exact values of the torsional frequencies; and (5) neglect of the interactions or coupling with other vibrations.

Considering the factors which can lead to the higher order term even in the simple case of a symmetric rotor, it is very difficult to give an exact physical meaning to the V_6 terms obtained in ethanethiol except that experimental evidence shows that there is such a term present in the potential energy surface.

Discussion

The barrier to internal rotation around the C-C bond in ethanethiol (V_3 = 1359 cm^{-1}) is greater than that in ethane[12] (1028 cm^{-1}) and is very close to that determined for ethyl chloride[4] (1290 cm^{-1}).

The threefold term for barriers around the C-S bond in ethanethiol (V_3 = 474 cm^{-1}) is found to be similar to the value of 444 cm^{-1} reported[13-16] for methanethiol. It is the most predominant term in the potential corresponding to trans and gauche conformations. Negative values of both V_1 and V_2 reflect a stabilization of the gauche conformation more than trans.

Acknowledgments. The work has been supported in part by funds from the National Science Foundation (GP-22943). The authors acknowledge the free computer time provided by the Mellon Institute NMR Facility for Biomedical Research (NIH Grant - RR00292). A. S. M wishes to thank Dr. E. C. Tuazon for his assistance and helpful discussions.

References and Notes

(1) Work presented in this paper represents a portion of the thesis to be submitted to Carnegie-Mellon University in partial fulfillment of the requirements for Doctor of Philosophy degree in the Chemistry Department.

(2) E. B. Wilson, *Chem. Soc. Rev.*, **1**, 293 (1972).
(3) F. Inagaki, I. Harada, and T. Shimanouchi, *J. Mol. Spectrosc.*, in press.
(4) W. G. Fateley and F. A. Miller, *Spectrochim. Acta*, **19**, 611 (1963).
(5) A. Murray, III, and D. L. Williams, Ed., "Organic Synthesis with Isotopes," Interscience, New York, N.Y., 1958, Part II, p 1341.
(6) D. Smith, J. P. Devlin, and D. W. Scott, *J. Mol. Spectrosc.*, **25**, 174 (1968).
(7) D. W. Scott and G. A. Crowder, *J. Mol. Spectrosc.*, **26**, 477 (1968).
(8) K. Radcliffe and J. L. Wood, *Trans. Faraday Soc.*, **62**, 1678 (1966).
(9) E. Hirota, *J. Chem. Phys.*, **37**, 283 (1962).
(10) J. P. Lowe, *Progr. Phys. Org. Chem.*, **6**, 1 (1968).
(11) C. S. Ewig and D. O. Harris, *J. Chem. Phys.*, **52**, 6268 (1970).
(12) S. Weiss and G. E. Leroi, *J. Chem. Phys.*, **48**, 962 (1968).
(13) B. Kirtman, *J. Chem. Phys.*, **37**, 2516 (1962).
(14) T. Kojima and T. Nishikawa, *J. Phys. Soc. Jap.*, **12**, 680 (1957).
(15) N. Solimene and B. P. Dailey, *J. Chem. Phys.*, **23**, 124 (1955).
(16) J. L. Binden, *J. Chem. Phys.*, **17**, 499 (1949).

Size Effect of Ions in Polyelectrolytes

Kunihiko Iwasa

Department of Physics, Faculty of Science, Nagoya University, Chikusa-ku, Nagoya 464, Japan *(Received November 2, 1972; Revised Manuscript Received February 13, 1973)*

A formulation considering most simply the size of low molecular weight ions in polyelectrolyte systems was given and was compared with the results of titration experiments of polyacrylic acid. It was shown that this new equation yields better agreement with experiment than the Poisson-Boltzmann equation does.

Though the size effect of ions, especially of quaternary ammonium ions, in polyelectrolytes is known experimentally,[1] only little theoretical treatment has been reported. The difficulty lies in the complexity of the equation which describes the system. I wish to report here the effect of the ionic size considered on the basis of the two-body distribution function of low molecular weight ions.

Let us consider the system of volume V in which a polyion occupies a fixed place and there are N small ions of different species. The number of the αth species is N_α. The total potential energy is then written as the sum of the interaction potential v_α between the polyion and the αth ion species. The interaction potentials $u_{\alpha\gamma}$ and v_α are low molecular weight ion species

$$U = \sum_\alpha \sum_j v_\alpha(x_\alpha^j) + \sum_{\alpha\gamma} \sum_{j,l} u_{\alpha\gamma}(x_\alpha^j, x_\gamma^l) \tag{1}$$

where x_α^j is the coordinate of the jth ion particle of the αth ion species. The interaction potentials $u_{\alpha\gamma}$ and v_α are expressed by

$$v_\alpha(x) = \int dx' Z_\alpha \rho_p(x')/(\epsilon|x - x'|) + v_\alpha^*(x)$$

$$u_{\alpha\gamma}(x, x') = Z_\alpha Z_\gamma/(\epsilon|x - x'|) + u_{\alpha\gamma}^*(x, x')$$

where z_α is the charge of the αth ion species, ρ_p is the charge distribution in the polyion, the asterisk denotes the non-Coulombic part, and ϵ is the dielectric constant of the solvent. The number density n_α of the αth species is expressed by the integral

$$n_\alpha(x) = (N_\alpha Q_N) \int d\{N - 1\} \exp(-\beta U)|_{x_\alpha^1 = x}$$
$$Q_N = \int d\{N\} \exp(-\beta U) \tag{2}$$

where β is equal to $1/kT$ and $d\{N - 1\}$ denotes the phase integral except for x_α^1, which is equal to x. The mean force potential of the αth species $W_\alpha(x)$ is defined by

$$n_\alpha(x) = N_\alpha Q_N^{-1} \exp[-\beta W_\alpha(x)] \tag{2'}$$

Similarly, the density of the αth species at x and the γth species at x' is

$$n_{\alpha\gamma}(x, x') = N_\alpha N_\gamma Q_N^{-1} \int d\{N - 2\} \exp(-\beta U)|_{x_\alpha^1 = x,\ x_\gamma^1 = x'}$$

Substituting the mean force potential into (2) and taking the gradient yields

$$\frac{\partial}{\partial x} W_\alpha(x) = \frac{\partial}{\partial x} u_\alpha(x) + \sum_\gamma \int dx' \frac{n_{\alpha\gamma}(x, x')}{n_\alpha(x)} \frac{\partial}{\partial x} u_{\alpha\gamma}(x, x') \tag{3}$$

The size of the ions is expressed in terms of the hard-sphere potential. The radial distribution function of the hard-sphere gas or liquid is described by YBG, HNC, or PY equations and the radial distribution is shown in Figure 1.[2] In our problem, however, the electrostatic interaction and the charge asymmetry of small ions due to the existence of macroions make the problem much more complicated. In order to estimate the effect of the ionic size simply, let us assume that the pair distribution function for low molecular weight ions is a step function, in the first approximation. The part of the curve in Figure 1 where the pair distribution function is greater than unity should be lowered by the existence of Coulomb repulsion. Therefore this assumption will be valid, at least to the first order of estimation. Thus we have

$$n_{\alpha\gamma}(x, x') = n_\alpha(x) n_\gamma(x') \theta(|x - x'| - r_{\alpha\gamma}) \tag{4}$$

where θ is the step function defined by

$$\theta(z) = 0 \quad \text{for } z < 0$$
$$= 1 \quad \text{for } z \geq 0$$

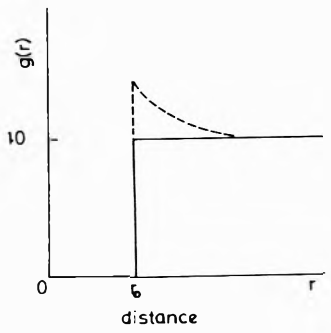

Figure 1. Radial distribution function. Hard-core radius is denoted by r_0. Broken line is radial distribution of hard-sphere gas, and full line represents present approximation.

and $r_{\alpha\gamma}$ is the sum of the hard-core radii of the species α and γ. Taking the divergence of eq 3, we obtain

$$\nabla^2 W_\alpha(x) = -\frac{Z_\alpha}{\epsilon}\left[4\pi\rho_p(x) + \sum_\gamma Z_\gamma \int dx' \frac{n_\gamma(x')\delta(|x - x'| - r_{\alpha\gamma})}{(x - x)^2}\right] \quad (5)$$

where the second term of the right-hand side is the surface integral. If the integration region has spherical symmetry, by transforming the variables, we obtain

$$2\pi \int d\varphi n_\gamma(x')|_{r=r_{\alpha\gamma}} \quad (6)$$

where φ denotes the angle against the axis connecting the small ion of the αth species at x and the macroion. If the point x is distant from the polymer, the integral tends to $4\pi n_\gamma(x)$ and eq 5 is reduced to the Poisson-Boltzmann equation.

The equilibrium condition for the dissociation of weak polyelectrolytes is given by[3]

$$pH = pK_\alpha - \log[\alpha/(1 - \alpha)] + 0.4343\beta W_H$$

where the change in free energy per ionized acid group which is usually denoted by ΔF has been replaced in this equation by W_H, the mean force potential for H^+ in the neighborhood of the residue. The potential W_H is calculated by solving the simultaneous equations of the type such as (5) with respect to all the ion species existing in the system.

In order to know the result of these equations briefly, numerical calculation was performed for the salt-free condition by using the rod model of polyelectrolytes due to Fuoss, Lifson, and Katchalsky.[4] Of course, even if a low molecular weight salt exists in the system, we can solve the equations with only increased computation time needed by the computer. The boundary condition is given by

$$W_\alpha(R) = 0; \frac{d}{dr} W_\alpha(R) = 0$$

where R is the radius of the model system employed. This boundary condition is similar to that for the Poisson-Boltzmann equation because the former condition gives the zero point of the potential and the latter implies the electroneutrality of the system for both cases.

In order to simplify the surface integral in the right-hand side of eq 5, the polymer was regarded to be an array of spheres, whose radius was the same as that of the polymer rod, only for calculating this surface integral. Thus the integral was replaced by (6). This assumption implies some reduction of the geometrical restriction near the polymer.

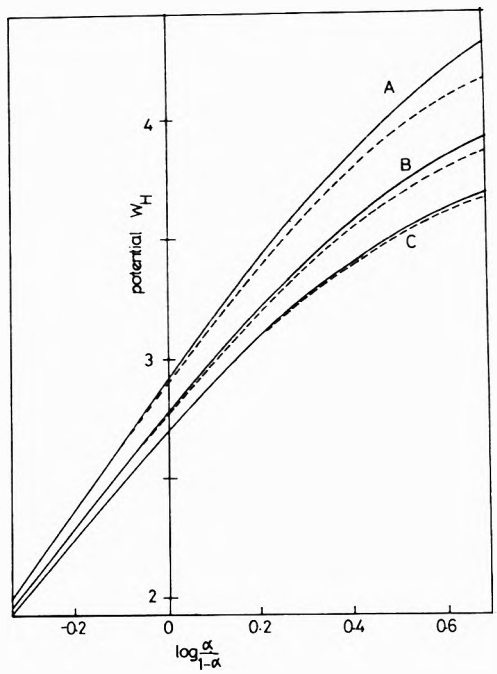

Figure 2. Henderson-Hasselbach plot. Full lines express the result due to the new equation, and broken lines show Poisson-Boltzmann result: A, ionic radius of counterions is 6.0 Å, which corresponds to Bu_4N^+; B, 3.5 Å, corresponds to Et_4N^+; C, 2.25 Å, Me_4N^+.

TABLE I: Comparison of Parameters in Henderson-Hasselbach Plot

		Experimental value[a]		Theoretical value	
	Radius, Å	Potential at $\alpha = 0.5$	Slope	Potential at $\alpha = 0.5$	Slope
K^+	1.33	2.54	2.26	2.64	1.95
Me_4N^+	2.25	2.50	2.72	2.71	2.11
Et_4N^+	3.50	2.70	2.93	2.79	2.33
Bu_4N^+	6.00	2.99	3.62	2.93	2.64

[a] See ref 1.

Calculation Procedure

As the first approximation, $n_\gamma(r)$ is replaced by the Poisson-Boltzmann distribution, and eq 5 is solved. This zero-order $W_\alpha(r)$ is substituted in eq 2′ to get $n_\alpha(r)$, and this is iterated till self-consistency is obtained. The variable r is limited within $r_p + r_\alpha \leq r \leq R$ for the equation with respect to the αth ion species, where r_p is the polymer radius and r_α is the hard-core radius of the αth ion species.

For each given value of $n_\alpha(R)$, we thus obtain N_α and $W_\alpha(x)$. Then the degree of dissociation is evaluated, if the polymer concentration and chain length of monomer unit are given. The numerical values of parameters used are dielectric constant, $\epsilon = 78.5$; chain length of monomer unit, 2.55 Å; polymer radius r_p, 4.0 Å; polymer concentration, 0.0128 N. These values are taken to correspond to polyacrylic acid.[1]

The results are shown in Figure 2 and Table I. In order to show the effect of the new equation, the result using the Poisson-Boltzmann equation instead of the new equation in solving for the potential W_H is also shown in Table I.[5] If the size of the counterions and the degree of disso-

ciation α are both large, the difference between the two equations is appreciable.

In comparing the result with the experiment, the following points are to be noted: (1) the value of the potential of mean force W_H at half-neutralization (*i.e.*, log $\alpha/(1 - \alpha)$ is equal to zero) is in good agreement with experiment; (2) the linearity, which is observed in the experiment is broken; and (3) the slope of the linear part of the curve calculated is smaller than that obtained from the experiment. It is also to be noted that the difference of the slope is smaller when the counterions are small.

Though polyacrylic acid cannot be supposed to be rodlike at this polymer concentration and in this range of the degree of dissociation, it is a fact that an improvement was accomplished by employing the new equation. This improvement suggests that the introduction of the simple pair distribution function is valid even in the frame of the Lifson-Katchalsky model. If we do not simplify the surface integral of eq 5 into eq 6, then the effect of the geometrical factor is larger and the calculated value is expected to be closer to the experimental value.

Acknowledgment. Numerical calculations were performed on the Facom 230-60 at the Nagoya University Computation Center.

References and Notes

(1) H. P. Gregor and M. Frederick, *J. Polym. Sci.*, **23**, 451 (1954).
(2) E. Waisman and J. L. Lebowitz, *J. Chem. Phys.*, **52**, 4307 (1970).
(3) A. Katchalsky, N. Shavit, and H. Eisenberg, *J. Polym. Sci.*, **13**, 69 (1954).
(4) R. M. Fuoss, A. Katchalsky, and S. Lifson, *Proc. Nat. Acad. Sci.*, **37**, 579 (1951).
(5) This treatment of the Poisson-Boltzmann equation corresponds to that of I. Kagawa and H. F. Gregor, *J. Polym. Sci.*, **23**, 467 (1957). Though their analytical expressions are correct, their numerical calculations include systematic errors.

Comparison of the Use of 3d Polarization Functions and Bond Functions in Gaussian Hartree–Fock Calculations

T. Vladimiroff

Propellants Division, Feltman Research Laboratory, Picatinny Arsenal, Dover, New Jersey 07801 *(Received April 12, 1973)*

Publication costs assisted by Picatinny Arsenal

The use of "bond functions" (Gaussian-type functions placed in the molecular bonding region) is examined for the nitrogen and oxygen molecules. On the basis of the total, ground-state energy and certain one-electron properties it is found that three optimized bond functions perform about as well as six optimized 3d functions. The incorporation of these bond functions reduces the computational time by a factor of 2 for the nitrogen molecule, when compared to the calculation using 3d functions. The use of 3d functions in conjunction with bond functions is also investigated and it is not found to be very encouraging.

Introduction

Recent advances in the capabilities of high-speed digital computers have made it possible to perform *ab initio* calculations on species of chemical interest. However, since the required computer time goes up rapidly as the number of atomic orbitals increases, picking the correct basis set is still a problem. For atoms, Slater-type orbitals seem to be the correct choice due to the infinite potential at the nuclus. However, multiple-center, two-electron integrals are difficult to evaluate if Slater orbitals are used so that Gaussian-type orbitals are becoming more popular for nonlinear polyatomic molecules. It is, nevertheless, recognized that Slater-type orbitals are the superior choice so that Gaussian orbitals are usually used in such a way as to imitate the Slater calculations. For example, only nuclear centers are employed or Slater-type orbitals are expanded in sets of Gaussians. In the bonding regions of a molecule the electrons no longer experience an infinite potential thus in these regions Slater-type orbitals are no longer clearly superior. For this reason, it has been suggested[1] that Gaussian orbitals should not necessarily be placed on nuclear centers. Many authors[2] have adopted this idea to their own particular point of view. However, a systematic study of the best exponents and positions to be used has only recently begun,[3] and this study makes no mention of the savings of computer time involved. In order to give this trend some impetus, we have studied the use of Gaussian orbitals placed at the center of the nitrogen and oxygen molecules and contrasted this study with a similar one reported by Dunning[4] using 3d polarization functions.

Upon the formation of a molecule from the individual atoms, we expect atomic orbitals to become distorted by the molecular fields. In order to describe this distortion, polarization-type functions are included in the calculation. A more elementary concept of a covalent bond is the piling up of negative charge between two positive nuclei so as to hold the molecule together by the classical electrostatic forces in agreement with the Hellman-Feyman theorem.[5] In accordance with this idea, it seems reason-

able to include functions which have their maximum values in the bonding region. For simplicity we shall refer to these functions as "bond functions" in order to indicate their molecular character and to differentiate them from free-floating Gaussian orbitals which are not necessarily placed in a bonding region. Since the potential in this region is finite, Gaussian orbitals could be better than Slater-type orbitals for this purpose. Also, this approach introduces new centers and, therefore, more multi-center two-electron integrals must be evaluated. Since this type of integral can be evaluated more quickly using Gaussian functions, it would seem that Gaussian-type orbitals should be a better choice for bond functions than Slater orbitals.

Computational Details

All LCAO-MO-SCF calculations performed in this work were conducted using POLYATOM,[6] a Gaussian system of computer programs kindly supplied by Professor Moskowitz. For the purposes of comparison with the work of Dunning,[4] we employed the (9s5p) atomic basis as suggested by Huzinaga[7] for both the oxygen and the nitrogen molecules. The functions were contracted to a (4s3p) according to Dunning's rules.[8] The experimental equilibrium distances of 2.068[9] au for nitrogen and 2.2808[9] au for oxygen were employed throughout these calculations. The z axis being the internuclear axis. Auxiliary functions were introduced midway between the two nuclei. We indicate this additional center by using a semicolon as follows: (4s3p;1s). The exponents of these functions were varied in order to minimize the total ground-state energy. Usually only one exponent was varied. The minimum was obtained by passing a fourth-degree polynomial through points in the vicinity of the suspected minimum and then finding the minimum for the polynomial using analytical techniques. In the case of nitrogen, two exponents were varied simultaneously. This minimum was found by passing a second-degree polynomial, including the cross term, through the points around the suspected minimum. The reported minimum was then found for this polynomial in the usual manner.

Results and Discussions

We began our calculations by placing a 1s Gaussian function midway between the two nitrogens and optimized the exponent, ζ_{1s}. A minimum in the total ground-state energy was obtained for $\zeta_{1s} = 1.11$. Then a p_x an a p_y function with exponent ζ_{2p} were added and the two exponents were optimized simultaneously. Values of $\zeta_{1s} = 1.13$ and $\zeta_{2p} = 0.68$ were obtained. The results of these calculations are summarized in Table I and compared with the results of Dunning[4] using no polarization functions and one set of Gaussian 3d function on each center. The important conclusion that can be made from Table I is that three-bond functions do almost as well as six 3d polarization functions. The energy is lowered by 0.0767 au by the addition of three-bond functions while Dunning[4] achieves a lowing of 0.0789 with the 3d Gaussians. The quadrupole moment decreases by 31% in Dunnings work[4] and 30% for our calculation. The force on the nitrogen nuclei decreases by 76% for the 3d functions and 72% for the bond functions. This comparison is not quite fair since we optimized the ζ_{1s} and ζ_{2p} separately while Dunning[4] employed one exponent for his 3d functions. However, Dunning[4] did test the asymmetrically optimized exponents for the two-term contraction of a Slater 3d function and this was found to give results for most properties with 1–2% of those obtained with a symmetrically optimized set.

TABLE I: Comparison of the Use of Polarization Functions and Bond Functions for the Nitrogen Molecule[a]

	Primitive basis			
	(9s5p)[b]	(9s5p1d)[b]	(9s5p;1s)	(9s5p;1s1p)
	Contracted basis			
Gaussian exponents	[4s3p]	[4s3p1d]	[4s3p;1s]	[4s3p;1s1p]
ζ_{1s}			1.11	1.13
ζ_{2p}				0.68
ζ_{3d}		0.98		
E_{HF}	−108.8877	−108.9666	−108.9146	−108.9644
$-V/T$	1.9998	2.0012	2.0006	2.0016
$\epsilon(1\sigma g)$	−15.7072	−15.6803	−15.7011	−15.6846
$\epsilon(2\sigma g)$	−1.5252	−1.4756	−1.5156	−1.4779
$\epsilon(3\sigma g)$	−0.6267	−0.6311	−0.6348	−0.6297
$\epsilon(1\sigma u)$	−15.7036	−15.6766	−15.6975	−15.6810
$\epsilon(2\sigma u)$	−0.7723	−0.7744	−0.7741	−0.7739
$\epsilon(1\pi u)$	−0.6237	−0.6131	−0.6153	−0.6146
$\langle x^2\rangle$(cm)[c]	7.5704	7.5730	7.5903	7.6146
$\langle y^2\rangle$(cm)[c]	24.3304	23.7861	24.2535	23.8372
Q_{zz}(cm)[c,d]	−1.7918	−1.2450	−1.6950	−1.2545
$\langle 1/r_N\rangle$[e]	21.6367	21.6590	21.6398	21.6539
$E_z(N_1)$[f]	−0.2138	−0.0511	−0.1365	−0.0591
$q_{zz}(N_1)$[g]	1.2480	1.3364	1.2295	1.3034
$\langle\delta(r-N)\rangle$[h]	195.4258	195.3038	195.4084	195.3436

[a] All quantities in atomic units. For definitions of the properties see, for example, M. Krauss, *Nat. Bur. Std. (U.S.), Tech Note*. No. 438, (1967). In addition see D. B. Neumann and J. W. Moskowitz, *J. Chem. Phys.*, 49, 2056 (1968); 50, 2216 (1969). [b] Taken from ref 4. [c] cm denotes the center of mass which for nitrogen is at (0.0, 0.0, 1.034). [d] Quadrupole moment. 1 au = 1.34492 × 10^{-26} esu/cm^2. [e] This property only has an electronic contribution. [f] Electric field. 1 au = 1.71524 × 10^7 esu/cm^2. [g] Electric field gradients. 1 au = 3.24140 × 10^{15} esu/cm^3. [h] Density at the nuclei.

We also optimized a set of bond orbital exponents for the oxygen molecule. Values of $\zeta_{1s} = 0.94$ and $\zeta_{2p} = 0.77$ were obtained. It was encouraging to find that the values were approximately the same as those obtained for the nitrogen molecule. A p_z orbital was also tried for O_2 but the effect on the energy of this type of function was found to be small, about 0.001 au.

The reduction of the number and type of functions used results in significant savings in computer time. With POLYATOM the integrals using the three bond functions could be calculated 2.3 times faster than if the six 3d functions were employed. This is because fewer integrals have to be calculated and because integrals involving 3d functions take the most time. The SCF iteration time is about twice as fast using the bond functions. However, our version of POLYATOM will not allow the contraction of functions of different symmetry. Thus integrals involving d_z^2 could not be stored on tape but had to be assembled using $(2z^2 - x^2 - y^2)$ at each iteration. This results in somewhat longer running times since integrals over ten 3d functions rather than six have to be processed. We, therefore, estimate that comparable results can be obtained using about half the time if bond functions are used rather than 3d polarization functions.

An unsatisfactory aspect of the use of bond functions is that it is not immediately obvious how to improve the result by adding more functions. This contrasts with the use of polarization functions where it seems reasonable[4] to

TABLE II: Comparison of the Use of Bond Functions in Conjunction with 3d Polarization Functions to a Calculation Performed Using Two Gaussian Functions to Represent One Slater 3d Function for the Nitrogen Molecule[a]

Gaussian exponents	Primitive basis (9s5p1d;1s1p) [4s3p1d;1s1p]	Primitive basis (9s5p1d;1s1p) Contracted basis [4s3p1d;1s1p]	(9s5p2d)[b] [4s3p1d]
ζ_{1s}	1.13	1.13	
ζ_{2p}	0.68	0.68	
ζ_{3d}	0.98	1.75	0.56, 1.88
E_{HF}	−108.9672	−108.9688	−108.9716
$-V/T$	2.0016	2.0014	2.0014
$\epsilon(1\sigma g)$	−15.6833	−15.6820	−15.6793
$\epsilon(2\sigma g)$	−1.4768	−1.4765	−1.4726
$\epsilon(3\sigma g)$	−0.6314	−0.6319	−0.6321
$\epsilon(1\sigma u)$	−15.6797	−15.6783	−15.6757
$\epsilon(2\sigma u)$	−0.7746	−0.7747	−0.7748
$\epsilon(1\pi u)$	−0.6132	−0.6131	−0.6120
$\langle x^2\rangle$(cm)	7.6210	7.9191	7.6029
$\langle z^2\rangle$(cm)	23.7786	23.7805	23.6067
Q_{zz}(cm)	−1.1894	−1.1932	−1.0356
$\langle 1/r_N\rangle$	21.6552	21.6570	21.6596
$E_z(N_1)$	−0.0528	−0.0420	−0.0324
$q_{zz}(N_1)$	1.3389	1.3809	1.3320
$\langle\delta(r-N)\rangle$	195.3204	195.3244	195.2895

[a] All quantities in atomic units. For an explanation of the properties, see footnotes a and *c–h* of Table I. [b] Taken from ref 4.

add Gaussian polarization functions so as to approximate a Slater polarization function. One way to improve our calculation was to include both bond functions and 3d-type polarization functions. This seemed reasonable since it would provide enough flexibility for both the polarization and the bonding effect. For these calculations we first employed Dunning's[4] optimum value of ζ_{3d} = 0.98. This exponent was then varied. It was found that it increased until a value of 1.75 was found to correspond to the minimum energy. Since the 3d functions were no longer needed to describe the wavefunction in the bonding region, they were free to shrink and describe the polarization effects in the vicinity of the nuclei. The results of these calculations are summarized in Table II.

A glance at Table II reveals that the optimized 3d functions in conjunction with the bond functions do not perform as well as two Gaussian 3d functions contracted to represent one Slater 3d function. The two-term Slater 3d function decreases the energy by an additional 0.0050 au and further decreases of 17% in the quadrupole moment and 37% in the force on the nitrogen nucleus are observed.[4] The addition of a set of 3d functions with ζ_{3d} = 0.98 (1.75) reduces the energy by 0.0028 au (0.0044 au), decreases the quadropole moment by 5% (5%), and decreases the force on the nitrogen nucleus by 11% (29%). The use of a mixed basis of 3d functions and bond functions does not seem to be a very good idea and defeats the original goal of this work which was to increase the speed of the calculation. An alternative way to improve the calculation would be to add more, carefully optimized, bond functions. However, getting near Hartree–Fock solutions may not be the most promising use for bond functions. We feel that once bond functions have been optimized for different types of chemical bonds, they could be most efficiently employed in *ab initio* calculations on first-row polyatomic molecules when the addition of 3d functions is too costly but it still desired to obtain results which are better than can be obtained with an sp basis.

Acknowledgment. The author thanks Dr. E. G. Sharkoff for supporting this research, Miss Debora G. Vander Berg for helping with the preparation of the manuscript, and the MUCOM MISD for providing computer facilities. Professor Jules Moskowitz and Dr. Charles Hornback have kindly supplied computer programs. Thanks are also due to Drs. Yvon P. Carignan and George F. Adams for their interest and encouragement.

References and Notes

(1) H. Preuss, *Z. Naturforsch. A*, **11**, 823 (1956); J. L. Whitten, *J. Chem. Phys.*, **44**, 359 (1966).
(2) A. A. Frost, *J. Chem. Phys.*, **47**, 3707 (1967); *Theor. Chim. Acta*, **18**, 156 (1970); H. Preuss, *Z. Naturforsch. A*, **20**, 21 (1965); F. Fratev, R. Janoschek, and H. Preuss, *Int. J. Quantum Chem.*, **4**, 529 (1970); R. Ahlrichs, *Theor. Chim. Acta*, **17**, 348 (1970); R. Ahlrichs and W. Kutzelnigg, *Chem. Phys. Lett.*, **1**, 651 (1968); S. Rothenberg and H. F. Schaefer, III, *J. Chem. Phys.*, **54**, 2764 (1971).
(3) P. Russegger, H. Lischka, and P. Schuster, *Chem. Phys. Lett.*, **12**, 392 (1971).
(4) T. H. Dunning, Jr., *J. Chem. Phys.*, **55**, 3958 (1971).
(5) J. Hellmann, "Einfuhrung in die Quantenchemie," Deuticke and Co., Leipzig, 1937; R. Feynman, *Phys. Rev.*, **56**, 340 (1939).
(6) I. G. Csizmadia, M. C. Harrison, J. W. Moskowitz, and B. T. Sutcliffe, *Theor. Chem. Acta*, **6**, 191 (1966).
(7) S. Huzinaga, *J. Chem. Phys.*, **42**, 1293 (1965).
(8) T. H. Dunning, Jr., *J. Chem. Phys.*, **53**, 2823 (1970).
(9) G. H. Herzberg, "Spectra of Diatomic Molecules," Van Nostrand, New York, N. Y., 1950.

Effect of Side Groups on Unperturbed Chain Dimensions of Atactic Hydrocarbon Polymers

Raymond L. Arnett*

Birkerød, Denmark

and Carl J. Stacy

Phillips Petroleum Company, Bartlesville, Oklahoma 74004 *(Received January 31, 1973)*

Publication costs assisted by Phillips Petroleum Company

The unperturbed mean-square molecular radius, s_0^2 (determined from intrinsic-viscosity measurements), of ethyl-branched atactic polymers are reported for several degrees of branching. These are compared with polymethylene (zero branches) and atactic poly(1-butene) (250 ethyl branches per 1000 carbon atoms). Relations are presented which describe the observed temperature and structure dependence these data display. The relations also fit the observed values of s_0^2 for the following diverse atactic polymers: polypropylene, polyisobutylene, poly(1-pentene), and polystyrene.

Introduction

If one attempts to discover the effects of various substituents in polymers of substituted ethylenes on the unperturbed chain dimensions, he is immediately confronted with the problem of the seemingly haphazard relation of the temperature dependence of the mean-square radius, s_0^2, with polymer molecular structure. Reported values of $\partial \ln s_0^2/\partial T$ (T is the temperature) for polymers of ethylene and its hydrocarbon-substituted derivatives vary from negative to positive values with no obvious structural relationship even for polymers having the same kind of tacticity. We have examined a series of model atactic polymers having various amounts of ethyl branches with the hope of establishing the trend in s_0^2/M (M is polymer molecular weight) and $\partial \ln s_0^2/\partial T$ in going from linear polyethylene (with zero branches) to atactic poly(1-butene) (with 250 ethyl branches per 1000 carbon atoms). We report our measurements and findings here.

Experimental Section

The polymers reported on here are hydrogenated polybutadienes. The syntheses of the several polybutadienes were accomplished by published routes[1] which produce polymers with narrow molecular-weight distribution at controlled levels of molecular weight and 1,2 addition; the latter results, on hydrogenation, in controlled amounts of ethyl branches. The hydrogenation was carried to completion by the techniques of Moberly.[2] The parent polybutadienes were analyzed for microstructure by standard infrared techniques.[3] The measurements for vinyl content were interpreted as ethyl content in the hydrogenated polymer; the values found are 69, 130, and 183 branches per 1000 carbon atoms for the three series reported here.

Weight-average molecular weights were determined by scattered light photometry, using 1-chloronaphthalene as solvent.[4] The necessary specific refractive increments were measured on samples from each series. Number-average molecular weights were determined by osmotic pressure measurements.[5] Intrinsic viscosity determinations were made for all samples in a number of solvents[6] to permit the determination of s_0^2/M by the technique described previously.[7]

Results

Molecular weights of the several polymers studied are given in Table I;[8] weight-average molecular weights, M_w, appear in column 3 and number-average, M_n, in column 4. The value for $M_\theta^{1/2}$ needed in the Stockmayer–Fixman relation[7,9]

$$[\eta] = KM_\theta^{1/2} + JM_w, \quad K = \Phi\left(\frac{6s_0^2}{M}\right)^{3/2} \tag{1}$$

was taken as

$$M_\theta^{1/2} \equiv (M^{1/2})_w = (M_n M_w^3)^{1/8}$$

a relation valid for a logarithmic-normal distribution of molecular weights. In relation 1, the parameter J provides a measure of the perturbation of the polymer molecule by the solvent, Φ is considered a universal constant, and $[\eta]$ is the intrinsic viscosity of the polymer solution. Values determined for $[\eta]$ for each polymer in three solvents at each of two temperatures are listed in Table II.[8] The data in Tables I and II are plotted in Figure 1 (for one temperature only, 130°) according to the procedure given in ref 7. The lines drawn in the figure are least-squares fits to the data constrained to give a common intercept after demonstrating that intercepts from fitting without constraint were indeed measures of the same quantity (90% confidence limits). The parameters K and J determined by this fitting are given in Table III; columns 3 and 4 give the values of K and its standard deviation, respectively, and columns 5 and 6 give the value of J with its standard deviation.

From the meaning of K given in (1) and taking 2.5×10^{21} for the value of Φ, we calculate s_0^2/M for each polymer structure and list the results in Table IV. Also included are results for the polymer having 20 ethyl branches per 1000 C atoms, taken from ref 7. Columns 2 and 3 give the values of s_0^2/M at the two temperatures measured.

Figure 2 displays the values of s_0^2/M appearing in Table IV and includes values for both linear polyethylene[6,10] and atactic poly(1-butene)[11] adjusted to the same two temperatures. It is at once apparent that the behavior of

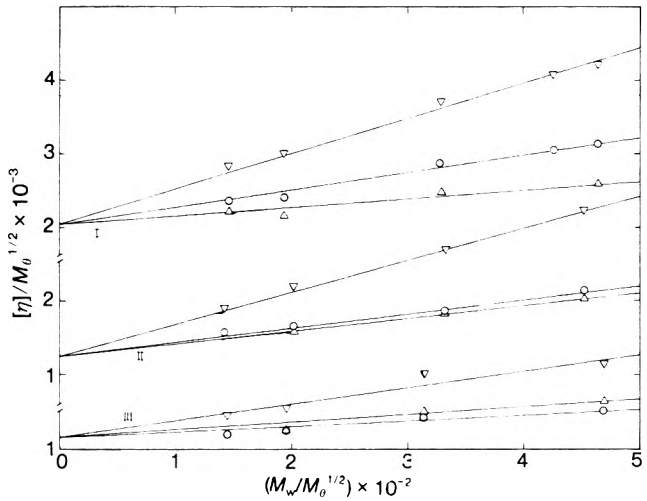

Figure 1. Stockmayer–Fixman plot for ethyl-branched macroparaffins at 130°: (I) 69 branches/1000 C atoms; (II) 130 branches/1000 C atoms; (III) 183 branches/1000 C atoms: O, biphenyl; Δ, 1-dodecanol; ∇, 1-chloronaphthalene.

TABLE III: Stockmayer–Fixman Parameters for Hydrogenated Polybutadienes

Et branches/ 1000 C	Solvent[a]	$K \times 10^3$	$\sigma_k \times 10^3$	$J \times 10^6$	$\sigma_j \times 10^6$
		At 35°			
69	4			2.88	0.23
	5	2.64	0.08	4.75	0.24
	6			8.07	0.27
130	4			3.07	0.32
	5	1.88	0.11	4.02	0.32
	6			6.63	0.35
183	4			1.92	0.42
	5	1.71	0.15	2.52	0.42
	6			4.22	0.42
		At 130°			
69	1			1.16	0.20
	2	2.05	0.08	2.33	0.20
	3			4.75	0.21
130	1			1.71	0.10
	2	1.27	0.04	1.92	0.10
	3			4.34	0.11
183	1			1.00	0.24
	2	1.17	0.09	0.74	0.24
	3			2.23	0.25

[a] (1) 1-Dodecanol, (2) biphenyl, (3) 1-chloronaphthalene, (4) 2,4-dimethylpentane, (5) heptane, (6) cyclohexane.

ln (s_0^2/M) with number of branches depends on the temperature. The logarithm of s_0^2/M at 35° is almost linear with ethyl branch content; it does not display this behavior at 130°.

Discussion

The difference in behavior of s_0^2/M with side chain content at the two temperatures, 35 and 130°, suggests that there may be a temperature for which ln (s_0^2/M) is linear with that polymer content not in the main chain of atactic polymers. Our first step in exploring this possibility is to examine the temperature coefficient, $\partial \ln s_0^2/\partial T$, and its dependence on polymer composition.

Figure 3 displays our values of $\partial \ln s_0^2/\partial T$ for hydrogenated polybutadienes as well as literature values for poly-

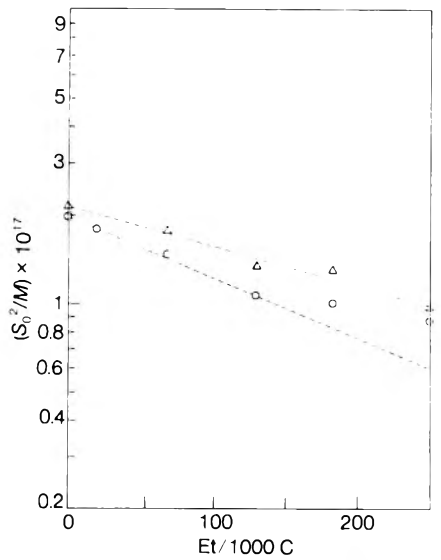

Figure 2. Dependence of unperturbed chain dimensions on ethyl branch content for macroparaffins: O, 130°; Δ, 35°.

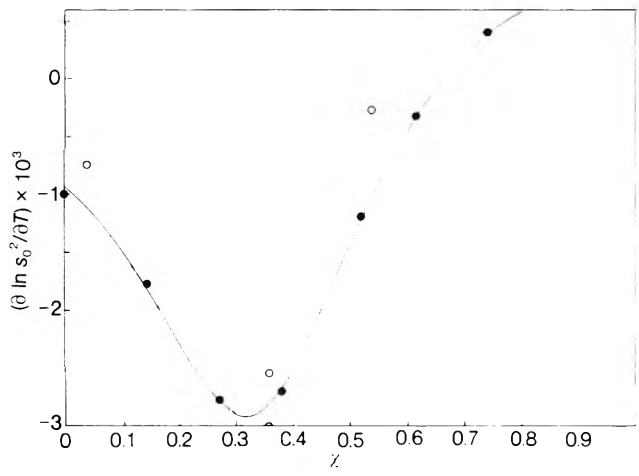

Figure 3. Dependence of temperature coefficient of unperturbed mean-square radius on mass fraction of polymer as substituents for hydrocarbon polymers.

TABLE IV: Unperturbed Chain Dimensions for Hydrogenated Polybutadienes

	$s_0^2/M \times 10^{17}$	
Et Branches/1000 C	35°	130°
20	1.80[a]	1.78[b]
69	1.73	1.46
130	1.38	1.06
183	1.30	1.00

[a] At 125°. [b] At 140°.

methylene and atactic poly(1-butene). Also included in the figure are values for other atactic polymers for which the branch differs from an ethyl group: polypropylene, polyisobutylene, poly(1-pentene), and polystyrene. In order to put these different structures on the same basis, we use χ, the fraction (by mass) of polymer that is not in the main chain. Values of the quantities required for Figure 3, together with references, are given in Table V.[12-17] We find that the empirical relation

$$\frac{\partial \ln s_0^2}{\partial T} = a - \frac{b}{1 + (\chi - c)^2(1 + \tanh \beta\chi)} \quad (2)$$

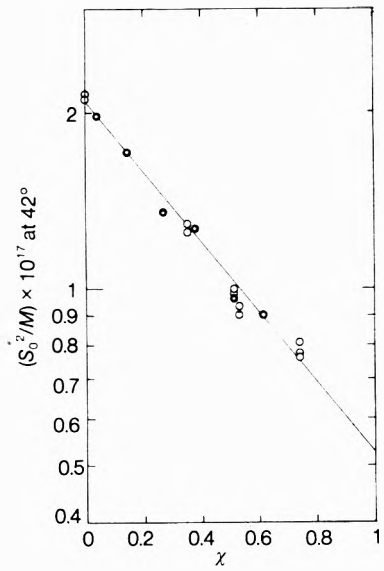

Figure 4. Dependence of unperturbed chain dimensions (at 42°) on mass fraction of polymer as substituents for hydrocarbon polymers.

TABLE V: Temperature Coefficients of Unperturbed Chain Dimensions

Polymer	χ	$(\partial \ln s_0^2/\partial T) \times 10^3$ (deg^{-1})	Ref
Polymethylene	0	−1.0 (±0.1)	12
20 Et/1000 C	0.039	−0.8 (±1.6)	7
69 Et/1000 C	0.143	−1.77 (±0.3)	This work
130 Et/1000 C	0.269	−2.77 (±0.4)	This work
Polypropylene[a]	0.357	−2.55	13
		−3.51	14
183 Et/1000 C	0.379	−2.71 (±0.3)	This work
Poly(1-butene)[a]	0.518	−1.2 (±0.2)	11
Polyisobutylene	0.536	−0.28	15
Poly(1-pentene)[a]	0.614	−0.33 (±0.2)	16
Polystyrene[a]	0.740	0.37	17
		0.44	17

[a] Atactic polymers.

with $a = 1.53 \times 10^{-3}$, $b = 4.45 \times 10^{-3}$, $\beta = 2.83$, and $c = 0.316$ fits the data well within the experimental error with the possible single exception of the value reported for polyisobutylene. The curve drawn in Figure 3 is the least-squares fit of (2) to those data of Table V which appear as filled circles in the figure; values of the four parameters given above result from this fit. Those data not used in the fitting were omitted because of the large uncertainty of their values.

According to relation 2, and as seen in the figure, both positive and negative values for $\partial \ln s_0^2/\partial T$ exist; the most negative value occurs for the structure having about one-third of its mass as substituent on the main chain. On the other hand, s_0^2 becomes temperature independent for that structure with two-thirds of the mass as substituents. Values of χ greater than $\frac{2}{3}$ result in positive values of the temperature coefficient approaching a maximum value of $+0.66 \times 10^{-3}$ at $\chi = 1$. In the main, we list in Table V only those values from intrinsic viscosity measurements, for consistency with the experimental determination of s_0^2/M.

TABLE VI: Summary of Unperturbed Chain Dimensions

Polymer	χ	$(s_0^2/M) \times 10^{17}$	T, °C	Ref	$(s_0^2/M) \times 10^{17}$ At 42°
Polymethylene	0	1.93	138	6, 10	2.11
	0	1.96	142	10, 18	2.15
20 Et/1000 C	0.039	1.80	125	7	1.97
	0.039	1.78	140	7	1.98
69 Et/1000 C	0.143	1.73	35	This work	1.71
	0.143	1.46	130	This work	1.71
130 Et/1000 C	0.269	1.38	35	This work	1.35
	0.269	1.06	130	This work	1.36
Polypropylene[a]	0.357	1.28	34	13	1.25
	0.357	1.23	58	13	1.29
183 Et/1000 C	0.379	1.30	35	This work	1.27
	0.379	1.00	130	This work	1.27
Poly(1-butene)[a]	0.518	1.10	−46	11	0.98
	0.518	0.98	23	11	0.96
	0.518	0.94	61	11	0.96
	0.518	0.95	83	11	1.00
Polyisobutylene	0.536	0.95	24	19	0.93
	0.536	0.85	100	19	0.90
Poly(1-pentene)[a]	0.614	0.91	33	16	0.90
	0.614	0.89	64	16	0.90
	0.614	0.90	85	16	0.91
	0.614	0.87	149	16	0.90
Polystyrene[a]	0.740	0.77	32.8	21	0.77
	0.740	0.81	34.8	18, 20, 21	0.81
	0.740	0.76	35.9	20	0.76

[a] Atactic polymer.

The determination of the last named quantity for several different polymers has shown that $\ln (s_0^2/M)$ is linear with temperature over a rather broad temperature range (more than 100°). We therefore test the relation

$$\ln \frac{s_0^2}{M} = \ln p - q\chi + \frac{\partial \ln s_0^2}{\partial T}(T - \tau) \qquad (3)$$

to determine if there is a temperature, $T = \tau$, for which $\ln (s_0^2/M)$ would be linear with χ for a more diverse group of atactic polymers. For this test we use all the polymers listed in Table V covering a temperature range from −46 to +149°, a total of 25 observations. These observations are listed in Table VI together with references.[18-21] Relation 3 is fitted to the data of Table VI using (2) for the dependence of $\partial \ln s_0^2/\partial T$ on χ. The fitting procedure determines $\tau = 42 \pm 6°$, $p = 2.09 \pm 0.03 \times 10^{-17}$, $q = 1.38 \pm 0.03$. Figure 4 displays the values of s_0^2/M at 42° together with the least-squares line. In adjusting the determined values (in Table VI) to 42° from the temperature of measurement, we used temperature coefficients calculated from (2); values for s_0^2/M so adjusted to 42° appear in the last column of Table VI. We note that the temperature coefficient listed for polyisobutylene in Table V is not consistent with the two values of s_0^2/M for that polymer listed in Table VI; a more negative value is required. Finally, it appears from Figure 4 that the values of $\ln (s_0^2/M)$ do determine a linear relationship with χ at 42° whether the substituents be methyl, ethyl, propyl, or phenyl groups. It would be interesting to learn if the quantitative trend predicted here is in fact followed by more massive substituents on other atactic polymers.

Characteristic Ratio. Since the characteristic ratio, s_0^2/nl^2, is related to s_0^2/M by

$$s_0^2/nl^2 = (s_0^2/M)(M_0/l^2)$$

and since

$$M_0 = C/(1 - \chi)$$

we have

$$\ln \frac{s_0^2}{ln^2} = \ln \frac{s_0^2}{M} + \ln C - 2 \ln l - \ln (1 - \chi) \quad \chi = 1 \quad (4)$$

where n is the number of C–C bonds in the main chain, l is the mean length of those bonds, M_0 is the mean molecular weight of a main chain atom considering the substituent as part of its mass so that $M = nM_0$, and C is the mean molecular weight of a main chain carbon atom with its attached hydrogen. The value of C is nearly constant; it varies from 12 (for a polymer of tetrasubstituted ethylene) to 14 (for polymethylene). Relation 4 together with (2) and (3) give a satisfactory account of the temperature and structure dependence of the unperturbed dimensions for the atactic hydrocarbon chain polymers examined here.

Acknowledgment. The experimental portion of this work was carried out entirely in the Research Laboratories of Phillips Petroleum Co. Polymers were prepared under the direction of R. P. Zelinski and were hydrogenated by C. W. Moberly; osmotic pressure measurements were made under the direction of R. Q. Gregg; and most of the scattered-light and intrinsic viscosity measurements were carried out by J. R. Donaldson.

References and Notes

(1) R. P. Zelinski and C. F. Wofford, *J. Polym. Sci., Part A-3*, 93 (1965).; H. L. Hsieh, *ibid.*, 191 (1965); J. N. Short, R. P. Zelinski, and O. F. McKinney, IUPAC Symposium on Macromolecular Chemistry, Tokyo, Japan, 1966.
(2) C. W. Moberly in "Encyclopedia of Polymer Science and Technology," Vol. VII, Wiley, New York, N. Y., 1967.
(3) R. S. Silas, J. Yates, and V. Thornton, *Anal. Chem.*, **31**, 529 (1959).
(4) C. J. Stacy and R. L. Arnett *J. Polym. Sci., Part A-2*, 167 (1964).
(5) R. L. Arnett and R. Q. Gregg, *J. Phys. Chem.*, **74**, 1593 (1970).
(6) C. J. Stacy and R. L. Arnett *J. Phys. Chem.*, **69**, 3109 (1965).
(7) C. J. Stacy and R. L. Arnett *J. Phys. Chem.*, **77**, 78 (1973).
(8) The molecular weights and intrinsic viscosities (contents of Tables I and II) will appear following these pages in the microfilm edition of this volume of the journal. Single copies may be obtained from the Business Operations Office, Books and Journals Division, American Chemical Society, 1155 Sixteenth St., N.W., Washington, D. C. 20036. Remit check or money order for $3.00 for photocopy or $2.00 for microfiche, referring to code number JPC-73-1986.
(9) W. H. Stockmayer and M. Fixman, *J. Polym. Sci., Part C-1*, 137 (1963).
(10) R. Chiang, *J. Phys. Chem.*, **70**, 2348 (1966).
(11) G. Moraglio, G. Gianotti, and F. Danusso, *Eur. Polym. J.*, **3**, 251 (1967).
(12) A. Ciferri, C. A. J. Hoeve, and P. J. Flory, *J. Amer. Chem. Soc.*, **83**, 1015 (1961).
(13) F. Danusso and G. Moraglio, *Rend. Ist. Lomb. Sci. Lett., A*, **93**, 666 (1959).
(14) J. B. Kinsinger and R. E. Hughes, *J. Phys. Chem.*, **67**, 1922 (1963).
(15) J. E. Mark and G. B. Thomas, *J. Phys. Chem.*, **70**, 3588 (1966).
(16) G. Moraglio and G. Gianotti *Eur. Polym. J.*, **5**, 781 (1969).
(17) T. A. Orofino and A. Ciferri, *J. Phys. Chem.*, **68**, 3136 (1964).
(18) A. Nakajima, F. Hamada and S. Hayashi, *J. Polym. Sci., Part C-15*, 285 (1966).
(19) T. G. Fox, Jr., and P. J. Flory, *J. Amer. Chem. Soc.*, **73**, 1909 (1951).
(20) T. A. Orofino and J. W. Mickey, Jr., *J. Chem. Phys.* **38**, 2513 (1963).
(21) T. Altares, D. P. Wyman, and V. R. Allen, *J. Polym. Sci., Part A-2*, 4533 (1964).

Electronic Conductivity in Molten Lithium Chloride–Potassium Chloride Eutectic[1]

R. J. Heus and J. J. Egan*

Brookhaven National Laboratory, Upton, New York 11973 *(Received February 20, 1973)*

Publication costs assisted by Brookhaven National Laboratory

Polarization measurements, similar to those used in the solid state, have been employed to measure a small electronic component of conductivity in molten LiCl-KCl eutectic in the presence of a larger ionic component of conductivity. Convection in the melt has been eliminated. Current-potential curves have been obtained on the cell Ta|LiCl-KCl(l)eut|LiCl-KCl(l), $PbCl_2$ (5% wt)|Pb to obtain the electron conductivity and on the cell C|LiCl-KCl(l)eut|C-Cl_2 to obtain the electron hole conductivity. Applications of the results to problems of molten salt electrochemistry are given.

Introduction

If sodium metal is added to molten NaCl the total electrical conductivity of the melt increases continuously with addition of the metal. The increased conductivity has been analyzed as electronic conductivity and the phenomena is common to many metal–molten salt systems. Reviews of the techniques and results for many systems have been given by Bredig,[2a] Corbett,[2b] and Grantham and Yosim.[3] The theory has been examined by Raleigh,[4] Rice,[5] as well as others.

The same phenomena occur in ionic solids but here a variety of very sensitive techniques have been developed to measure the electronic component of conductivity in the presence of a much larger component of ionic conductivity. Wagner[6] has described several suitable techniques and derived appropriate equations from the transport

theory of solids. It has been found that the electronic conductivity depends markedly upon the chemical potential of the component elements of the ionic compound, for example, the electronic conductivity of AgBr depends strongly upon the chemical potential or partial pressure of Br_2 gas above the sample.

It was thought advantageous to study molten salts using experimental techniques previously used with solids. By eliminating convection in the melt the same transport equations used for solids should be valid in the melt. The polarization technique[6-18] in particular has been helpful to study electronic conductivity in solids that are predominantly ionic, so that it was used in this work. In this method dc current flowing through a cell is measured at various applied voltages, which are below the decomposition potential of the sample to ensure that the measured current is only electronic current. The pertinent equations are given below. Derivations and discussions are available in the literature.[6,19] The system LiCl-KCl eutectic was studied since it has been a popular solvent in studies of molten salt electrochemistry.

The cell used to measure the electron conductivity may be represented as

$$\mathrm{Ta}\,|\,\mathrm{LiCl\text{-}KCl(l)eut}\,|\,\frac{\mathrm{PbCl_2}\,(5\%\,\mathrm{wt})}{\mathrm{LiCl\text{-}KCl(l)eut}}\,|\,\mathrm{Pb} \qquad \text{(I)}$$

where the inert tantalum electrode is negative. A voltage E measured in volts is applied and the electronic current i, in amperes, is given by

$$i = \frac{RT}{FG}\left\{\sigma_e^{\mathrm{ref}}\left[\exp\left(\frac{EF}{RT}\right)-1\right]+\sigma_h^{\mathrm{ref}}\left[1-\exp\left(-\frac{EF}{RT}\right)\right]\right\} \qquad (1)$$

where G is the cell constant, σ_e^{ref} is the electron conductivity of the salt equilibrated with the Ph-$PbCl_2$ reference electrode, and σ_h^{ref} is the electron hole conductivity of the salt equilibrated with the reference electrode.

When $E \gg RT/F$, eq 1 reduces to

$$i = \frac{RT}{FG}\,\sigma_e^{\mathrm{ref}}\left[\exp\left(\frac{EF}{RT}\right)-1\right] \qquad (2)$$

The value of σ_e^{ref} is thus obtained from current-potential curves using eq 2. Values of σ_e are calculated at various other activities of Li in the melt by

$$\sigma_e = \sigma_e^{\mathrm{ref}}(a_{\mathrm{Li}}/a_{\mathrm{Li}}^{\mathrm{ref}}) \qquad (3)$$

where $a_{\mathrm{Li}}^{\mathrm{ref}}$ is the activity of Li in a melt equilibrated with the Pb-$PbCl_2$ reference electrode. This activity can be calculated by considering the following equations

$$\mathrm{Pb} + 2\mathrm{LiCl(KCl)} = \mathrm{PbCl_2(LiCl\text{-}KCl)} + 2\mathrm{Li}$$

$$\Delta G^\circ = \Delta G^f_{\mathrm{PbCl_2}} - 2\Delta G^f_{\mathrm{LiCl}} = -RT\ \ln\left[(a_{\mathrm{Li}}^{\mathrm{ref}})^2 a_{\mathrm{PbCl_2}}/a_{\mathrm{LiCl}}^2\right]$$

where $\Delta G^f_{\mathrm{PbCl_2}}$ and $\Delta G^f_{\mathrm{LiCl}}$ are the free energies of formation of $PbCl_2$ and LiCl so that

$$a_{\mathrm{Li}}^{\mathrm{ref}} = \exp(-\Delta G^\circ/2RT)[a_{\mathrm{LiCl}}/a_{\mathrm{PbCl_2}}^{1/2}] \qquad (4)$$

where the activity values for a_{LiCl} in LiCl-KCl are taken from Aukurst, *et al.*,[20] and the values of $a_{\mathrm{PbCl_2}}$ in 5% wt LiCl-KCl are taken from Yang and Hudson.[21]

The activity of lithium at the tantalum electrode is a function of the applied voltage and is given by the expression

$$a_{\mathrm{Li}} = a_{\mathrm{Li}}^{\mathrm{ref}} \exp(EF/RT)$$

Thus the electronic conductivity is obtained as a function of Li activity in the melt instead of mole per cent lithium which is the usual form of reporting results for molten salts.

In the study of electron hole conductivity a chlorine gas reference electrode was used similar to the use of Br_2 gas to study electron hole conductivity in solid AgBr as reported by Raleigh.[10] The cell used was

$$\mathrm{C}\,|\,\mathrm{LiCl\text{-}KCl(l)eut}\,|\,\mathrm{C\text{-}Cl_2} \qquad \text{(II)}$$

with the left-hand electrode negative.

In this case eq 1 is also applicable but σ_e^{ref} and σ_h^{ref} are the electron and electron hole conductivities of the salt in equilibrium with chlorine gas at 1 atm pressure. In this case $\sigma_e^{\mathrm{ref}} \ll \sigma_h^{\mathrm{ref}}$ (see Figure 4) so that eq 1 takes the form

$$i = \frac{RT}{FG}\,\sigma_h^{\mathrm{ref}}\left[1-\exp\left(-\frac{EF}{RT}\right)\right] \qquad (5)$$

when $E < \sim 1.5$ V.

The current-potential curve shows a plateau in this case in contrast to the exponential form in the case of cell I. On the plateau

$$i = (RT/FG)\sigma_h^{\mathrm{ref}} \qquad (6)$$

Values of σ_h at other values of chlorine partial pressure can be obtained from the equation

$$\sigma_h = \sigma_h^{\mathrm{ref}} p_{\mathrm{Cl_2}}^{1/2} \qquad (7)$$

The chlorine partial pressure and the lithium activity of the melt are interrelated by the equation

$$a_{\mathrm{Li}} p_{\mathrm{Cl_2}}^{1/2} = (a_{\mathrm{LiCl}})\ \exp(\Delta G^f_{\mathrm{LiCl}}/RT)$$

where a_{LiCl} is the activity of LiCl in the melt taken from values of Aukurst[20] and $\Delta G^f_{\mathrm{LiCl}}$ is the free energy of formation of LiCl.

The assumptions underlying the validity of eq 1 and 2 are discussed by Wagner.[6] Briefly they imply a cell of constant cross section, a constant mobility of electrons and electron holes, small deviations from ideal metal to nonmetal ratio, and electron concentrations dilute enough so that classical statistics can be applied.

Experimental Section

The experimental arrangement of cell I is shown in Figure 1. A quartz tube of constant cross section approximately 10 cm long and in the form of a spiral to conserve space is filled with finely powdered inert alumina (120 mesh, Aluminum Co. of America). The LiCl-KCl eutectic fills the void spaces in this powder and with careful temperature control convection is eliminated. A tantalum rod acts as cathode. The reference compartment of the cell is contained in a large quartz tube and the level of salt in the spiral and reference compartment are the same so that no flow will occur. A coarse frit of quartz holds the alumina powder in the spiral. The entire cell as shown is contained in a larger vycor tubing (not shown) which contains an inert atmosphere of purified argon gas.

The experimental arrangement of cell II is shown in Figure 2 and is similar to the design of cell I except for the electrode materials. The chlorine gas at 1 atm pressure flows over a graphite electrode in the center compartment. The cathode is a large glassy carbon cup. The spiral arrangement is the same as in cell I.

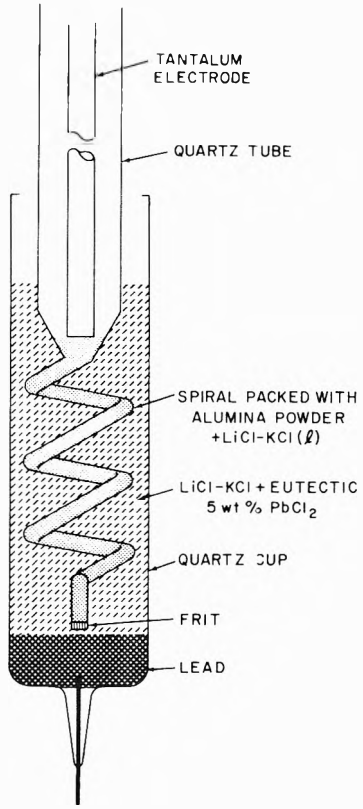

Figure 1. Experimental arrangement of cell I.

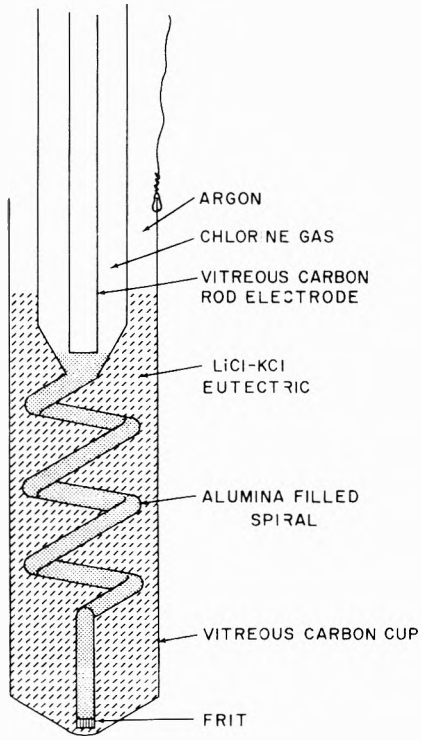

Figure 2. Experimental arrangement of cell II.

The LiCl–KCl salt was carefully treated with pure HCl and Cl_2 gases before use to remove traces of water.

The cell constants were obtained by measuring the ac resistance of the cell at 1000 Hz. This yields the ionic resistance R_{ion} and using the known values[22a] for the ionic conductivity (σ_{ion}), the cell constant is given by

$$G = R_{ion}\sigma_{ion}$$

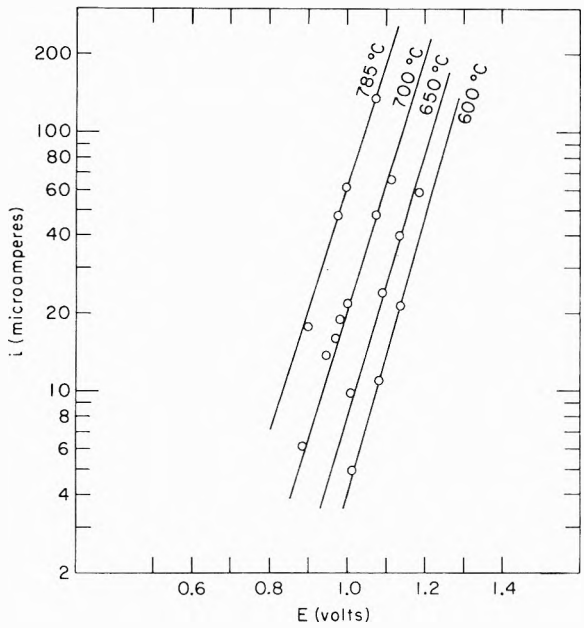

Figure 3. Current–potential curves measured using cell I.

Results

Current–potential curves measured on cell I are shown in Figure 3 at four different temperatures, 600, 650, 700, and 785°. The cell was slow to come to steady-state values and sometimes several hours were needed to reach a constant current after the voltage was changed, but the experimental arrangement allowed one to operate the cell for several weeks. It can be seen that the results conform to the exponential form of eq 2.

The voltage range studied was between approximately 0.85 and 1.15 V. Lower voltages were not used since here the current was quite low and interference from small impurities in the melt could be expected. Higher potentials could not be used since here the lithium activity at the tantalum electrode would become high enough that the lithium would react with the quartz container. At 700° for $E = 1.15$ V, the lithium activity at the tantalum is 10^{-5}.

Values of the current measured on the plateau of the current–potential curve from cell II are given at three temperatures in Table I. Difficulty was encountered in the measurements of cell II from an ionic current brought about by release of Cl_2 gas at the cathode. Raleigh encountered the same trouble in his studies of solid AgBr but it was more pronounced with the molten salt since the ionic conductivity here is considerably higher. The current was constant between 0.8 and approximately 1.2 V and these values of the current were used to calculate σ_h^{ref}.

From the results of Figure 3 and Table I using eq 2–4, 6 and 7, one can construct the diagram shown in Figure 4 for 700°. Here the electron and electron hole conductivities are shown in relation to the ionic conductivity as a function of lithium activity in the melt.

Temperature coefficients of σ_e^{ref} and σ_h^{ref} have been used to extrapolate results to 450°, and the diagram in Figure 5 is based on these values.

Previous measurements on electronic conductivity have been carried out in the region of high lithium activity which was inaccessible in these studies due to the use of quartz as a container. Nevertheless the results can be of use for the study of certain aspects of molten salt electrochemistry as is shown below. Further measurements are

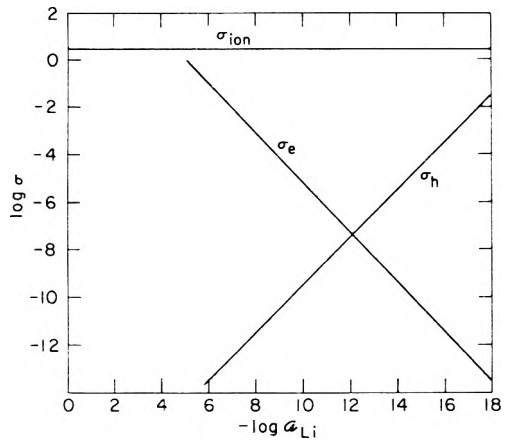

Figure 4. Electron, electron-hole, and ionic conductivity of LiCl–KCl eutectic at 700°.

TABLE I: Results from Cell II with $G = 261$ cm^{-1}

T,°C	i, μA	σ_h^{ref}, ohm^{-1} cm^{-1}	Log σ_h^{ref}
680	6.5	0.020	−1.68
730	17	0.0513	−1.29
785	50	0.143	−0.844

underway to examine the region of higher metal activities. This requires a new experimental arrangement as well as possible alteration of the equations due to the necessity of using Fermi statistics for higher electron concentrations.

Applications

LiCl–KCl eutectic is often employed as an electrolyte in concentration cells used for measuring activities of metals in liquid alloys.[22b] From the results of the present work one can calculate which metals may be examined with such cells without interference from electronic conductivity.

Consider the following cell[23] at 800°K.

$$\text{U(s)} \mid \text{LiCl–KCl} + 3\%\ \text{UCl}_3 \mid \text{U–Bi(l)} \qquad \text{(III)}$$

Wagner[24] has derived equations which describe the emf of galvanic cells with partial electronic conductivity. For cell III without electronic conductivity the emf is given by the general equation

$$E = -(RT/3F) \ln a_U''$$

where a_U'' is the activity of uranium at the right-hand electrode. Using Wagner's equations, the emf of cell III with electronic conductivity is given by

$$E = -\frac{RT}{3F} \ln a_U'' - \frac{RT}{F} t_e^0[1 - (a_U'')^{1/3}] \qquad (8)$$

where t_e^0 is the transference number of electrons in the electrolyte at the left-hand electrode, *i.e.*, equilibrated with U metal. Here

$$t_e = \sigma_e/(\sigma_e + \sigma_{ion})$$

In order to use the data from the present investigation one has to calculate the Li activity at the left-hand electrode, then with the aid of the diagram shown in Figure 5 one obtains t_e^0. By considering the reaction

$$\text{U} + 3\text{LiCl(KCl)} = \text{UCl}_3\text{(LiCl–KCl)} + 3\ \text{Li} \qquad (9)$$

one obtains

$$a_{Li} = \exp(-\Delta G^\circ/3RT)[a_{LiCl}/a_{UCl_3}^{1/3}]$$

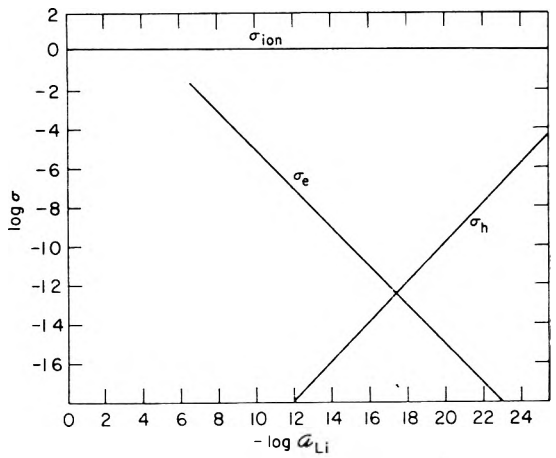

Figure 5. Electron, electron-hole, and ionic conductivity of LiCl–KCl eutectic at 450°.

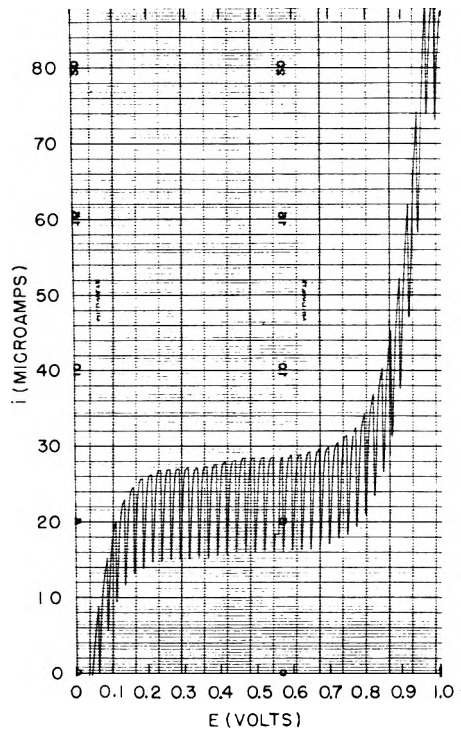

Figure 6. Polarogram of a 1.8 m*M* $PbCl_2$ solution in LiCl–KCl eutectic at a drop time of 4 sec.

where ΔG° is the free-energy change of reaction 9 with reactants in their standard state. The value of a_{UCl_3} is estimated as 1.8×10^{-3} so that $a_{Li} = 10^{-7}$ with $\Delta G^f_{LiCl} = -81{,}481$ cal,[25] $\Delta G^f_{UCl_3} = -162{,}000$ cal,[26] $a_{LiCl} = 0.40$,[20] and $a_{UCl_3} = 1.8 \times 10^{-3}$. Using Figure 5 for the values of σ_e (σ_e varies very little with temperature) and the literature value of σ_{ion}, one obtains $t_e = 0.0032$ so that the second term in eq 8 is less than 1 mV. Electronic conductivity therefore does not interfere with measurements using U metal. As one increases the temperature to 900°K, however, the correction term is approximately 1.2 mV; therefore temperature coefficients used to obtain the entropy of mixing would be unreliable for cell III.

In contrast to the U cell if one considers the following cell at 800°K

$$\text{Mg(s)} \mid \text{LiCl–KCl} + 10\%\ \text{MgCl}_2 \mid \text{Mg–Pb(l)} \qquad \text{(IV)}$$

at an alloy composition where $a_{Mg} \ll 1$, one obtains a cor-

rection term as high as 25 mV, therefore LiCl–KCl should not be used as an electrolyte with Mg cells.

The results of this study can also be applied to molten salt polarography. Figure 6 shows a polarogram taken on a 1.8 mM solution of $PbCl_2$ in LiCl–KCl at 450°.[27] The current increases very rapidly at about 0.8 V greater than the half-wave potential of $PbCl_2$. This has been ascribed by the authors to the reduction of the solvent, but it is now believed to be due to electronic conductivity. The cell

$$\text{Bi}\,|\,\text{LiCl-KCl} + PbCl_2\,|\,\text{reference electrode} \quad (\text{V})$$

is the same as cell I except spherical diffusion occurs at the dropping electrode and linear diffusion takes place in cell I. The diffusion at a dropping electrode is governed by the Ilkovic equation for dropping bismuth

$$i = 880D^{1/2}Cm^{2/3}t^{1/6} \quad (10)$$

where i is the diffusion current in microamperes measured at the maximum current of each drop, t the drop time in seconds, m the mass of the flowing bismuth in mg/sec, D the diffusion coefficient in cm^2/sec, and C the concentration in millimoles/liter.

One can now apply this equation to the current of the quasielectrons and it reads

$$i_e = 880D_e^{1/2}C_e^{\text{ref}}m^{2/3}t^{1/6} \quad (11)$$

where D_e is the diffusion coefficient of quasielectrons, and C_e^{ref} is their concentration in LiCl–KCl in equilibrium with the reference electrode. From the well-known equation

$$\sigma_e = u_e n_e e \quad (12)$$

where u_e is the mobility of electrons, n_e is their concentration in electrons/cc, and e is the charge on the electron one obtains

$$C_e^{\text{ref}} = \sigma_e^{\text{ref}}10^6/u_e e N_A \quad (13)$$

after changing units to comply with eq 11 where N_A is Avagadro's number. From the Nernst–Einstein relation

$$D_e = u_e(RT/F) \quad (14)$$

and the relation $C_e = C_e^{\text{ref}}\exp(EF/RT)$ one obtains

$$i_e = 880\left(\frac{RT}{F}\right)^{1/2}\frac{m^{2/3}t^{1/6}\sigma_e^{\text{ref}}}{eN_A u_e^{1/2}}\exp\left(\frac{EF}{RT}\right) \quad (15)$$

Since $m^{2/3}t^{1/6} = 2.30$ for the polarogram shown in Figure 6 one obtains

$$i_e = 5.24 \times 10^3\frac{\sigma_e^{\text{ref}}}{u_e^{1/2}}\exp\left(\frac{EF}{RT}\right) \quad (16)$$

One can estimate from the half-wave potential of $PbCl_2$ that the Li activity at the reference electrode of cell V is 3.16×10^{-16} so that from Figure 5 $\sigma_e^{\text{ref}} = 3.16 \times 10^{-11}$. From eq 16 and the polarogram, the mobility at 450° is $u_e = 1.25 \times 10^{-4}$ cm/sec.

Other applications of a qualitative nature are apparent from this study. In the production of metals by electrolysis of molten salts where there is a possibility of electronic conduction it is advantageous to minimize convection in the melt. In measurements of double layer capacitance in molten salts where an ideal polarized electrode is desired, one is limited to a narrow potential region; otherwise, a small but measurable current due to electrons or electron holes will interfere with the capacitance measurements. Also in the purification of molten salts by electrolysis of reducible impurities, the current will decrease upon reduction of impurities but will probably not go to zero due to electronic conductivity.

References and Notes

(1) This work was performed under the auspices of the U. S. Atomic Energy Commission.
(2) (a) M. A. Bredig in "Molten Salt Chemistry," M. Blander, Ed., Interscience, New York, N. Y., 1964, pp 367–425; (b) J. D. Corbett in "Fused Salts," B. R. Sundheim, Ed., McGraw-Hill, New York, N. Y., 1964, pp 341–407.
(3) L. F. Grantham and S. J. Yosim in "Molten Salts. Characterization and Analysis," G. Mamantov, Ed., Marcel Dekker, New York, N. Y., 1969, pp 409–441.
(4) D. O. Raleigh, *J. Chem. Phys.*, **38**, 1677 (1963).
(5) S. A. Rice, *Discuss. Faraday Soc.*, **32**, 181 (1961).
(6) C. Wagner, *Proc. Comite Int. Thermodyn. Cinet. Electrochem.*, **7**, 361 (1957).
(7) C. Wagner, *Z. Electrochem.*, **60**, 4 (1956).
(8) J. B. Wagner and C. Wagner, *J. Chem. Phys.*, **26**, 1597 (1957).
(9) B. Illschner, *J. Chem. Phys.*, **28**, 1109 (1958).
(10) D. Raleigh, *J. Phys. Chem. Solids*, **26**, 329 (1965).
(11) A. Morkel and H. Schmalzried, *J. Chem. Phys.*, **36**, 3101 (1962).
(12) J. Patterson, E. Bogren, and R. Rapp, *J. Electrochem. Soc.*, **114**, 752 (1967).
(13) Y. J. van der Meulen and F. A. Kroger, *J. Electrochem. Soc.*, **117**, 69 (1970).
(14) K. Weiss, *Electrochim. Acta*, **16**, 201 (1971).
(15) L. D. Burke, H. Rickert, and R. Steiner, *Z. Phys. Chem. (Frankfurt am Main)*, **74**, 146 (1971).
(16) J. D. Schieltz, J. W. Patterson, and D. R. Wilder, *J. Electrochem. Soc.*, **118**, 1257 (1971).
(17) M. S. Whittingham and R. A. Huggins, *J. Electrochem. Soc.*, **118**, 1 (1971).
(18) A. V. Joshi and J. B. Wagner, Jr., *J. Phys. Chem. Solids*, **33**, 205 (1972).
(19) D. Raleigh in "Progress in Solid State Chemistry," Vol. 3, H. Reiss, Ed., Pergamon Press, New York, N. Y., 1966, p 83.
(20) E. Aukrust, H. Björge, H. Flood, and T. Forland, *Ann. N. Y. Acad. Sci.*, **79**, 830 (1960).
(21) L. Yang and R. G. Hudson, *Trans. Met. Soc. AIME*, **215**, 589 (1959).
(22) (a) R. A. Oriani, *J. Electrochem. Soc.*, **103**, 194 (1956); (b) E. R. Van Artsdalen and I. S. Yaffee, *J. Phys. Chem.*, **59**, 118 (1955).
(23) R. H. Wiswall and J. J. Egan, *Proc. Int. At. Energy Ag., Symp., 1962*, 345 (1962).
(24) C. Wagner in "Advances in Electrochemistry and Electrochemical Engineering," Vol. 4, P. Delahay and C. Tobias, Ed., Wiley-Interscience, New York, N. Y., 1966, pp 1–46.
(25) JANAF Thermochemical Tables, *Nat. Stand. Ref. Data Ser., Nat. Bur. Stand.*, **No. 37** (1971)
(26) J. J. Egan, W. McCoy, and J. Bracker, *Proc. Int. At. Energy Ag., Symp., 1962*, 163 (1962).
(27) R. J. Heus and J. J. Egan, *J. Electrochem. Soc.*, **107**, 824 (1960).

Association of Protons with Oxygen-Containing Molecules in Aqueous Solutions. IV. Esters

C. F. Wells

Department of Chemistry, University of Birmingham, Edgbaston, Birmingham B15 2TT, England *(Received November 10, 1972)*

The equilibrium constant K_c for the penetration of $(H_2O)_4H_{aq}^+$ by esters has been determined in dilute solution in aqueous HCl using spectrophotometric measurements on *p*-nitroaniline. The influence of electron-releasing groups on K_c is not as clear as for alcohols, ketones, and carboxylic acids due to steric hindrance involving the alkyl groups, but it is concluded that protonation *via* hydrogen-bonded attachment occurs predominately on the carbonyl oxygen atom.

Previous investigations[1] in this series have included measurements on the replacement of water molecules in the aquo proton $(H_2O)_4H_{aq}^+$ by alcohols, glycols, ketones, and carboxylic acids. Distribution of the proton affinity among the bonds in the protonated complex containing water and the oxygen-containing organic molecule, probably accompanied by rearrangement of the molecules within the complex, results in effective protonation of the organic molecule at an O atom. The concentration quotient $K_c = [ROH_{2aq}^+]/[ROH][(H_2O)_4H_{aq}^+]$ has been determined in aqueous HCl using *p*-nitroaniline (B). It has been shown that eq 1 is obeyed,[1,2] where c_0, c_R, and c are [B] without added HCl or ROH, with added HCl and ROH, and with added HCl only, respectively, and w and a are the concentrations of unprotonated water and the total added concentration of ROH.

$$\frac{cc_R}{c_R - c} = \frac{K_2F_2w}{K_1F_1a}\left|\frac{c_0c_R}{c_0 - c_R} + \frac{c_0w}{K_1F_1a}\right. \qquad (1)$$

K_1F_1 and K_2F_2 are the concentration quotients for reactions 2 and 3, respectively, with $F_2 = f_Bf(ROH_2^+)/f(BH^+)f_{ROH}$ and $F_1 = f_Bf_P/f(BH^+)f(H_2O)$ (ROH_2^+ = $ROH(H_2O)_3H_{aq}^+$ and $P = (H_2O)_4H_{aq}^+$).

$$B + (H_2O)_4H_{aq}^+ \rightleftharpoons BH_{aq}^+ + \text{water} \qquad (2)$$

$$B + ROH(H_2O)_3H_{aq}^+ \rightleftharpoons BH_{aq}^+ + ROH_{aq} \qquad (3)$$

Experimentally, plots of $cc_R/(c_R - c)$ *vs.* $c_R/(c_0 - c_R)$ are linear with an intercept = c_0w/K_1F_1a using K_1F_1/w determined in the absence of substrate, showing that the ratio F_1 is independent of a. From the symmetrical nature of F_1 it would be expected that $F_1 \sim 1$, and the agreement of the intercepts with the calculated values suggest that any deviation of F_1 from unity due to differential solvation effects must be small. In particular, the suggestion[3] that solvation effects make variations in f_B predominate over variations in f_P, $f(BH)^+$, and $f(H_2O)$ is not in accord with these observations on the intercepts. Although f_B decreases with increasing a,[3] *e.g.*, for methanol $f_B = 0.85$ in 5% v/v and $f_B = 0.17$ in 40% v/v, and for 2-propanol $f_B = 0.83$ in 5% v/v and $f_B = 0.054$ in 40% v/v, any variation in F_1 of a similar magnitude to that in f_B would show clearly in changes in the intercept.[2] It is also of interest in this connection that the linearity of the plots of $(-d[O_2]/dt)^{-1}$ *vs.* $[substrate]^{-1}$ observed in the oxidation of secondary alcohols and an ether by the photoexcited anthraquinone-2-sulfonate ion in acidic conditions requires the symmetrical term $f_{ROH}f_P/f(ROH_2^+)f(H_2O)$ to remain ~ 1 with varying a. Values for K_c are derived in two ways: (i) directly from the slopes of the plots of $cc_R/(c_R - c)$ *vs.* $c_R/(c_0 - c_R)$ or (ii) indirectly, by determining K_2F_2 from the ratio slope/intercept of the latter plots, from which $[ROH(H_2O)_3H_{aq}^+]$ is derived and then K_c. K_c from ii is independent of [HCl] at any particular value of a and the close agreement with K_c from i supports the above conclusion that F_1 is independent of a and ~ 1.0; the relationship between these two methods for calculating K_c has been critically examined.[2,3] These values[1] for K_c also agree well with K_c determined from conductivity, ionic transport, calorimetry, and the kinetics of acid-catalyzed reactions in dilute aqueous solutions of mineral acids.[1,2,4,5]

From the earliest consideration of these equilibria arising from observations of the photosensitized autoxidation of alcohols,[6] it has been assumed that they occur between solvated protons containing the organic molecule and other solvated protons without ROH. In highly aqueous media, ROH from the bulk solvent replaces an H_2O molecule in $(H_2O)_4H_{aq}^+$ followed probably by a rearrangement of the molecules and hydrogen bonds, and in media of low water content, *e.g.*, H_2SO_4, ROH replaces either an H_2O or a solvent molecule in a solvated proton quite different from $(H_2O)_4H_{aq}^+$.[1] Nevertheless, in both cases, a protonated, solvated ROH is involved, the difference in the equilibrium constants[1] arising from the difference in the nature of the solvation.

K_c is independent of a when $a \leq 10\%$ v/v and is usually determined at $a = 2$ or 5% v/v[1] where $f_B \rightarrow 1.0$ and is $\gtrsim 0.85$.[3] Such values for K_c have been determined over a range of temperatures,[1,6] and $ROH(H_2O)_3H_{aq}^+$ is oxidatively inert compared with ROH_{aq}.[1,6] This method involving the spectrophotometric estimation of c_R and c has now been applied to esters.

Experimental Section

Materials. All the esters used were purified by fractional distillation. All other materials were as used and prepared previously.[1]

Procedure. This was as used previously with $c_0 = 1.45 \times 10^{-4}$ *M*, except that, to avoid any acid-catalyzed hydrolysis of the esters, the HCl solution was added to the aqueous mixture containing NaCl, *p*-nitroaniline, and ester just before sampling for the spectrophotometric

measurement. Negligible hydrolysis occurred during the time required to measure the optical density.[7]

Results and Discussion

Figure 1 shows plots of $cc_R/(c_R - c)$ *vs.* $c_R/(c_0 - c_R)$ for methyl acetate, ethyl acetate, *n*-propyl acetate, isopropyl acetate, and methyl *n*-propionate all in aqueous HCl at 25.0° with ionic strength adjusted to $\mu = 1.00$ by the addition of sodium chloride. The concentrations of methyl acetate and ethyl acetate were 5% v/v, but for all the other esters the maximum concentration obtainable was 2% v/v. The plots for methyl and ethyl acetates, where the higher concentrations of 5% v/v could be used, show good straight lines with little scatter of the points and the intercepts agreeing well with those calculated from K_1F_1/w. The linearity of these plots and the agreement between the observed and calculated intercepts is as good as found previously for the other substrates.[1] Although the plots for the other esters in Figure 1 are not as good, with a greater scatter of the points due to the necessity for using the lower concentration of 2% v/v, the agreement found for the other substrates between the calculated and the observed intercepts,[1] now extended here to methyl and ethyl acetates, allows the use of the calculated intercepts as an additional point with these esters. The deviation of the point with the lowest [HCl], *i.e.*, the highest $c_R/(c_0 - c_R)$, for *n*-propyl acetate probably arises from incomplete solubility of the ester at low [HCl] in $\mu = 1.00$. Values for K_c determined by method i are given in Table I together with values for K_2F_2 determined by method ii. Values for K_c determined *via* K_2F_2 as in (ii) are given in Table II, and these are in good agreement with K_c from method i, as found with all other substrates.[1,2,6] Unfortunately, the solubility of other suitable esters is too low in these solutions of electrolytes for a complete set of observations over the range of [HCl] indicated in Table II, but in two cases, methyl *n*-butyrate and methyl isobutyrate, c_R is determinable at the high end of the [HCl] range, and estimates of K_c can therefore be made for these esters using these observations and the intercept calculated from K_1F_1/w with $a = 0$. These approximate values for K_c are included in Table I.

When the substrate is an alcohol (= ROH), K_c increases with the increasing electron-releasing inductive effect of R, but branching in R produces steric hindrance to the penetration of $(H_2O)_4H_{aq}^+$ by ROH and, similarly, for ketones R_1R_2CO and carboxylic acids R_3COOH, K_c increases with the increasing electron-releasing inductive effect of R_1, R_2, and R_3 with a corresponding reduction for branching. Table I shows that for esters R_4COOR_5 there is no similar straightforward explanation for the variation of K_c with unbranched R_4 and R_5. With $R_5 = CH_3$, K_c decreases when R_4 changes from CH_3 to CH_3CH_2 and then increases when R_4 becomes $CH_3CH_2CH_2$, but, nevertheless, excluding $R_4 = CH_3$, K_c increases with change in R_4 in the order $CH_3CH_2 < CH_3CH_2CH_2 < CH_3CH_2(CH_3)CH$. Likewise, with $R_4 = CH_3$, K_c first increases when R_5 changes from CH_3 to CH_3CH_2 but then decreases again in changing R_5 from CH_3CH_2 to $CH_3CH_2CH_2$. However, contrary to the effect of branching in R for alcohols, in R_1 and R_2 for ketones, and in R_3 for carboxylic acids, change of R_5 from $CH_3CH_2CH_2$ to $(CH_3)_2CH$ with R_4 remaining as CH_3 *increases* K_c, and a similar effect is also suggested by the increase in K_c in going from $R_4 = CH_3CH_2CH_2$ to $R_4 = (CH_3)(CH_3CH_2)CH$ with $R_5 = CH_3$. The interpretation of the variation of K_c for esters with the structure of R_4 and R_5 is complicated by the existence of two possible sites for the protonation. This ambiguity also exists in the interpretation of the mechanistic data on the acid-catalyzed hydrolysis of esters.[8] Ingold and coworkers[9,10] prefer pro-

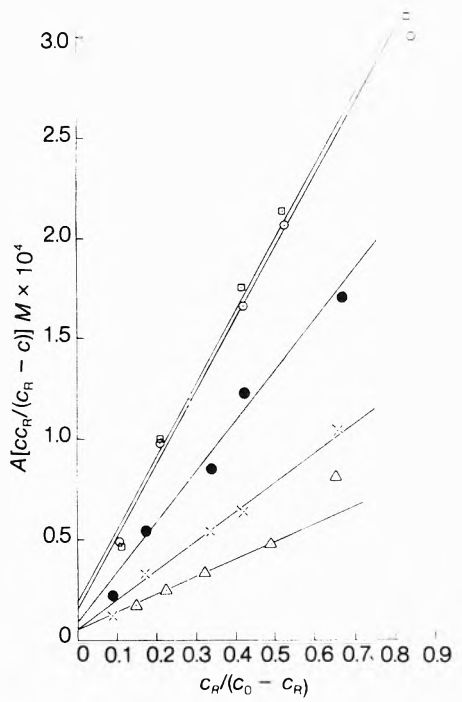

Figure 1. Plots of $cc_R/(c_R - c)$ *vs.* $c_R/(c_0 - c_R)$ at 25° and $\mu = 1.00$: ⊙, 5% v/v methyl acetate, $A = 1.0$; ⊡, 5% v/v ethyl acetate, $A = 1.0$; △, 2% v/v *n*-propyl acetate, $A = 0.10$; ×, 2% v/v isopropyl acetate, $A = 0.10$; ●, 2% v/v methyl *n*-propionate, $A = 0.20$.

TABLE I: K_c Calculated by Method i for 25° and $\mu = 1.00$

Ester	K_2F_2	K_c, M^{-1}	Hindrance relative to CH_3COOCH_3 at >C=O	Hindrance relative to CH_3COOCH_3 at acyl O
$CH_3C(=O)OCH_3$	25	0.64	...	...
$CH_3C(=O)OCH_2CH_3$	20	0.78	Small	None
$CH_3C(=O)OCH_2CH_2CH_3$	33	0.48	Large	Small
$CH_3C(=O)OCH(CH_3)_2$	27	0.58	Large	None
$CH_3CH_2C(=O)OCH_3$	29	0.55	Small	Small
$CH_3CH_2CH_2C(=O)OCH_3$	...	~0.67	Small	Large
$CH_3CH(CH_2CH_3)C(=O)OCH_3$	...	~1.5	Small	Large

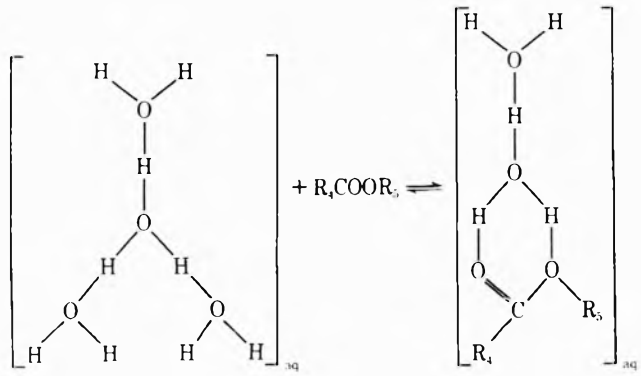

Figure 2. Possible penetration of trigonal pyramidal $(H_2O)_4H_{aq}^+$ by an ester R_4COOR_5 involving protonation of both the carbonyl and acyl O atoms.

TABLE II: Values of K_c Calculated by Method ii for 25° and μ = 1.00

[HCl], *M*	5% v/v methyl acetate	5% v/v ethyl acetate	2% v/v *n*-propyl acetate	2% v/v isopropyl acetate	2% v/v methyl *n*-propionate
0.10	0.67	0.84	...	0.62	0.59
0.16	0.67	0.82	...	0.60	0.58
0.20	0.66	0.78	0.50	0.60	0.56
0.28	...	...	0.48	...	...
0.40	0.64	0.79	0.47	0.58	0.55
0.60	...	...	0.47	...	...
0.80	0.61	0.73	0.43	0.56	0.53
1.00	...	...	0.44	...	...
Av	0.65	0.79	0.47	0.59	0.56

tonation on the acyl O atom, whereas Bender prefers protonation on the carbonyl O atom.[11] Bender uses the argument developed by Stewart and Yates[12] from a comparison of values for pK_a for the corresponding conjugate acids of substituted acetophenones and substituted benzoic acids. There is a close correlation between pK_a for the acetophenones and their carbonyl stretching frequencies $\nu_{C=O}$ in the infrared, and although there is only a rough correlation between pK_a and $\nu_{C=O}$ for the benzoic acids, pK_a for the benzoic acids correlate linearly with pK_a for the acetophenones. This latter evidence is convincing for carbonyl protonation in 44–96% H_2SO_4 where, however, the structure of water is largely collapsed and the solvated proton $(H_2O)_nH_{solv}^+$ has $n < 4$.[13] In these conditions, the apparent acid dissociation constant of protonated water is considerably less than that of the trigonal pyramidal complex $(H_2O)_4H_{aq}^+$ in aqueous solution,[1,2] and Stewart and Yates' results are not necessarily comparable with those in aqueous solution. Indeed, on the picture of penetration of $(H_2O)_4H_{aq}^+$ by the substrate,[1,2] both the carbonyl and the acyl O atoms could share in the proton affinity by hydrogen bonding, as in Figure 2, whereas this is less likely with $(H_2O)_2H_{solv}^+$ and $(H_3O^+)_{solv}$ in concentrated sulfuric acid.

It is instructive, therefore, to consider how the structures of R_4 and R_5 might inhibit the penetration into $(H_2O)_4H_{aq}^+$, and to this end Catalin models were constructed of all the esters in Table I. Assuming free rotation round all single bonds insofar as this is allowed by neighboring groups, the hindrance to access at the carbonyl and acyl O atoms by R_4 and R_5 has been assessed visually relative to that in methyl acetate. To allow for the crudity of the assessment, a three-point scale is adopted, *i.e.*, none, small, and large, and these are recorded in Table I. The following points emerge from consideration of these scales of hindrance in relation to the values for K_c.

(a) A large hindrance at the carbonyl O atom reduces K_c and a large hindrance at the acyl O atom has only a small effect on K_c, so that the effect on K_c of hindrance at the carbonyl O atom predominates over hindrance at the acyl O atom. (b) In general, an increasing electron-releasing effect in R_4 increases K_c, but an electron-releasing effect in R_5 produces only a small increase in K_c.

The small change in K_c arising from an increase in the electron-releasing effect in R_5 may be a distant effect on the carbonyl O atom, and although it is not possible to say that protonation occurs exclusively at that O atom, the conclusion from a and b is that protonation occurs predominately at the carbonyl O atom.

References and Notes

(1) C. F. Wells, *Trans. Faraday Soc.*, **61**, 2194 (1965); **62**, 2815 (1966); **63**, 147 (1967).
(2) C. F. Wells, *J. Chem. Soc., Faraday Trans. 1*, **68**, 993 (1972).
(3) J. Sierra, E. Teixido, and P. A. H. Wyatt, *J. Chem. Soc., Faraday Trans. 1*, **68**, 290 (1972).
(4) U. L. Haldna and A. I. Talvik in "Chemistry of the Carbonyl Group," S. Pattai, Ed., Interscience, New York, N. Y., 1966, p 429; V. A. Palm and U. L. Haldna, *Dokl. Akad. Nauk SSR*, **135**, 667 (1960); U. L. Haldna, L. Ploom, and A. Maroos, *Zap. Tartu Gos. Univ.*, **127**, 65 (1962); U. L. Haldna and R. K. Püss, *Russ. J. Phys. Chem.*, **38**, 1529 (1964); U. L. Haldna, *Org. Reactiv. (USSR)*, **1**, 184 (1964); **2**, 381 (1965).
(5) C. F. Wells, *J. Phys. Chem.*, **77**, 1997 (1973).
(6) C. F. Wells, *Discuss. Faraday Soc.*, **29**, 219, 255 (1960); *Trans. Faraday Soc.*, **57**, 1703, 1719 (1961); C. F. Wells and G. Davies, *ibid.*, **63**, 2737 (1967); C. F. Wells, C. Barnes, and G. Davies, *ibid.*, **64**, 3069 (1968); C. F. Wells and C. Barnes, *J. Chem. Soc. A*, 1626 (1968); 430, 1405 (1971); *Trans. Faraday Soc.*, **66**, 1154 (1970); **67**, 3297 (1971); C. F. Wells and M. Husain, *ibid.*, **66**, 679, 2855 (1970); **67**, 1086 (1971); R. Varadarajan and C. F. Wells, *J. Chem. Soc., Faraday Trans. 1*, **69**, 521 (1973); C. F. Wells and A. F. M. Nazer, to be submitted for publication.
(7) H. M. Dawson and W. Lowson, *J. Chem. Soc.*, 2146 (1928).
(8) H. B. Watson, "Modern Theories of Organic Chemistry," 2nd ed, Oxford University Press, London, 1941, Chapter 9.
(9) E. H. Ingold and C. K. Ingold, *J. Chem. Soc.*, 756 (1932); S. C. Datta, J. N. E. Day, and C. K. Ingold, *Trans. Faraday Soc.*, **37**, 636 (1941).
(10) C. K. Ingold, "Structure and Mechanism in Organic Chemistry," 2nd ed, Bell, London, 1969, Chapter 15.
(11) M. L. Bender, *Chem. Rev.*, **60**, 53 (1960).
(12) R. Stewart and K. Yates, *J. Amer. Chem. Soc.*, **80**, 6355 (1958); *Can. J. Chem.*, **37**, 664 (1959); *J. Amer. Chem. Soc.*, **82**, 4059 (1960).
(13) P. A. H. Wyatt, *Discuss. Faraday Soc.*, **24**, 162 (1957).

Association of Protons with Oxygen-Containing Molecules in Aqueous Solutions. V. The Determination of the Protonation Equilibrium Constant from Kinetic Measurements

C. F. Wells

Department of Chemistry, University of Birmingham, Edgbaston, Birmingham B15 2TT, England *(Received November 10, 1972)*

Kinetic equations derived for acid-catalyzed reactions show that the test for a preequilibrium involving a proton solvated by both water and substrate molecules, a protonated, water-solvated substrate, is the presence of an intercept in plots of (rate constant)$^{-1}$ against (antilog H_0)$^{-1}$ in conditions where the activity of water $a_w \sim 1$ and the solvated aquo proton is $(H_2O)_4H_{aq}^+$. Application of this test to a range of substrates in aqueous hydrochloric acid or aqueous perchloric acid shows that the protonated, water-solvated substrate is involved in six, and probably seven, cases; in the other cases, the intercept is indistinguishable from the origin. Good agreement is found between values for the formation equilibrium constant K of the protonated substrate derived from the kinetics and values derived from a static, spectrophotometric method using *p*-nitroaniline, where the latter data are available. Assuming the protonation preequilibrium to be generally involved, values for the equilibrium constants are in line with structural variations found in other substrates using the static method. Deviations from these values at high [acid] where $a_w < 1$ are discussed. Values for the rate constant $\times K$ and for the rate constant at 25° are calculated.

The kinetics of various reactions of organic molecules containing oxygen atoms which are catalyzed by acids have been investigated over wide ranges of acid concentrations,[1,2] *e.g.*, the hydrolysis of esters, acetals, and lactones and the iodination of ketones, and although there is general agreement about a preequilibrium involving protonation of the substrate, it is generally assumed that the protonation equilibrium constant is very small. However, a static method[3] for determining the protonation equilibrium constant K_c = [protonated substrate]/[unprotonated substrate][solvated aquo protons] using the spectrophotometric estimation of *p*-nitroaniline suggests that, at concentrations of acid low enough for the solvated proton to be $(H_2O)_4H_{aq}^+$, $K_c \sim 0.1$–$1.5\ M^{-1}$ for many organic substrates containing a basic oxygen atom, and it should therefore be possible to determine K_c from the kinetics of acid-catalyzed reactions. There is a dispute[1,2] about whether many of these reactions involve water molecules in the rate-determining step or in subsequent steps, and these two possibilities will be considered in turn.

Derivation of Kinetic Equations

No Water Involved in the Rate-Determining Step. This situation is described by eq 1 and 2, where A = organic substrate, $H_s^+ = (H_2O)_4H_{aq}^+$, $AH_s^+ = A(H_2O)_3H_{aq}^+$, S = solvent water, and C* is the transition state. K and K_1* are thermodynamic equilibrium constants and are given by

$$K = ([AH_s^+]a_w/[A][H_s^+])(f_{AH^+}/f_A f_{H^+})$$

and

$$K_1^* = ([C_1^*]/[AH_s^+])(f_c/f_{AH^+})$$

where a_w is the activity of water and f represents the activity coefficient for the species indicated by the subscript. The rate of reaction is given by eq 3, using the

$$A + H_s^+ \rightleftharpoons AH_s^+ + S \qquad (1)$$

$$AH_s^+ \overset{K_1^*}{\rightleftharpoons} C_1^* \xrightarrow{k} \text{products} \qquad (2)$$

$$\text{rate} \propto [C_1^*] = k[C_1^*] = kK^*K[A][H_s^+](f_A f_{H^+}/f_c a_w) \qquad (3)$$

above expressions for K and K_1*. However, the total concentration of substrate $[A]_T = [AH_s^+] + [A]$, which is given by

$$[A]_T = [A]\{1 + K[H_s^+]/a_w)(f_A f_{H^+}/f_{AH^+})\} \qquad (4)$$

which, when substituted into eq 3, gives

$$\text{rate} = kK_1^*K[A]_T[H_s^+](f_A f_{H^+}/f_c a_w)/\{1 + (K[H_s^+]/a_w)(f_A f_{H^+}/f_{AH^+})\} \qquad (5)$$

If the acidity function is now introduced by substituting for the activity a_h of the solvated proton $(H_2O)_4H_{aq}^+$ from eq 6, where h_0 is

$$a_h = h_0 f_{BH^+}/f_B = [H_s^+]f_{H^+} \qquad (6)$$

the antilog of the Hammett acidity function $-H_0$ and f_{BH^+} and f_B are the activity coefficients for the protonated and unprotonated indicator molecule used in determining H_0,[4] and eq 5 is compared with the experimental rate equation at constant acidity

$$\text{rate} = k_1[A]_T \qquad (7)$$

the pseudo-first-order rate constant k_1 is given by eq 8. Plots of k_1^{-1} *vs.* h_0^{-1} should be linear with an intercept = $f_c(kK_1^*f_{AH^+})^{-1}$ and a slope = $a_w f_B f_c(kK_1^*Kf_{BH^+}f_A)^{-1}$, provided a_w, $f_B f_c/f_{BH^+}f_A$, and f_c/f_{AH^+} remain unchanged; this latter condition is expected to be fulfilled from the symmetrical nature of the activity coefficient terms, and $a_w \sim 1.0$ if [acid] does not become too high.[5-7]

$$\frac{1}{k_1} = \frac{a_w}{kK_1^*Kh_0}\frac{f_B f_c}{f_{BH^+}f_A} + \frac{f_c}{kK_1 f_{AH^+}} \qquad (8)$$

The ratio intercept/slope of such plots should be given by eq 9. The activity coefficient term in eq 9 is symmetrical and ~1.0, so that eq 9 can be modified to (10), where

the concentration quotient $K_c = [AH_s^+]/[A][H_s^+]$ is the same quantity as that derived from the static method of measuring basicity with *p*-nitroaniline.[3] As $f_{AH^+} \sim f_{H^+}$, $Ka_w^{-1} \sim K_c f_A^{-1}$, and provided $a_w \sim 1$ and $f_A \sim 1$, intercept/slope = K_c.

$$\text{intercept/slope} = (K/a_w)(f_{BH^+}f_A/f_B f_{AH^+}) \quad (9)$$

$$\text{intercept/slope} \sim K/a_w = K_c(f_{AH^+}/f_A f_{H_s^+}) \quad (10)$$

Water Involved in the Rate-Determining Step. The situation is now described by eq 11 and 12 and the rate is given by eq 13, where $K_2^* = ([C_2^*]/[AH_s^+]a_w)(f_c'/f_{AH^+})$. Proceeding as before, eq 14 is obtained for the relationship between k_1 and h_0. Again linear plots for k_1^{-1} *vs.* h_0^{-1} should be obtained provided the conditions stated before hold, but now the intercept = $f_c'(k'K_2^* f_{AH^+}a_w)^{-1}$ and the slope = $f_B f_c'(k'K_2^* K f_{BH^+}f_A)^{-1}$, which are of different forms from that obtained above. However, the ratio intercept/slope is given by eq 15, which is identical with eq 9 obtained above for the condition where water is not involved in the rate-determining step. As above, provided $a_w \sim 1$, intercept/slope = K_c.

$$A + H_s^+ \overset{K}{\rightleftharpoons} AH_s^+ + S \quad (11)$$

$$AH_s^+ + S \overset{K_2^*}{\rightleftharpoons} C_2^* \xrightarrow{k'} \text{products} \quad (12)$$

$$\text{rate} = k'[C_2^*] = k'K_2^*[AH_s^+]a_w f_{AH^+} f_c'^{-1} \quad (13)$$

$$\frac{1}{k_1} = \frac{1}{k'K_2^* K h_0} \frac{f_B f_c'}{f_{BH^+} f_A} + \frac{f_c'}{k'K_2 f_{AH^+} a_w} \quad (14)$$

$$\text{intercept/slope} = (K/a_w)(f_{BH^+}f_A/f_B f_{AH^+}) \quad (15)$$

Correction to h_0

The acidity functions available for the media in which such reactions are carried out give a measure of the acidity of the solvated proton $(H_2O)_4H_{aq}^+$, but when $[A]_T$ is approximately equal to the concentration of the added acid, $[H^+]_T > [H_s^+]$ by an extent depending on the magnitude of K and K_c. If the latter are low enough for $[H_s^+] = [H^+]_T$, then h_0 derived from $[H^+]_T$ may be used, but if K and K_c are high enough for $[H_s^+] < [H^+]_T$ then h_0 derived from $[H^+]_T$ does not represent the acidity of $(H_2O)_4H_{aq}^+$ due to appreciable formation of a solvated proton containing the substrate molecule, $A(H_2O)_3H_{aq}^+$. It is necessary, therefore, to calculate $[H_s^+]$ before h_0 can be taken from the appropriate calibration curve of H_0 *vs.* acid]. $[H^+]_T$ and $[H_s^+]$ are related as follows

$$[H^+]_T = [H_s^+] + [AH_s^+] = [H_s^+]\{1 + (K[A]/a_w)(f_A f_{H^+}/f_{AH^+})\} = [H_s^+](1 + K_c[A])$$

and if $[A] \sim [A]_T$ then

$$[H_s^+] = [H^+]_T/(1 + K_c[A]_T) \quad (16)$$

As the difference between $[H_s^+]$ and $[H^+]_T$ is not likely to be large, a plot of k_1^{-1} *vs.* h_0^{-1} with the latter derived from $[H^+]_T$ should be approximately linear also if a plot of k_1^{-1} *vs.* h_0^{-1} with the latter derived from $[H_s^+]$ is linear. This is shown to be the case. From such a plot using $[H^+]_T$ a value for K_c can be derived from the ratio intercept/slope, and then corrected by calculating $[H_s^+]$ from eq 16 with k_1^{-1} replotted *vs.* h_0^{-1} using $[H_s^+]$ on the H_0 − [acid] calibration curves. It was found that a second correction made little, if any change in h_0. As it is necessary to use the concentration of $(H_2O)_4H_{aq}^+$ (*i.e.*, without substrate in the solvation shell) present at equilibrium with the substrate added, it is not possible to determine experimentally the H_0 (or h_0) derived from this entity when $[H_s^+] < [H^+]_T$ by measurements on the acidic solutions containing the substrate as this represents the *total* acidity of the solution including *all* species of solvated proton.

Application of Eq 8 and 14 to Experimental Data

If plots of k_1^{-1} *vs.* h_0^{-1} are to be used to compute values for K, the data used must be restricted to comparatively low values of $[H^+]_T$ so that the deviation of a_w from unity may be neglected. The available data[5-7] for a_w in aqueous HCl and $HClO_4$ show that a_w has decreased by ~4% at 1 *M* acid, by ~10% at 2 *M* acid, and by ~40% in 7 *M* acid. The examination of the experimental data is therefore restricted to data obtained in the acid range 0.1–1.0 *M* with some use of results at $[H^+]_T$ up to 2.0 *M*. Unfortunately, most of the kinetic data available[1,2,8] have been obtained at $[H^+]_T \sim 1$–7 or 8 *M*, with only a limited number of substrates studied at $[H^+]_T \sim 0.1$–1.0 *M*. The values of H_0 used to compute h_0 are either those quoted with the kinetic data or calculated from calibration curves constructed from the data of Hammett and coworkers,[4,9] Bell, Dowding, and Noble,[10] and Satchell.[11] These latter calibration curves were used in making the correction to h_0 discussed above. Only kinetic data at 25° are used to compare with H_0 at 25°.

Ketones

Kinetic data are available on the iodination of acetone in the range $[H^+]_T \sim 0.1$–1.0 *M* from Dawson and Powis[12] and from Satchell[11] using acetone = 0.273 *M* at 25° in aqueous HCl. Under these conditions, the rate is zero order in iodine and the rate of the acid-catalyzed enolization is measured. Figure 1 shows that plots of k_1^{-1} *vs.* h_0^{-1} for both sets of data coincide, and $K = 0.43$ from the ratio intercept/slope. When the correction is applied to h_0, the new value for K from the linear plot of k_1^{-1} *vs.* h_0^{-1} (corrected) is 0.49. Figure 1 shows that a second correction to h_0 using $K = 0.49$ produces no significant change in h_0.

Using the data of Zucker and Hammett[13] determined under similar conditions for the rate of enolization of acetophenone from iodination experiments in aqueous $HClO_4$, Figure 1 shows a linear plot for k_1^{-1} *vs.* h_0^{-1}, and $K = 0.27$. As [acetophenone] ~ 0.01 *M*, the correction for $[CH_3PhCOH_{aq}^+]$ does not change h_0.

Esters

Figure 2 shows the linear plot of k_1^{-1} *vs.* h_0^{-1} using the data of Dubroux and de Sousa for the acid-catalyzed hydrolysis of methyl acetate in 0.1 *M* solution with [HCl] ~ 0.1–1.5 *M*.[14] From the ratio intercept/slope, $K = 0.51$ and the linear plot with h_0(corrected) (Figure 2) gives $K = 0.57$; a second correction to h_0 using $K = 0.57$ produces little change with $K = 0.60$.

A similar treatment is given in Figure 2 for the data of Harned and Pfanstiel[15] for the acid-catalyzed hydrolysis of ethyl acetate in 0.470 *M* solution with HCl ~ 0.05–1.4 *M*;[15] the data of Bell, *et al.*,[10] in the range [HCl] = 0.45–10.2 *M* agree well with that in Figure 2 in the small area of overlap. The linear plot in Figure 2 gives $K = 0.72$ and the first and second corrections give $K = 0.62$ and 0.69, respectively.

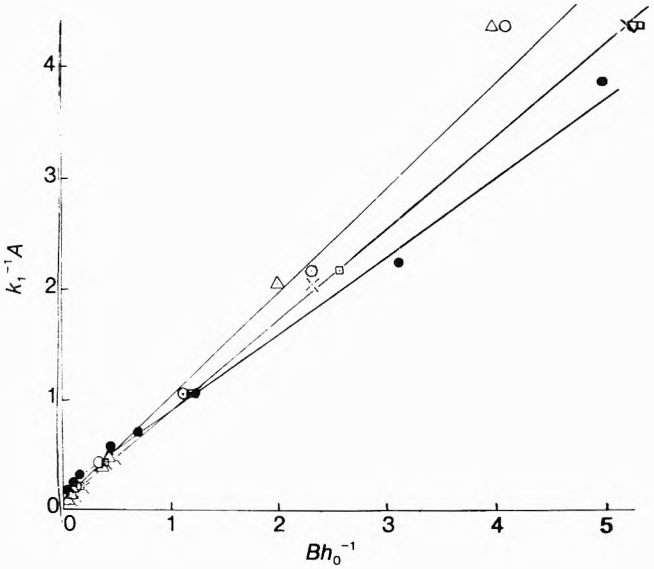

Figure 1. Plots of k_1^{-1} *vs.* h_0^{-1} for acetone ($A = 1.00 \times 10^{-4}$ (min), $B = 0.20$: data of Dawson and Powis ⊙, first correction ⊡; data of Satchell ▲, first correction ×, second correction ▽) and acetophenone ($A = 1.00 \times 10^{-5}$ (sec), $B = 1.00$, data of Zucker and Hammett ●).

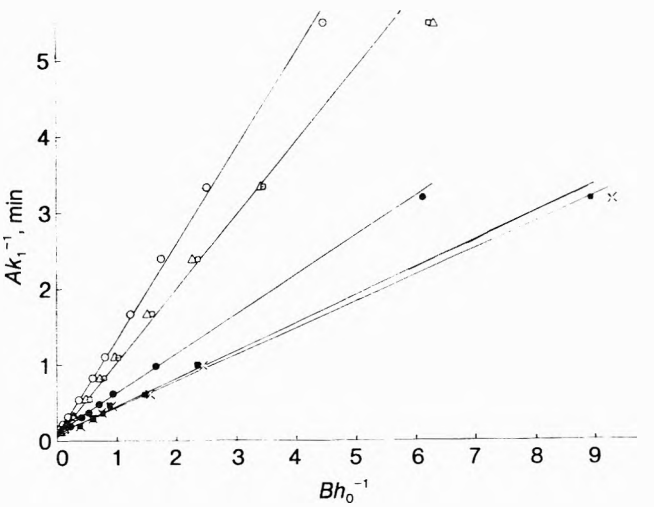

Figure 2. Plots of k_1^{-1} *vs.* h_0^{-1} for methyl acetate ($A = 2.00 \times 10^{-3}$, $B = 0.50$: data of Dubroux and de Sousa, ●; first correction, ■; second correction, ×) and ethyl acetate. ($A = 1.00 \times 10^{-3}$, $B = 0.10$: data of Harned and Pfanstiehl, ⊙; first correction, ⊡; second correction, ▲).

Salomaa's results[16] for acid-catalyzed hydrolysis of isopropyl acetate and *tert*-butyl acetate in 2% v/v solution using HCl are also plotted in Figure 3; the lowest [HCl] = 0.31 *M* for isopropyl acetate and 0.25 *M* for *tert*-butyl acetate. With isopropyl acetate the linear plot is similar to those for methyl and ethyl acetates with an intercept on the ordinate, but the linear plot for *tert*-butyl acetate apparently passes through the origin. The initial value of K for isopropyl acetate = 0.14, and as $K = 0.13$ after the first correction (Figure 3), no further correction was made. The negligible intercept with *tert*-butyl acetate shows that K is very small for this ester with an upper limit of 0.03; similar plots (Figure 3) are found for ethyl, isopropyl, and *tert*-butyl formates[17] with $K < 0.06$, 0.06, and 0.1, respectively.

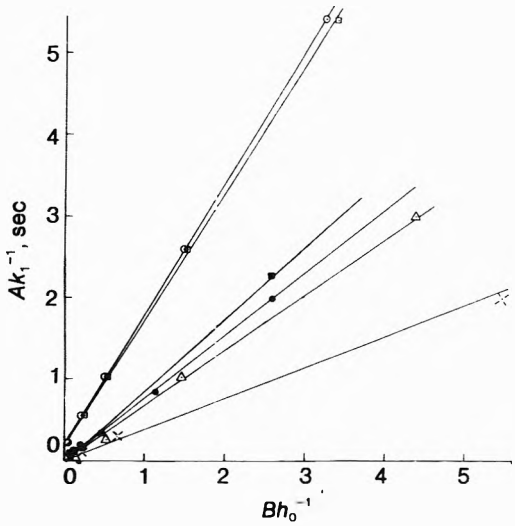

Figure 3. Plots of k_1^{-1} *vs.* h_0^{-1} using Salomaa's data for isopropyl acetate ($A = 1.00 \times 10^{-4}$, $B = 1.00$, ⊙; first correction, ⊡), *tert*-butyl acetate ($A = 1.00 \times 10^{-4}$, $B = 1.00$, ▲), ethyl formate ($A = 1.00 \times 10^{-3}$, $B = 0.40$, ●), isopropyl formate ($A = 1.00 \times 10^{-3}$, $B = 0.40$, ■), and *tert*-butyl formate ($A = 1.00 \times 10^{-3}$, $B = 0.40$, ×).

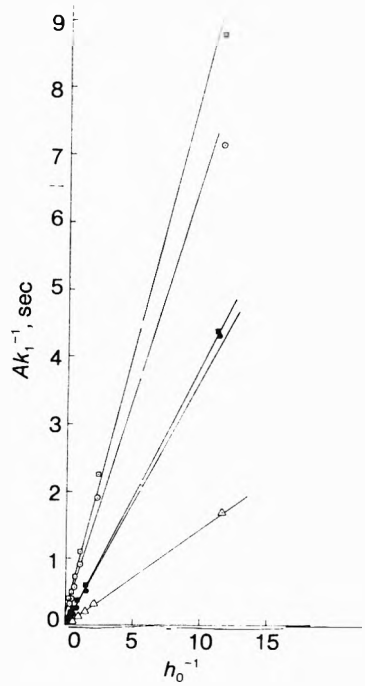

Figure 4. Plots of k_1^{-1} *vs.* h_0^{-1} using Salomaa's data for methylene diacetate ($A = 1.00 \times 10^{-4}$, ⊙), ethylidene diacetate ($A = 1.00 \times 10^{-4}$, ⊡), methoxymethyl formate ($A = 4.00 \times 10^{-3}$, ■) methoxymethyl acetate ($A = 4.00 \times 10^{-4}$, △), and ethoxymethyl acetate ($A = 4.00 \times 10^{-3}$, ●).

The hydrolysis of ethylidene diacetate has been investigated by Salomaa[18] with [HCl] = 0.1–8.0 *M* and by Bell and Lukianenko[19] with [HCl] = 0.33–8.9 *M*. The two sets of rate constants are in good agreement where they overlap, and the linear plot for Salomaa's data with [HCl] = 0.1–2.0 *M* is shown in Figure 4. The linear plot of Salomaa's data[18] for the hydrolysis of methylene diacetate with [HCl] = 0.1–2.0 *M* is also shown in Figure 4. From the ratio of intercept/slope, $K = 0.31$ for ethylene diacetate and $K = 0.34$ for methylene diacetate. As the concentration of these diacetates is ~0.05 *M* the correction to h_0

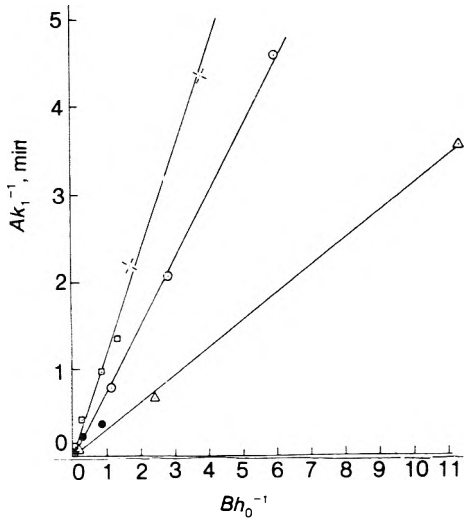

Figure 5. Plots of k_1^{-1} *vs.* h_0^{-1} for methylal ($A = 1.00 \times 10^{-3}$, $B = 0.50$: data of McIntyre and Long, ⊡; data of Skrabal and Schiffrer, ×), ethylal ($A = 4.00 \times 10^{-3}$, $B = 0.50$: data of Skrabal, *et al.*, ⊙; data of Leiniger and Kilpatrick, ●), and dipropylformal ($A = 1.00 \times 10^{-4}$, $B = 0.10$: data of Olson and Tong, ▲).

for the protonated diacetate is negligible. Salomaa has also investigated[20] the kinetics of the hydrolysis of alkoxyalkyl esters catalyzed by hydrochloric acid to concentrations of 0.1 *M*. Linear plots passing through the origin are obtained for this data (Figure 4), with $K \leq 0.07$ for methoxymethyl acetate and $K \leq 0.05$ for both ethoxymethyl acetate and methoxymethyl formate.

Acetals

Suitable data for methylal has been obtained from the work of Leiniger and Kilpatrick[21] and of Skrabal and Schiffrer[22] in aqueous HCl, and Figure 5 shows a linear plot for k_1^{-1} *vs.* h_0^{-1} passing through the origin. Similar plots are also obtained for ethylal (Figure 5) using the data of McIntyre and Long[23] and of Skrabal, *et al.*,[22,24] and for di-*n*-propylformal using the data of Olson and Tong[25] all in aqueous HCl. For methylal $K < 0.03$, for ethylal $K < 0.05$, and for di-*n*-propylformal $K < 0.06$.

Ring Compounds

Under this heading we include the acid-catalyzed depolymerization of paraldehyde and trioxane, the acid-catalyzed hydrolysis of β-isovalerolactone, and the acid-catalyzed inversion of sucrose, although the latter differs from the others in that the carbohydrate rings are not broken. The data for paraldehyde[26] and trioxane[27] in aqueous hydrochloric acid with [HCl] $\lesssim 1.4$ *M* give linear plots of k_1^{-1} *vs.* h_0^{-1} (Figure 6) which pass through the origin: $K < 0.07$ for paraldehyde and $K < 0.1$ for trioxane. The hydrolysis of β-isovalerolactone[28] in aqueous perchloric acid gives a linear plot passing through the origin (Figure 7) for k_1^{-1} *vs.* h_0^{-1} with [$HClO_4$] ~ 0.1–2.0 *M* and $K < 0.08$. The data of Dubroux, *et al.*,[29] for the hydrolysis of sucrose in aqueous hyorochloric acid gives a similar linear plot (Figure 7) with [HCl] ~ 0.1–2.0 *M* and $K < 0.1$.

Comparison of K and K_c

The values for K calculated from the above treatment of the kinetics of acid-catalyzed reactions are collected in Table I, which also includes values for K_c where they are

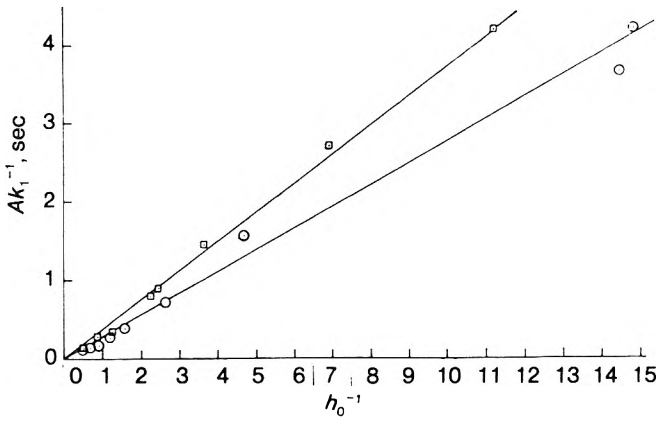

Figure 6. Plots of k_1^{-1} *vs.* h_0^{-1} for trioxane ($A = 1.00 \times 10^{-8}$, data of Bell, Bascombe, and McCoubry, ⊙) and paraldehyde ($A = 4.00 \times 10^{-5}$, data of Bell and Brown, ⊡).

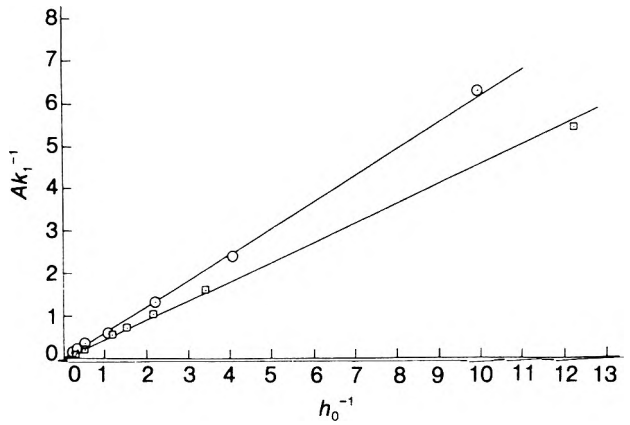

Figure 7. Plots of k_1^{-1} *vs.* h_0^{-1} for β-isovalerolactone ($A = 1.00 \times 10^{-3}$ (sec), data of Liang and Bartlett, ⊙) and sucrose ($A = 1.00 \times 10^{-2}$ (min), data of Dubroux and Rochat, ⊡).

available from the spectrophotometric measurements using *p*-nitroaniline.[3]

Table I shows that there is good agreement between K and K_c for acetone, methyl acetate, and ethyl acetate suggesting that eq 10 applies with $f_{AH^+}/f_{H^+} \sim 1.0$ and $f_A \sim 1.0$ under the conditions [acid] $\lesssim 1$ *M*. The agreement between K and K_c is not good for isopropyl acetate, but the kinetic data has only three points below 1.4 *M* HCl and none below 0.31 *M* HCl whereas all the other data (except *tert*-butyl acetate) extends to 0.1 *M* HCl; hence the data for isopropyl acetate are not suitable as a good test of the relationships. However, the low value of K for isopropyl acetate supports the existence[3] of steric hindrance to the protonation of the carbonyl O atom where the *i*Pr group has considerable effect compared with that at the acyl O atoms as shown by a Catalin model. Similarly, Catalin models for *tert*-butyl acetate and for the alkoxymethyl acetates show that the *t*-Bu and alkoxy groups have large steric hindrance to approach by $(H_2O)_4H_{aq}^+$ at the carbonyl O atom compared with only a small effect at the acyl O atom. Thus, the low values for K for these substrates support the view[3] deduced from the variation of K_c with structure using Catalin models that protonation of esters occurs predominantly on the carbonyl O atom rather than the acyl O atom. The low values of K found for all the formates are in line with the low value of K_c for formic acid compared with that for other carbox-

TABLE I: Values of K and K_c (M^{-1}) and of Rate Constants (sec^{-1}) at 25°

Substrate	K	K_c	$k''K$	k''
Acetone	0.49	0.46	1.01×10^{-5}	2.2×10^{-5}
Acetophenone	0.27		1.42×10^{-5}	5.3×10^{-5}
Methyl acetate	0.59	0.64	1.15×10^{-4}	2.0×10^{-4}
Ethyl acetate	0.71	0.78	1.65×10^{-4}	2.3×10^{-4}
Isopropyl acetate	0.14	0.58	6.3×10^{-5}	4.5×10^{-4}
tert-Butyl acetate	<0.03		1.47×10^{-4}	$>5 \times 10^{-3}$
Methoxymethyl acetate	<0.07		2.86×10^{-3}	>0.04
Ethoxymethyl acetate	<0.05		1.07×10^{-2}	>0.2
Ethyl formate	<0.06		3.2×10^{-3}	>0.05
Isopropyl formate	<0.06		2.86×10^{-3}	>0.05
tert-Butyl formate	<0.1		6.5×10^{-3}	>0.06
Methoxymethyl formate	<0.05		1.03×10^{-2}	>0.2
Methylene diacetate	0.34		1.55×10^{-4}	4.6×10^{-4}
Ethylidene diacetate	0.31		1.28×10^{-4}	4.1×10^{-4}
Methylal	<0.03		2.84×10^{-5}	$>1 \times 10^{-3}$
Ethylal	<0.05		1.75×10^{-4}	$>4 \times 10^{-3}$
Di-*n*-propylformal	<0.06		5.3×10^{-5}	$>9 \times 10^{-4}$
Paraldehyde	<0.07		1.34×10^{-4}	$>2 \times 10^{-3}$
Trioxane	<0.1		3.6×10^{-8}	$>4 \times 10^{-7}$
β-Isovalerolactone	<0.08		1.64×10^{-3}	$>2 \times 10^{-2}$
Sucrose	<0.1		3.7×10^{-4}	$>4 \times 10^{-3}$

ylic acids, and they are presumably due to the absence of the electron-releasing inductive effect in R_4 of R_4COOR_5.[3] It seems likely that the low values for K found for methylene and ethylidene diacetates, methylal, ethylal, and di-*n*-propylformal arise from the considerable effect of the electron-attracting alkoxy and acetate groups at the basic site which will cause a greater decrease in basicity than that observed when the electron-attracting group is on a more distant C atom.[3] Presumably, this latter effect is responsible for the low values for K in all the ring compounds. The low value of K for acetophenone compared with that for acetone may be due to a combination of the electron-attracting inductive effect of the phenyl group and steric hindrance to penetration of the $(H_2O)_4H_{aq}^+$ complex by the large phenyl group.

It is of interest to enquire what happens to the plots of k_1^{-1} *vs.* h_0^{-1} at high acidities. Archer and Bell[30] have investigated the variation of the rate of bromination of acetone with H_0 in the acidity range [HCl] = 1.0–8.0 M. The plot of k_1^{-1} *vs.* h_0^{-1} is approximately linear but with pronounced deviations at [HCl] $\gtrsim$ 6.0 M, and from the ratio intercept/slope Ka_w^{-1} = 0.064. For ethyl acetate with [HCl] ~ 1.0–6.0 M,[10] Ka_w^{-1} = 0.10, and for methylene[18] and ethylidene[18,19] diacetates with [HCl] ~ 1.0–8.0 M Ka_w^{-1} = 0.090 and 0.071, respectively. All these values are lower than the corresponding values for K in Table I when [HCl] ~ 0.1–1.0 M by a factor of between 4 and 8. If the change was due to the numerical decrease in a_w at high [HCl], the ratio intercept/slope should increase with increasing [HCl], and thus the actual decrease in Ka_w^{-1} is somewhat greater than this apparent decrease. The explanation for this probably lies in a change in the solvated species of the proton, *i.e.*, a change in the acid species responsible for the protonation. At low [HCl] in highly aqueous media, the solvated proton is the trigonal pyramidal $(H_2O)_4H_{aq}^+$ and the organic substrate is protonated by replacement of an H_2O molecule in the complex[3] with sharing of the proton affinity among all the H···O···H bonds in the complex. Thus, the complexes $(H_2O)_nH$ with n = 3, 2, or 1 which exist at increasing [HCl] as H_2O molecules in the solvent mixture are gradually replaced by HCl molecules have lower acid dissociation constants than the complex with n = 4, due to differences in the internal hydrogen bonding.[3] This results in a lower value for K (or K_c) at high [HCl], similar to those found in high concentrations of H_2SO_4.[3]

Rate Constant for the Hydrolysis

From eq 8 the reciprocal of the slope of the plots of k_1^{-1} *vs.* h_0^{-1} is kK_1^*K when a_w = 1.0, and similarly if eq 14 applies the reciprocal of the slope is $k'K_2^*K$, depending on which mechanism operates. However, irrespective of whether or not the mechanism involves a water molecule in the transition state, kK_1^* and $k'K_2^*$ represent the rate constant k'' for the hydrolytic step, and consequently, using the data for K in Table I values for k'' or lower limits for k'' can be obtained for 25°. These values are also collected in Table I.

Although there are dangers in comparing rate constants at one temperature only when there is an energy of activation, three apparent conclusions might be drawn from the values for k'': (a) for the simple esters R_4COOR_5, k'' increases with increasing alkylation in R_5; (b) substituting $R_5 = CH_3$ with an alkoxy group greatly increases k''; (c) methylation on the carbon atoms in the trioxane ring increases k'' considerably. Although various attempts[1,2] have been made to differentiate between mechanisms with and without an H_2O molecule in the transition state (called A2 and A1, respectively[31]), these assignments are not definite. However, on mechanisms such as eq 1 and 2 or 11 and 12 where the substrate penetrates $(H_2O)_4H_{aq}^+$, a range of transition states between A1 and A2 would be expected with H_2O molecules surrounding the substrate molecule in $A(H_2O)_3H_{aq}^+$ having a variable influence depending on the substrate. Most assignments[1,2] as A1 have been made in high [acid] where $n < 4$ in $(H_2O)_nH_{solv}^+$ and A1 might be preferred due to the deficiency of water, and changes to A2 have been found[2] as $n \to 4$ in lower [acid] and the availability of water increases. The use of ^{18}O to distinguish[2,32] between acyl oxygen (A_{AC}) and alkyl oxygen (A_{AL}) fission shows that the hydrolysis of

methyl, ethyl, and isopropyl acetates and methylene and ethylidene diacetates ($k'' \sim 2\text{-}5 \times 10^{-4}$ sec^{-1}) are $A_{AC}2$ in high [acid], whereas the hydrolysis of *tert*-butyl acetate and the alkoxymethyl esters which are $A_{AL}1$ in high [acid] have much higher values for k''. Although the latter may be $A_{AL}2$ at the low [acid] where k'' is determined, the large increase in k'' mentioned in (a) above between isopropyl and *tert*-butyl acetates and those in (b) above may arise from stabilization of the carbonium ion in the A_{AL} mechanism by the inductive effect of the CH_3 groups in *tert*-butyl acetate and the lone pairs on the alkoxy O atom. (c) must arise from the assistance given to fission of the C–O bond by the inductive electron-release effect of the methyl groups.

Conclusion

Given the evidence[3] for the existence of protons solvated by both water molecules and oxygen-containing organic molecules, constituting protonation of the organic molecule, it would seem likely that acid-catalyzed reactions in aqueous media will proceed within these solvated complexes containing a proton, a substrate molecule, and water molecules. The equations developed in this paper show that it is necessary for the linear plots of (rate constant)$^{-1}$ *vs.* h_0^{-1} to have an intercept to demonstrate the participation of this intermediate solvated complex in the reaction. All the kinetic data presently available to the author in the acid region where $a_w \sim 1$ have been examined in this way, and of the twenty-one substrates, seven show a positive intercept on the k_1^{-1} axis (Table I). Of these seven, six unambiguously have a positive intercept as they have an adequate number of points at the low values of h_0^{-1} to show that the linear plot cannot pass through the origin. Moreover, these points at low h_0^{-1} ensure a reasonably accurate value for the equilibrium constant K taken from the intercept/slope. The substrate displaying an intercept with less certainty is isopropyl acetate, which only has a few values for k_1 in the region of h_0 where $a_w \sim 1$. Of the six with unambiguous intercepts, K is high enough for three, acetone, methyl acetate, and ethyl acetate, to require a correction to h_0 to allow for the protons present as $A(H_2O)_3H_{aq}^+$, but the intercept is present both before and after the correction. Moreover, for three of these six, the value for the equilibrium constant has also been obtained using the static, spectrophotometric method,[3] and the agreement between the static and the kinetic values is very good in two cases and good in the other case. We can be reasonably sure, therefore, that in six cases, and probably seven, acid hydrolysis in conditions where $a_w \sim 1$ proceeds by a mechanism involving the intermediate proton complex containing the substrate, *i.e.*, the protonated water-solvated substrate.

In the other fourteen cases, although plots of k_1^{-1} *vs.* h_0^{-1} are linear, the intercepts are indistinguishable from the origin, and they do not constitute a test of the mechanism involving the protonated intermediate. Nevertheless, if one assumes that the mechanism established for the six (or seven) substrates above is the general case, the low values for the equilibrium constants indicated by the low intercepts are consistent with what is expected for these substrates on the basis of steric and structural variations found from the static experiments[3] on other organic molecules. If the mechanism with the intermediate complex is general, only limiting values for the equilibrium constant and rate constant are obtainable for these substrates, but an accurate value for the product of the rate constant and the equilibrium constant can be calculated (Table I).

The postulation that protons in highly aqueous media are solvated by organic oxygen-containing molecules when the latter are added in low concentration, originally suggested to explain spectrophotometric measurements on added indicators,[3] conductivity measurements,[33] and the kinetics of oxidation,[3,34] now receives support from measurements on the kinetics of hydrolysis. Further, studies of free energies of transfer of ions from water into aqueous mixtures containing these organic molecules suggest that the latter in dilute solution also solvate other cations[35,36] or enhance the basicity of solvating H_2O molecules.[37] All these phenomena support the view that, in general, these organic oxygen-containing molecules *in dilute aqueous solutions* are more basic than water; however, *in dilute solutions of water in these organic solvents,* the contrary holds, *i.e.*, H_2O molecules are more basic than the organic solvent.[38] Constants analogous to K_2F_2 for the proton exchange equilibrium between the indicator and solvent[3] also show an extremum in their variation with solvent composition.[39] Presumably the reason for this variation with solvent composition lies in the difference in the solvent structures at the opposite ends of the composition scale.[3,34]

It was emphasized in the earlier papers on the spectrophotometric measurements with indicators,[3] that these latter observations are not dependent on possible variations[40] in *individual* activity coefficients, but only on the constancy of "symmetrical" *ratios* of activity coefficients. This assumption of the constancy of these latter ratios was originally supported[3] by the agreement found between observed and calculated intercepts of experimental plots[3] using two methods for calculating K_c and the absence of any influence of glycerol which has a very low basicity,[3] and it is further justified by the close agreement[3] between the spectrophotometric, conductivity, and kinetic values for K_c. Moreover, K_c is independent of ionic strength.[3]

These conclusions are not in conflict with the observation that acid dissociation constants and rate constants in mixed hydroxylic solvents[41] depend on both the organic acid and the specific medium effects produced by the hydroxylic organic component of the solvent. These latter free-energy changes, expressed as degenerate activity coefficients, have been discussed[3] in relation to the interpretation of basicity proposed in this and earlier papers.[3] In the analysis of our spectrophotometric data,[3] a molecular interpretation of these free-energy changes is discussed. The basicity effects of the organic solvent are separated into that involving the solvated proton and that involving the solvated indicator acid, as expressed by the concentration quotients K_c and K_2F_2, respectively.[3] When the concentration of organic solvent $\lesssim$10% v/v, K_c is insensitive to this concentration and both K_c and K_2F_2 vary with the molecular structure of the organic component in the manner expected from the changes in electronic effects on the basicity at the O atom.[3] However, at concentrations of organic solvent $\gtrsim$10% v/v, both K_c and K_2F_2 vary with solvent composition, K_c increasing and K_2F_2 decreasing with increasing concentration of the organic component.[3] This variation of K_c with solvent composition is expected from the observation, mentioned above, that, in dilute solutions of water in the organic component, the latter is less basic than H_2O.[38] K_c therefore passes through a maximum in the region of solvent composition where the sol-

vent structure changes from predominantly that of water to that of the organic component; the aquo proton in water is $(H_2O)_4H_{aq}^+$ and in nearly pure organic solvent is $H_3O_{solv}^+$. As quoted above, constants analogous to K_2F_2 for similar acids have an extremum in their variation with solvent composition.[39]

Although these observations on the solvation of protons[3,34] and other cations[34-37] constitute a basicity effect of alcohols, ethers, ketones, and esters in dilute aqueous solution greater than that of water, the molecular picture of the aquo-organo-solvate complex presented in these papers may be oversimplified; any elaboration must await a more precise formulation of the molecular interactions in such aqueous mixtures. Certainly, an interpretation of phenomena in conditions near a 50% mixture water-organic solvent must await a more detailed knowledge of the solvent structure in this region. Nevertheless, within these limitations, this present interpretation of the aquo-organo-solvate complex allows an adequate discussion of these effects in dilute aqueous solution at the molecular level.

References and Notes

(1) F. A. Long and M. A. Paul, *Chem. Rev.*, **57**, 935 (1957).
(2) C. H. Rochester, "Acidity Functions," Academic Press, London, 1970, Chapters 4 and 5.
(3) C. F. Wells, *Trans. Faraday Soc.*, **61**, 2194 (1965); **62**, 2815 (1966); **63**, 147 (1967); J. Chem. Soc., Faraday Trans. 1, **68**, 993 (1972); *J. Phys. Chem.*, **77**, 1994 (1973); C. F. Wells, C. Barnes, and G. Davies, *Trans. Faraday Soc.*, **64**, 3069 (1968). C. F. Wells and C. Barnes, *ibid.*, **66**, 1154 (1970).
(4) L. P. Hammett and A. J. Deyrup, *J. Amer. Chem. Soc.*, **54**, 2721 (1932); L. P. Hammett, *Chem. Rev.*, **16**, 67 (1935).
(5) M. Randall and L. E. Young, *J. Amer. Chem. Soc.*, **50**, 989 (1928).
(6) J. N. Pearce and A. F. Nelson, *J. Amer. Chem. Soc.*, **55**, 3075 (1933).
(7) G. Åkerlöf and J. W. Teare, *J. Amer. Chem. Soc.*, **59**, 1855 (1937).
(8) J. F. Burnett, *J. Amer. Chem. Soc.*, **83**, 4956 (1961).
(9) M. A. Paul and F. A. Long, *Chem. Rev.*, **57**, 1 (1957).
(10) R. P. Bell, A. L. Dowding, and J. A. Noble, *J. Chem. Soc.*, 3110 (1955).
(11) D. P. Satchell, *J. Chem. Soc.*, 2878 (1957).
(12) H. M. Dawson and F. Powis, *J. Chem. Soc.*, **103**, 2135 (1913).
(13) L. Zucker and L. P. Hammett, *J. Amer. Chem. Soc.*, **61**, 2791 (1939).
(14) M. Dubroux and A. de Sousa, *Helv. Chim. Acta*, **23**, 1381 (1940).
(15) H. S. Harned and R. Pfanstiel, *J. Amer. Chem. Soc.*, **44**, 2193 (1922).
(16) P. Salomaa, *Suom. Kemistilehti B*, **32**, 145 (1959).
(17) P. Salomaa, *Acta Chem. Scand.*, **14**, 577 (1960).
(18) P. Salomaa, *Acta Chem. Scand.*, **11**, 247 (1957).
(19) R. P. Bell and B. Lukianenko, *J. Chem. Soc.*, 1686 (1957).
(20) P. Salomaa, *Acta Chem. Scand.*, **11**, 132 (1957).
(21) P. M. Leiniger and M. Kilpatrick, *J. Amer. Chem. Soc.*, **61**, 2510 (1939).
(22) A. Skrabal and A. Schiffrer, *Z. Phys. Chem.*, **99**, 290 (1921).
(23) D. McIntyre and F. A. Long, *J. Amer. Chem. Soc.*, **76**, 3240 (1954).
(24) A. Skrabal and H. H. Eger, *Z. Phys. Chem.*, **122**, 349 (1926).
(25) A. R. Olson and L. K. J. Tong, *J. Amer. Chem. Soc.*, **66**, 1555 (1944).
(26) R. P. Bell and A. H. Brown, *J. Chem. Soc.*, 774 (1954).
(27) R. P. Bell, K. N. Bascombe, and J. C. McCoubrey, *J. Chem. Soc.*, 1286 (1956).
(28) H. T. Liang and P. D. Bartlett, *J. Amer. Chem. Soc.*, **80**, 3585 (1958).
(29) M. Dubroux, *Helv. Chim. Acta*, **21**, 236 (1938); M. Dubroux and J. Rochat, *Helv. Chim. Acta*, **22**, 563 (1939).
(30) G. Archer and R. P. Bell, *J. Chem. Soc.*, 3228 (1959).
(31) J. N. E. Day and C. K. Ingold, *Trans. Faraday Soc.*, **37**, 686 (1941); C. K. Ingold, "Structure and Mechanism in Organic Chemistry," 2nd ed, Bell, London, 1969, p 1129.
(32) S. C. Datta, J. N. E. Day, and C. K. Ingold, *J. Chem. Soc.*, 838 (1939); F. A. Long and L. Friedman, *J. Amer. Chem. Soc.*, **72**, 3692 (1950).
(33) See ref 3 for appropriate papers.
(34) (a) C. F. Wells in "Hydrogen-Bonded Solvent Systems," A. K. Covington and P. Jones, Ed., Taylor and Francis, London, 1968, pp 323-334; (b) C. F. Wells, *Discuss. Faraday Soc.*, **29**, 219 (1960); *Trans. Faraday Soc.*, **57**, 1703, 1719 (1961).
(35) C. F. Wells, *J. Chem. Soc., Faraday Trans. 1*, **69**, 984 (1973).
(36) E. Grunwald, G. Baughman, and G. Kohnstam, *J. Amer. Chem. Soc.*, **82**, 5801 (1960).
(37) D. Feakins in "Physico-Chemical Processes in Mixed Solvents," F. Franks, Ed., Elsevier, New York, N. Y., 1967, pp 71-90; D. Feakins and P. J. Voice, *J. Chem. Soc., Faraday Trans. 1*, **68**, 1390 (1972); D. Feakins, A. S. Willmott, and A. R. Willmott, *ibid.*, **69**, 122 (1973).
(38) H. Strehlow, *Z. Phys. Chem., Frankfurt am Main*, **24**, 240 (1960); P. Salomaa, *Acta Chem. Scand.*, **11**, 125 (1957); J. Koskikallio, *Suom. Kemistilehti B*, **30**, 38 (1957); I. M. Kolthoff and S. Bruckenstein, *J. Amer. Chem. Soc.*, **78**, 1 (1956); E. A. Braude and E. S. Stern, *J. Chem. Soc.*, 1976 (1948); L. S. Guss and I. M. Kolthoff, *J. Amer. Chem. Soc.*, **62**, 1494 (1940); L. Thomas and E. Marum, *Z. Phys. Chem.*, **143**, 191 (1929); H. Goldschmidt and L. Thomas, *ibid.*, **126**, 24 (1927); H. Goldschmidt and E. Mathiesen, *ibid.*, **121**, 153 (1926); H. Goldschmidt and P. Dahll, *ibid.*, **114**, 1 (1925); see also ref 34b.
(39) C. L. de Ligny, *Recl. Trav. Chim. Pays-Bas.*, **79**, 731 (1960); A. L. Bacarella, E. Grunwald, H. P. Marshall, and E. L. Purlee, *J. Org. Chem.*, **20**, 747 (1955); B. Gutbezahl and E. Grunwald, *J. Amer. Chem. Soc.*, **75**, 559 (1953).
(40) J. Sierra, E. Teixido, and P. A. H. Wyatt, *J. Chem. Soc., Faraday Trans. 1*, **68**, 290 (1972).
(41) E. Grunwald and S. Winstein, *J. Amer. Chem. Soc.*, **70**, 846 (1948); S. Winstein, E. Grunwald, and H. W. Jones, *ibid.*, **73**, 2700 (1951); E. Grunwald and B. J. Berkowitz, *ibid.*, **73**, 4939 (1951); B. Gutbezahl and E. Grunwald, *ibid.*, **75**, 559, 565 (1953); E. Grunwald and E. Price, *ibid.*, **86**, 4517 (1964); D.-W. Fong and E. Grunwald, *J. Phys. Chem.*, **73**, 3909 (1969).

Measurement of Negative Thermal Diffusion Coefficients by Observing the Onset of Thermohaline Convection

Douglas R. Caldwell

School of Oceanography, Oregon State University, Corvallis, Oregon 97331 *(Received December 22, 1972)*

Publication costs assisted by the National Science Foundation

The determination of negative thermal diffusion (Soret) coefficients by observation of the onset of thermohaline convection is practicable. Measurements made with this method show that thermal diffusion in 0.5 N NaCl solutions changes direction, relative to the heat flux, at about 10°, being reversed at the lower temperatures.

Introduction

The Soret effect (also called thermal diffusion) was first seen by Ludwig[1] and more carefully observed by Soret.[2] In a fluid mixture of several different gases or of solute and solvent a mass flux is caused by a thermal gradient. For example, in a solution initially uniform the imposition of a thermal gradient causes the solute to migrate in a direction either parallel or antiparallel to the thermal gradient. This transport continues until enough solute has moved to set up a concentration gradient. Down-gradient diffusion will then oppose the Soret diffusion, and in a closed container an equilibrium between fluxes may be reached so that the solute distribution no longer changes with time. The reciprocal effect, a thermal gradient caused by a concentration gradient, is called the DuFour effect. It is very small in liquids.

One formulation of these ideas is[3]

$$\vec{J}_Q = -k\vec{\nabla}T - \rho TC\frac{\partial\mu}{\partial C}D'\vec{\nabla}C$$

$$\vec{J}_C = -\rho D\vec{\nabla}C - \rho DS_T C(1 - C)\vec{\nabla}T$$

Here J_Q is the heat flux, J_C the solute flux, k the thermal conductivity, ρ the density, T the absolute temperature, C the solute concentration (mass fraction), μ the chemical potential of the solute, D the diffusivity, S_T the Soret coefficient, and D' the DuFour coefficient. In liquids one can neglect the second term in J_Q, the DuFour heat transport, as can be seen from the Onsager reciprocal relations. The second term in J_C, the Soret transport, may be quite important, however.

When the Soret coefficient of a solution is negative, thermal diffusion carries it from cooler parts of the solution to warmer parts. Thus if the fluid was gravitationally stable under the influence of the temperature field only (and the thermal expansion is positive), the Soret flux will have a destabilizing influence and may cause convective mixing which in turn obscures the thermal diffusive effect. For this reason measurement of negative Soret coefficients by the common methods is subject to error.[4]

The conductivity cell[5] works well for determining positive coefficients and can be adapted by the "initial slope" method to the measurement of slightly negative coefficients. In this method, a heat flux is suddenly imposed from above on a horizontal layer of solution. The ratio of the mean concentration in the top half of the solution to that in the lower half is monitored as a function of time and the coefficient calculated, assuming no convection. When the Soret coefficient is positive, solute moves down the gradient of temperature, in the same direction as the heat flux, to the lower part of the solution, so the solution is stabilized by both the temperature and concentration fields, and convection causes no difficulties. When the Soret coefficient is negative the solute flows to the upper part of the solution and convection is caused. Snowden and Turner[5] measured the initial rate of solute movement, before it has altered the density profile enough to cause convection. This method only works, of course, for solutions for which the electrical conductivity can be used to trace solute movement, and is still subject to convection error. Also it works only for solutions sufficiently dilute that the alteration of the density distribution by the Soret flux is not too great.

One can, however, take advantage of the effect of salt displacement on convective instability. Just as the thermal expansion of a fluid can be determined by observing the temperature gradient above which convection takes place,[6] the temperature gradient necessary to overcome stabilization by salt flux can be used to determine Soret coefficients in solutions sufficiently concentrated for the thermal-diffusive salt flux to have an appreciable effect on the density distribution. This idea appears in a paper by Legros, van Hook, and Thomaes.[7]

For aqueous salt solutions of concentration similar to sea water, we found this method to work quite well. The method and apparatus will be described in detail and results will be reported for 0.5 N NaCl.

Method

Consider a layer of fluid confined between horizontal plates. The temperature of the top plate is controlled, and the lower plate is heated, so the bottom of the fluid is warmer than the top. If the solution has a positive thermal expansion coefficient, it will be unstable but will not convect until a certain dimensionless group, the Rayleigh number, reaches a "critical value." The Rayleigh number is defined as $g\beta\Delta Td^3/\nu\chi$, where g is the acceleration of gravity, β the thermal expansion coefficient, ΔT the temperature difference across the fluid layer, d the depth of the fluid layer, ν the kinematic viscosity, and χ the thermal diffusivity. On a plot of the temperature difference between the plates as a function of applied heat flux (Figure 1), a change in slope is seen as the Rayleigh number

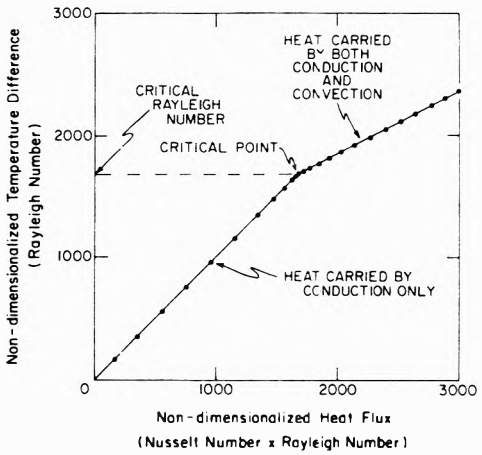

Figure 1. Nondimensionalized temperature difference (Rayleigh number) *vs.* nondimensionalized heat flux (Rayleigh number × Nusselt number) for a pure fluid. When the Rayleigh number reaches its "critical" value, theoretically 1708, heat is carried more efficiently, so the slope of the line changes. Because of uncertainties about some of the properties of saline solutions, some error in Rayleigh number calculations is to be expected.

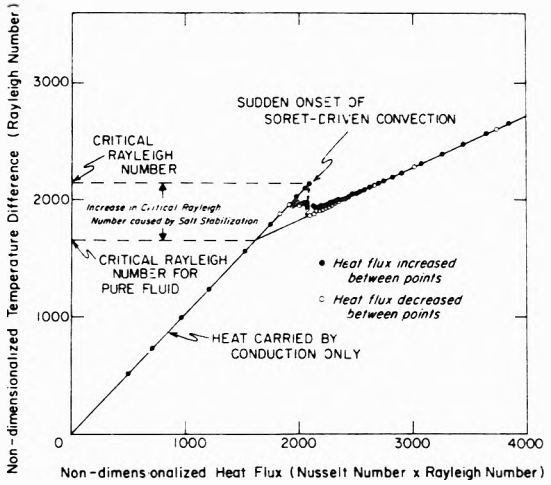

Figure 2. Nondimensionalized temperature difference (Rayleigh number) *vs.* nondimensionalized heat flux (Rayleigh number × Nusselt number) for an 0.5 *N* NaCl solution. The mean temperature was 3.33° at onset of convection. Note the catastrophic nature of the onset.

passes 1708. Convection begins, and heat is transferred more efficiently through the layer. Dimensionless parameters are used in these plots. The Rayleigh number is considered a dimensionless form of the temperature difference, and the Rayleigh number multiplied by the Nusselt number is a dimensionless form of the heat flux. The Nusselt number is defined as the heat flux through the layer divided by the heat flux carried by conduction alone (for the specified temperature difference). The theory of this phenomenon is give by Chandrasekhar.[8]

The above holds for a pure fluid. In a solution the situation is more complicated. Thermal diffusion causes a solute flow which can stabilize or destabilize the fluid. If the Soret coefficient is negative, the solute flows from cold to warm, that is from top to bottom, making the lower fluid denser, thus stabilizing the system. To get convection started, the Rayleigh number must be increased until the destabilizing effect of the thermal gradient can overcome the stabilizing effect of the salt gradient. Once this is done, the convective motions tend to mix the salt and the

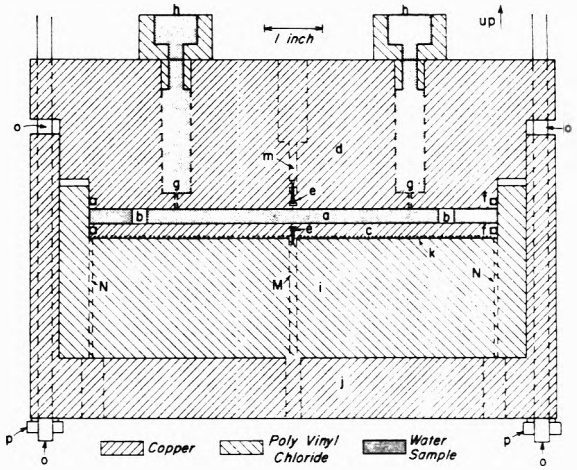

Figure 3. Section view of the apparatus. This device should be imagined immersed in hydraulic oil, inside a temperature bath. Top plate (d) and bottom plate (c) are separated by three (only two are shown) 0.635-cm high quartz blocks (b). Heat supplied by resistance wire (k) flows through fluid layer (a), plate (d), the cap [located above plate (d) but not shown here], and finally to an external water bath. O rings (f) seal the fluid layer from the hydraulic oil. Polyvinyl chloride (i) insulates fluid sample and bottom plate. Thermistors (e) measure plate temperatures. Reservoirs (h) supply or accept fluid through 0.08-cm holes (g) as changes in temperature require. Plate (c) is 17.8 cm in diameter, 0.635 cm thick. Insulation (i) has a 5.08 cm thick bottom and 1.27 cm thick walls

fluid is further destabilized; the onset of convection is catastrophic (Figure 2).

The Rayleigh number required for convection in a solution has been calculated theoretically as a function of the Soret coefficient.[9] Once the value of ΔT corresponding to the onset of convection has been measured for a sample, the Soret coefficient can be calculated, if other properties of the solution are known.

Apparatus

The essential part of this device (Figure 3) is the horizontal fluid layer bounded top and bottom by two parallel plates; the top plate is cooled and the bottom heated. The plates must be maintained parallel and their separation kept constant as temperature changes. To do so, fused quartz is used to separate the plates because of its low compressibility, thermal expansion, and thermal conductivity. As shown (Figure 3), the top plate rests on three 0.635-cm fused quartz blocks (cut from one piece) and slides freely on the rods which support the device from below. The parallelism of the plates is determined by the heights of the three blocks, which are matched to 0.001 cm.

The sample is heated by passing current from a power supply (voltage regulated to 0.01%) through a spiral coil of Karma wire (resistance constant to 0.01%) which is in contact with the underside of the bottom plate. The bowl-like piece of polyvinyl chloride (PVC) that surrounds the bottom plate and sides of the sample provides insulation from external heat sources and causes most of the heater's output to flow upward, through the sample. (PVC was chosen more for its availability and ease of machining than any particularly desirable insulating characteristic; no really good thermal insulation can be provided at the high pressures at which this device was originally built to operate.) Heat loss is further minimized by using very fine (No. 40) electrical leads to the heating coil and thermis-

tors. 85% of the heat goes through the sample while most of the remainder escapes through the PVC.

Horizontal heat flows within the device are to be avoided because they could induce motion in the fluid and thereby obscure the change of slope in the heat flow plot or, worse, produce sufficient perturbations in the initial state that the theory would no longer apply. These flows could conceivably be caused by the separation between the wires of the heater coil, the heat loss from the vertical sides of the fluid layer, the difference in the thermal conductivity of quartz and the fluid, or external heat sources (although the effect of such sources is reduced by a 1.27-cm thick copper shell which surrounds the device). However, for each of these effects, the ratio of horizontal temperature variation to the difference in temperature of the top and bottom plates is less than the ratio of the thermal conductivity of the fluid to that of the plates; for this reason, the plates were made of copper (plated with nickel to inhibit corrosion) which has a thermal conductivity about 1000 times that of water.

Temperature control is very important. The device shown was placed in a box made of 1.27-cm thick Plexiglas and this was submerged in a Neslab TE-45 constant-temperature bath. The Plexiglas box, together with the thermal inertia of the device itself, produced a 12-hr thermal lag. Thus, although short-term temperature fluctuations in the bath were as much as 0.01°, the lag smoothed them to less than 0.0001° at the plates.

The only measurements made in the course of the experiment which enter into the final calculations are of ΔT, the temperature difference of the top and bottom plates, and T_m, the mean temperature of the sample. They were made with two VECO 32A11 thermistors, mounted at the centers of the plates within 0.2 cm of the fluid. The temperature drop between a thermistor and the nearest fluid boundary was calculated to be less than 0.03% of ΔT. A Hewlett-Packard crystal thermometer was the calibration standard, and the thermistor resistances were measured with a Leeds and Northrup Wheatstone bridge and a Fluke null detector. By carefully reading the null detector, thermistor resistances (typically 3000 Ω) could be determined to 0.01 Ω; since the sensitivity of the thermistors is 3.8%/°C, resolution in temperature is about 0.1 mdeg. Typically ΔT was 1–2°.

Procedure

The heat introduced at the bottom plate is increased very slowly in steps (because of our thermal lag we had to wait 0.5 day between increases in heat). The temperature difference is measured for each value of the heat, and a plot similar to Figure 2 is made, using standard values of the required physical properties at the mean sample temperature given by the thermistors to calculate the Rayleigh number. From this plot the critical Rayleigh number, R_c, is read.

Calculations

Given R_c and T_m we now calculate the Soret coefficient, S_T, which at the mass transfer steady state is given by

$$S_T = \Delta C/C(1 - C)\Delta T$$

where C is concentration of solute in mass fractions.

On page 673 of their paper, Hurle and Jakeman[9] have given a prescription for calculating R_c, given (1) Pr, the Prandtl number ν/χ, (2) Sc, the Schmidt number ν/D, and (3) γ. Here D is the solute diffusivity and γ is a quantity representing the effect of the salt gradient on stability, $S_T C(1 - C)\beta'/\beta$, where β' is the solutal expansion coefficient.

The procedure is to compute values of R_c, using values of Pr and Sc at the mean temperature, T_m, making successive guesses for γ until it is evident what γ corresponds to the experimentally determined R_c. The formula given by Hurle and Jakeman for free bounding surfaces (eq 21) can be used to provide a first guess. R_c is not at all sensitive to Pr and Sc, so these need not be known very closely. Once γ is found, S_T is easily calculated

$$S_T = \gamma\beta/\left(\left(\frac{C}{v}\frac{\partial v}{\partial C}\right)(1 - C)\right)$$

where v is the specific volume.

For saline solutions the free surface formula gives values of S_T only in error by 4%

$$S_T = \frac{\beta}{\beta' C(1 - C)} \frac{1 + \mathrm{Pr}}{\mathrm{Pr}} \left[1 + \frac{(1 + 1/\mathrm{Sc})}{R_c/1708}\right] °\mathrm{C}^{-1}$$

Here $(\mathrm{ScPr})^{-1}$ has been neglected compared to 1, and the pure fluid value of R_c has been changed from $27\pi^4/4$ to 1708, because the boundaries are rigid, not free.

Results

Errors in the coefficients measured in this way may be caused by a number of factors. Most significantly we must wonder if the convective mode we detect in the heat flow plots is the one predicted by the Hurle-Jakeman theory. This is the basic assumption of the method. It can be justified by experiment; if values of S_T obtained by our method agree with values obtained by a method operating on a different principle, we can feel some confidence. We are especially worried because Hurle and Jakeman use linear stability theory in their calculations but the heat flow plots have an appearance characteristic of a "finite amplitude" instability.

There is some evidence that in a similar situation[10] the onset of convection is as predicted by the linear theory, but once started a finite amplitude mode is generated. This would account for the appearance of the plots. (Since this paper was submitted the author has completed an experimental study of this matter which reveals that stimulation of the nonlinear mode by the finite amplitude convection does in fact occur.)

Errors in measurements may also be caused by inaccuracies in temperature measurements and in values of properties of the solution used in calculation. These latter will be only a few per cent; from experience with Rayleigh number calculations in the past, ±2% is a reasonable estimate of the error to be expected. The thermal expansion is a problem here. Values are simply not known very well for salt solutions. This causes a particular problem because, in the calculation of S_T from γ, β occurs as a multiplicative factor, so any error in β appears as an error in S_T. One correction has been made in the experimentally determined value of R_c used in calculations. The value of R_c measured for positive S_T in the same solution at higher temperatures was 1670, whereas we expected 1708. We therefore corrected R_c by a multiplicative factor of 1708/1670 in calculating S_T. (The values of R_c given in Table I are not corrected in this way). This is a first-order correction to compensate for inaccuracies in the values of physi-

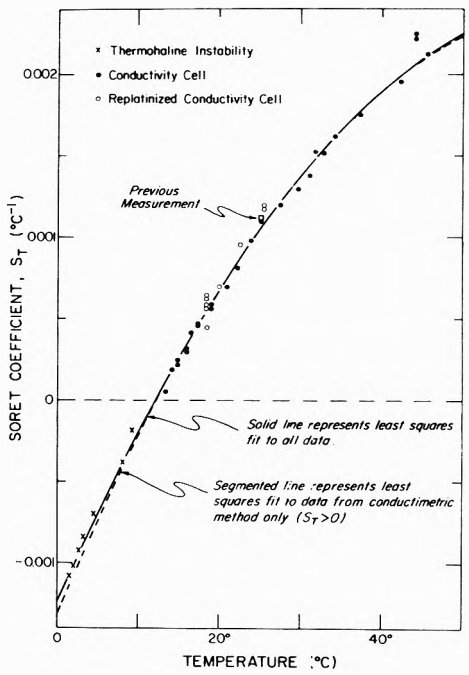

Figure 4. Soret coefficient *vs.* temperature.

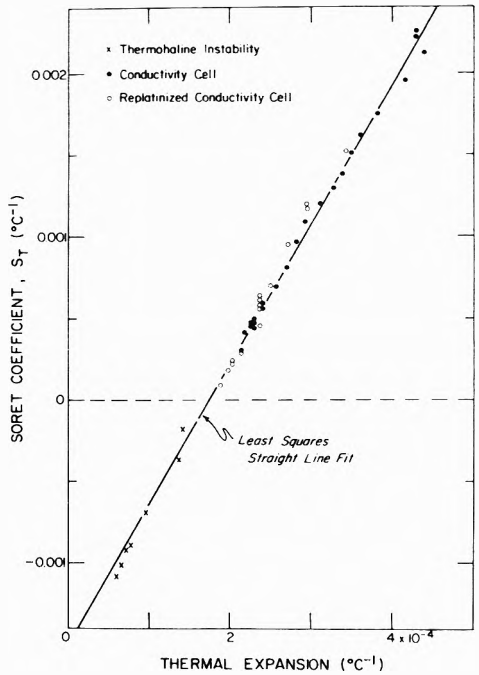

Figure 5. Soret coefficient *vs.* thermal expansion.

TABLE I

T, °C	R_c	S_T(measd) × 10^3 °C^{-1}	S_T(extrap) × 10^3 °C^{-1}	S_T(measd) − S_T(extrap) × 10^3 °C^{-1}
1.76	2690	−1.08	−1.10	+0.02
2.10	2515	−1.02	−1.06	+0.04
2.72	2300	−0.92	−0.99	+0.07
3.33	2137	−0.84	−0.92	+0.08
3.58	2160	−0.89	−0.89	+0.00
4.63	1975	−0.70	−0.78	+0.08
8.28	1770	−0.37	−0.39	+0.02
9.25	1713	−0.18	−0.29	+0.11

cal constants used to calculate P_c. Thus we have forced agreement with theory at high temperatures so that only variations with temperature remain to injure our experimental accuracies.

We have also measured the Soret coefficient of 0.5 *N* NaCl by an independent method. The method described in this paper was used for temperatures where S_T is negative, and a conductimetric device similar to that used by Snowden and Turner[5] was used at the higher temperatures where S_T is positive. These latter measurements are described in another paper.[11] Figure 4 shows all data, plotted against temperature, together with the only previous measurement.[12] A line representing a second-order least-squares fit to the data for positive values is shown, and the negative values fit this well. Table I gives the measurements by the new method, together with the differences between these values and values extrapolated from conductimetric measurements. The root mean square deviation for 33 positive values used in the fit was 0.000055 °C^{-1} while the root mean square deviation for the negative values (which were *not* used to make the fit) was 0.000065 °C^{-1}.

The agreement in the results between the two methods can be quickly appreciated by a glance at Figure 5, which shows the data plotted against thermal expansion, rather than temperature. The Soret coefficient seems to depend linearly on thermal expansion.

A change in sign of S_T was noticed by Longsworth[13] in 1 *M* KCl. It appears from Figure 8 of his paper that S_T = 0 at about 20° for that solution. Extrapolation of Agar and Turners[14] result's for much more dilute NaCl at 25 and 34.7° to lower temperatures suggests a change in sign at 5° or so.

The agreement seems good enough for it to be regarded as confirmation of our assumption that the Hurle-Jakeman theory applies, in the sense that it predicts the onset of instability to the accuracy to which we can measure it.

Discussion

The method clearly works well, with a precision of a few per cent in this case. It should work on any solution having a negative Soret coefficient, except solutions so dilute that solute distribution has a negligible effect on the density structure.

When the Soret coefficient is positive and the heat flux is from *below*, thermal diffusive salt movement destabilizes the solution, and convection begins when the Rayleigh number is much smaller than the pure fluid value of 1708. This convection is so weak, however, that it does not perceptably affect the heat flux, and so is indetectable in our apparatus. It could be detected if we were equipped to measure the salt distribution, which will show a change when this convection begins. The onset of this instability might be useful for measuring positive coefficients.

Acknowledgments. Support for this work has been provided by National Science Foundation under Grant No. GA-23336.

References and Notes

(1) C. Ludwig, *Sitzungsber. Akad. Wiss. Wien*, **20**, 539 (1856).
(2) Ch. Soret, *Arch. Sci. Phys. Nat., Greneve*, **3**, 48 (1879).
(3) S. R. DeGroot and P. Mazur, "Non-equilibrium Thermodynamics," North-Holland Publishing Co., Amsterdam, 1962.
(4) R. S. Schecter and M. G. Velarde, *Chem. Phys. Lett.*, **12**, 312 (1971).
(5) P. N. Snowden and J. C. R. Turner, *Trans. Faraday Soc.*, **56**, 1409 (1960).

(6) D. R. Caldwell, *Rev. Sci. Instrum.*, **41**, 1856 (1970).
(7) J. C. Legros, W. A. van Hook, and G. Thomaes, *Chem. Phys. Lett.*, **1**, 696 (1968).
(8) S. Chandrasekhar, "Hydrodynamic and Hydromagnetic Stability," Oxford University Press, London, 1961.
(9) D. T. J. Hurle and E. Jakeman, *J. Fluid Mech.*, **47**, 667 (1971).
(10) T. G. L. Shirtcliffe, *J. Fluid Mech.*, **35**, 677 (1969).
(11) D. R. Caldwell, *Deep Sea Res.*, in press.
(12) J. Richardson, *U.S. Off. Saline Water Res. Progr. Rep.*, **No. 211** (1965).
(13) L. G. Longsworth, *J. Phys. Chem.*, **61**, 1557 (1957).
(14) J. N. Agar and J. C. R. Turner, *Proc. Roy. Soc., Ser. A*, **255**, 307 (1960).

Bond Dissociation Energies of the Metallic Vapor Species Aluminum–Silver and Aluminum–Gold Measured by Knudsen-Cell Mass Spectrometry

A. M. Cuthill, D. J. Fabian,* and S. Shu-Shou-Shen

Department of Metallurgy, University of Strathclyde, Glasgow C1, Scotland *(Received February 20, 1973)*

Dissociation energies of the metallic gaseous species AlAg and AlAu were determined using a double-focusing mass spectrometer with Knudsen-cell source. The values obtained for $D°_0$(AlAg) and $D°_0$(AlAu), using the third-law method, are respectively 180 ± 9 and 325 ± 13 kJ mol^{-1}. These are in line with the relative bond strengths in the alloys, indicated by their thermodynamic parameters and by electronic structure studies. The accuracy and reproducibility of the instrument were assessed from vaporization studies on the pure metals silver, aluminum, and iron, for which measured enthalpies of vaporization are reported.

Introduction

As part of a program of research aimed at relating thermodynamic parameters of alloys to their electronic structure, measurements were made of the dissociation, or atomization, energies of the metallic vapor species AgAl and AuAl in equilibrium with respectively the alloys silver–aluminum and gold–aluminum. Drowart[1] reports an apparent parallel between the strength of the bond in the gaseous intermetallic molecule and the corresponding bond in the solid alloy.

There has been considerable interest recently[2-4] in the electronic structure of gold–aluminum and silver–aluminum alloys. Gold and aluminum form a series of intermetallic compounds, Au_2Al, AuAl, and $AuAl_2$; of these $AuAl_2$, which is strongly colored (purple) and brittle, has aroused particular attention. It has become clear from such studies that, in addition to a transfer of s electrons from the Al atoms to the Au atoms, there is a strong depletion of the 5d electrons from the d band of gold, and participation of these electrons in the bonding between the atoms. Pauling[5] has argued that a large contribution of the gold 5d electrons is made to the bond in $AuAl_2$, on the basis of relative electronegativities for the two atoms. There is much evidence of particularly strong bonding in gold–aluminum alloys: high melting points and heats of formation, for example. With silver–aluminum, on the other hand, the bonding appears to be weaker than might be expected. Thermodynamic studies of liquid and solid Ag–Al alloys[6,7] in fact indicate a positive deviation from Raoult's law ideality for the aluminum-rich alloys.

Thus, as a further indication of the respective strengths of the Au–Al and Ag–Al bonds in these alloys, an examination was made of the corresponding metallic vapor species using a mass spectrometer equipped with a Knudsen effusion cell ion source. From optical emission and absorption studies of the gaseous species AuAl, Barrow and Travis[8] have reported a value of 268 kJ mol^{-1} for its dissociation energy. No recorded value for the dissociation energy of the molecule AgAl appears to have been tabulated, although Blue and Gingerich[9] indicated measurements giving 318 ± 4 and 186 ± 8 kJ mol^{-1} for AuAl and AgAl, respectively.

Experimental Section

Knudsen-cell mass spectrometry is now an established technique[10-12] for the measurement of thermodynamic parameters of solid and liquid solutions, and for the determination of dissociation energies of equilibrium gaseous species. In the investigation to be described a double-focusing spectrometer was employed (an AEI-MS702 with electron-bombardment ion source) together with electron multiplier and ion-counting detection. The instrument, and Knudsen-cell arrangement, have been adequately described elsewhere.[13,14] The high resolution (~3000 for most of the measurements reported here) permits much lower ion intensities from metallic vapor species to be detected in the presence of background hydrocarbon peaks of similar masses. For the present measurements an improved Knudsen-cell heater was employed. This comprises a platinum-wound cylindrical furnace (25 mm diameter by 40 mm length) with its upper and lower portions controlled by separate stabilized power supplies so that temperature gradients along the cell can be eliminated. For temperature measurement and control three platinum—

platinum–13% rhodium thermocouples are introduced into small wells bored along the length of the cell.

Binary alloys were prepared by melting together weighed quantities of the 99.99% pure metals, gold with aluminum and silver with aluminum, in proportions to give approximately equal partial pressures for the two components in each case. The gaseous equilibria measurements are not affected by the specific alloy composition. A tungsten effusion cell with graphite liner was employed. The cell lid, whose temperatures also was monitored by one of the thermocouples, contains the orifice of 1 mm diameter. The orifice-to-sample surface ratio was generally ~1:50.

The molecular species vaporizing and effusing from the cell were identified by several methods. These include measurement of mass-to-charge ratio using both electrical detection and photoplate recording; determination of isotopic abundance distribution; examination of intensity profile with changing molecular-beam shutter position; and study of appearance potentials obtained from ionization efficiency curves. The gaseous atomic and molecular species Ag, Al, Ag_2, Al_2, and AgAl, in the case of aluminum–silver, and Au, Al, Au_2, Al_2, and AuAl, in equilibrium with aluminum–gold, were positively identified. Examination of the ionization efficiencies for the ions Ag^+, Al^+, $AgAl^+$, Au^+, and $AuAl^+$ were made, and these measurements were used also to ascertain the optimum electron energy for ionization and study of the ion species; 60-eV electrons were employed in the gaseous equilibria measurements. For the ion species $AgAl^+$ and $AuAl^+$ appearance potentials of 7.8 ± 0.5 and 9.0 ± 1.0 eV, respectively, were recorded, and ionization efficiencies were broadly constant at 60 eV. Ion currents for these species indicated approximate partial pressures in the Knudsen-cell of $\sim 10^{-4}$ and $\sim 10^{-5}$ Torr, respectively.

Equilibrium constants, K_p, for the gaseous equilibria

$$Ag_{(g)} + AgAl_{(g)} = Al_{(g)} + Ag_{2(g)} \quad (1)$$

and

$$Au_{(g)} + AuAl_{(g)} = Al_{(g)} + Au_{2(g)} \quad (2)$$

were measured directly from the product of the relative ion intensities for the respective species. Atomization energies were obtained from reaction enthalpy changes, calculated by the third-law method

$$\Delta H°_0 = -RT \ln K_p - T[(G°_t - H°_0)/T] \quad (3)$$

$$= D°_0(\text{M-Al}) - D°_0(\text{M}_2) \quad [\text{M} = \text{Ag, Au}] \quad (4)$$

using statistical mechanical formulae for the free-energy functions. In theory the reaction enthalpy changes can be obtained from the slopes of ln K_p *vs.* $1/T$ by the second-law method

$$\Delta H°T = R \, d \ln K_p/d(1/T) \quad (5)$$

using enthalpy increments, required for reducing $\Delta H°_T$ to $\Delta H°_0$, calculated from statistical mechanical formulae. However, for this method measurements are desirable over a larger range of temperature than was possible in the present investigation.

Results and Discussion

The stability and reproducibility of the instrument and Knudsen-cell combination were assessed from enthalpy of vaporization studies made on the pure metals silver and aluminum, and the less volatile iron. The results, for the

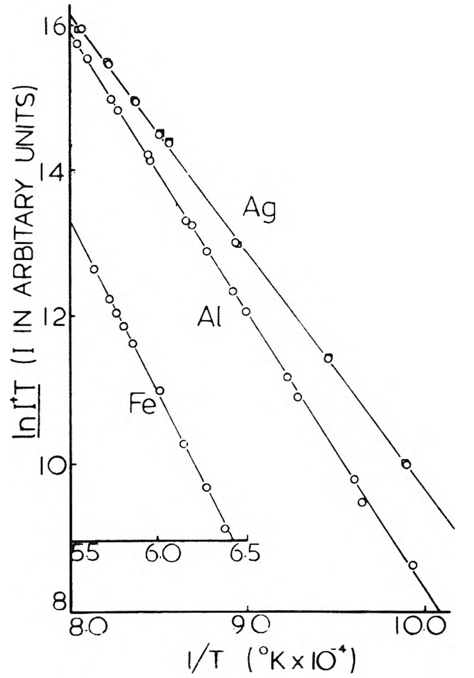

Figure 1. Variation of ion intensities of Ag^+, Al^+, and Fe^+ with temperature for the pure metals silver, aluminum, and iron, expressed in the form of ln I^+T as a function of reciprocal temperature. For silver, day-to-day reproducibility has been indicated by superimposing the ion counts obtained in two separate experiments, for which the same series of Knudsen-cell temperatures was established.

ion species Ag^+, Al^+, and Fe^+, are shown in Figure 1, where ln I^+T is expressed as a function of the reciprocal temperature. The slopes in each case, through the second-law Clausius–Clapeyron expression (5), yield values for the vaporization enthalpies $\Delta H°_T$ for the mid-range of $1/T$. These, when corrected to the standard 298°K, give the results $\Delta H°_{298}$(Ag) = 284 kJ mol^{-1}, $\Delta H°_{298}$(Al) = 334 kJ mol^{-1}, and $\Delta H°_{298}$(Fe) = 397 kJ mol^{-1}, which compare well with the values of 285, 323, and 398 kJ mol^{-1}, respectively, reported by Nesmeyanov[15] and Kubaschewski and Evans.[16]

For silver, the day-to-day reproducibility of the instrument was examined. Measurements from experiments done on two separate days, although without recharging the Knudsen cell or de-aligning the assembly, are shown superimposed for Ag in Figure 1. The ion count recorded at each established temperature was almost precisely the same from one experiment to another.

To measure the bond dissociation energies of AlAg and AlAu, K_p values for equilibrium 1 were obtained directly from the product of the relative ion intensities of $AlAu^+$, Au^+, Al^+, and Au_2^+ measured at several different temperatures in the range 1560–1645°K; and K_p values for equilibrium 2 from the ion intensities of $AlAg^+$, Ag^+, Al^+, and Ag_2^+ measured at four temperatures in the range 1390–1440°K. The results in these limited temperature ranges, for which instrumental stability and sufficient ion counts for accurate detection and measurement coincided, are summarized in Tables I and II and in Figure 2 where K_p is expressed graphically as a function of reciprocal temperature. It was assumed that the relative ionization cross sections, and multiplier-yield factors, mutually compensate one another. Hildenbrand[17] has estimated that the errors in equilibrium constants estimated in this way, directly from ion currents, are not larger than a factor of

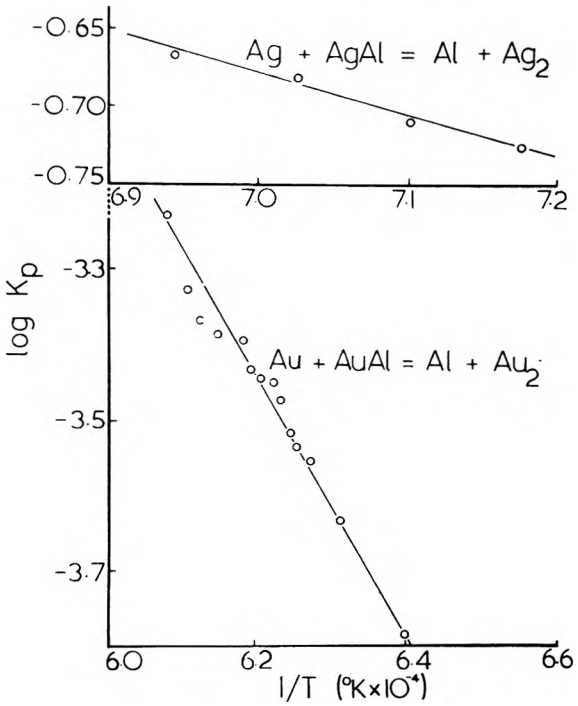

Figure 2. Measured K_p values for the gaseous equilibria vaporizing from aluminum–silver and aluminum–gold alloys, expressed in the form of log K_p as a function of reciprocal temperature.

TABLE I: Equilibrium Constants and Third-Law Enthalpies for the Gaseous Reaction AuAl + Au = Au_2 + Al

T, °K	I_{Al}/I_{Au}	I_{Au_2}/I_{AuAl} × 10^{-4}	K_p × 10^{-4}	$\Delta H°_0$, kJ mol^{-1}
1562	1.20	1.37	1.65	115.8
1583	1.34	1.74	2.33	112.7
1594	1.47	1.92	2.81	112.5
1598	1.52	1.93	2.92	110.8
1601	1.55	1.97	3.04	110.8
1604	1.58	2.13	3.37	109.5
1608	1.64	2.18	3.57	109.0
1611	1.65	2.18	3.60	109.0
1615	1.69	2.19	3.69	109.0
1617	1.70	2.37	4.04	108.2
1627	1.75	2.33	4.09	108.2
1634	1.71	2.49	4.26	108.2
1638	1.71	2.73	4.67	107.2
1644	1.65	3.57	5.88	105.0

2, which introduces only a small error into the third-law or absolute-entropy calculation.

The numerical values of the free-energy functions of Au(g), Ag(g), and Al(g) were taken from the compilation by Hultgren.[18] Those for Au_2(g), AlAu(g), Ag_2(g), and AlAg(g) were calculated using statistical mechanical methods from the molecular parameters listed in Table III. The enthalpies of reaction $\Delta H°_0$ for equilibria 1 and 2 were then calculated (using eq 3), and $D°_0$ values for AlAu and AlAg obtained (eq 4) using reported values[1,19] for the dissociation energies of the pure metal diatomic gaseous molecules Au_2 and Ag_2: $D°_0(Au_2)$ = 215 ± 9.2 kJ mol^{-1} and $D°_0(Ag_2)$ = 157.5 ± 8.4 kJ mol^{-1}.

The results obtained for the dissociation energies of the species AlAu and AlAg were then $D°_0$(AlAu) = 325 ± 12 kJ mol^{-1} and $D°_0$(AlAg) = 180 ± 8 kJ mol^{-1}, which are

TABLE II: Equilibrium Constants and Third-Law Enthalpies for the Gaseous Reaction AgAl + Ag = Ag_2 + Al

T, °K	I_{Al}/I_{Ag}	I_{Ag_2}/I_{AgAl}	K_p	$\Delta H°_0$, kJ mol^{-1}
1393	1.54	0.123	0.189	22.45
1409	1.61	0.120	0.194	22.26
1424	1.76	0.119	0.209	21.80
1440	1.83	0.118	0.216	21.70

TABLE III: Molecular Parameters Used for Statistical Mechanical Calculation of Free-Energy Functions

	Electronic ground state	Vibration frequency, ω_e, mm^{-1}	Interatomic distance, r_e pm	Ref
Au_2	$^1\Sigma$	19.09	247.2	1
AlAu	$^1\Sigma$	33.30	233.8	8
Ag_2	$^1\Sigma$	19.24	268	1
AlAg	$^1\Sigma$	25.66	247.2	19

in good agreement with the values found by Blue and Gingerich[9] and in fair agreement with the value for AuAl obtained spectroscopically by Barrow and Travis.[8] The values estimated using the linear Birge-Sponer extrapolation of the vibrational levels of the ground state, $D_0'' = \omega^2/4\omega$, are respectively 283 and 174.5 kJ mol^{-1}; both consistently smaller than the experimental values, in common with comparisons made[1] for most metallic diatomic gaseous molecules.

It is of interest to examine the difference between the measured $D°_0(MM')$, where M and M′ are the atomic constituents of the metallic molecule, and the arithmetic mean of the energies for the symmetric molecules M_2 and M_2'. Taking for $D°_0(Al_2)$, the reported value[1] of 180 kJ mol^{-1}, we obtain

$$\Delta(AuAl) = D°_0(AuAl) - {}^1/_2[D°_0(Al_2) + D°_0(Au_2)] = 127 \text{ kJ mol}^{-1}$$

and

$$\Delta(AgAl) = D°_0(AgAl) - {}^1/_2[D°_0(Al_2) + D°_0(Ag^2)] = 12 \text{ kJ mol}^{-1}$$

According to the Pauling relationship,[5] the quantity Δ measures the ionic contribution to the bond of the molecule, and is proportional to $[\chi(M) - \chi(Al)]^2$ where χ is the electronegativity. The results for Δ agree quite well with those expected from the accepted[20] electronegativities for the respective metals: χ_{Al} = 1.5, χ_{Au} = 2.4, χ_{Ag} = 1.8; *i.e.*, $\Delta(AuAl)/\Delta(AgAl) \sim [0.9/0.3]^2 = 9$.

Conclusions and Comments

The results for Al–Au and Al–Ag alloys confirm the suggested parallelism[1] of the strengths of the bond in the intermetallic molecule with the bonds in the corresponding alloy. The bond dissociation energies and predicted negativities are in line with the pronounced tendency for intermetallic compound formation between aluminum and gold, contrasting the absence of intermetallic compounds between aluminum and silver. Much weaker chemical bond effects in Al–Ag alloys, compared with Al–Au alloys, have also been observed in electronic structure studies using soft X-ray emission,[4,21-23] where a peak in the aluminum band emission for the alloy, attributed to hybridization with the d band of the noble metal, is much sharper and more intense in the case of Au–Al al-

loys than with Ag-Al. Thermodynamic activity data for Al-Ag alloys[6,7,24,25] show positive deviations from ideality for the Al-rich alloys indicating a slightly weaker Ag-Al bond in the alloy compared with the Al-Al bond in pure aluminum, in agreement with the results for the metallic vapor molecules AgAl and Al_2.

Acknowledgments. We are indebted to the Science Research Council for a grant in support of this research, to the late Professor E. C. Ellwood for his support and encouragement, and to Professor A. J. B. Robertson for helpful discussions. A. M. C. and S. S. Shen held SRC Fellowships during the course of the work.

References and Notes

(1) J. Drowart in "Phase Stability in Metals and Alloys," P. S. Rudman, J. Stringer, and R. I. Jaffee, Ed., McGraw Hill, New York, N. Y., 1967, p 305.
(2) D. J. Fabian, L. M. Watson, and G. M. Lindsay, *Nat. Bur. Stand. (U. S.), Spec. Publ.*, **No. 323,** 307 (1971)
(3) M. L. Williams, R. C. Dobbyn, J. R. Cuthill, and A. J. McAlister, *Nat. Bur. Stand. (U. S.). Spec. Publ.*, **No. 323,** 303 (1971).
(4) Q. S. Kapoor, L. M. Watson, D. Hart, and D. J. Fabian, *Solid State Commun.*, **11,** 503 (1972).
(5) L. Pauling, "The Nature of the Chemical Bond," Cornell University Press, Ithaca, N. Y., 1948, p 58.
(6) M. Hillert, B. L. Averbach, and M. Cohen, *Acta Met.*, **4,** 31 (1956).
(7) T. C. Wilder and J. F. Elliott, *J. Electrochem. Soc.*, **107,** 628 (1960).
(8) R. F. Barrow and D. N. Travis, *Proc. Roy. Soc., Ser. A.*, **273,** 133 (1963).
(9) G. D. Blue and K. A. Gingerich, *Ann. Conf. Mass Spectrom. Allied Topics, 16th,* (1968) unpublished results.
(10) M. G. Inghram and J. Drowart in "High Temperature Technology," McGraw Hill, New York, N. Y., 1960, p 219.
(11) D. J. Fabian, *Met. Rev.*, [113], **12,** 28 (1967).
(12) J. Drowart, *"J. Stefan" Inst., Rep.*, 187 (1971).
(13) Associated Electrical Industries, *AEI (Ass. Elec. Ind.) Eng. Rev.*, 2033-72 EdA, 2032-87 aEdA (1965).
(14) A. M. Cuthill, P. B. Brown, and D. J. Fabian, *"J. Stefan" Inst., Rep.*, 243 (1971).
(15) A. N. Nesmeyanov, "Vapcur Pressure of the Chemical Elements," Elsevier, London, 1963.
(16) O. Kubaschewski and E. L. L. Evans, "Metallurgical Thermochemistry," Pergamon, London, 1955.
(17) D. L. Hildenbrand, *J. Chem. Phys.*, **51** 807 (1969).
(18) R. Hultgren, "Selected Values of Thermodynamic Properties of Metals and Alloys," Wiley, New York, N. Y., 1963.
(19) R. M. Clements and R. T. Barrow, *Trans. Faraday Soc.*, **64,** 2893 (1968).
(20) L. Pauling, *J. Amer. Chem. Soc.*, **69,** 542 (1947).
(21) D. J. Fabian, *J. Phys. (Paris)*, **32,** C4 (1971).
(22) A. J. McAlister, J. R. Cuthill, R. C. Dobbyn, and M. L. Williams in "Band Structure Spectroscopy of Metals and Alloys," D. J. Fabian and L. M. Watson, Ed., Academic Press, London, 1972, p 191.
(23) E. Källne in ref 22.
(24) G. R. Belton and R. J. Fruehan, *Trans. AIME*, **245,** 113 (1969).
(25) T. Thomasson, D. J. Fabian, and A. M. Cuthill, *Acta Met.*, submitted for publication.

Solubility of Alcohols in Compressed Gases. A Comparison of Vapor-Phase Interactions of Alcohols and Homomorphic Compounds with Various Gases. I. Ethanol in Compressed Helium, Hydrogen, Argon, Methane, Ethylene, Ethane, Carbon Dioxide, and Nitrous Oxide[1]

S. K. Gupta, R. D. Lesslie, and A. D. King, Jr.*

Department of Chemistry, University of Georgia, Athens, Georgia 30602 *(Received January 29, 1973)*

Publication costs assisted by the National Science Foundation

The solubility of ethanol in compressed He, H_2, Ar, CH_4, C_2H_4, C_2H_6, CO_2, and N_2O has been measured at pressures ranging from 10 to 60 atm at 25, 50, and 75°. Second cross virial coefficients representing deviations from ideality caused by ethanol-gas interactions have been evaluated from these data. The solubility data for ethanol with all gases except CO_2 and N_2O yield virial coefficients which are identical within experimental error with those for the homomorph propane with corresponding gases. The enhancement in solubility, hence apparent cross virial coefficients of ethanol in CO_2, is larger than expected if physical forces alone were operative in this system. This anomaly is interpreted as resulting from a reversible one-to-one chemical association between CO_2 and ethanol in the gas phase. Values for K_{eq} and standard enthalpies and entropies of association are estimated. A similar, though very much weaker association, appears to exist in the case of N_2O with ethanol.

Introduction

Various investigations over the years have produced evidence suggesting that carbon dioxide is chemically reactive toward alcohols, and oxygen-containing compounds in general, to the extent that weak complexation occurs in condensed mixtures of these substances.[2-4] Recently, measurements of vapor composition in liquid-compressed gas mixtures have indicated that weakly bound complexes are formed between CO_2 and both water[5] and methanol[6] in the gas phase as well. While the qualitative evidence for such gaseous association is unequivocal, past efforts to establish values for the thermodynamic parameters defining the equilibria have shared a common weakness in that empirical combining rules had to be used in conjunction

with either assumed potential functions or the principle of corresponding states in order to estimate values for cross virial coefficients of a hypothetical system in which physical interactions alone are operative. Such values are necessary in order to partition the vapor molecules properly according to whether they exist in a complexed or an unbound state.

This paper reports measurements of the solubility of ethanol in a series of compressed gases. The work was motivated by preliminary results which indicated that physical interactions in the gas phase involving simple alcohols having carbon numbers of two or greater are essentially identical with corresponding interactions involving saturated hydrocarbon molecules which are one carbon larger. This being the case, experimentally determined cross virial coefficients involving aliphatic homomorphs with CO_2 could be used in estimating K_{eq} for the alcohol-CO_2 systems.

Experimental Section

A detailed description of the experimental techniques used can be found in ref 5 and will not be repeated here. Briefly, however, the method entails bubbling the gas of interest through liquid ethanol at elevated pressures and subsequently expanding the saturated gas-vapor mixture into a low-pressure section where the alcohol vapor is removed from the gas stream by a series of cold traps. The weight of alcohol vapor accompanying a known volume of gas passing through the low-pressure section is recorded, thus providing the vapor composition of the high-pressure gaseous mixture. The amounts of ethanol collected in these experiments were relatively large, ranging from 1 to 9 g depending on the temperature and duration of each run. The trapping efficiency of the individual cold traps was quite high (*ca.* 80%) so that four cold traps were adequate to assure maximum removal of alcohol vapor from the gas stream. Before calculating mole fractions, each value of total weight of alcohol collected was corrected for slight losses of vapor under the assumption that the gas leaving the last trap is in equilibrium with liquid ethanol at the temperature of the cold bath (from −80 to −70° depending on the gas studied).

Initial experiments showed that three high-pressure saturation cells were adequate to ensure saturation with alcohol vapor at the flow rates used in these studies (~0.4 l./min). The virial coefficients calculated from the experimental vapor composition data were examined for directional trends with pressure as a further check for experimental errors or mean field effects at higher densities. No such trends were observed.

The hydrocarbon gases and nitrous oxide used in these experiments (CP grade) were obtained from Matheson Co., Inc., while the helium, hydrogen, argon, and carbon dioxide were purchased from Selox Corp., having quoted purities of 99.995, 99.9, 99.995, and 99.5%, respectively. Reagent grade absolute ethanol was used in all experiments.

Results and Discussion

The experimental data will not be included here for the sake of brevity. However, listings of the experimentally determined vapor composition can be obtained from this journal.[7] These results are shown graphically in Figure 1. At equilibrium the vapor composition of a given system can be expressed as a function of total pressure P by[8]

$$y_2 = \frac{(1 - x_1)P_2^0}{P}\left(\frac{\phi_2^0}{\phi_2}\right)\exp\left[\frac{V_2^{0(l)}(P - P_2^0)}{RT}\right] \quad (1)$$

where P_2^0 and $V_2^{0(l)}$ represent the vapor pressure and molar volume of pure ethanol (component 2) at temperature T. Also, x_1 is the mole fraction of dissolved gas (component 1) at P and T, while ϕ_2^0 and ϕ_2 designate fugacity coefficients of pure ethanol vapor at P_2^0 and T and ethanol vapor in the dense gas medium at P and T, respectively. At densities sufficiently low that contributions from third and higher order virial coefficients can be neglected, the fugacity coefficient ϕ_2 can be expressed in terms of the virial expansion as

$$\ln \phi_2 = (2/V)[y_2 B_{22}(T) + y_1 B_{12}(T)] - \ln Z \quad (2)$$

Here V and Z denote the molar volume and compressibility factor of the gaseous mixture having a composition given by the mole fraction y_1 and y_2. The symbols $B(T)$ designate second virial coefficients representing deviations from ideality caused by bimolecular interactions indicated by the subscripts. Equations 1 and 2 are combined and solved in an iterative fashion using any of the experimentally determined y_2 and the appropriate virial expansions for V and Z to yield a value for $B_{12}(T)$ for that particular ethanol-gas system.[5] Alternatively, eq 1 and 2 can be combined by making the appropriate expansions for V^{-1} and $\ln Z$ to yield

$$y_2 = [(1 - x_1)P_2^0/P]\exp\{[y_1^2(B_{11}(T) - 2B_{12}(T)) + V_2^{0(l)} + (y_1^2 - 1)B_{22}(T)](P/RT) + [B_{22}(T) - V_2^{0(l)}](P_2^0/RT)\} \quad (3)$$

It is seen from this latter equation that under the conditions of these experiments, $y_1 \cong 1$, $P_2^0 \ll P$, the values for $B_{12}(T)$ calculated from mole fraction data are quite insensitive to the relatively large (~100 cc/mol) uncertainties associated with literature values for the second virial coefficient of pure ethanol, $B_{22}(T)$, at these low temperatures.

Average values of second cross virial coefficients calculated from the experimental mole fraction data are listed in Table I. Values for molar volume and vapor pressure of ethanol used in these calculations were taken from ref 9 and 10. Gas solubilities in the liquid phase were estimated using Henry's law expressed in terms of fugacity. Values for the Henry's law constants were calculated from solubility data found in ref 11–17 and are listed in Table II. In several cases, short extrapolations or interpolations of experimental solubility data were necessary in arriving at the values listed in Table II. Where this was necessary, it was assumed that the entropy of solution of these gases in ethanol at 1 atm was sufficiently independent of temperature that accurate estimates of Henry's law constants could be obtained through linear extrapolations of log concentration *vs.* log T. Fugacity coefficients were derived from PVT data of ref 18–25. Values for pure component second virial coefficients occurring in the expansions for ϕ_2, V, and Z in eq 1 and 2 were obtained from ref 26.

These ethanol-gas cross virial coefficients are compared with those involving the homomorph propane in Figure 2. Sources of this latter data are C_3H_8-He, Ar, ref 27; C_3H_8-H_2, ref 27, 28; C_3H_8-CH_4, ref 28–30; C_3H_8-CO_2, ref 28, 29; C_3H_8-C_2H_6, ref 30. Also included in this figure is a single value for the second cross virial coefficient of ethanol with CO_2 measured by Sie, *et al.*,[31] using the method of high-pressure chromatography. No other sources of data

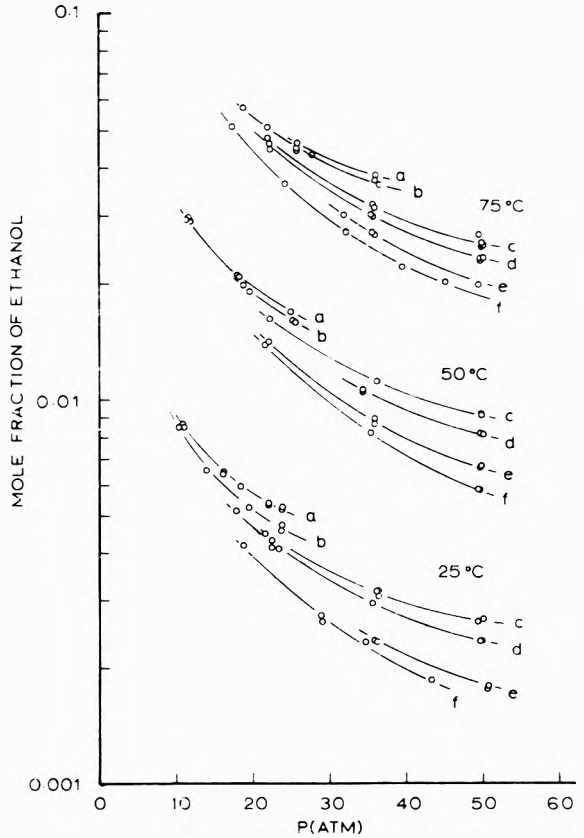

Figure 1. Mole fraction of ethanol in several gases as a function of pressure: a = CO_2, b = C_2H_4, c = CH_4, d = Ar, e = H_2, f = He.

TABLE I: Second Cross Virial Coefficients for Ethanol with Various Gases

Gas	T, °C	$B_{12}(T)$,[a] cm^3/mol
He	25	32 ± 6
	50	41 ± 2
	75	42 ± 6
H_2	25	5 ± 5
	50	6 ± 4
	75	5 ± 2
Ar	25	−73 ± 5
	50	−63 ± 2
	75	−50 ± 3
CH_4	25	−122 ± 2
	50	−107 ± 3
	75	−84 ± 10
C_2H_4	25	−243 ± 10
C_2H_6	25	−276 ± 13
	50	−200 ± 7
	75	−190 ± 7
CO_2	25	−307 ± 6
	50	−238 ± 3
	75	−196 ± 3
N_2O	25	−274 ± 5
	50	−215 ± 5
	75	−177 ± 5

[a] Error expressed as average deviation from the mean.

involving ethanol-gas systems are known to the authors. It is seen that, with the exception of CO_2, cross virial coefficients of ethanol and propane with a given gas are substantially identical in all cases for which comparisons can be made. Thus, in situations where hydrogen bonding

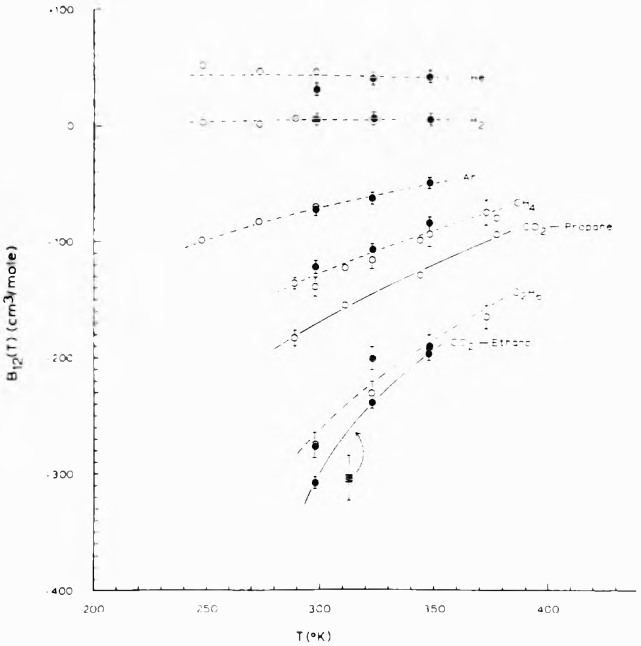

Figure 2. Second cross virial coefficients for propane (open circles) and ethanol (shaded circles) with a series of gases. Square symbol indicates value for ethanol with CO_2 from ref 31.

TABLE II: Henry's Law Constants for Ethanol–Gas Systems

Gas	T, °C	K_H, atm[a]	Ref
He	25	13,000	11
	50	10,300	
	75	8,300	
H_2	25	4,650	12
	50	4,130	
	75	3,680	
Ar	25	1,610	11
	50	1,660	
	75	1,700	
CH_4	25	911	13
	50	1,050	
	75	1,210	
C_2H_4	25	167	14
C_2H_6	25	180	13, 15
	50	235	
	75	302	
CO_2	25	156	16, 17
	50	239	
	75	353	
N_2O	25	149	17
	50	222	
	75	322	

[a] The Henry's law constants are taken to be good to three significant figures, *i.e.*, the precision of the solubility data as listed by the original authors.

plays no role, the physical properties of ethanol and propane are identical. This is, of course, not wholly unexpected since the two molecules have the same structure, are isoelectronic, and have similar, though not identical, polarizabilities (Table III). The fact that the cross virial coefficients agree so well in spite of the fact that ethanol is less polarizable than propane probably reflects a trade-off between decreased dispersion forces and permanent dipole–induced dipole interactions.

A comparison of the data of Table I and Figure 2 with the molecular constants of Table III shows that, with the

TABLE III: Molecular Parameters

Substance	Average polarizibility $\times 10^{24}$ cm^3 [a]	Quadruple moment $\Theta \times 10^{24}$ esu cm^2 [c]
He	0.216	
H_2	0.79	+0.662
Ar	1.63	
CH_4	2.60	
CO_2	2.65	−4.3
N_2O	3.00	−3.0
C_2H_4	4.26	+1.5
C_2H_6	4.47	−0.65
C_2H_5OH	5.11[b]	
C_3H_8	6.38[b]	

[a] With exception of those from ref b, all data taken from H. A. Landolt and R. Bornstein, "Zahlenwerte und Functionen," Vol 1, 6th ed, Springer, Berlin, 1951; Part 1, p 401; Part 2, p 509. [b] J. Applequist, J. R. Carl, and K. Fung, *J. Amer. Chem. Soc.*, **94**, 2952 (1972). [c] D. E. Stogryn and A. P. Stogryn, *Mol. Phys.*, **11**, 371 (1956).

exception of ethanol with CO_2 and N_2O, the values of $B_{12}(T)$ at a given temperature become more negative with increasing polarizability of the gas as is typically found for systems in which dispersion forces constitute the dominant mode of interaction.[32-35]

While the cross virial coefficients of the propane–CO_2 system fall in the usual pattern for systems which interact through dispersion forces (*i.e.*, have values slightly more negative than those for CH_4), the $B_{12}(T)$ for the ethanol–CO_2 system are the order of 100 cc/mol more negative than those for propane with CO_2. Although the ethanol–CO_2 system has additional modes for attraction which are absent in the case of propane with CO_2, that is dipole–quadrupole and dipole–induced dipole interactions, estimates based on derivations by Pople[36,37] show that such interactions can be expected to contribute a maximum of about −20 cm^3/mol to the second cross virial coefficient of ethanol with CO_2. Thus it is difficult to see how the large discrepancy between the cross virial coefficients of these two homomorphic systems could be caused by electrostatic interactions. This contention is further supported by data taken in this laboratory[38] on several chloroform–gas systems. The results of this work show that at 25° the cross virial coefficients of chloroform (μ = 1.0 D) with N_2, CH_4, CO_2, and C_2H_4 are −100 ± 4, −199 ± 7, −316 ± 15, and −373 ± 15 cm^3/mol, respectively. These fall in substantially the same order and magnitude as those for carbon tetrachloride with the same gases at 25°:[35] −102, −205, −287, and −384 cm^3/mol. Thus the evidence points to a conclusion similar to that made earlier in the cases of water[5] and methanol,[6] that is, the abnormally large cross virial coefficients derived from the solubility data for ethanol in CO_2 reflect the influence of a chemical association between carbon dioxide and the alcohol in the vapor phase.

It can be readily shown that (a) the enhanced solubility caused by such a weak association will lead to abnormally large "apparent" cross virial coefficients; and (b) that if cross virial coefficients are known or can be estimated for a homomorphic system in which physical forces alone are operative (propane with CO_2 in this case), values of K_{eq} for the association can be derived from the solubility, hence virial coefficient data. Consider the vapor-phase reaction postulated here: alcohol (g) + CO_2 (g) $\rightleftharpoons$ complex (g). Since excess liquid alcohol is present, the fugacity of the alcohol in the gas phase, f_2^g, is constant at a given pressure, being equal to the fugacity of the liquid phase, f_2^l

$$f_2^g = f_2^l = \gamma_2^l(1 - x_1)\phi_2^0 P_2^0 \exp[(V_2^{(l)}/RT)(P - P_2^0)] \quad (4)$$

where γ_2^l is an activity coefficient accounting for departures of the liquid phase from ideal solution behavior caused by dissolved gas. Because of the low gas solubilities, γ_2^l can be taken to equal unity under the conditions of these experiments. Because of this constancy in fugacity, each molecule of alcohol converted to complex in the vapor-phase reaction is replaced by one from the liquid reservoir with the result that the total number of moles in the gas phase over the liquid remains unchanged at a given pressure. Thus, for weak associations in which the concentration of complex remains small relative to the majority constituent (in this case CO_2), the vapor-phase mole fraction of uncomplexed alcohol, $y_2 = f_2^l/\phi_2 P$, remains constant. The experiment, however, measures the vapor composition of the gaseous mixture after an expansion to ambient pressure conditions during which the complex has presumedly dissociated completely leaving an excess amount of alcohol to be collected in the cold traps. The measured mole fraction therefore is $y_2^{tot} = (y_2 + y\ \text{complex})/(1 + y\ \text{complex})$. The equilibrium constant for formation expressed in molar units, $Kc(M^{-1})$, can be expressed in terms of y_2^{tot} as

$$K_c/V = K_y = \frac{y\ \text{complex}}{y_1 y_2} = \frac{(y_2^{tot} - y_2)}{y_1 y_2(1 - y_2^{tot})} \cong \frac{y_2^{tot}}{y_2} - 1 \quad (5)$$

since $y_1 \cong 1$ in these experiments. Thus if a reasonable estimate of deviations from ideality experienced by the uncomplexed alcohol can be obtained using $B_{12}(T)$ data of a homomorphic system, then values for ϕ_2 hence y_2 can be calculated, allowing one to evaluate K_c of eq 5.

In fitting the data for ethanol with CO_2 to give the cross virial coefficients in Table II and Figure 2, no distinction was made between complexed and uncomplexed alcohol. That is, the virial coefficient values listed are "apparent" in that they are defined in terms of an apparent fugacity coefficient, $\phi_2^{app} = f_2^l/y_2^{tot}P$, as

$$\ln \phi_2^{app} = (2/V)[y_2^{tot}B_{22}(T) + y_1 B_{12}^{app}(T)] - \ln Z \quad (6)$$

Combining eq 5 and 6 it follows that since both y_2^{tot} and y_2 are assumed small

$$\ln \phi_2^{app} - \ln \phi_2 \cong (2/V)[B_{12}^{app}(T) - B_{12}(T)] = -\ln[K_c/V + 1] \cong -K_c/V + \ldots$$

so that

$$[B_{12}^{app}(T) - B_{12}(T)] \cong -Kc/2 \cong -RT/2K_p \quad (7)$$

where K_p is the equilibrium constant for dissociation expressed in the usual units of pressure. While the derivations leading to eq 5 and 7 are simple indeed, it is important to note that in no way do they invoke any artificial separation of intermolecular potential functions, the validity of which has been the subject of some question.[39]

Values of K_p for the proposed association of ethanol with CO_2 have been calculated using the difference between experimental values of $B_{12}(T)$ for the ethanol–CO_2 and propane–CO_2 systems as $[B_{12}^{app}(T) - B_{12}(T)]$ in eq 7. One obtains values of 91 ± 6, 141 ± 8, and 190 ± 10

atm for K_p at 25, 50, and 75°, respectively. The standard enthalpy and entropy for dissociation (standard state of 1 atm, 298°K) corresponding to these equilibrium constants are $\Delta H^\circ = 3.2 \pm 0.5$ kcal/mol and $\Delta S^\circ = 20 \pm 2$ eu. These are essentially identical with those characterizing the association of methanol with CO_2[6] but somewhat smaller than found in the case of water with CO_2.[5]

In the case of ethanol with N_2O, a comparison of the virial coefficients in Table I with those found for methanol and the same gases[6] reveals that cross virial coefficients fitted to ethanol–nitrous oxide solubility data are more negative relative to those of the other gases than was found in the case methanol. This suggests that N_2O may also form weak adducts with ethanol in the gas phase. The assumption that the parallelism noted earlier between cross virial coefficients resulting from physical interactions and gas polarizability extends to N_2O leads one to infer that the complexes formed between ethanol and N_2O are considerably weaker than those involving carbon dioxide. Unfortunately, no propane–N_2O virial coefficient data are available for quantitative comparisons.

Acknowledgment. The authors are grateful for support provided by the National Science Foundation as a grant (NSF Grant No. GP-29324) and in the form of summer support for one of us (R. D. L.) through the NSF Undergraduate Research Participation Program GY-9859.

Supplementary Material Available. A listing of the experimentally determined vapor mole fraction data will appear following these pages in the microfilm edition of this volume of the journal. Photocopies of the supplementary material from this paper only or microfiche (105 × 148 mm, 20 × reduction, negatives) containing all the supplementary material for the papers in this issue may be obtained from the Journals Department, American Chemical Society, 1155 16th St., N.W., Washington, D. C. 20036. Remit check or money order for $3.00 for photocopy or $2.00 for microfiche, referring to code number JPC-73-2011.

References and Notes

(1) This work was supported by the National Science Foundation.
(2) W. Hempel and J. Seidel, *Berichte*, **31**, 3000 (1898).
(3) E. Baur and M. Namek, *Helv. Chim. Acta*, **23**, 1101 (1940).
(4) J. H. Hildebrand and R. L. Scott, "The Solubility of Nonelectrolytes," Reinhold, New York, N. Y., 1950; reprinted by Dover Publications, New York, N. Y., 1964, p 243.
(5) C. R. Coan and A. D. King, Jr., *J. Amer. Chem. Soc.*, **93**, 1857 (1971).
(6) B. Hemmaplardh and A. D. King, Jr., *J. Phys. Chem.*, **76**, 2170 (1972).
(7) See paragraph at end of paper regarding supplementary material.
(8) J. M. Prausnitz and P. R. Benson, *AIChE J.*, **5**, 161 (1959).
(9) J. Timmermans, "Physico-Chemical Constants of Pure Organic Compounds," Vol. 1, Elsevier, New York, N. Y., 1950.
(10) T. E. Jordan, "Vapor Pressures of Organic Compounds," Interscience, New York, N. Y., 1954.
(11) A. Lannung, *J. Amer. Chem. Soc.*, **52**, 68 (1930).
(12) G. Just, *Z. Phys. Chem.*, **37**, 342 (1901).
(13) A. S. McDaniel, *J. Phys. Chem.*, **15**, 587 (1911).
(14) F. L. Boyer and L. J. Bircher, *J. Phys. Chem.*, **64**, 1330 (1960).
(15) J. Chr. Gjaldback and H. Niemann, *Acta Chem. Scand.*, **12**, 1015 (1958).
(16) C. Bohr, *Ann. Phys.*, **1**, 244 (1900).
(17) W. Kunnerth, *Phys. Rev.*, **19**, 519 (1922).
(18) R. Wiebe, V. L. Gaddy, and C. Heins, Jr., *J. Amer. Chem. Soc.*, **53**, 1721 (1931).
(19) A. Michels and M. Goudeket, *Physica*, **8**, 347 (1941).
(20) A. Michels, H. Wijker, and H. K. Wijker, *Physica*, **15**, 627 (1949).
(21) A. Michels and G. W. Nederbragt, *Physica*, **3**, 569 (1936).
(22) A. Michels, S. R. DeGroot, and M. Geldermans, *Appl. Sci. Res.*, **A1**, 55 (1947).
(23) J. A. Beattie, N. Poffenberger, and C. Hadlock, *J. Chem. Phys.*, **3**, 93 (1935).
(24) A. Michels and C. Michels, *Proc. Roy. Soc., Ser. A*, **153**, 201 (1935).
(25) L. J. Hirth and K. A. Kobe, *J. Chem. Eng. Data*, **6**, 233 (1961).
(26) J. H. Dymond and E. B. Smith, "The Virial Coefficients of Gases," Oxford University Press, London, 1969.
(27) J. Brewer, "Determination of Mixed Virial Coefficients," Final Report, Dec 1967, Contract No. AF 49(638)-1620, AFOSR, NTIS No. AD 663 448.
(28) D. McA. Mason and B. E. Eakin, *J. Chem. Eng. Data*, **6**, 499 (1961).
(29) J. A. Huff and T. M. Reed, III, *J. Chem. Eng. Data*, **8**, 306 (1963).
(30) E. M. Dantzler, C. M. Knobler, and M. L. Windsor, *J. Phys. Chem.*, **72**, 676 (1968).
(31) S. T. Sie, W. Van Beersum, and G. W. A. Rijnders, *Sep. Sci.*, **1**, 459 (1966).
(32) A. D. King, Jr., *J. Chem. Phys.*, **49**, 4083 (1968).
(33) H. Bradley, Jr., and A. D. King, Jr., *J. Chem. Phys.*, **52**, 2851 (1970).
(34) G. C. Najour and A. D. King, Jr., *J. Chem. Phys.*, **52**, 5206 (1970).
(35) S. K. Gupta and A. D. King, Jr., *Can. J. Chem.*, **50**, 660 (1972).
(36) S. Kielich, *Acta Phys. Pol.*, **20**, 433 (1961).
(37) J. A. Pople, *Proc. Roy. Soc., Ser. A*, **221**, 508 (1954).
(38) Previously unreported data from this laboratory. Experimental data available upon request.
(39) L. S. Moore and J. P. O'Connell, *J. Phys. Chem.*, **76**, 890 (1972).

Solubility of Alcohols in Compressed Gases. A Comparison of Vapor-Phase Interactions of Alcohols and Homomorphic Compounds with Various Gases. II. 1-Butanol, Diethyl Ether, and *n*-Pentane in Compressed Nitrogen, Argon, Methane, Ethane, and Carbon Dioxide at 25°[1]

R. Massoudi and A. D. King, Jr.*

Department of Chemistry, University of Georgia, Athens, Georgia 30602 *(Received February 12, 1973)*

The vapor concentrations of 1-butanol, diethyl ether, and *n*-pentane have been determined as a function of pressure in a series of compressed gases, including carbon dioxide. Second cross virial coefficients representing deviations from ideality caused by bimolecular interactions of these three compounds with the individual gases have been evaluated from the data. With the exception of CO_2, the cross virial coefficients of each of the three homomorphic molecules with a given gas are found to be the same within experimental error. In the case of CO_2, it is found that the cross virial coefficients of 1-butanol and diethyl ether with CO_2 are similar in magnitude but considerably larger than that resulting from pentane-CO_2 interactions. This anomaly is interpreted as indicating that the alcohol and ether undergo a reversible association with CO_2 in the gas phase.

Introduction

In a series of papers reporting vapor compositions at elevated pressures for various compressed gases in equilibrium with liquid water,[2] methanol,[3] and ethanol,[4] considerable evidence has accumulated indicating that weak complexation occurs between gaseous CO_2 and vapors of these oxygen containing liquids. Various arguments based on comparisons involving N_2O and CO_2,[3] solubility measurements of chloroform in dense gases,[4] as well as theory[3,4] all suggest that the stabilization leading to the formation of these complexes does not arise from electrostatic forces but rather involves either hydrogen bonding or the direct interaction of the oxygen atom of the vapor molecules with CO_2, either through a simple donor-acceptor mechanism or possibly an esterification reaction leading to carbonic acid or its monoalkyl esters. This paper reports an extension of the above studies in which gas-phase solubility measurements are used to compare the vapor-phase behavior of three homomorphs, 1-butanol, diethyl ether, and *n*-pentane in dilute gaseous solutions involving various unreactive gases as well as carbon dioxide.

Experimental Section

The experimental apparatus and techniques used in this work are the same as those outlined in a previous paper.[5] The *n*-pentane, diethyl ether, and 1-butanol used in these experiments were reagent grade or the equivalent.

Results and Discussion

In this study, vapor compositions have been determined as a function of total pressure for two phase systems involving three homomorphic liquids, *n*-pentane, diethyl ether, and 1-butanol with a series of gases including CO_2, all at 25°. The vapor composition data determined in these experiments will not be listed here for the sake of brevity but can be obtained from this journal.[6] Second cross virial coefficients representing deviations from ideality resulting from bimolecular interactions between molecules of the liquid component and those of the gas have been evaluated from the vapor composition-pressure data, as outlined in the previous paper, and are listed in Table I. Values for molar volumes and vapor pressures of the pure liquids used in these calculations were taken from ref 7-9. The pure component virial coefficients required were obtained from ref 10.

The only additional information required for these calculations is a knowledge of the liquid-phase composition as a function of pressure. This was estimated by using Henry's law expressed in terms of fugacity. The Henry's law constants used in these calculations are listed in Table II.[11-16] It is seen that in many cases experimental gas solubility data were not available from the literature. Fortunately, for systems where chemical interactions are unimportant, reliable estimates of gas solubility can be obtained using a method developed by Shair and Prausnitz.[17] Correlations given by these authors suggest that Henry's law constants can be estimated to an accuracy of better than 10% for the systems of interest here. Since the values calculated for $B_{12}(T)$ are relatively insensitive to gas solubility at the pressures of these experiments, inclusion of an assumed error of 10% for K_H leads to a total error of only ±30 cc/mol for diethyl ether and pentane with C_2H_6, and ±12, ±8, and ±7 cc/mol for pentane with CH_4, Ar, and N_2, respectively. The solubilities of CO_2 in *n*-pentane and diethyl ether were determined in this laboratory by a very simple technique in which known amounts of these solvents are first saturated with CO_2 then allow to react with standardized aqueous solutions of sodium hydroxide. After the extraction of CO_2 is complete, the remaining sodium hydroxide is titrated with strong acid to the bicarbonate end point. The number of equivalents of acid necessary to effect this is subtracted from that required to neutralize an equal volume of the pure sodium hydroxide solution, the difference being equal to the number of moles of CO_2 extracted from the known volume of organic solvent. The results obtained

using this method were checked against literature values for several CO_2–solvent systems and the agreement was excellent.

An inspection of the data in Table I shows that the values obtained here for systems involving *n*-pentane generally agree, within experimental error, with values obtained from high-pressure gas–liquid chromatography. They are, however, consistently outside the estimates of error and smaller in magnitude than those derived from *PVT* measurements. A detailed review of our experimental procedure and methods of calculation show no source of error in this work which could lead to such a discrepancy.

Secondly, it is seen that the second cross virial coefficients of the three homomorphs with nonreactive gases are the same within experimental error. This is, of course, not unexpected since there is no reason to expect purely physical interactions to differ significantly among these systems. As pointed out previously,[4] this close similarity suggests that any decrease in dispersion forces among the oxygen-containing systems (relative to *n*-pentane) arising from the fact that an oxygen atom is less polarizable than a methylene group is either insignificant or is cancelled out by the additional dipole–induced dipole attraction.

In contrast with this, it is seen that with carbon dioxide, the cross virial coefficients of the alcohol and ether are considerably more negative than the value for pentane with CO_2. If the cross virial coefficient for pentane with CO_2 is taken as representative of the deviations from ideality caused by physical forces in these systems, then one concludes that the excessively large values for the oxygen-containing homomorphs with CO_2 reflect contributions arising from chemical interactions. While it can be argued that dipole–quadrupole and dipole–induced dipole forces provide additional modes of attraction which are absent in the CO_2–*n*-pentane system, estimates based on derivations by Pople[18] and Kielich[19] show that such interactions would be expected to contribute approximately -10 cm^3/mol to the second cross virial coefficients of these systems. This is far less than the observed discrepancies which are the order of 100–200 cm^3/mol.

If it is assumed that the differences between the virial coefficients of the alcohol and ether with CO_2 and that for *n*-pentane with CO_2 result from an increase in vapor concentration caused by bimolecular complex formation of the oxygen-containing homomorphs with CO_2, then one can arrive at values for the equilibrium constant for dissociation of the complex, K_p, from the simple relationship[4]

$$\Delta B = B(T)_{\text{alc, ether CO}_2} - B(T)_{\text{pent CO}_2} = -RT/2K_p \quad (1)$$

Here all symbols have their usual meaning and the subscripts are self-explanatory. On substituting the values in the last row of Table I in eq 1, one obtains values of K_p = 87 ± 23 and 56 ± 12 atm for the complexes of 1-butanol and diethyl ether with CO_2 at 25°. The value for 1-butanol is essentially the same as K_p = 91 atm found for the lower alcohols, methanol and ethanol, with CO_2 at this temperature.

The inability of an ether to form a hydrogen bond or an ester with an acid anhydride like CO_2 suggests strongly that the complex formed between diethyl ether and CO_2 is of a charge transfer type, presumedly involving donation of lone pair electrons localized on the ether oxygen atom to an antibonding orbital of CO_2. While it can not be proven in the absence of direct spectroscopic observations, it is not unreasonable to assume that the chemical bonding responsible for the alcohol–CO_2 complexes is of a similar nature. The observed trend in the dissociation constants with the ether having a similar but somewhat smaller value than the alcohol is in keeping with such an assumption.

TABLE I: Second Cross Virial Coefficients for 1-Butanol, Diethyl Ether, and *n*-Pentane with Various Gases[a]

	B_{12} (25°)		
Gas	1-Butanol	Diethyl ether	*n*-Pentane
N_2	-72 ± 10[b]	-67 ± 9	-77 ± 7 (-103 ± 6[c])
Ar	-90 ± 11	-89 ± 6	-97 ± 8 (-98 ± 6,[c] -125 ± 23[d])
CH_4	-160 ± 12	-161 ± 3	-170 ± 12 (-207 ± 42,[e] -218,[f] -222 ± 13[g])
C_2H_6	-375 ± 35	-388 ± 30	-386 ± 30 (-414 ± 171,[e] -448 ± 16[g])
CO_2	-414 ± 14	-491 ± 23	-273 ± 23

[a] Literature values for *n*-pentane shown in parentheses. [b] Error expressed as average deviation from mean. [c] A. J. B. Cruickshank, M. L. Windsor, and C. L. Young, *Proc. Roy. Soc., Ser. A*, **295**, 271 (1966); glc method. [d] E. M. Dantzler, C. M. Knobler, and M. L. Windsor, *J. Chromatogr.*, **32**, 433 (1968); *PVT* method. [e] R. L. Pecsok and M. L. Windsor, *Anal. Chem.*, **40**, 1238 (1968); glc method. [f] Sh. D. Zaalishvili, *Zh. Fiz. Khim.*, **30**, 1891 (1956) *PVT* method. [g] E. M. Dantzler, C. M. Knobler, and M. L. Windsor, *J. Phys. Chem.*, **72**, 676 (1968); *PVT* method.

TABLE II: Henry's Law Constants for 1-Butanol, Diethyl Ether, and *n*-Pentane with Various Gases at 25°

Liquid	Gas	K_H, atm	Ref
1-Butanol	N_2	2110	11
	Ar	1080	11
	CH_4	524	11
	C_2H_6	91.7	11
	CO_2	134	12
Diethyl ether	N_2	799	13
	Ar	390	14
	CH_4	221	13
	C_2H_6	29.6	15
	CO_2	29.6	16
n-Pentane	N_2	665	15
	Ar	357	15
	CH_4	197	15
	C_2H_6	28.5	15
	CO_2	64.7	16

Acknowledgment. The authors are grateful for support provided by the National Science Foundation (NSF Grant No. GP-29324).

Supplementary Material Available. A listing of the experimentally determined vapor mole fraction data will appear following these pages in the microfilm edition of this volume of the journal. Photocopies of the supplementary material from this paper only or microfiche (105 × 148 mm, 20 × reduction, negatives) containing all the supplementary material for the paper in this issue may be obtained from the Journals Department, American Chemical Society, 1155 16th St., N.W., Washington, D. C. 20036. Remit check or money order for $3.00 for photocopy or $2.00 for microfiche, referring to code number JPC-73-2016.

References and Notes

(1) This work was supported in part by the National Science Foundation (NSF Grant No. GP-29324).
(2) C. R. Coan and A. D. King, Jr., *J. Amer. Chem. Soc.*, **93**, 1857 (1971).
(3) B. Hemmaplardh and A. D. King, Jr., *J. Phys. Chem.* **76**, 2170 (1972).
(4) S. K. Gupta, R. D. Lesslie, and A. D. King, Jr., *J. Phys. Chem.*, **77**, 2011 (1973).
(5) C. R. Coan and A. D. King, Jr., *J. Chromatogr.*, **44**, 429 (1969).
(6) See paragraph at end of paper regarding supplementary material.
(7) R. R. Dreisbach, *Advan. Chem. Ser.*, **No. 22** (1959).
(8) E. D. Washburn, Ed., "International Critical Tables," Vol. 3, McGraw-Hill, New York, N. Y., 1928.
(9) T. E. Jordan, "Vapor Pressures of Organic Compounds," Interscience, New York, N. Y., 1954.
(10) J. H. Dymond and E. B. Smith, "The Virial Coefficients of Gases," Oxford University Press, London, 1969.
(11) F. L. Boyer and L. J. Bircher, *J. Phys. Chem.*, **64**, 1330 (1960).
(12) R. Mayer and M. Hoffman, *J. Prackt. Chem.*, **11**, 327 (1960).
(13) J. Horiuti, *Sci. Pap. Inst. Phys. Chem. Res., Tokyo*, **17**, no. 311, 125 (1931). Cited in J. H. Hildebrand and R. L. Scott, "The Solubility of Nonelectrolytes," Reinhold, New York, N. Y., 1950; reprinted by Dover Publications, New York, N. Y., 1964, p 243.
(14) W. F. Linke, Seidell, Ed., "Solubilities of Inorganic and Metal-Organic Compounds," 3rd ed, Van Nostrand, Princeton, N. J., 1958.
(15) Calculated using method of ref 17.
(16) Measured in this laboratory.
(17) J. H. Hildebrand, J. M. Prausnitz, and R. L. Scott, "Regular and Related Solutions," Van Nostrand-Reinhold, New York, N. Y., 1970, p 125.
(18) J. A. Pople, *Proc. Roy. Soc., Ser. A*, **221**, 508 (1954).
(19) S. Kielich, *Acta Phys. Pol.*, **20**, 433 (1961).

COMMUNICATIONS TO THE EDITOR

On the Partial Molal Volume of Helium in Water and Aqueous Sodium Chloride Solutions

Publication costs assisted by the National Science Foundation

Sir: Recently Gardiner and Smith[1] have reported some excellent new data for the solubility of helium in water and aqueous NaCl solutions. The experimental results compare favorably with the best values previously available[2] due to an improved reduction of the raw data including a necessary meniscus correction. However, we would like to offer as a possibility an alternative thermodynamic analysis and interpretation of the experimental results.

There are two expressions commonly used to evaluate the effects of pressure on gas solubility,[3] and it is essential to recognize the assumptions involved. Basically, both stem from the expression of the fugacity of the ith component in the liquid phase f_i in terms of its mole fraction x_i, an activity coefficient γ_i, and a reference state fugacity f_i^0

$$f_i = x_i \gamma_i f_i^0 \qquad (1)$$

The Krichevsky-Kasarnovsky equation[4,5] assumes for a binary mixture that the reference state is the infinitely dilute solute 2 in pure solvent 1, at the temperature and total pressure of the mixture, and that γ_2 is unity.

$$\ln (f_2/x_2) = \ln H_{2,1} + \left[\int_{P_1^s}^{P} \bar{v}_2^{\infty} \, dP/RT \right] \qquad (2)$$

where $H_{2,1}$ is the Henry's law constant for 2 in 1 defined at the saturation pressure P_1^s, and $\bar{v}^2$ is the partial molal volume at infinite dilution. The last term in eq 2 corrects the reference state fugacity $H_{2,1}$ from pressure P_1^s to the reference pressure, chosen as P.

Unless the solvent is expanded (*i.e.*, near its critical point) the usual assumption is that the compressibility of the solute is not unusually large;[3] thus $\bar{v}_2^{\infty}$ is relatively pressure independent, and the last term may be integrated

$$\ln (f_2/x_2) = \ln H_{2,1} + [\bar{v}_2^{\infty}(P - P_1^s)/RT] \qquad (3)$$

Equation 3 may be used to analyze data in the dilute range (low x_2, where $\gamma_2 = 1$) generally by plots of $\ln (f_2/x_2)$ *vs.* P to yield straight lines giving two unknown parameters, $H_{2,1}$ from the intercept and $\bar{v}_2^{\infty}$ from the slope. At higher concentrations, it has frequently been noted that curvature occurs,[3] and this is presumed to be due to deviations from Henry's law ($\gamma_2 \neq 1$). In the unsymmetric convention, the simplest possible nontrivial solution to the Gibbs-Dichem equations is a one-term Margules expression, which yields the Krichevsky-Ilinskaya equation[6]

$$\ln \frac{f_2}{x_2} = \ln H_{2,1} + \frac{\int_{P_1^s}^{P} \bar{v}_2^{\infty} \, dP}{RT} + \frac{A}{RT}(x_1^2 - 1) \qquad (4)$$

where even if $\bar{v}_2^{\infty}$ is assumed constant, there are three parameters to be evaluated from the data, and quite extensive and accurate data are needed to evaluate so many parameters.

Smith and his coworkers[1,7] have chosen to interpret curvature in terms of variation of $\bar{v}_2^{\infty}$ with pressure, assuming that the coefficient of isothermal compressibility β is a constant. This in effect introduces three parameters into eq 2 and certainly precludes any attempt to look at variations in γ_2. Although the possibility of variation of $\bar{v}_2^{\infty}$ with concentration is discussed, this is clearly not possible, as the definition of the reference state *defines* the concentration at which $\bar{v}_2^{\infty}$ must be evaluated, that is at $x_2 = 0$.

By this analysis, some astounding values of β resulted, ranging from a negative compressibility of -30×10^{-5} atm^{-1} in pure water at 25° to $+150 \times 10^{-5}$ atm^{-1} in water and one solution at 100°. For comparison β for pure water is just below 5×10^{-5} atm^{-1} over this range, while for most organics, not near their critical points, the range is $4\text{-}20 \times 10^{-5}$ atm^{-1}. Gardiner and Smith explain their negative values in terms of the effect of dissolved helium on the structure of the water.

We wish to offer as an alternative possibility that although there does appear to be slight curvature in some of the data sets, the five or six points per set do not justify fitting three adjustable parameters, nor do they justify the decision of whether such curvature is due to compressibility of the solute rather than due to deviations from Henry's law. We find that the two-parameter eq 3 represents the actual (not smoothed) experimental data to at least the degree of its precision, and gives superior values of $H_{2,1}$ and $\bar{v}_2^{\infty}$.

Rather than the smoothed data presented in ref 1, we fit the actual experimental points[8] and found that at 25 and 50° the precision of the fit of eq 3, with constant $\bar{v}_2^{\infty}$, was virtually as good as the three-parameter fit, and within probable experimental error. Moreover, the values of the Henry's law constants thus determined (see Table I) appear to be in at least as good agreement with literature data as those reported in ref 1. At 100° we found that even a three-constant fit of the $\ln (f_2/x_2)$ data gave standard deviations of 3-5%. Thus although compressibility of the solute would be greatest at the highest temperature, the data do not appear to justify evaluation of three parameters.

The only value of $\bar{v}_2^{\infty}$ for which comparison can be made is that for helium in pure water at 50°. Using eq 3

TABLE I: Henry's Law Constants and Partial Molal Volumes for Helium in Water and Aqueous NaCl Solutions

Temp, °C	Solvent	Eq 3		$H_{2,1}$, atm × 10^{-5} (ref 1)	$H_{2,1}$, atm × 10^{-5} (ref 9)
		$\bar{v}_2^\infty$, cc/mol	$H_{2,1}$, atm × 10^{-5}		
25	1.003 *m* NaCl	15.6	1.78	1.790	1.80
	4.067 *m* NaCl	14.7	3.31	3.041	3.36
50	H_2O	15.3	1.42	1.337	1.43, 1.44
	1.003 *m* NaCl	14.4	1.78	1.698	
	4.067 *m* NaCl	17.9	3.06	2.917	
100	H_2O	21.1	1.32	1.197	1.04, 1.10
	1.003 *m* NaCl	23.1	1.57	1.390	
	4.067 *m* NaCl	20.8	2.64	2.495	

we find 15.3 cc/mol from the data in ref 1, and exactly the same value from those in ref 2a. Using their three-parameter fit, Gardiner and Smith[1] reported a value of 26.9 cc/mol from their data and 20.0 cc/mol from the data of ref 2a. Since there are such large discrepancies between the values of $\bar{v}_2^\infty$ calculated from eq 3 and those reported by Gardiner and Smith, we suggest that a feasible approach for choosing between these alternative interpretations could be the experimental determination of $\bar{v}_2^\infty$ from dilatometric data at modest pressures. However, the experimental determination of β for helium would be most difficult, requiring high-pressure dilatometry.

In conclusion, we feel that the unusual values of β found for helium may not be real, but rather the results of smoothing and round-off in the data reduction. A great many extraordinarily precise data would be required for the evaluation of three adjustable parameters to verify such possible compression of a dissolved gas, and for the data reported, the Krichevsky-Kasarnovsky equation gives an adequate representation.

Acknowledgment. The authors are grateful to the National Science Foundation for financial support, and they wish to express their appreciation to Professor Smith for supplying the original experimental data.

References and Notes

(1) G. E. Gardiner and N. O. Smith, *J. Phys. Chem.*, **76**, 1195 (1972).
(2) (a) R. Wiebe and V. L. Gaddy, *J. Amer. Chem. Soc.*, **57**, 847 (1935); (b) H. A. Pray, C. E. Schweikert, and B. H. Minnich, *Ind. Eng. Chem.*, **44**, 1146 (1952).
(3) J. M. Prausnitz, "Molecular Thermodynamics of Fluid-Phase Equilibria," Prentice-Hall, Englewood Cliffs, N. J., 1969, Chapter 8.
(4) I. R. Krichevsky and J. S. Kasarnovsky, *J. Amer. Chem. Soc.*, **57**, 2168 (1935).
(5) B. F. Dodge and R. H. Newton, *Ind. Eng. Chem.*, **29**, 718 (1937).
(6) I. R. Krichevsky and A. A. Ilinskaya, *Zh. Fiz. Khim. USSR*, **19**, 621 (1945).
(7) T. D. O'Sullivan and N. O. Smith, *J. Phys. Chem.*, **74**, 1460 (1970).
(8) N. O. Smith, personal communication, 1972.
(9) (a) T. J. Morrison and N. N. B. Johnstone, *J. Chem. Soc.*, 3441 (1954); (b) T. J. Morrison and N. N. B. Johnstone, *ibid.*, 3655 (1955); (c) S. K. Shorr, R. D. Walker, Jr., and K. E. Gubbins, *J. Phys. Chem.*, **73**, 312 (1969).

Department of Chemical Engineering
School of Chemical Sciences
University of Illinois, Urbana 61801

C. K. Hsieh
C. A. Eckert*

Received March 2, 1973

Journal of Chemical and Engineering Data

JULY 1973, Vol. 18, No. 3

TABLE OF CONTENTS

■Supplementary material for this paper is available separately, in photocopy or microfiche form. Ordering information is given in the paper.

The leading American journal devoted to general organic chemistry:

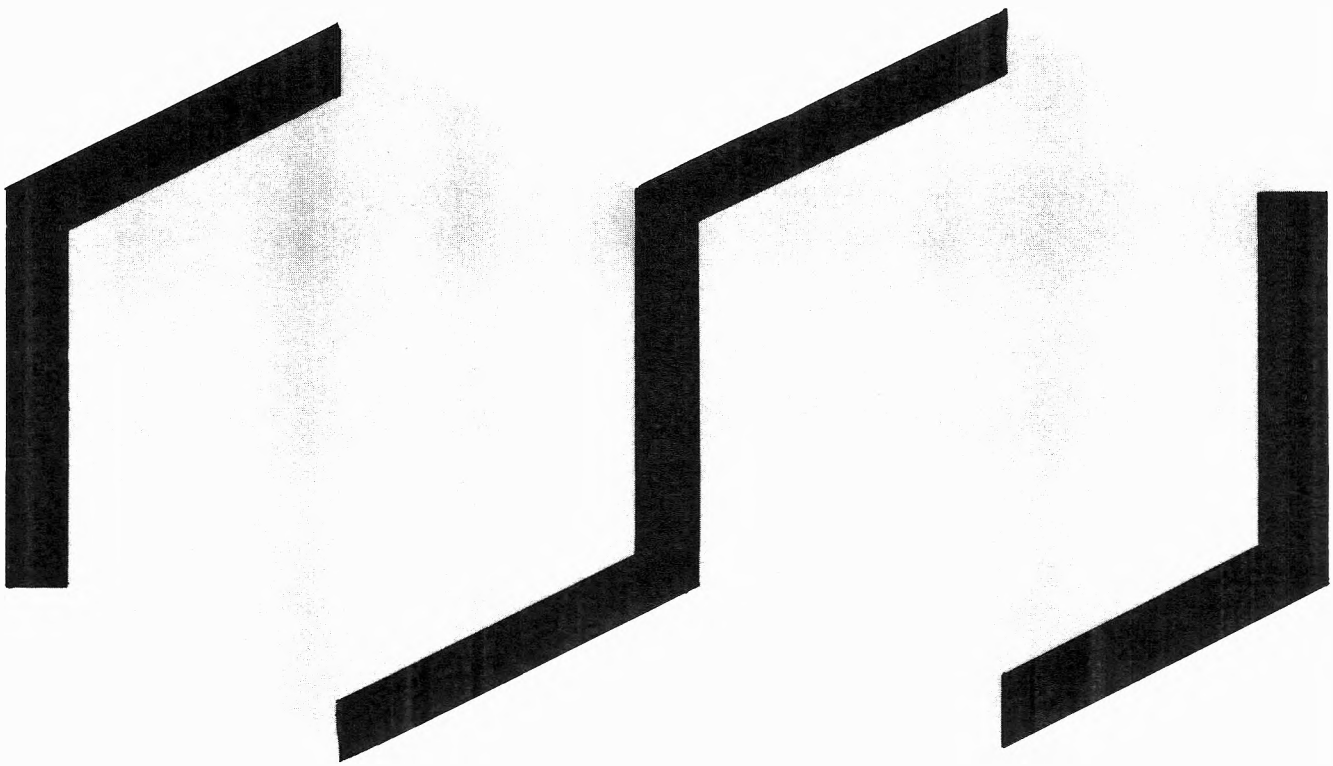

The Journal of Organic Chemistry

The career wise way to keep up with current thinking in the field. You get the *total picture* presented through forty some papers per biweekly issue. Areas of emphasis include:

- Organic reactions
- Natural products
- Studies of mechanism
- Theoretical organic chemistry
- Various aspects of spectroscopy related to organic chemistry

You get all of this, in the 1100 articles and NOTES (brief, concise accounts of studies of smaller scope) and over 4000 pages a year from your big informative issues of THE JOURNAL.

You owe it to your career to find out for yourself why The Journal of Organic Chemistry is the leader in its field.

Send your order today.

. . . *another ACS service*

The Journal of Organic Chemistry
American Chemical Society
1155 Sixteenth Street, N.W.
Washington, D.C. 20036

Yes, I would like to receive THE JOURNAL OF ORGANIC CHEMISTRY at the one-year rate checked below:

	U.S.	*Canada*	*Latin America*	*Other Nations*
ACS Member Personal-Use One-Year Rate	☐ $20.00	☐ $25.00	☐ $25.00	☐ $26.00
Nonmember	☐ $60.00	☐ $65.00	☐ $65.00	☐ $66.00

Bill me ☐ Bill company ☐ Payment enclosed ☐

Name _____

Street _____ Home ☐ Business ☐

City _____ State _____ Zip _____

G-73

You don't have to search the archives for data . . .

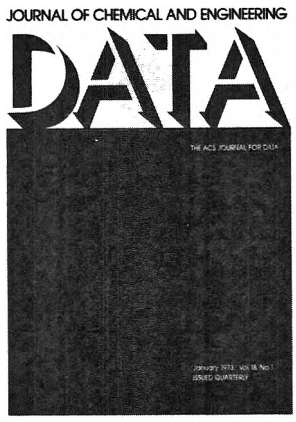

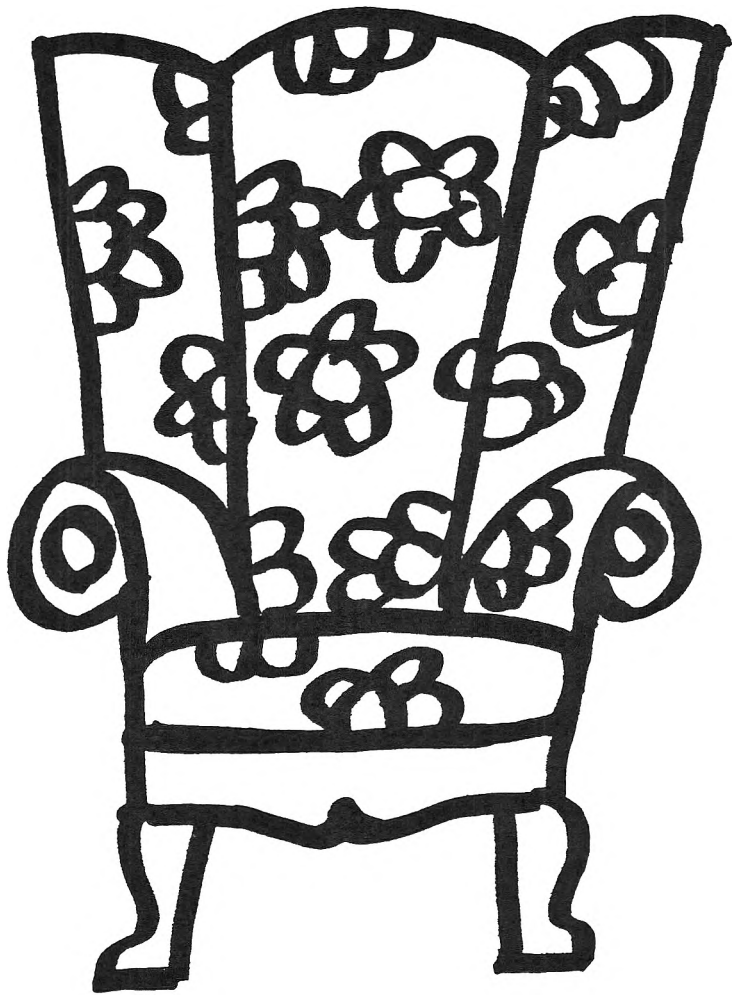

. . . because THE JOURNAL OF CHEMICAL AND ENGINEERING DATA will bring precise, reliable, useful technical information right to your fingertips quarterly! With a year's subscription, you'll receive a total of over 500 pages of valuable science and engineering data that are especially relevant now in light of today's new instrumentation. The information in JCED includes:

- experimental data relating to pure compounds or mixtures covering a range of states;
- manuscripts based on published experimental information which make tangible contributions through their presentation or which set forth a sound method of prediction of properties as a function of state;
- experimental data which aid in identifying or utilizing new organic or inorganic compounds; and
- papers relating primarily to newly developed or novel synthesis of organic compounds and their properties.

Start to benefit now from this "armchair" source of pertinent technical data—with your own personal subscription to JCED . . . just complete and return the form below . . . get your data without the dust.

. . . *another ACS service*

Journal of Chemical & Engineering Data
American Chemical Society
1155 Sixteenth Street, N.W.
Washington, D.C. 20036

Yes, I would like to receive the JOURNAL OF CHEMICAL & ENGINEERING DATA at the one-year rate checked below:

	U.S.	*Canada*	*Latin America*	*Other Nations*
ACS Member Personal-Use One-Year Rate	☐ $15.00	☐ $18.00	☐ $18.00	☐ $18.50
Nonmember	☐ $45.00	☐ $48.00	☐ $48.00	☐ $48.50

Bill me ☐ Bill company ☐ Payment enclosed ☐

Name _____

Street _____ Home ☐ Business ☐

City _____ State _____ *Zip* _____

T-73

Journal of Chemical & Engineering Data